Low Temperature Quantum Sensing with Single Nitrogen-Vacancy Centers in Diamond

Inauguraldissertation

zur
Erlangung der Würde eines Doktors der Philosophie
vorgelegt der
Philosophisch-Naturwissenschaftlichen Fakultät
der Universität Basel

von

Jodok Maria Happacher

Basel, 2025

Genehmigt von der Philosophisch-Naturwissenschaftlichen Fakultät
auf Antrag von

Erstbetreuer: Prof. Dr. Patrick Maletinsky
Zweitbetreuer: Prof. Dr. Martino Poggio
Externer Experte: Prof. Dr. Neil B. Manson

Basel, den 17.10.2023

Prof. Dr. Marcel Mayor
Dekan

Abstract

Color centers in solid-state hosts are important for a variety of quantum technologies. Among the many available systems, the Nitrogen-Vacancy (NV) center in diamond stands out due to its remarkable optical and spin properties, which have led to multiple demonstrated applications in areas such as quantum information processing and quantum sensing, including promising use-cases of scanning magnetometry at cryogenic temperatures.

The NV ground state (GS) is well-studied, and most applications of NV centers rely on the highly coherent ground state electron spin and the ability to efficiently initialize and read out this spin optically. These techniques are based on a spin-dependent intersystem crossing (ISC) from the NV's excited state (ES) to a metastable spin-singlet manifold, from which the system decays into a well-defined spin sublevel of the NV's ground state. This intersystem crossing, and therefore the mechanism of NV spin initialization and readout, results from the properties of the NV's orbital excited states and their coupling to the NV's singlet state.

The ES energy levels of the NV center are sensitive to magnetic and electric fields as well as crystal strain. They exhibit a strong electron-phonon interaction activated by temperature, which leads to an effective ES orbital structure that differs markedly in going between cryogenic and ambient conditions. Although the specific excited state level structure and its effect, particularly on the optical spin contrast, are crucial for many applications based on NV centers, their influence on the NV photophysics, especially at low temperatures, has received limited attention so far.

In this thesis, we close this gap and show how the orbital excited state structure affects the NV's photophysical properties under various experimental conditions. We first investigate the magnetic field-dependent photophysics of individual NV centers in diamond at low temperatures. At distinct magnetic fields, we observe significant reductions in the NV photoluminescence (PL) rate, resulting in a decrease in the optical readout efficiency of the ground-state spin. We assign these PL dips to excited state level anti-crossings (ESLACs), which occur at magnetic fields that strongly depend on the effective, local strain environment of the NV center. Our results offer new insights into the structure of the NVs' excited states and a new tool for their effective characterization at low temperatures. We observe strong indications for strain-dependent variations of the NV's orbital g-factor, explore the NV charge state dynamics in the singlet, and draw important conclusions regarding the applicability of NV centers for low-temperature quantum sensing.

We also extend our studies of the magnetic field-dependent photoluminescence to the temperature range from cryogenic to ambient conditions, to investigate the changes in the effective orbital structure of the excited state and its implications for the NV photophysics. We directly observe the emergence of the NV room-temperature effective excited state structure and provide a clear explanation for the previously poorly understood broad quenching of NV photoluminescence at intermediate tem-

peratures. We develop a model that quantitatively explains all of our experimental findings, including the strong impact of strain on the temperature dependence of the NV PL. These results complete our understanding of orbital averaging in the NV excited state and have significant implications for the photophysical properties of the NV center and its applications in quantum sensing at intermediate temperatures.

We further present our steps towards single-spin magnetometry implemented in a closed-cycle dilution refrigeration system operating at ultra-low temperatures. This system is designed to address open questions in condensed matter physics and expand the capabilities of the technique beyond current experimental limitations. We present the development and implementation of a scanning NV magnetometer probe with an integrated microwave near-field coupling device, designed for optimized spin driving, which is crucial for maintaining ultra-low temperatures. The broadband loop antenna is directly integrated into the attachment structure for the diamond scanning probe tip, which is created by a subtractive laser-exposure process followed by a single gold evaporation step. The manufacturing process involves only a few steps and does not rely on lithography. It is highly reproducible and yields robust devices that efficiently deliver stable microwave fields to the NV while reducing instrumentational complexity. This represents a significant improvement over state-of-the-art near-field microwave antennas used for low-temperature NV magnetometry. Additionally, we investigate the low-temperature charge stability of single near-surface NVs in our diamond scanning probes. In our cryostat, we encounter an NV^- electron loss which manifests as a gradual shift from an initially favoured NV^- to an NV^0 charge state. We describe the observed phenomenology in detail and present various mitigation strategies ranging from improving the vacuum environment and optical stabilization schemes to surface treatments, in order to enable long measurement times.

Finally, we propose new perspectives for further fundamental research on the NV system as well as future directions for technological work on extending the applicability of the NV center.

Contents

List of symbols and abbreviations

General symbols

t	Time
τ	Evolution time
T	Environmental temperature
λ	Optical wavelength
S	Total electron spin
m_s	Electron spin quantum number

NV center

C	Carbon
N	Nitrogen
V	Vacancy
x, y, z	NV coordinates
C_{3v}	Symmetry point group of the NV center
${}^3A_2$, ${}^3E$	NV^- ground and excited state manifolds
${}^1E$, ${}^1A_1$	NV^- singlet manifolds
${}^2E$, ${}^2A_2$	NV^0 ground and excited state manifolds
D_0^{GS}	Ground state zero-field splitting (ZFS)
$D_0^{\mathrm{ES}} := D_{es}^{\parallel}$	Effective excited state ZFS at room temperature
g_l	Orbital g-factor
$\lambda_{es}^{\perp}$, $\lambda_{es}^{\parallel}$	Excited state mixing terms
E_x, E_y	Excited state orbital branches
T_1	Spin relaxation time
T_2^*	Spin dephasing time
T_2	Spin coherence time
T_{Rabi}	Rabi decay time
Γ, γ, k	Relaxation rates
β	Optical pumping parameter
I_{PL}	NV photoluminescence signal
I_{PL}^0	NV^0 photoluminescence signal
I_{PL}^-	NV^- photoluminescence signal

$\mathcal{C}$	Optical spin contrast
$\Delta\nu$	ODMR linewidth
η	Magnetic field sensitivity

Static external fields

$\boldsymbol{B} = (B_x, B_y, B_z)$	Magnetic field in NV frame
B_{NV}, $B_{\parallel}$	Magnetic field amplitude along the NV axis
$B_{\perp}$	Transverse magnetic field amplitude
ϕ_B	Polar angle of the magnetic field
θ_B	Azimuthal angle of the magnetic field
$\boldsymbol{E} = (E_x, E_y, E_z)$	Electric field in NV frame
$E_{\perp}$	Transverse electric field amplitude
$E_{\parallel}$	Axial electric field amplitude
ϕ_E	Polar angle of the electric field
θ_E	Azimuthal angle of the electric field
$\boldsymbol{\delta} = (\delta_x, \delta_y, \delta_z)$	Strain field in NV frame
$\delta_{\perp}$	Transverse strain field amplitude
$\delta_{\parallel}$	Axial strain field amplitude
ϕ_{δ}	Polar angle of the strain field
θ_{δ}	Azimuthal angle of the strain field
$\boldsymbol{\Pi} = (\Pi_x, \Pi_y, \Pi_z)$	Effective field in NV frame
$\Pi_{\perp}$	Transverse effective field amplitude
$\Pi_{\parallel}$	Axial effective field amplitude
ϕ_{Π}	Polar angle of the strain field
θ_{Π}	Azimuthal angle of the strain field
Δ_Z	Zeeman splitting
Δ_S	Stark splitting
ξ	Strain-dependent parameter of the RT ES

States and operators

$\lvert m_s \rangle$	Ground state or excited state fine structure states
$\lvert \pm 1 \rangle$	Mixed ground state or excited state fine structure states
$\lvert X \rangle$,$\lvert Y \rangle$	State vectors of the ES E_x and E_y manifolds
$\hat{\mathcal{H}}_{gs}$	Effective fine structure ground state Hamiltonian
$\hat{\mathcal{H}}_{es}$	Effective fine structure excited state Hamiltonian
$\hat{\mathcal{V}}_{gs}$	Magnetic, electric and strain field potential for the GS
$\hat{\mathcal{V}}_{es}$	Magnetic, electric and strain field potential for the ES

$\hat{\boldsymbol{S}} = (\hat{S}_x, \hat{S}_y, \hat{S}_z)$	Dimensionless $S = 1$ spin operators
$\hat{\sigma}_x, \hat{\sigma}_y, \hat{\sigma}_z$	Pauli matrices
ρ	Density matrix
Tr_σ	Partial trace over orbital subsystem

Constants

$e = 1.602 \cdot 10^{-19}\,\mathrm{C}$	Elementary charge
$h = 6.626 \cdot 10^{-34}\,\mathrm{m^2\,kg/s}$	Planck constant
$\hbar = 1.055 \cdot 10^{-34}\,\mathrm{m^2\,kg/s}$	Reduced Planck constant
$\mu_\mathrm{B} = 9.274 \cdot 10^{-24}\,\mathrm{J/T}$	Bohr magneton
$k_\mathrm{B} = 1.380\,649 \cdot 10^{-23}\,\mathrm{J/K}$	Boltzmann constant
$\gamma_e = 27.9\,\mathrm{GHz/T}$	Gyromagnetic ratio of NV electron spin

Units

A	Ampere
cps	Counts per second
dB	Decibel
dBm or $\mathrm{dB_{mW}}$	Decibel milliwatts
eV	Electron volt
F	Farad
Hz	Hertz
K	Kelvin
kg	Kilogram
m	Meter
Ω	Ohm
Pa	Pascal
s	Second
T	Tesla
V	Volt
W	Watt

Abbreviations

AC	Alternating current
AFM	Atomic force microscopy
AOM	Acousto-optic modulator
APD	Avalanche photodiode
AWG	Arbitrary waveform generator
CFM	Confocal microscope
CVD	Chemical vapor deposition

CW	Continuous wave
DC	Direct current
ES	Excited state
ESLAC	Excited state level anticrossing
ESR	Electron spin resonance
FIB	Focused ion beam
GND	Ground
GS	Ground state
GSLAC	Ground state level anticrossing
IQ	In-phase and quadrature
ISC	Intersystem crossing
LAC	Level anticrossing
LT	Low temperature
MW	Microwave
NA	Numerical aperture
NIR	Near-infrared
NMR	Nuclear magnetic resonance
NV	Nitrogen-Vacancy
NV^-	Negatively charged NV center
NV^0	Neutrally charged NV center
NV^+	Positively charged NV center
ODMR	Optically detected magnetic resonance
OFHC	Oxygen-free high thermal conductivity copper
PCB	Printed circuit board
PDMR	Photoelectrically detected magnetic resonance
PL	Photoluminescence
PLE	Photoluminescence excitation
PSB	Phonon sideband
RF	Radio frequency
RT	Room temperature
RT-ESLAC	Room temperature exited state level anticrossing
SEM	Scanning electron microscope
SIL	Solid immersion lens
SiV	Silicon-Vacancy
SiV^-	Negatively charged SiV center
SiV^0	Neutrally charged SiV center
STM	Scanning tunneling microscope
TF	Tuning fork
TTL	Transistor–transistor logic
UV	Ultraviolet
VIS	Visible
VTI	Variable temperature inset
ZFS	Zero-field splitting
ZPL	Zero-phonon line

1. Introduction

After the discovery of quantum theory at the beginning of the last century [1], a lot of effort has been directed towards the in-depth understanding of its principles and possible applications. This has led to the development of technologies based on quantum effects, such as lasers and transistors, which have had a profound impact on science and transformed our society.

Recent experimental advances [2] have led to an unprecedented degree of control over various quantum systems, which enables us to go beyond a purely fundamental understanding and engage in practical quantum engineering. The development of physical platforms for quantum control is currently one of the most pursued scientific and technological objectives and supported by large government-led initiatives [3].

Quantum technologies will not only enable the investigation of fundamental questions in physics, but also allow concrete applications in the fields of computing, communication, and sensing. Harnessing the advantages of quantum properties represents a technological leap forward and has the potential to revolutionize how we measure physical quantities and how we interact with information.

These efforts are also driven by current technological challenges in the area of classical computer engineering, where incremental innovation of state-of-the-art approaches through transistor scaling reaches their physical limitations [4, 5]. Miniaturization does not yield the same increase in computational power as in the last decades due to the limitations of Joule's law and difficulties in gate design. This motivates novel technological approaches in the field of spintronics, where the electron spin is used for information processing [6]. Such paradigm change to using quantum degrees of freedom as information carriers could enable electronic devices to become smaller and more energy efficient as well as add new capabilities [7].

In this context, various physical systems are promising candidates for quantum engineering [2] and share certain common properties. DiVincenzo proposed a list of criteria for a quantum computer [8] which also apply more generally to quantum control necessary for quantum communications, quantum information processing, quantum simulations, and quantum sensing. Among these are the initialization of the quantum state, its manipulation, and readout, alongside long coherence times, all of which are ultimately necessary for quantum control.

A number of electronic spins in solid-state hosts possess all of these properties, some even at room temperature, and are therefore particularly attractive as quantum platforms to enable robust, scalable, and simple quantum systems [9]. Among the various solid-state quantum systems available, color centers stand out in particular due to their optical addressability and ease of use, even under extreme conditions. Many feature strong optical transitions and exceptionally long spin coherence lifetimes.

One of the most prominent color centers is the Nitrogen-Vacancy (NV) center in diamond [10] which is known for its versatility and its use over a large range of environmental conditions [11–13]. It has multiple demonstrated applications in quantum

information processing [14–17] and quantum sensing [18–21], in particular, the application as a magnetometer has gained widespread use in recent years due to excellent magnetic sensitivities [22]. It can be combined with atomic force microscopy (AFM) to provide a sensing modality known as scanning NV magnetometry or scanning NV magnetic imaging [23–25]. This approach has emerged as a leading technology for high-sensitivity imaging of nanoscale magnetic phenomena. Particularly interesting are recent advances in cryogenic scanning NV magnetometry [26–29], which have enabled the exploration of magnetic systems under low-temperature conditions.

The quantum state of the NV electron spin can be initialized [30, 31] and read out [32, 33] optically with high fidelity using simple, non-resonant optical driving while coherent quantum gate operations can be implemented by microwave pulses. The NV spin shows excellent quantum coherence times up to tens of milliseconds even at room temperature. At cryogenic temperatures, the ability to tune the optical transition of the NV center using electric fields [10, 34] allows for the use in quantum entanglement schemes and more generally quantum communication where single, indistinguishable photons are crucial [15].

The initialization and readout of the spin state with high fidelity is key for all these applications and their control schemes. The mechanism is based on a spin-dependent intersystem crossing [35, 36] from the NV's excited state (ES) to a metastable spin-singlet manifold and a subsequent decay to the NV's ground state (GS), which efficiently pumps the system into a well-defined GS spin sublevel [10]. The resulting spin readout contrast can be improved by increasing the overall photon collection [37] or through lifetime engineering [38].

While optical spin initialization and readout processes are well established [10] and thoroughly tested at room temperatures [31], they have only been sparsely explored under cryogenic conditions ($T < 100\,\mathrm{K}$). It is not obvious that the room-temperature model for NV spin readout contrast immediately applies in the same way to low temperature conditions when orbital averaging is suppressed [39, 40] and the rich NV orbital excited state structure emerges. Thus far, the photophysics of individual NVs in this regime has received limited attention, even though significant and unexplained reductions in NV photoluminescence (PL) and spin readout contrast have been observed in the context of low-temperature NV magnetometry [29, 41]. Furthermore, it is remarkable that spin initialisation and readout are observed both at cryogenic and ambient conditions, where the effective ES level structures are notably different [10]. Even though the effects of the effective ES level structure on spin contrast are critical for many applications of the Nitrogen-Vacancy center, the influence of the effective ES structure has not yet been fully studied or understood. This shortcoming is particularly critical for quantum sensing, due to increasing interest in low temperature NV magnetometry applications to study exotic condensed matter systems [28].

Scope of this thesis

In this thesis, we present a comprehensive study of the photophysical properties of individual Nitrogen-Vacancy centers in diamond. We study the dependence of the NV photoluminescence rate on magnetic fields, electric fields, and temperature for various levels of strain, thereby characterizing the NV excited state structure and

evolution. We investigate the effects on optical spin readout contrast under various experimental conditions and analyse the influence of the NV excited states on spin-dependent photoluminescence. This improves our fundamental understanding of the NV center and provides a simple yet precise and quantitative tool to characterize the excited-state structure of individual NV centers over a wide temperature range. Using this technique, we gain insights not only into the NV orbital structure but also into the dynamics of the NV charge state. This work is relevant to applications in quantum information processing and quantum sensing, where precise knowledge of the excited state structure is key for optimal experimental conditions, such as high-fidelity initialization and readout. In particular, we determine the conditions that lead to incomplete optical spin contrast and depolarization, both of which are detrimental to NV sensing applications. Furthermore, our findings enable the development of an all-optical electric field sensing scheme at low temperatures. In parallel, we develop technological advances and start the implementation of scanning NV magnetometry at ultra-low temperatures to access unexplored phenomena in condensed matter physics.

In Chapter 2, we present a theoretical description of the Nitrogen-Vacancy center in diamond. We discuss its physical structure, the different charge states of the center, as well as the transitions between its electronic energy levels. We explain the mechanism of the intersystem crossing as the origin of the optical spin contrast, a key property that makes NV centers highly versatile for a wide range of applications. For the negatively charged Nitrogen-Vacancy (NV^-) center, we describe how the ground and excited state level spins are interacting with static external magnetic $\boldsymbol{B}$ and electric fields $\boldsymbol{E}$ as well as with crystallographic strain $\boldsymbol{\delta}$ and discuss their influence on the NV spin levels and transitions. Finally, we give a brief introduction to current sensing applications based on NV centers in diamond.

In Chapter 3, we present the study of the dependence of the NV photoluminescence on static magnetic fields applied along the NV quantisation axis at cryogenic temperatures and its implications on cryogenic applications, specifically scanning NV magnetometry. We first investigate the magnetic field-dependent photophysics of individual Nitrogen-Vacancy centers and observe significant reductions in the NV photoluminescence rate at distinct magnetic fields, which indicate a marked decrease in the optical readout efficiency of the NV's ground state spin. We investigate the physical origin of these dips and attribute them to level anticrossings (LACs) between NV excited states, which lead to efficient NV spin mixing and subsequent intersystem crossings. Moreover, we investigate the strong dependence of the PL on the effective, local strain environment and develop a rate equation model that explains our findings. We observe strong indications of a strain-dependent variation of the NV's orbital g-factor and investigate an additional ionization mechanism in the metastable singlet state. Through our understanding, we identify optimal conditions where spin initialization and readout are most effective, enabling high-fidelity measurements that are crucial for various applications.

In Chapter 4, we expand our study of the magnetic field-dependent photoluminescence of single NV centers to a large temperature range and track the evolution of the excited state structure, offering a concise and complete picture of the NV's temperature-dependent photophysics. We explore the transition of the ES level structure from cryogenic temperatures up to room temperature and directly observe the emergence of the NV's room-temperature effective ES structure. We develop a model

that incorporates phonon-induced effects to explain our findings and gain further insights into the strain-dependent nature of orbital averaging. These results give a better understanding of the photophysical properties of the NV center which have significant implications for applications such as quantum sensing at intermediate temperatures.

In Chapter 5, we discuss the novel implementation of a nanoscale magnetometer based on single spins in diamond for operation at milli-kelvin temperatures. We present the development and realization of an optimized scanning NV magnetometer probe with an integrated near-field coupling device for efficient spin driving, which is critical for maintaining ultra-low temperatures. Besides efficient spin manipulations, the device offers several advantages over state-of-the-art microwave delivery schemes currently used for low-temperature NV magnetometry. Additionally, we investigate the low-temperature charge stability of our diamond scanning probes, which contain single near-surface NVs. We describe in detail the observed phenomenology of a charge state change from an initially favoured NV^- to NV^0 state and present our working hypothesis on the mechanisms compromising the NV^- photostability. Finally, we investigate various mitigation strategies and evaluate their application to our intended use case of low-temperature NV magnetometry.

At the end of the thesis in Chapter 6, we summarize our main results and give an outlook for further studies as well as prospective new NV applications. We discuss the effect and the implications of our work regarding the photophysics of single NV centers on quantum sensing and quantum information processing, thus enabling their optimal use. We then present challenging perspectives for further fundamental research on the NV system, as well as future directions for technological advances to expand the fields of operation of NV-based quantum technologies. We also propose concrete applications of the NV scanning probe microscopy in low and ultra-low temperature environments to investigate fundamental questions in condensed matter and increase our understanding of material properties.

Parts of this thesis have been previously published in Happacher *et al.* (2022) [42] and Happacher *et al.* (2023) [43], while other parts will appear in a manuscript currently in preparation [44].

2. Fundamentals of the Nitrogen-Vacancy center in diamond

The Nitrogen-Vacancy center is a point defect in diamond. It consists of a nitrogen atom (N) replacing a carbon atom, and a neighboring empty lattice site called vacancy (V) [45]. The corresponding symmetry group of the defect is a triagonal C_{3v} symmetry [46] with the main symmetry axis passing through the vacancy and the nitrogen atom. The symmetry determines the nature of the possible electronic states as well as the allowed transitions between them.

Depending on the location of the Fermi level within the diamond band gap [47, 48], the NV can exist in three different charge states: the neutrally charged NV^0, the negatively charged NV^-, and the positively charged NV^+ states. The NV^- carries an electron spin which can be easily manipulated. Due to its optical properties and the resulting spin-readout techniques, NV^- is the most prominent charge state and has received significant attention over the years [10].

The electronic structure in the ground state of the NV^- can be described by a $S = 1$ spin system which has three states with the magnetic quantum number $m_s = -1, 0, +1$ along the quantisation axis of the C_{3v} symmetry. The $m_s = 0$ state and the two degenerate $m_s = \pm 1$ states exhibit a highly spin-dependent fluorescence due to the specifics of the NV's photophysical properties and electronic structure [10]. This effect can be used to optically detect electron spin resonance (ESR) [49] and thereby probe the external environment experienced by the NV, for example, magnetic fields along the NV symmetry axis, which split the $m_s = \pm 1$ states due to the Zeeman effect.

The excited state (ES) of NV^- is an orbital doublet, $S = 1$ spin triplet with a total of six states, which at room temperatures reduces to an effective orbital singlet with three states due to orbital averaging [39, 40]. The ES room temperature structure is better known and closely resembles the one from the ground state (GS).

The NV^- electron spin stands out due to its excellent quantum coherence properties [10], which persist across a wide range of temperatures [11] and pressures [12] as well as its efficient optical spin initialisation and readout resulting from the spin-dependent intersystem crossing (ISC) [35]. The simple experimental implementation to measure the NV spin projection in the GS by photon counting led to widespread use in quantum sensing [26, 28, 29, 50] and quantum information processing [14–17].

In the following sections, we give an introduction to the Nitrogen-Vacancy center in the context of our work. We will discuss the different charge states of the NV center, their positions within the diamond band gap, and their electronic structures. We present the optical transitions of the NV and go into details on the mechanisms for spin polarization. Afterwards, we discuss the theoretical description of the effects of magnetic and electric fields as well as crystallographic strain on the level structure

of the NV^- ground and excited states as deduced from symmetry considerations and observed at low temperatures. Then, we introduce phonon-induced orbital averaging, which is responsible for the effective excited-state structure observed at room temperature, and conclude with a brief introduction to the applications of the NV center in quantum sensing.

An excellent and comprehensive review of the Nitrogen-Vacancy center is provided by Doherty *et al.* [10], which serves as a key reference for the discussion in this chapter.

2.1. Electronic structure and charge states

Diamond features a large indirect bandgap of 5.5 eV, which determines its electronic properties and can host a wide variety of electronic states, including those of color centers such as the Nitrogen-Vacancy and the Silicon-Vacancy center. The Fermi level is normally located in the band gap, resulting in a filled valence band and an empty conduction band. The electron donor concentration influences the exact position of the Fermi level in the bandgap and thus the charge state of the NV [47]. If the Fermi level lies above or below the transition energy between two charge states, the NV either gains or loses an electron [48, 51]. In Figure 2.1, we show the various transition energies for the NV and compare them to the ones from the SiV.

The position of the Fermi level with respect to the bandgap depends on a variety of factors, but can differ fundamentally between bulk and close to the surface. Deep inside the diamond, the impurity concentration determines the exact position of the bandgap with respect to the Fermi level and the charge state of the NV, which usually is NV^- in our diamonds. However, in the absence of any defects or dopants in the lattice, the most stable charge state would be the NV^0 [47]. For near-surface NVs, band bending from surface states as well as the electron affinity of the surface and NV-related gap states [52] determine the charge state. The surface terminations have been found to play a crucial role in stabilizing the NV charge state [52, 53]. The position of the bandgap with respect to the Fermi level, and thus the charge state, can be changed by applying voltages [48, 51, 54] and by controlling the impurity content or surface termination [10].

The C_{3v} symmetry of the NV is characterized by a principal axis along the [111]-diamond crystal axis with 120° rotation symmetry and three vertical planes of symmetry [55]. This results in three irreducible representations [56] A_1, A_2 and E where A is a one-dimensional representation which can be either symmetric ($_1$) or anti-symmetric ($_2$), and E is a two-dimensional representation [55, 56]. The point group allows for the prediction of physical properties, allowed states, and selection rules. Each state within the individual NV charge states is characterized by one of the irreducible representations setting the orbital symmetry [10]. The pre-subscript indicates the number of allowed values of the spin's projection along the symmetry axis, "^{1}" for a spin singlet, "^{2}" for a spin doublet, and "^{3}" for a spin triplet. The dynamics of the NV center are determined by the available electrons to occupy the orbitals [46].

The NV system is made up of three unpaired electrons from the dangling bonds of the carbon atoms and two unpaired electrons from the nitrogen atom. This charge configuration is the neutrally charged NV (NV^0). It has a ^2E spin $S = 1/2$ orbital

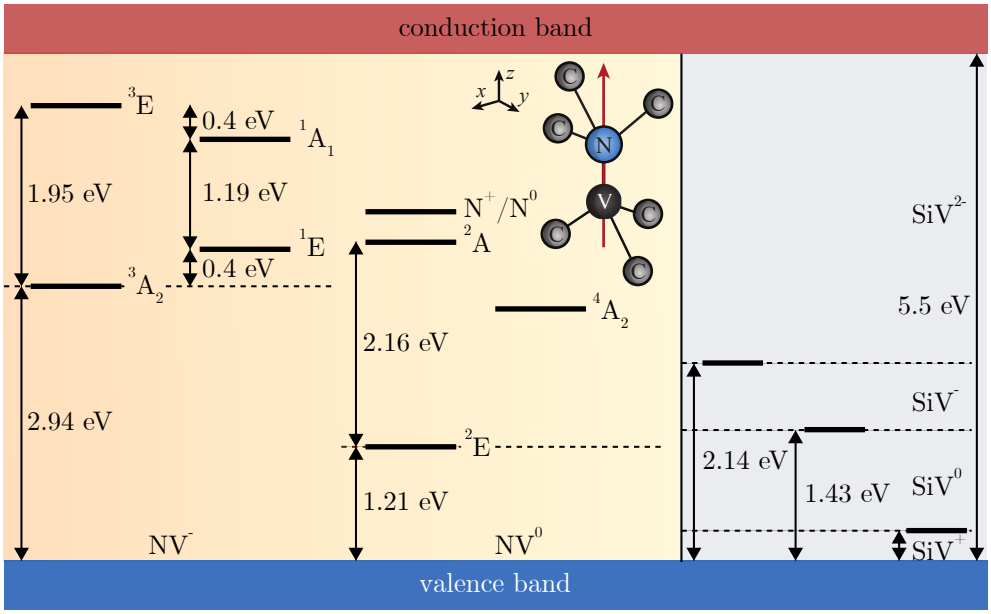

Figure 2.1.: Band diagram of diamond with a band gap of 5.5 eV with the top of the valence band and the bottom of the conduction band for the Nitrogen-Vacancy (left and middle) and Silicon-Vacancy center (right). On the right, it shows the energy levels of the NV^- and NV^0 with their ground and excited states as well as their metastable states [10]. In our diamonds, the Fermi level typically lies above the $NV^{-/0}$ charge transition, resulting in a charge-stable NV^-. Inset: Atomic structure of the Nitrogen-Vacancy center in diamond with the blue sphere as the N atom and the black sphere as the vacancy. The main symmetry axis is defined from the vacancy to the nitrogen atom depicted in red, together with the defined coordinate system. On the right, the charge transition levels of the Silicon-Vacancy center in diamond are shown, which feature deeper energies in the bandgap [57]. Note the lower charge transition level of the SiV^- compared to the NV^-.

doublet ground state and $^2A_2$ spin $S = 1/2$ orbital singlet excited state manifold. Further details about this charge state can be found in Refs. [10, 58, 59]

If the Fermi level lies lower than the NV^0 charge transition level, the NV loses an electron and the positively charged NV (NV^+) is formed. In contrast to the photo-active charge states, NV^0 and NV^-, it is more difficult to detect experimentally and has only been sparsely investigated [60, 61].

The NV can gain an additional electron from a nearby electron donor to create the negatively charged NV (NV^-) [62, 63]. Two of the six total electrons are unpaired, and one of the vacancy electrons forms a spin $S = 1$ pair with the additional electron. The resulting ground state is a $^3A_2$, spin $S = 1$ orbital singlet manifold, and the excited state a ^3E spin $S = 1$ orbital doublet manifold. There are two metastable singlet states, ^1E and $^1A_1$, which are connected to the triplet states via an intersystem crossing (ISC). The ground state triplet spin states are $m_s = -1, 0, +1$ with a zero

field splitting (ZFS) D_0^{GS}. At low temperature, and in the limit of sizeable strain, the NV ES exhibits two orbital branches, commonly denoted as E_x and E_y [10]. Each of these branches in turn splits into three electronic spin sub-levels with magnetic quantum numbers $m_s = -1, 0, +1$. At room temperature the excited state structure is simplified due to orbital averaging [40] which effectively reduces the NV ES to a single orbital with only three states where the $m_s = \pm 1$ are split from the $m_s = 0$ with a ZFS D_0^{ES} [64]. We go into the details of this process in Section 2.4.

The NV can be directly experimentally detected in either the neutral (NV^0) or negative (NV^-) charge state. If the Fermi level is close to the $NV^{-/0}$ transition energy, both charge states are observed. Changes between the two charge states happen through both ionization and recombination, either in the dark or under optical excitation [65]. Photo-conversion ultimately leads to an equilibrium of the charge state ratio [66] and is the reason that under green excitation, both charge states are present.

In literature, there is an ambiguity between the NV and NV^- notations. In this work, we aim to avoid this ambiguity, particularly in cases where it may cause confusion. However, for historical reasons, readability and convention, in some instances, the abbreviation NV still refers to the negatively charged NV. The neutral and positive charge states are always explicitly indicated.

2.2. Optical properties and spin polarization

The neutrally charged NV features a broad absorption spectrum [10, 67] and can be excited resonantly or non-resonantly to its excited state. Such excitation is followed by a radiative decay back to the ground state. The zero-phonon line of the NV^0 is at 575 nm, but most of the emission goes into a large phonon sideband (PSB). The NV^0 center does not show any spin-dependent fluorescence.

The negatively charged NV can also be optically excited with a large range of excitation wavelengths from the ground state to the excited state in a spin-conserving way through dipole-allowed transitions. Only a few percent of the light is emitted into the ZPL at 637 nm [10], whereas the rest is emitted in the wide PSB from 650-800 nm. The metastable states feature an infrared transition at 1042 nm [10].

The NV^- is particular due to its optical properties that lead to efficient optical spin initialization and readout. It has a highly coherent ground-state electron spin [68], which can be excited optically with resonant or non-resonant light. The spin decays back from the excited state either radiatively or non-radiatively in a spin-dependent process. The $m_s = \pm 1$ spin states will decay preferentially to the dark singlet manifold through an intersystem crossing and then to the spin sublevels of the ground state, whereas the $m_s = 0$ states dominantly decay radiatively to the ground state $m_s = 0$. The intersystem crossing, which has been thoroughly studied [35, 36], is ultimately responsible for spin readout and initialization. It results from the properties of the NV's orbital excited states (ES) and their coupling to the NV's $^1A_1$ singlet state [10]. When the NV center is optically excited with a transition rate similar to the radiative decay rate γ_{NV}, a spin population initially in the $m_s = \pm 1$ spin sublevels non-radiatively decays into the singlet manifold, whereas a population in the $m_s = 0$ spin sublevel cycles radiatively producing photoluminescence. [69]. The radiative decay rate γ_{NV} is fast compared to the decay through the singlet and thus the

singlet lifetime determines the dynamics under optical excitation. The optical cycling behavior is very similar at both low and room temperatures.

Optical excitation thereby leads to spin polarization of the $m_s = 0$ ground state with a fidelity of 80% [70] and features spin-dependent photoluminescence, which can be used to optically read out the spin state. The optical spin readout contrast persists only for a short time ($\approx 300\,\mathrm{ns}$) and vanishes as the singlet population decays back to the ground state and the system reaches a steady state. Spin initialization and readout processes of NVs are well established [10] and observed both at cryogenic and ambient conditions, even though the effective ES level structures are markedly different in the two cases. The application of a microwave can be used to coherently control the spin state in the GS. With these mechanisms, the NV can be used to create a two-level quantum system which can be used as a qubit for quantum experiments with initialisation through optical pumping, creating the initial state $|0\rangle$ while one of the $m_s = \pm 1$ spins serves as logical $|1\rangle$. The optical spin contrast is the basis for a variety of NV applications. A good summary of the spin readout techniques for the NV$^-$ can be found in Ref. [69].

2.3. Effects of external fields on the NV$^-$ ground and excited state

In this section, we present the theoretical description of the ground and excited states of the negatively charged NV center, which are derived from symmetry considerations. We present the construction of the GS and ES Hamiltonians as described in Ref. [10].

The NV$^-$ energy levels in the ground and excited states are sensitive to various environmental parameters such as magnetic and electric fields, crystal strain, and temperature [10]. Magnetic fields couple to both states similarly, whereas the excited state is much more susceptible to electric and strain fields than the ground state.

For the definition of the Hamiltonians and the incorporation of the interaction with external fields, we define a coordinate system where the z-axis is aligned with the symmetry axis of the NV center pointing from the vacancy site to the nitrogen atom and the x-axis pointing towards one of the carbon atoms [10].

The NV$^-$ spin's internal hyperfine coupling and nuclear quadrupole splitting are neglected in the following description since they have limited effects on the photophysical properties relevant for our studies. We also do not consider the implicit temperature dependence of any of the involved interaction parameters, since it does not affect the population dynamics of the spin states.

Ground state NV$^-$ spin Hamiltonian

The ground state of the negatively charged Nitrogen-Vacancy is an electron spin triplet and described in detail in Refs. [10, 71]. The fine-structure Hamiltonian of the NV$^-$ spin's ground state is described by the Hamiltonian

$$\hat{\mathcal{H}}_{gs} = D_0^{\mathrm{GS}} \Big[\hat{S}_z^2 - S(S+1)/3 \; \mathbb{1}_3 \Big], \tag{2.1}$$

where $D_0^{\mathrm{GS}} \approx 2.87\,\mathrm{GHz}$ [10] is the zero-field splitting (ZFS) between the spin states $m_s = 0$ ($|0\rangle$) and $m_s = \pm 1$ ($|-1\rangle$ and $|1\rangle$) of the spin projection operator $\hat{S}_z$ that arise

from spin-spin interactions. Additionally, $S = 1$ denotes the spin of the system and $\mathbb{1}_3$ is the identity matrix. The GS zero-field splitting exhibits a known temperature dependence [72] which we neglect since it does not affect the photophysics of the NV.

The NV$^-$ spin's ground state level structure is further modified by static electric $\boldsymbol{E}$, magnetic $\boldsymbol{B}$, and strain $\boldsymbol{\delta}$ fields, whose contributions are given by

$$\begin{aligned}\hat{\mathcal{V}}_{gs} = \mu_\mathrm{B} g_{gs}^{\parallel} \hat{S}_z B_z + \mu_\mathrm{B} g_{gs}^{\perp} \Big(\hat{S}_x B_x + \hat{S}_y B_y\Big) + d_{gs}^{\parallel}(E_z + \delta_z)\Big[\hat{S}_z^2 - S(S+1)/3\ \mathbb{1}_3\Big] \\ + d_{gs}^{\perp}(E_x + \delta_x)\Big(\hat{S}_y^2 - \hat{S}_x^2\Big) + d_{gs}^{\perp}(E_y + \delta_y)\Big(\hat{S}_x\hat{S}_y + \hat{S}_y\hat{S}_x\Big),\end{aligned} \tag{2.2}$$

where μ_B is the Bohr magneton in units of GHz, $g_{gs}^{\parallel}$ and $g_{gs}^{\perp}$ are the components of the ground state electronic g-factor tensor which we set to be equal to 2, and $d_{gs}^{\parallel}$ and $d_{gs}^{\perp}$ are the components of the ground state electric dipole moment. $\hat{S}_x$, $\hat{S}_y$ and $\hat{S}_z$) are the $S = 1$ spin operators and $\mathbb{1}_2$ is the identity matrix. All the values for the interaction parameters are taken from Ref. [10].

Magnetic fields along the NV axis B_NV, lift the degeneracy of the $m_s = \pm 1$ states and shift them by an energy $m_s \mu_\mathrm{B} g_{gs}^{\parallel} B_\mathrm{NV}$. At a magnetic field of $B_\mathrm{NV} \approx 102.4\,\mathrm{mT}$, a level anticrossing between the $|0\rangle$ and $|-1\rangle$ states occurs, which is called ground state level anticrossing (GSLAC). Transverse magnetic fields $B_\perp$ mix the electronic spin states, which leads to quenching of the NV$^-$ photoluminescence [31].

Electric fields and crystallographic strain have a similar effect on the NV$^-$ and can therefore be combined to an effective field $\boldsymbol{\Pi} = \boldsymbol{E} + \boldsymbol{\delta}$ in units of energy. The influence of electric and strain fields on the NV$^-$ ground state is small compared to the excited state (see below) due to the difference in orbital angular momentum and the absence of spin-orbit coupling [10].

Excited state NV$^-$ spin Hamiltonian

The excited state of the negatively charged Nitrogen-Vacancy is an orbital doublet, spin triplet, which at higher temperatures reduces to an effective orbital singlet with three spin sublevels due to orbital averaging (see Section 2.4). The structure of the excited state has been investigated in detail [39, 73, 74] and summarized in Refs. [10, 46]. The fine structure of the NV's excited state spin is given by the Hamiltonian

$$\begin{aligned}\hat{\mathcal{H}}_{es} = \mathbb{1}_2 \otimes D_{es}^{\parallel}\Big[\hat{S}_z^2 - S(S+1)/3\ \mathbb{1}_3\Big] \\ - \lambda_{es}^{\parallel}\,\hat{\sigma}_y \otimes \hat{S}_z + D_{es}^{\perp}\Big[\hat{\sigma}_z \otimes \Big(\hat{S}_y^2 - \hat{S}_x^2\Big) - \hat{\sigma}_x \otimes \Big(\hat{S}_x\hat{S}_y + \hat{S}_y\hat{S}_x\Big)\Big] \\ + \lambda_{es}^{\perp}\Big[\hat{\sigma}_z \otimes \Big(\hat{S}_x\hat{S}_z + \hat{S}_z\hat{S}_x\Big) - \hat{\sigma}_x \otimes \Big(\hat{S}_y\hat{S}_z + \hat{S}_z\hat{S}_y\Big)\Big],\end{aligned} \tag{2.3}$$

consisting of orbital and spin subsystems $\hat{\mathcal{H}}_\mathrm{orbit} \otimes \hat{\mathcal{H}}_\mathrm{spin}$, where $D_{es}^{\parallel}/h \approx 1.42\,\mathrm{GHz}$ ($D_0^\mathrm{ES} := D_{es}^{\parallel}$) and $D_{es}^{\perp}$ are the spin-spin interaction terms, $\sigma_{x,y,z}$ are the standard two level Pauli spin matrices representing the orbital degrees of freedom, and $\lambda_{es}^{\parallel}$ and $\lambda_{es}^{\perp}$ are mixing terms that arise from spin-orbit and spin-spin interactions.

The influence of static electric $\boldsymbol{E}$, magnetic $\boldsymbol{B}$, and strain $\boldsymbol{\delta}$ fields on the NV spin's excited states level structure is given by

$$\begin{aligned}\hat{\mathcal{V}}_{es} = d_{es}^{\parallel}\Big(E_z + \delta_z\Big)\ \mathbb{1}_2 \otimes \mathbb{1}_3 + d_{es}^{\perp}\Big(E_x + \delta_x\Big)\ \hat{\sigma}_z \otimes \mathbb{1}_3 - d_{es}^{\perp}\Big(E_y + \delta_y\Big)\ \hat{\sigma}_x \otimes \mathbb{1}_3 \\ + \mu_\mathrm{B}\, l_{es}^{\parallel}\, B_z\, \hat{\sigma}_y \otimes \mathbb{1}_3 + \mathbb{1}_2 \otimes \Big[\mu_\mathrm{B}\, g_{es}^{\parallel}\, B_z\ \hat{S}_z + \mu_\mathrm{B}\, g_{es}^{\perp}\Big(B_x \hat{S}_x + B_y \hat{S}_y\Big)\Big],\end{aligned} \tag{2.4}$$

where $d_{es}^{\parallel}$ and $d_{es}^{\perp}$ are components of the electronic dipole moment, $l_{es}^{\parallel}$ is the orbital magnetic moment also referred as g_l, the effective orbital g-factor, and $g_{es}^{\parallel}$ and $g_{es}^{\perp}$ are components of the electronic g-factor tensor which we set to be equal. The values for the interaction parameters are taken from Refs. [10, 39]. In the limit of high strain, the Hamiltonian results in two spin-1 systems, one for each of the two orbital branches, which we call E_x and E_y.

Instead of in the basis of σ_z and S_z, Maze *et al.* give an equivalent definition of the excited state of the ES triplet manifold in the case of zero strain [75] which yields the same energy structure with $\Delta := D_0^{\mathrm{ES}}/3$, $\Delta' := D_{es}^{\perp}$, $\Delta'' := \lambda_{es}^{\perp}$ and $\lambda_z := \lambda_{es}^{\parallel}$.

Magnetic fields along the NV axis B_{NV}, as well as non-axial electric $E_\perp$ or strain $\delta_\perp$ fields, can lift the double degeneracy. Similar to the GS, magnetic fields along the NV axis split the $m_s = \pm 1$ states in the two orbitals.

In contrast to the GS, in-plane electric and strain fields E_x, E_y, δ_x, and δ_y have a strong effect on the ES. Axial electric E_z or strain δ_z fields, on the other hand, shift all energy levels in the ES [39]. Electric field and crystal strain have a similar effect on the excited state of the NV^- and can again be combined into an effective field $\boldsymbol{\Pi} = \boldsymbol{E} + \boldsymbol{\delta}$ in units of energy.

2.4. Phonon-induced orbital averaging

The excited state level structure of NV^- experiences a strong dependence on temperature. As we have seen at low temperatures, the orbital structure is a spin-1 orbital doublet, whereas at room temperature it is a spin-1 orbital singlet. This change is caused by an effect called orbital averaging, which has been previously investigated [35, 36, 40, 76, 77].

Due to spin-orbit coupling, phonons induce a fast and spin-conserving population transfer in the excited state manifold, resulting in an occupation following the standard Boltzmann distribution [76]. Since phonons interact only with orbital degrees of freedom but not with spin, the transition rate is the same for all electronic spin states [10, 76]. The mixing leads to average states with quenched orbital angular momentum and averaged effective energies determined by spin-spin interactions for states with identical m_s-spin [10].

The phonon-induced population dynamics follow a T^5 dependence [40, 76] and are mainly driven by two-phonon processes. It is responsible for the temperature dependence of the polarization visibility as defined and shown in Ref. [40] and leads to broadening of the linewidth with temperature which is consistent with linear electron-phonon interactions with E-phonon modes [40].

Experimental and theoretical investigations found that the orbital averaging rate at room temperature is orders of magnitude faster than any other transition rate

involved in NV dynamics and established a temperature-dependent analytic expression of the spin-conserving transition rate between the two ES orbitals resulting from E-symmetry phonons. The rate can be written in the form [78]

$$\Gamma_{XY} \coloneqq W = \frac{64}{\pi}\hbar\eta_E^2 k_\mathrm{B}^5 T^5 I(\omega_\mathrm{c}, T, \delta_\perp), \tag{2.5}$$

where $\hbar$ is the reduced Planck's constant, η_E is the coupling strength of the E-symmetry phonons, k_B is the Boltzmann constant, and I is an integral over the phonon mode energies with the cutoff frequency ω_c and an additional dependence on non-axial strain $\delta_\perp$ and temperature T. More details on the phonon-induced transition rate and our specific phonon model can be found in Chapter 4 and Appendix A.2.

The value of the orbital averaging rate and in particular η_E has been investigated in previous studies and ranges between $\eta_E = 143 - 276\,\mathrm{MHz/meV}$ [35, 77, 78]. All of these studies use slightly different phonon models and thus different forms of the integral I and varying cutoff frequencies. At temperatures below 20 K, the resulting transition rate Γ_{XY} in all the models is smaller than the NV's radiative recombination rate $\gamma_\mathrm{NV} \approx 70\,\mathrm{MHz}$. At room temperature, however, the transition rate is around 1000 GHz that is orders of magnitudes larger than γ_NV. For low-strain NVs, fast orbital averaging completely removes the strain dependence of the excited state, whereas for high-strain values, a strain dependence remains in the form of a strain-dependent factor ξ (see below) [78, 79].

In contrast to the ES, the impact of phonons on the energy structure of the ground state Hamiltonian can in many cases be neglected. It is mostly limited to a temperature dependence of the ZFS D_0^GS, which shifts in proportion to the occupation numbers of two different phonon modes [80].

Effective excited state structure at room temperature

The excited state Hamiltonian of NV^- as presented in Section 2.3 includes an interaction between orbital and spin degrees of freedom. Once the phonon-induced transitions are significantly larger than the interactions within the individual spin systems, coherence between the orbital and spin subsystems is lost [79] and all orbital contributions are quenched [76]. The effective Hamiltonian of the excited state at room temperature can therefore be derived directly from the full low temperature Hamiltonian by taking the partial trace over the orbital states (Tr_σ) [79]. This results in the well-studied and commonly known room-temperature Hamiltonian [10].

The partial trace of the fine structure spin Hamiltonian $\hat{\mathcal{H}}_{es}$ from Equation (2.3) gives

$$\begin{aligned}\hat{\mathcal{H}}_{es}^\mathrm{RT} &= \frac{1}{2}\mathrm{Tr}_\sigma\{\hat{\mathcal{H}}_{es}\} \\ &= D_0^\mathrm{ES}\left[\hat{S}_z^2 - S(S+1)/3\ \mathbb{1}_3\right].\end{aligned} \tag{2.6}$$

The orbital doublet structure is reduced to a single orbital with spin-1 where states of magnetic quantum numbers $m_s = \pm 1$ are split from the $m_s = 0$ state by a zero-field splitting of $D_0^\mathrm{ES}/h \approx 1.42\,\mathrm{GHz}$ [40, 81].

The same applies also to the influence of external fields as considered in Equation (2.4). The partial trace over the orbital states of $\hat{\mathcal{V}}_{es}$ can be written as

$$\begin{aligned}\hat{\mathcal{V}}_{es}^{\mathrm{RT}} &= \frac{1}{2}\mathrm{Tr}_{\sigma}\{\hat{\mathcal{V}}_{es}\} \\ &= \mu_{\mathrm{B}} g_{es}^{\mathrm{RT}} \hat{S}_z B_z + \mu_{\mathrm{B}} g_{es}^{\mathrm{RT}} \left(\hat{S}_x B_x + \hat{S}_y B_y\right) \\ &\quad + d_{es}^{\parallel}\left(E_z + \delta_z\right) + \xi\left(\hat{S}_y^2 - \hat{S}_x^2\right)\end{aligned} \tag{2.7}$$

where g_{es}^{RT} is the isotropic room temperature electronic g-factor [82] and ξ is a strain-dependent factor resulting from an imbalance in the Boltzmann distribution of the excited state populations [79] which is caused by strain splitting between the orbitals from non-axial effective fields.

A magnetic field along the NV axis lifts the degeneracy of the $m_s = \pm 1$ spin states and shifts the states similarly to the GS. At $B_{\mathrm{NV}} \approx 50.5\,\mathrm{mT}$, a level anticrossing between the $|0\rangle$ and $|-1\rangle$ states occurs, which we call room temperature excited state level anticrossing (RT-ESLAC).

The value of ξ is only significant for very large strain splittings ($\delta_{\perp} \gg 100\,\mathrm{GHz}$) and also lifts the degeneracy of the $m_s = \pm 1$ spin states at zero magnetic field while shifting the position of the RT-ESLAC to lower magnetic fields. Very few studies directly investigate ξ and only one measures a value of $\xi = 0.07 \pm 0.03$ GHz for high strain NVs in nanodiamonds [81].

The total effective ES Hamiltonian $\hat{\mathcal{H}}_{es}^{\mathrm{RT}} + \hat{\mathcal{V}}_{es}^{\mathrm{RT}}$ is much simpler than the one at low temperature and has only a limited dependence on the electric fields $\boldsymbol{E}$ and crystallographic strain $\boldsymbol{\delta}$.

2.5. Applications of the NV center in sensing

The negatively charged Nitrogen-Vacancy center is sensitive to various physical quantities and therefore widely used in diverse sensing applications, due to its versatility and easy operation. The host material – diamond – is extremely hard, chemically inert, and electrically insulating while featuring high thermal conductivity. It protects the sensor from many external influences and allows its use in a wide range of environments. The optical addressability and readout capabilities of the NV [10] allow non-invasive measurements and the incorporation into samples that are transparent for visual (VIS) and near-infrared (NIR) light, such as biological cells. All of these properties, combined with the excellent photo-physical properties and long coherence times even at room temperature, make the NV a robust and versatile quantum sensor.

Quantum sensing [22] based on the NV center has been employed to measure magnetic fields [18, 75], electric fields [19, 83], crystallographic strain [21, 84, 85] and temperature [20, 86]. Other NV sensing applications are high-resolution nuclear magnetic resonance (NMR) spectroscopy [87, 88], rotational measurements [89, 90], and the use in diamond anvil cells [91, 92]. In all of the above cases, the NVs are stationary relative to their environment.

The most prominent application of the NV is its use as a magnetometer with excellent magnetic sensitivities [22–24, 93]. It is implemented as a magnetic field sensor with single NVs or NV ensembles [94–97] measuring the ground state Zeeman

splitting by optical detected magnetic resonance (ODMR). The NV has also been employed as an electric field sensor [19, 98–100] measuring the Stark shift in the ground state using ODMR-based techniques [19]. However, this performance cannot be compared to the excellent magnetic field sensitivity of the NV due to its weak coupling of the GS to electric fields, and therefore, However, the sensitivity of this approach is significantly lower than that for magnetic fields due to the weak coupling of the ground state to electric fields, which has so far limited its application as an electrometer.

The integration of the NV sensor in a scanning probe-based system [101], such as atomic force microscopy (AFM), allows harnessing the full potential of the atomic-sized nature of the NV for imaging. NV scanning experiments are more challenging than stationary measurements, but they allow for more complex investigations through spatial information. Especially in the context of magnetic field imaging, the high sensitivity combined with the sub-nanometer spatial resolution has led to widespread use and exceptional results.

After initial implementations [23–25], scanning NV magnetometry has emerged as a robust and powerful technique for high-sensitivity imaging of nanoscale magnetic systems [28, 93, 102, 103], even under cryogenic conditions [26, 29, 104, 105].

Other scanning experiments include nanoscale thermometry [106] as well as nanoscale electrometry [107, 108], which for the latter has only been shown recently due to the difficulties with screening effects and lower sensitivity.

3. Magnetic field dependent photophysics

The Nitrogen-Vacancy stands out due to its excellent quantum coherence properties, which persist across a wide range of environmental conditions [11, 12]. As a result of its performance and robustness, the NV spin has been employed in practical applications in quantum metrology [22], nanoscale imaging [26–29], and quantum information processing [14, 15]. The majority of these applications build on methods for efficient optical NV spin initialization [30, 31] and readout [32, 33]. These two key features result from properties of the NV's orbital excited states and the intersystem crossing, which allow the optical detection of spin contrast.

The excited state is mostly well studied at temperatures $T \gtrsim 150\,\mathrm{K}$. There, the NV spin excited state is well described as an effective spin-1 system due to orbital averaging, reducing its complexity [40, 76]. The spin states $|-1\rangle$, $|0\rangle$, $|1\rangle$, are characterized by their magnetic quantum number m_s along the Nitrogen-Vacancy axis [10]. Initialization and readout of the NV's ground-state spin-1 system result from optical transitions being largely spin-conserving for $|0\rangle$, while excited state spin levels $|\pm 1\rangle$ show a non-radiative intersystem crossing into NV spin singlet states, followed by a relaxation into the NV triplet ground state [10].

While optical spin initialization and readout processes of NVs are well established [10] and thoroughly tested at elevated temperatures [31], they have only been sparsely explored under cryogenic conditions. At low temperatures, the effective spin-1 description of the NV excited state does not hold [10]. Due to the significance of the excited state in this optical spin detection mechanism, the orbital structure is poised to influence the photophysics of the NV. Given the rich NV orbital excited state structure that emerges at temperatures where orbital averaging is suppressed [39, 40], it is not obvious that the established room-temperature model for NV spin initialization and readout immediately applies to cryogenic conditions. The question of how the orbital excited state structure affects the NV's photophysical properties is of relevance to most low-temperature experiments with NV spins, but has received remarkably little attention thus far. This information is, however, relevant for all cryogenic applications, but particularly for quantum sensing.

The NV excited state has been investigated with photoluminescence excitation (PLE) measurements at low temperatures [39], as spectroscopy of the excited state structure is difficult without resonant lasers. Previous work has investigated the low-temperature photophysics of single NVs close to zero magnetic field [17, 39] and the photoluminescence of NV ensembles as a function of magnetic field [76], for which a complete picture was obscured by ensemble averaging. A detailed understanding of the mechanisms of the low-temperature orbital excited state structure and its consequences on NV spin initialization and readout has not been established yet. Such understanding is particularly relevant for low-temperature NV magnetometry,

where consistent observations of significant reductions in sensitivity at low magnetic fields [26, 41] have been made but remain unexplained until now.

In this chapter, we present our systematic study of the photo-physical properties of individual NV centers at cryogenic temperatures. We investigate the dependence of the NV^- photoluminescence on static magnetic fields applied along the NV quantisation axis. This study offers new insights into the structure of the NVs' excited states as well as a new tool for their effective characterization.

We present experimental data for NVs with varying strain, observing significant reductions in photoluminescence at specific magnetic field values. We explain the physical origin of these dips and discuss their effect on the photophysics of the NV.

To get a better understanding, we develop a model based on a classical rate equation, which allows us to make predictions of the NV PL as a function of effective strain and magnetic fields. This also enables us to efficiently extract the strain parameter that defines the NV excited state structure without the need for complex spectroscopic techniques. On the basis of the model and additional experimental data, we discuss the strain dependence of the magnetic field response in more detail, leading to interesting new findings about the orbital g-factor.

We investigate the magnetic field behaviour of the neutrally charged NV by simultaneously collecting the NV^- and the NV^0 PL. Our measurements reveal a small buildup of NV^0 population at the excited state level anticrossings, which allows us to investigate a new mechanism behind NV charge state conversion. In this context, we also present our measurements on the laser polarization dependence of the NV^- and NV^0 PL, complementing the in-depth investigation of Fu *et al.* [40] where they report on the visibility of the excited state orbitals under non-resonant excitation.

Lastly, we discuss the impact of our findings on NV-based applications in quantum information processing and quantum sensing at low temperature, with a focus on the case of NV magnetometry. We consider the effect of the level anticrossings on the efficiency of NV spin initialization and readout, and its implications for the magnetic field sensitivity of the NV. This allows us to inform about strategies for selecting optimal experimental conditions for efficient NV-based quantum sensing in the presence of a specific effective strain field.

The results presented here have been published in Happacher *et al.* (2022) [42].

3.1. Magnetic field dependent photoluminescence measurements

Before presenting our measurements, we provide a brief introduction to the experimental setup, with a more detailed description provided in Appendix A.3.1. We perform our experiments in a closed-cycle refrigerator with optical access and three-axis vector magnetic field control. We investigate our samples at cryogenic temperatures, $T \approx 4\,\mathrm{K}$, using a confocal optical microscope. The NV centers are optically excited with a green, continuous-wave laser at power levels close to saturation of the NV's optical transition. For optical detection, we use an avalanche photodiode and appropriate color filters to detect the photoluminescence predominantly stemming from the NV's negative charge state (NV^-) with a corresponding photon count rates I_{PL}^-.

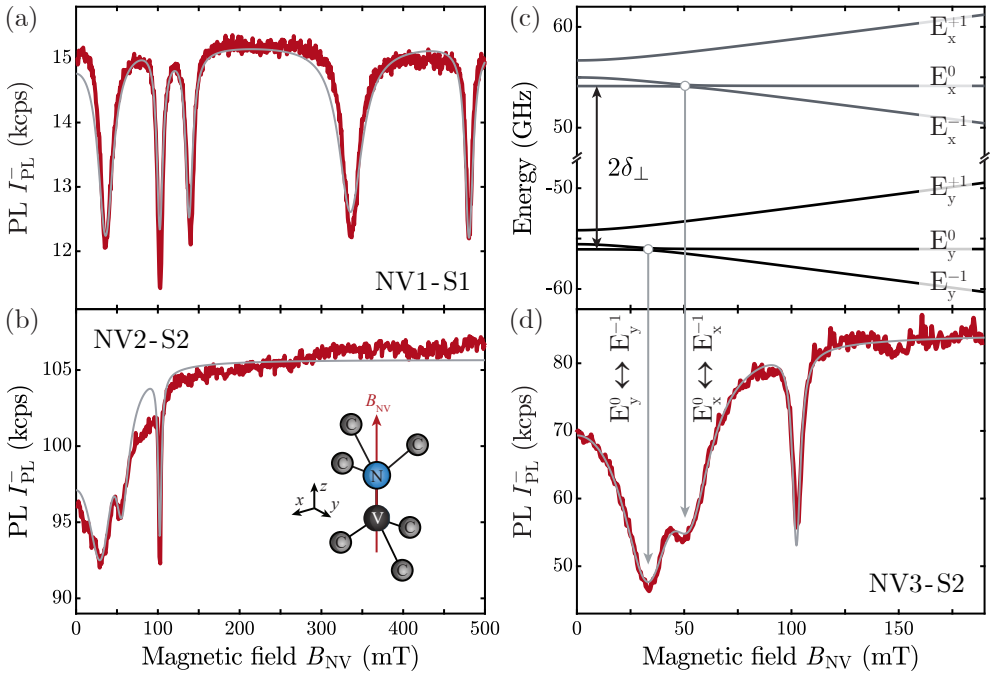

Figure 3.1.: (a) The NV^- photoluminescence (PL) signal, I^-_{PL}, as a function of magnetic field, B_{NV}, for a typical "low strain" NV, NV1-S1 with a transverse strain parameter $\delta_\perp = 4.444(3)$ GHz. (b) Same as (a), but for an NV center exhibiting more strain with $\delta_\perp = 38.6(7)$ GHz. The common I^-_{PL} dip at $B_{NV} = 102.4$ mT in (a) and (b) originates from the well-known ground-state level anticrossing (GSLAC), while additional dips result from excited-state level anticrossings (ESLACs). Grey lines are fits to our model (see text and Appendix A.5). All data were recorded at a temperature $T \approx 4$ K. Inset: Atomic structure of the Nitrogen-Vacancy center in diamond with the blue sphere as the N atom and the black sphere the vacancy. The main symmetry axis is defined from the vacancy to the nitrogen atom depicted in red, together with the defined coordinate system. (c) Example of NV^- excited state energies for an NV experiencing even higher strain ($\delta_\perp = 55.9(6)$ GHz). Labels indicate the orbital- and spin degree of freedom of the states. (d) B_{NV} dependence of I^-_{PL} for NV3-S2 with $\delta_\perp = 55.9(6)$ GHz. The vertical arrows assign the observed I^-_{PL} dips to the corresponding ESLACs shown in (c).

We investigate individual NV centers in two [100]−oriented, single-crystal "electronic grade" diamonds from *Element Six* grown by chemical vapour deposition. These two samples differ in the nature of their NVs. In sample S1, we study naturally occurring NV centers, several microns deep in the bulk, while in sample S2, we study near-surface (< 20 nm) NVs which have been created by $^{14}N^+$ ion implantation at 12 keV and subsequent annealing. These two types of NV defects allow us to study a broad range of local effective strain, as strain increases for implanted NVs close to the diamond surface [98]. Both samples feature photonic structures to enhance

the NV photoluminescence collection efficiency. Sample S1 features diamond solid immersion lenses [109] whereas sample S2 contains diamond nanopillars [37, 110]. In Appendix A.4.2, we present a detailed summary of all the samples studied in this chapter, along with their properties.

For each NV, we record the magnetic field-dependent NV^- photoluminescence rate. In Figures 3.1a and b, we show representative NV^- photoluminescence data as a function of magnetic field along the NV axis, for two NV centers, NV1-S1 and NV2-S2. In this chapter, we adopt the notation in which NV k-Sl denotes the k-th NV located in sample Sl. For both NVs, the NV^- photoluminescence shows several distinct, narrow local minima at specific values of the magnetic field, which we refer to as "dips". The prominent, narrow dip at $B_{\mathrm{NV}} = 102.4\,\mathrm{mT}$ results from the NV's well-known ground state level anticrossing (GSLAC) [111] and is present for all NVs we investigate. Conversely, the multiple additional dips, which reproducibly occur for each NV, but at different values of B_{NV}, are thus far unaccounted for.

Except for the reduction in PL at the GSLAC, we attribute the observed NV^- photoluminescence dips to excited state level anticrossings (ESLACs), which results in spin mixing and subsequent population shelving into the NV^- singlet manifold. In Figures 3.1c and d, we exemplify this concept for NV3-S2, where we show calculated NV^- excited state energies [10, 39, 46] alongside a measurement of $I^-_{\mathrm{PL}}(B_{\mathrm{NV}})$ for the same NV to illustrate the coalescence between two ESs into an anticrossing and the associated I^-_{PL} dips. To obtain the ES energy level from our model, we adjust the transverse effective strain parameter, $\delta_\perp$, in the NV excited state Hamiltonian to match the ESLAC positions in B_{NV} to the corresponding PL dips observed in the data.

3.2. Classical rate equation model

To obtain further, quantitative insights, we employ an extended version of a classical rate-equation model of the NV's magnetic field-dependent photophysics [31, 76], where we explicitly take into account the full, low-temperature excited state level structure of the NV^- [10, 46] as presented in Section 2.3. We consider the electronic states and relevant population decay channels of the NV^- as summarised in the inset of Figure 3.2. We fix all transition rates to literature values by Gupta *et al.* [112], but find that our main results remain largely identical when employing other literature values. The temperature dependence of some excited state transition rates, established for $T < 20\,\mathrm{K}$ [35], has little to no effect on the position and intensity of the PL dips, and we therefore do not consider it in our model. In Appendix A.1, we present a detailed summary of the model.

As seen in Chapter 2, the energy splittings between the NV^- excited states depend highly on the lattice strain, transverse to the NV symmetry axis. Such strain can result from electric fields or crystal strain [46], which we combine into a single perpendicular strain parameter $\delta_\perp = \sqrt{\delta_x^2 + \delta_y^2}$, where δ_x and δ_y are the corresponding strain parameters along the x- and y-axis in the coordinate system of the NV. We then calculate the NV excited state energies from the full Hamiltonian $\hat{\mathcal{H}}_{es} + \hat{\mathcal{V}}_{es}$ [10], as presented in Section 2.3, where $\hat{\mathcal{H}}_{es}$ is the fine structure Hamiltonian of the ^3E mani-

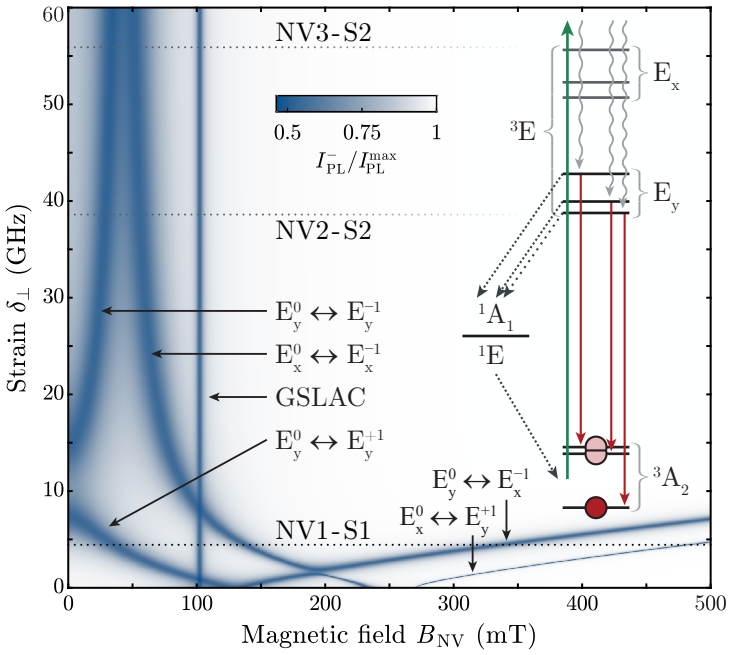

Figure 3.2.: PL intensity I^-_{PL} as a function of B_{NV} and $\delta_\perp$, calculated from a classical rate equation model for the 10-level system illustrated by the level diagram in the inset (for details see Appendix A.1). Labels indicate which ESLACs are responsible for the respective PL dips, while horizontal lines show the $\delta_\perp$-values for the NVs presented in panels of Figures 3.1a, b, and d. Inset: Electronic levels and transition pathways considered in simulating the magnetic field dependence of I^-_{PL}. The NV$^-$ excited state energies are illustrated for the limit of large strain.

fold and $\hat{\mathcal{V}}_{es}$ describes the effect of magnetic fields, electric fields, and crystallographic strain as defined in Section 2.3.

In Figure 3.2, we show the resulting model prediction for $I^-_{PL}(B_{NV})$ for varying values of strain, which illustrates the strong dependence of the I^-_{PL} dip locations on $\delta_\perp$. This accounts for the strong variations $I^-_{PL}(B_{NV})$ traces observed among different NV centers, each of which naturally experiences a different magnitude of $\delta_\perp$. Conversely, a measurement of $I^-_{PL}(B_{NV})$ offers a sensitive tool to determine $\delta_\perp$ for single NV which otherwise requires complex spectroscopic techniques [39].

We use our model to fit all NV$^-$ photoluminescence data as a function of the magnetic field. In all panels showing $I^-_{PL}(B_{NV})$ data, we also show the corresponding fits. For the fits, we only leave $\delta_\perp$ and a small misalignment angle in the magnetic field θ_B as free parameters in the ES Hamiltonian from Equation (2.4). In the case of the low-strain NV1-S1, we also determine the orbital g-factor, g_l, from the fits. In addition, we include in the fits scaling constants for contrast and normalization of I^-_{PL} and a parameter describing the relative excitation efficiency into orbitals E_x and E_y [40]. Despite these few degrees of freedom, our model yields excellent fits for NVs experiencing a large range of strain-values, from $\delta_\perp \lesssim ||\hat{\mathcal{H}}_{es}||$ in Figure 3.1a

to $\delta_\perp \gg ||\hat{\mathcal{H}}_{es}||$ in Figure 3.1b, where $||\cdot||$ is the operator norm. Details of the fit procedure and all resulting fit parameters with errors are reported in Appendix A.5.

3.3. Influence of strain on the magnetic field response

When studying $I^-_{\mathrm{PL}}(B_{\mathrm{NV}})$ for NVs with increased effective strain $\delta_\perp > 15\,\mathrm{GHz}$ at large magnetic fields, we observe significant deviations from our model which predicts two additional I^-_{PL} dips (labelled $E^0_{x(y)} \leftrightarrow E^{\pm1}_{y(x)}$ in Figure 3.2), which arise from spin-mixing ESLACs between orbitals E_x and E_y. Specifically, the four ESLAC-related I^-_{PL} dips seen in Figure 3.1a for the low strain NV should be observable for any value of $\delta_\perp$. Two of these ESLACs occur between spin states within the same orbital branch, which we therefore call intrabranch anticrossings. Two further ESLACs occur between spin states of different orbital branches, which we call interbranch anticrossings. To experimentally address this regime, we investigate single NV defects hosted in the (111)−oriented, electronic grade diamond S3 [110]. Figure 3.3a shows the low magnetic field $I^-_{\mathrm{PL}}(B_{\mathrm{NV}})$ data for the representative NV4-S3, where a fit yields $\delta_\perp = 42.3(5)\,\mathrm{GHz}$ (see Appendix A.5). For this NV, our model predicts the $E^0_{x(y)} \leftrightarrow E^{\pm1}_{y(x)}$ interbranch dips to occur at Tesla-range magnetic fields as depicted in Figure 3.3b. Importantly, the interbranch anticrossing locations also depend sensitively on the orbital g-factor, g_l, while the locations of the intrabranch I^-_{PL} dips at low magnetic field are largely independent from g_l, which is illustrated in Figures 3.3c and d. Conversely, an observation of the $E_{x(y)} \leftrightarrow E_{y(x)}$ interbranch LACs results in a sensitive determination of g_l on the level of single NVs. In the low-strain regime (NV1-S1), we are able to extract the orbital g-factor by fitting the position of the high-field features, which is $g_l = 0.1395(9)$. In contrast, for NV4-S3 or any other NV we studied in sample S3, we were unable to observe the $E^0_{x(y)} \leftrightarrow E^{\pm1}_{y(x)}$ interbranch ESLACs, despite extensive experimental efforts. Interestingly, this observation could be explained by an unexpected increase of g_l with effective strain. Specifically, for the $\delta_\perp$ value of NV4-S3, $g_l \approx 0.8$ is the lowest value consistent with our observations (see Figure 3.3d), and we find similar conclusions for about ten other NVs with comparable values of $\delta_\perp$, when examining $I^-_{\mathrm{PL}}(B_{\mathrm{NV}})$ for B_{NV} up to 5 T (see Appendix A.5).

The increase of g_l with $\delta_\perp$ that we infer from the absence of a visible interbranch anticrossing in our experiment could be explained by a suppression of the spin-orbit coupling between the two orbitals for higher strain values. Indeed, evaluating the matrix elements for the $E^0_{x(y)} \leftrightarrow E^{\pm1}_{y(x)}$ interbranch ESLACs from Equation (A.63) results in the mixing term

$$M_{E_xE_y} = d^\perp_{es}\delta_x\lambda^\perp_{es}/\sqrt{2}\sqrt{(d^\perp_{es}\delta_x)^2 + (B_z g_l \mu_{\mathrm{B}})^2}, \tag{3.1}$$

assuming strain acts only in the x-direction for simplicity. Numerically evaluating this state-mixing matrix element for high strain, we find that the mixing is not significantly reduced. It varies less than 1% over the range of $B_{\mathrm{NV}} = 0 - 5\,\mathrm{T}$, and thus can not explain the missing PL features.

Another possible explanation would be that a fast one-phonon-induced orbital mixing rate could explain the missing features. This transition rate between E_x and E_y

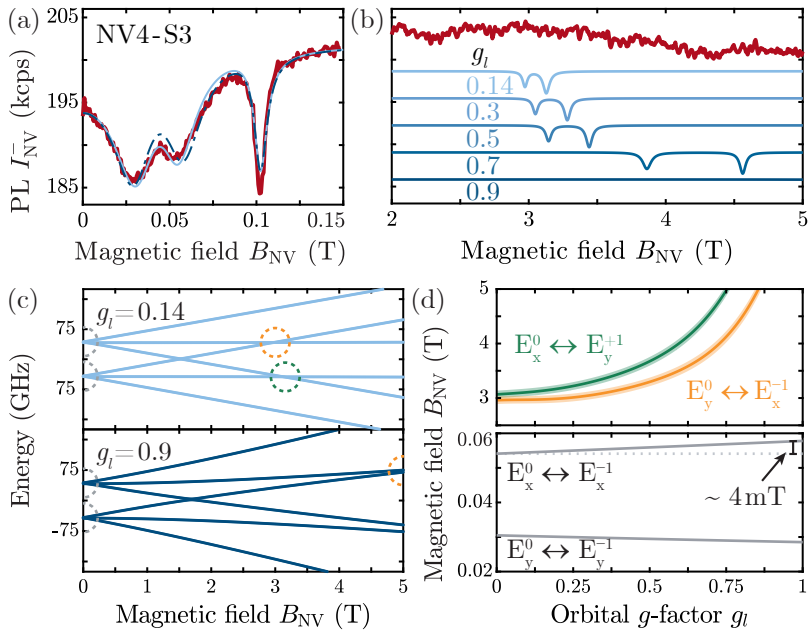

Figure 3.3.: (a) $I^-_{PL}(B_{NV})$ data (red) for NV4-S3 in the "low-field" regime ($B_{NV} \lesssim 150\,\mathrm{mT}$). The model fit (blue) yields $\delta_\perp = 42.3(5)\,\mathrm{GHz}$ and is largely unaffected by the value of g_l ($g_l = 0.14$ and 0.9; light and dark blue). (b) Same as (a) for stronger magnetic fields. Blue-shaded curves show model predictions (vertically offset for clarity) for $\delta_\perp = 42.3\,\mathrm{GHz}$ and $g_l = 0.14 - 0.9$ (see labels). (c) Calculated ^3E excited state energies for $g_l = 0.14$ and $g_l = 0.9$. Dashed circles highlight the position of the $E_{x(y)} \leftrightarrow E_{y(x)}$ (green) and $E_{x(y)} \leftrightarrow E_{x(y)}$ (gray) ESLACs. (d) g_l-dependence of the B_{NV} values at which various ESLACs occur. Shaded areas correspond to the propagated fitting errors in $\delta_\perp$ from (a).

is described by Goldmann *et al.* [36], providing the following, analytic expression

$$\Gamma^{\text{1-phon.}} \approx 8\eta_E k_B \delta_\perp T, \tag{3.2}$$

where η_E is a constant that parameterizes the coupling strength between states of the ^3E manifold and E-symmetric acoustic phonons (see Chapter 2), and k_B is the Boltzmann constant. However, phonon-induced orbital mixing can also be ignored as the expected coupling rate for high strain is $\Gamma^{\text{1-phon.}} \approx 450\,\mathrm{kHz}$, which is significantly less than the other coupling rates involved in the photophysics of the NV—in particular the intersystem crossing rate $\Gamma^{\text{ICS}} > 10\,\mathrm{MHz}$ and the state mixing rates $\Gamma^{\text{mixing}} > 100\,\mathrm{MHz}$.

Alternatively, the absence of the higher magnetic field features could also be explained by fluctuations in the electric noise around the NV center, which would effectively smear out these features. Such a smearing-out would imply that the fluctuation of the electric field is larger than 1 kV/cm and faster than 1 Hz, which are both larger than values reported in the literature [19].

Lastly, if laser-induced charge dynamics would lead to a significant broadening of the anticrossing features, we would not observe the interbranch features in any sample, regardless of the specific strain value.

Our observations thus suggest a surprising, strain-induced enhancement of the orbital g-factor of NV^- compared to reported literature values $g_l \approx 0.1 - 0.22$ [76, 113–115]. Such an effect has not been discussed in the literature thus far, but is made plausible here by qualitative arguments. At low strain, the NV's orbital excited states are near-degenerate, which allows for Jahn-Teller coupling to reduce the orbital angular momentum [114, 116]. With increasing strain, the energy splitting of the states increases, which suppresses Jahn-Teller mixing, and thereby restores orbital angular momentum, leading to an increase of g_l towards the classical value $g_l = 1$. Although a complete theoretical description of the suggested g_l enhancement is still lacking, we expect our findings to stimulate further theoretical work on the topic.

Ideally, we would determine the ESLAC positions for NVs with elevated strain and infer the orbital g-factor enhancement directly. However, there is only a very narrow window of strain values, where all four PL dips are experimentally accessible in our experiment that allows for the application of magnetic fields of $B_{\mathrm{NV}} < 5\,\mathrm{T}$ for (111)-oriented NVs. We put great effort into searching for such NVs, but to no avail. The robustness and reproducibility of this observation are a strong indication of the fundamental nature of our observation and support our hypothesis of a strain enhancement of g_l.

3.4. Insights into the charge dynamics of the NV center

Our measurement of the photoluminescence I_{PL}^{-} versus magnetic field B_{NV} also offers insights into the charge dynamics of the NV center. Specifically, we conduct experiments where we choose appropriate color filters as outlined in Appendices A.3.1 and A.3.3 to simultaneously record the PL intensity from the NV^- and the neutral charge state, NV^0 (Figures 3.4a and b). Strikingly, we find that all previously described NV^- photoluminescence dips are mirrored by peaks in the NV^0 photoluminescence I_{PL}^{0}. The resulting buildup of NV^0 population is small and therefore only minimally affects our conclusions thus far. We extend our model to include previously reported $NV^0 \leftrightarrow NV^-$ (de)ionization processes [65, 70] (Figure 3.4c). Importantly, in our model, we can only explain the observed I_{PL}^{0} peaks by including a recently proposed [65] decay channel from the NV^- singlet state ^1E to the ground state of NV^0. Without this process, our model yields dips instead of peaks in I_{PL}^{0}. Using previously measured ionization and deionization rates (see Appendix A.1.3), our model gives a quantitative prediction for $I_{\mathrm{PL}}^{0}(B_{\mathrm{NV}})$, without any free fit parameters other than scaling constants for contrast and normalization of I_{PL}^{0} which we present in Figures 3.4a and b. The existence of this additional relation between the charge states is, in general, detrimental to most NV experiments.

The optical pumping from the ground state to the excited state orbital doublet exhibits a slight polarization dependence [40]. Depending on the polarization angle, one of the excited state orbitals E_x or E_y is preferentially populated. Therefore, it is possible to control the amount of spin mixing and the depth of the PL reduction by changing the laser polarization angle. In Figure 3.5, we show this dependence

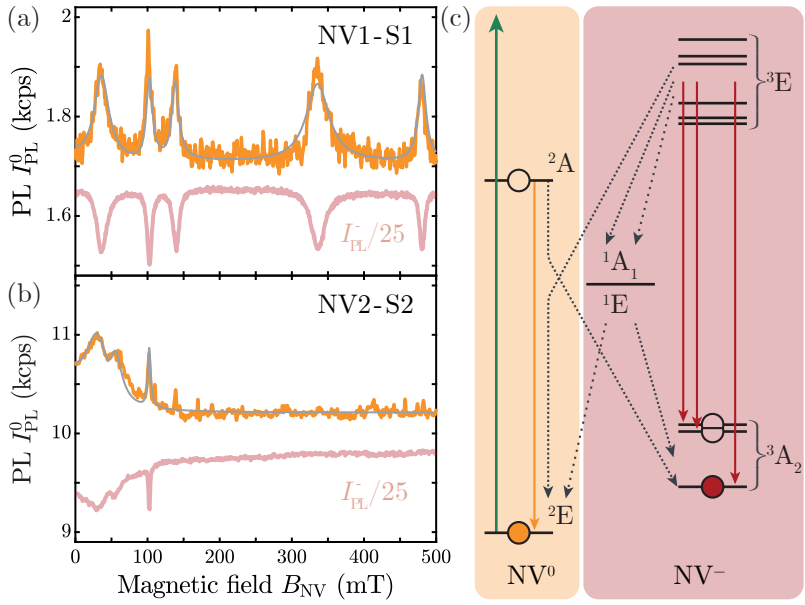

Figure 3.4.: (a) Magnetic field dependence of the NV^0 PL rate, $I^0_{PL}(B_{NV})$, for NV1-S1 and (b) NV2-S2, along with the corresponding I^-_{PL}-data (gray data-points taken from Figures 3.1a and b, but rescaled for clarity). Gray lines are theory predictions based on the fits shown in Figures 3.1a and b. (c) Electronic states of the NV^0-NV$^-$ system, with corresponding (de-)ionization rates, used to include charge-state dynamics into the model introduced in Figure 3.2, inset.

of the NV$^-$ PL on the laser polarization angle. The charge dynamics at the crossings are similarly affected by the selective excitation, resulting in a change in NV^0 PL intensity. While this is not a significant amount of tuning, it may be increased further by changing the excitation wavelength or optimizing the polarization control. Additionally, the use of NVs with an out-of-plane NV orientation in (111)-oriented diamond would further enhance the tuning.

3.5. Implications for low temperature NV applications

The ESLAC-induced reductions in the NV$^-$ photoluminescence I^-_{PL} have important implications for the spin readout contrast used in most NV applications and, in particular, the magnetic field sensitivity of low-temperature NV magnetometry. The dips in I^-_{PL} are accompanied by corresponding dips in the spin readout contrast $\mathcal{C}$ of the optically detected magnetic resonance [49]. In Figure 3.6a, we show the evolution of the spin readout contrast $\mathcal{C}$ as a function of magnetic field along the NV axis for NV5-S2. Two typical ODMR traces recorded near and away from an I^-_{PL} dip ($B_{NV} = 0$ and 200 mT, respectively) are shown in Figure 3.6c.

The combined reduction in I^-_{PL} and $\mathcal{C}$ severely affect the NV's magnetic field sen-

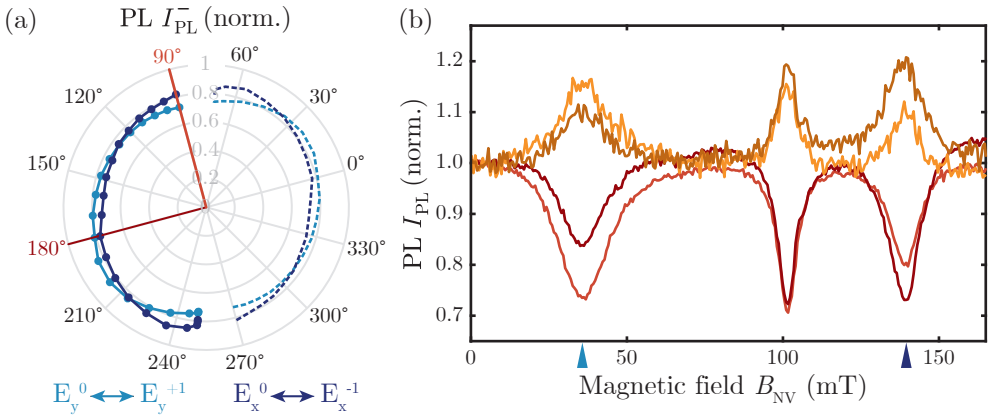

Figure 3.5.: (a) Dependence of the normalized NV^- photoluminescence (PL) at the positions of the two intrabranch ESLACs of NV1-S1 at $B \approx 35\,\mathrm{mT}$ and $B \approx 140\,\mathrm{mT}$ on the excitation polarization angle. (b) Magnetic field dependence of the normalized NV^- PL rate, I^-_{PL}, and the normalized NV^0 PL rate, I^0_{PL}, of NV1-S1 for two orthogonal polarization directions of the linearly polarized excitation laser indicated in (a). Depending on the polarization angle, excited state orbitals E_x or E_y are preferentially populated [40], which modifies the contrast of the corresponding I^-_{PL} dips, accordingly. The NV^- and NV^0 countrate at the ESLACs show a mirrored dependence on laser polarization, while the countrate at the GSLAC remains unchanged.

sitivity η. Using the well-established estimate [32, 117]

$$\eta = \frac{4}{3\sqrt{3}} \frac{\Delta\nu}{\gamma_e \mathcal{C} \sqrt{I^-_{\mathrm{PL}}}}, \tag{3.3}$$

where $\Delta\nu$ is the ODMR linewidth, and $\gamma_e = 28\,\mathrm{GHz/T}$ is the NV's gyromagnetic ratio, we extract the magnetic field sensitivity shown in Figure 3.6b which is inversely proportional to the signal to noise ratio SNR $\propto \frac{1}{\eta} \propto \mathcal{C}\sqrt{I^-_{\mathrm{PL}}}$. As expected, the locations of the observed dips in contrast $\mathcal{C}$ coincide with the locations of the reduction in sensitivity. Compared to typical sensitivity values of $\eta \approx 3\,\mu\mathrm{T}/\sqrt{\mathrm{Hz}}$ away from the ESLACs such as at $B_{\mathrm{NV}} \approx 200\,\mathrm{mT}$, η worsens by almost an order of magnitude at the I^-_{PL} dips. Therefore, the region of spin mixing is detrimental to the performance of the NV^- as a magnetometer, and for most other NV applications as well.

For nanoscale NV magnetometry, near-surface NV centers in nanopillars with typical strain values of $\delta_\perp > 20\,\mathrm{GHz}$ (Figure 3.2, inset) are used. This leads to a decrease of magnetometry performance, which predominantly affects magnetometry at $B_{\mathrm{NV}} \lesssim 100\,\mathrm{mT}$. The fact that all these "shallow" NVs exhibit large values of $\delta_\perp$ can be tentatively assigned to internal electric fields due to band bending near the diamond surface [98, 118], or to near-surface crystal stress [119]. Strained NVs exhibit spin mixing already at zero magnetic field, which results in a reduced spin readout contrast when no magnetic field is applied. It is generally possible to avoid areas of decreased magnetic field sensitivity by applying a bias magnetic field along the NV

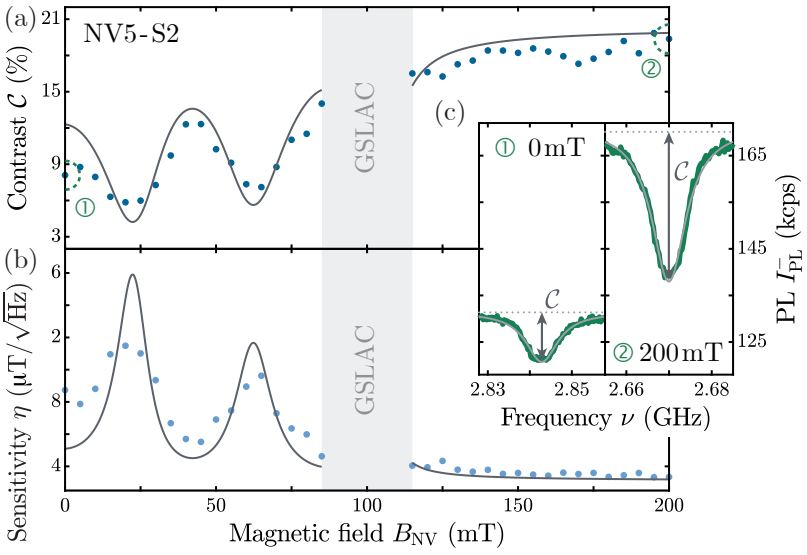

Figure 3.6.: (a) Dependence of the optically detected magnetic resonance (ODMR) contrast on magnetic field B_{NV} for NV5-S2. The microwave field amplitude (Rabi frequency) was held constant while varying B_{NV}. (b) Magnetic field dependence of the magnetic field sensitivity extracted from data according to Equation (3.3). Dark grey lines in a and b show theory predictions based on independently recorded $I_{PL}^-(B_{NV})$ data (see Appendix A.5). (c) Exemplary ODMR traces recorded at values of B_{NV} (dotted circles in (a)), where magnetic field sensitivity is strongly (left) and minimally (right) affected by excited state level anticrossings.

axis, thereby restoring full photoluminescence. In the future, magnetic field sensitivity for such NVs could be restored by material engineering to reduce the effective strain near diamond surfaces, by working with NVs oriented normal to the diamond surface [120] or by harnessing the dependence of the I_{PL}^- dip depth on the excitation laser polarization [40] outlined above. Further improvements could be achieved by optimising laser excitation power or by exploiting resonant laser excitation, where specific ESLACs could be avoided by choosing the proper laser excitation frequency.

It is also possible to use these ESLACs to perform microwave-free magnetometry or effective strain sensing, in a similar fashion to previous work on magnetic field sensing with the NV GSLAC [121]. Since the sensitivity is a function of the width and contrast of the feature, only the ESLACs in the low-strain regime or the high-magnetic-field interbranch crossings of high-strain NVs offer sensitivities comparable to the GSLAC for magnetometry.

3.6. Summary and outlook

We presented a systematic study of the photoluminescence of single Nitrogen-Vacancy centers in diamond at low temperatures. By combining experimental results and the-

oretical modelling, we are able to investigate a number of largely unexplored features in the magnetic field-dependent photo-dynamics of the NV.

Our results provide a simple yet precise and quantitative tool for characterizing the excited-state structure of individual NV centers. These findings not only give insights into the NV center orbital structure and the possible strain-induced enhancement of the orbital g-factor, but are also relevant to applications in quantum information processing and quantum sensing. Precise knowledge of the excited state structure enables us to understand and push the limitations of NV applications in cryogenic environments by optimizing optical spin initialization and readout. The simple implementation of the method enables fast and easy determination of the NV effective strain parameter, which is important to nearly all NV-based quantum communication applications. Moreover, this technique allows for probing the excited state structure without the need for resonant laser spectroscopy [39] which is significantly more complex and, in some cases, not applicable at all. We further advance our understanding of fundamental NV physics by simultaneous measurement of the photoluminescence of the neutrally charged NV I^0_{PL} as a function of magnetic field B_{NV}, which yields relevant information on NV charge dynamics. We are able to confirm a recently proposed NV^- deionization process involving a direct laser-induced process and its resulting decay of NV^- from its metastable singlet state to NV^0.

The methodology presented in this chapter offers exciting prospects for various research areas on NV centers and beyond. The simple measurement of the strain parameter of individual NVs can facilitate the convergence on better diamond fabrication and surface termination techniques, which minimise the strain and electric noise experienced by near-surface NV centers. Technological progress in this area will be useful not only for NV-based experiments but also for experiments involving other color centers in diamond. This work also offers interesting future perspectives for sensing. The ESLAC-induced photoluminescence dips strongly depend on strain and electric fields. Therefore, our findings open the way for novel measurement techniques like microwave-free sensing of these quantities at low temperature. The employed method is also ideal for exploring the temperature dependence of the excited state level structure, which transitions from a combination of spin- and orbital-like behavior at low temperatures to an almost purely spin-like behavior at room temperature due to phonons. The transition gives insights into orbital averaging processes that dominate the NV's photophysics at elevated temperatures [40] and is presented in Chapter 4. Furthermore, the technique can also be applied to other optically active solid-state spin defects, potentially improving their prospects for quantum technologies. The energy structure of any color center featuring shelving states that can be populated through magnetic-field-tunable LACs, such as the neutral Silicon-Vacancy center in diamond [122], could be investigated. Moreover, the observed enhancement of the orbital g-factor can open a discussion about the effect of strain on the spin-orbit coupling in other systems.

4. Temperature dependent photophysics

In Chapter 3, we investigated the photophysical properties of single Nitrogen-Vacancy centers at low temperatures. We look at the magnetic and electric field as well as the crystal strain dependence of the NV^- excited state energy level structure and gain new insights into the charge dynamics of the NV. We also discuss how this energy level structure affects the excited state at low temperatures, the optical spin initialization and readout processes, which are crucial for the majority of NV applications, such as nanoscale magnetic imaging [26, 27, 29] and quantum information processing [14–17].

The low-temperature excited-state structure of the NV^- undergoes significant changes with increasing temperature. The orbital doublet structure of the excited state is effectively reduced to an orbital singlet structure at room temperature by a process called orbital averaging (see Chapter 2). This effect has been investigated by looking at the width of the zero phonon line (ZPL) of the NV^-. Fu *et al.* [40] revealed that the process scales with temperature as T^5 and is mainly driven by two-phonon processes, which effectively average the populations in the two orbitals in a spin-conserving manner.

Even though there is a significant difference between the effective ES level structure at cryogenic and ambient conditions, optical spin initialization and readout are observed in both cases. While the foundations of the intersystem crossing [35, 36] which is ultimately responsible for the optical spin contrast, and orbital averaging [40, 76, 78] have been studied in the past, the transition between the low-temperature and the high-temperature limits, and the emergence of the effective RT ES spin structure, have never been explored in a systematic way. Prior work on NV ensembles has established a non-trivial temperature dependence of the NV PL intensity at zero magnetic field [76], including a local minimum of the NV PL at $T \approx 35$ K, which remained unexplained thus far.

As we have seen in the previous chapters, the exact structure of the NV^- excited state is inherently important for the properties of the NV^- and its performance as a sensor. Due to scientific interest and increasing technological availability, temperature studies using the NV are becoming more relevant as shown by the recent attempt to study the phonon-mediated hydrodynamic flow in WTe_2 with NV scanning magnetometry at temperatures between 5 and 90 K [123], as well as other work at various other temperatures [94–97, 124, 125]. For experiments spanning a broad temperature range, understanding the transition of the excited state energy level structure is crucial for leveraging the full potential of the Nitrogen-Vacancy center and extending its use beyond the current scope.

In this chapter, we present a systematic experimental study of the photoluminescence intensity of single Nitrogen-Vacancy centers, as a function of both magnetic field and temperature in the range of $T = 2 - 300$ K, that offers a concise and complete pic-

ture of the NV's temperature dependent photophysics. The interest of the community in this topic is reflected by the recent and complementary work in Refs. [126–128].

Using the methodology presented in Chapter 3, we systematically explore the transition of the ES level structure from the cryostat base temperature ($T \approx 2\,\mathrm{K}$) to ambient temperature ($T \approx 300\,\mathrm{K}$) for two NVs with different effective strain. In both cases, we track the emergence of the resulting high-temperature ES level structure.

We also develop a model, analogous to the one in Chapter 3, based on a Lindblad master equation, taking into account the explicit effect of two-phonon mixing processes on the excited state orbitals. This enables us to reproduce the experimental data and extract key parameters of the temperature-dependent evolution. In particular, we investigate the strain-dependent temperature evolution of the photoluminescence at the magnetic field position of 50.5 mT corresponding to the room temperature excited state anticrossing (RT-ESLAC).

Finally, we discuss the implications of our findings for quantum information processing and quantum sensing using NV centers, identifying the challenges posed by certain temperature regimes. We then provide recommendations on how to best employ the NV to achieve optimal performance.

The presented results have been published in Happacher *et al.* (2023) [43].

4.1. Temperature dependent photoluminescence measurements

Before we discuss our measurements, we provide a brief introduction to the experimental setup and the samples under investigation. A more detailed description can be found in the respective Appendices A.3.2 and A.4.2.

We perform our experiments on two representative single NV centers in a variable-temperature closed-cycle cryostat equipped with a confocal microscope. The NV centers, NV #1 and #2, are each located in a diamond photonic structure, a few microns from the surface. The first diamond, containing NV #1, is a [100]-oriented, electronic grade diamond from *Element Six* and the second diamond, containing NV #2, is a [111]-oriented, custom-grown diamond [110]. The photonic structures are microscopic diamond solid immersion lenses (SILs) created by focused ion beam (FIB) milling and significantly increase the photon collection efficiency [129]. The in-house fabrication process of SILs is described in Appendix A.4.1. In the experiments, the NVs are excited with green laser light ($\lambda = 532\,\mathrm{nm}$) under conditions of continuous optical excitation close to saturation.

The two NVs differ in the magnitude of their ES strain splitting parameter $\delta_\perp$, which is $\delta_\perp = 1.685 \pm 0.003\,\mathrm{GHz}$ for NV #1 and $\delta_\perp = 75 \pm 2\,\mathrm{GHz}$ for NV #2. Thus, the strain splitting for NV #1 is comparable to the NV ES fine-structure splittings, which are $\lesssim 5\,\mathrm{GHz}$ [10] and much larger for NV #2. These strain values are extracted through a model-fit to the NV PL $I_{\mathrm{PL}}(B_{\mathrm{NV}})$ at $T = 2\,\mathrm{K}$, as described in Chapter 3.

In Figure 4.1a, we show a simplified level diagram of NV^- with the allowed transitions. For the excited state, we show the well-understood cases of low and room temperature, which differ in their orbital structure. At low temperatures, the ES is an orbital doublet which at room temperature is effectively reduced by orbital averaging [40] to a single orbital with spin 1. Its states of magnetic quantum numbers $m_s = \pm 1$ are

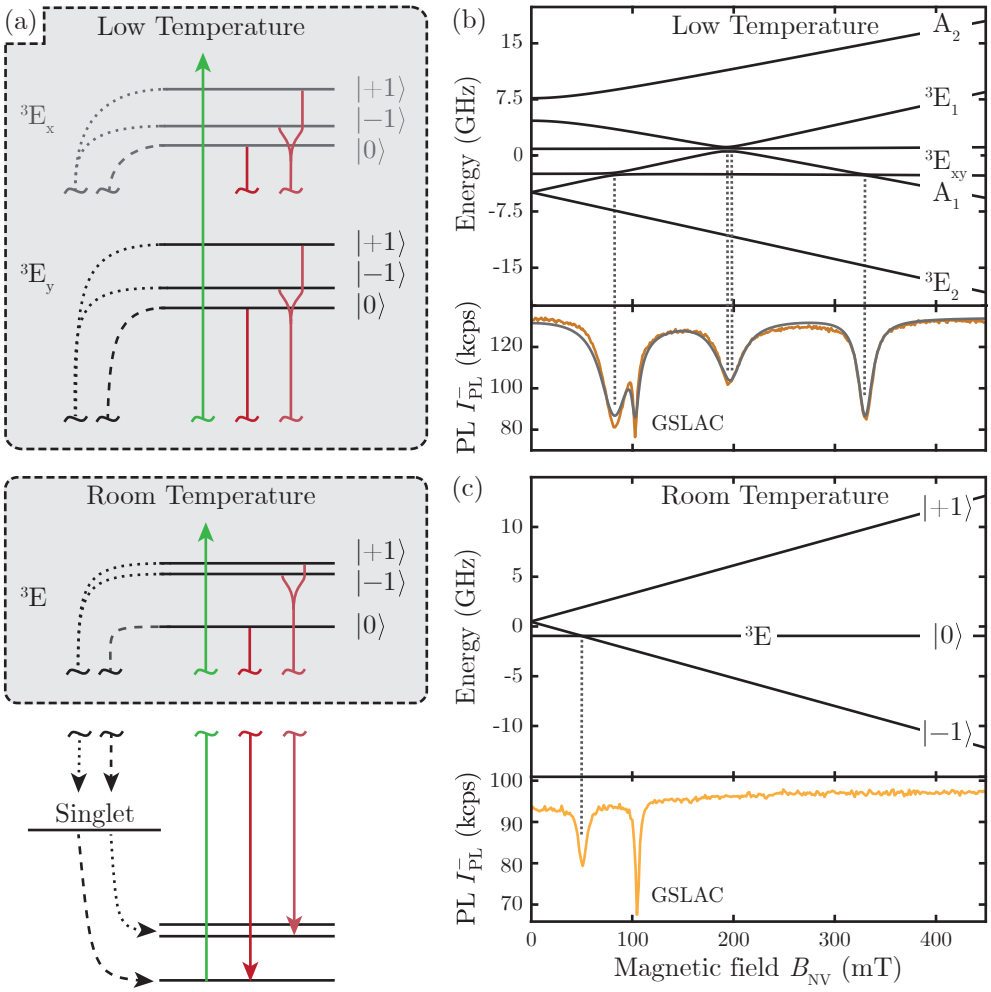

Figure 4.1.: (a) NV level structure for optical spin pumping and spin readout with the excited state manifold for low temperatures (top panel) as an orbital doublet, and room temperature as an orbital-averaged singlet (middle panel). Additionally, the metastable spin singlet and ground state are also shown, which are applicable for both regimes (bottom panel). (b) The excited state manifold for an NV spin at $T = 2\,\mathrm{K}$ with relatively low strain $\delta_\perp = 1.685 \pm 0.003\,\mathrm{GHz}$ (top panel) and the corresponding experimental NV PL I_{PL} as a function of applied magnetic field B_{NV} (orange) and fit (grey). (c) Same as in (b) but for $T = 300\,\mathrm{K}$, for the same low strain NV. Note that the drop in NV PL occurring at $B_{\mathrm{NV}} \approx 100\,\mathrm{mT}$ corresponds to the ground state level anticrossing (GSLAC).

split from the $m_s = 0$ state by a zero-field splitting of $D_0^{\mathrm{ES}}/h = 1.42\,\mathrm{GHz}$ [39, 40, 81] as we discussed in Section 2.4.

This experimental study is an extension of the results presented in Chapter 3 that reveal key fingerprints of the NV's cryogenic ES level structure through dips in NV

photoluminescence, I_{PL}, that occur at specific magnetic fields, B_{NV}, applied along the NV quantisation axis. These dips are the result of ES level anticrossings (ESLACs) between levels of different spin states that cause an increased intersystem crossing into the dark singlet states and therefore a drop in I_{PL}. This process is illustrated in the data presented in Figure 4.1b that shows the measurement of photoluminescence as a function of magnetic field at $T = 2\,\mathrm{K}$ for NV #1, which has a relatively low strain-induced E_x-E_y level splitting. At low temperature, we can identify the multiple-level anticrossings in the excited state, which lead to a reduction in the photoluminescence I_{PL}. At room temperature, we present the same in Figure 4.1c, which shows only one single level anticrossing in the excited state at $B_{\mathrm{NV}} = 50.5\,\mathrm{mT}$, which we identify as the RT-ESLAC (see Section 2.4). The additional reduction at $B_{\mathrm{NV}} = 102.4\,\mathrm{mT}$ for both temperature regimes originates from the well-understood GS level anticrossing (GSLAC) [111, 130] (see Section 2.3).

So far, only these well-known extreme cases at cryogenic and ambient temperatures have been studied in detail. In the following, we exploit the methodology presented above and in Chapter 3 to explore the transition of the ES level structure from cryostat base temperature ($T \approx 2\,\mathrm{K}$) to ambient ($T \approx 300\,\mathrm{K}$) and track the emergence of the resulting high-temperature ES level structure.

We record the photoluminescence I_{PL}, while sweeping the magnetic field along the NV axis B_{NV}, at each temperature T. The experiment is challenging since the measurement relies on an absolute value of I_{PL}, which requires stable optical excitation power and polarization. During the measurement series, we experience laser fluctuations which introduce significant noise to the measurement and are particularly prevalent for the low-strain measurement series (NV #1). Therefore, we perform a normalization to mitigate the effect of these slow fluctuations of I_{PL}, which we attribute to drifts in experimental parameters over the course of our experiment. For the normalization, we first fit the model described below in Equation (4.1) as well as in Appendix A.2 to the raw $I_{\mathrm{PL}}(T)$ data as shown in Figures 4.2a and 4.3a. The fit yields key model parameters (see Appendix A.6 for details) and shows qualitatively good agreement, with deviations occurring at temperatures where signal drifts were dominant. For each temperature we use the model-prediction for $I_{\mathrm{PL}}(B_{\mathrm{NV}})$ at our maximal experimentally available magnetic field $B_{\mathrm{NV}} = 800\,\mathrm{mT}$, where I_{PL} shows the least variations with temperature, to normalise the corresponding dataset $I_{\mathrm{PL}}(B_{\mathrm{NV}})$. In Appendix A.6, we show the raw I_{PL} data for both studied NVs, which shows qualitative agreement with the data (see Figures A.15 and A.16). We also describe the normalization procedure in more detail there.

For the low-strain NV #1, we present the normalized $I_{\mathrm{PL}}(B_{\mathrm{NV}}, T)$ data in Figure 4.2a. At $T = 2\,\mathrm{K}$, the NV level structure of NV #1 results in four sharp I_{PL} dips, which arise from ESLACs occurring both within and between the orbital branches E_x and E_y as shown in Figure 4.1b. With increasing temperature, these ESLAC dips broaden and reach a maximal width at $T \approx 60\,\mathrm{K}$, where they span almost the entire magnetic field range accessible in our experiment. Qualitatively, this broadening is well-described by the T^5 scaling expected from two-phonon orbital mixing processes [40] and depicted with a dotted line in Figure 4.2a.

Remarkably, upon further increasing the temperature, the strongly broadened ESLAC dips disappear, and between $T \approx 70 - 150\,\mathrm{K}$, the only discernible feature is the narrow dip located at $B_{\mathrm{NV}} = 102.4\,\mathrm{mT}$ corresponding to the GSLAC. Only at

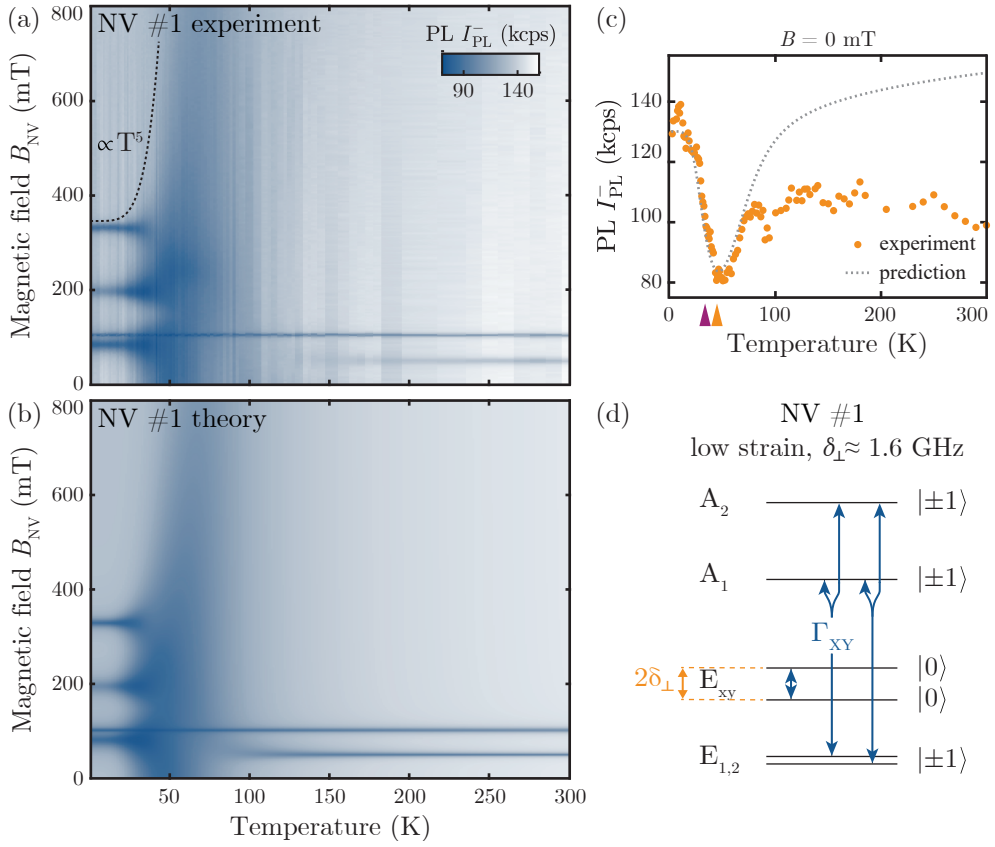

Figure 4.2.: (a) Experimental data of photoluminescence (PL) intensity I_{PL} of a single NV center (NV #1) with "low" strain ($\delta_\perp = 1.685 \pm 0.003\,\mathrm{GHz}$) as a function of temperature T and magnetic field B_{NV} applied along the NV symmetry axis. I_{PL} data are normalized as described in the text and appendix. The dotted line is a guide to the eye for T^5, scaled to follow the half-width contour of the I_{PL} dip. (b) Model prediction of $I_{\mathrm{PL}}(B_{\mathrm{NV}}, T)$. The rate Γ_{XY} is extracted from fits to NV #2 data as illustrated in Figure 4.3c. All other NV transition rates are taken from literature (see Appendix A.6). The dip in I_{PL} occurring at $B_{\mathrm{NV}} \approx 100\,\mathrm{mT}$ across all temperatures corresponds to the ground-state level anticrossing (GSLAC). (c) Raw $I_{\mathrm{PL}}(T)$ data obtained at $B_{\mathrm{NV}} = 0\,\mathrm{mT}$, together with a model prediction using the extracted phonon coupling from NV #2 data. Note the different position of the minima in $I_{\mathrm{PL}}(T)$ for the NV #1 (orange) and NV #2 (purple). (d) Excited state level structure for NV #1.

significantly higher temperatures $T \approx 150\,\mathrm{K}$, the single, sharp dip at $B_{\mathrm{NV}} = 50.5\,\mathrm{mT}$ appears, which corresponds to the NV's well-known RT-ESLAC illustrated in the level structure of Figure 4.1c.

We repeat the same experiment on the high-strain NV #2. The normalized data is shown in Figure 4.3a. Compared to our findings on NV #1, we find several differences in the evolution of $I_{\mathrm{PL}}(B_{\mathrm{NV}})$ with temperature. At $T = 2\,\mathrm{K}$, the high-strain level

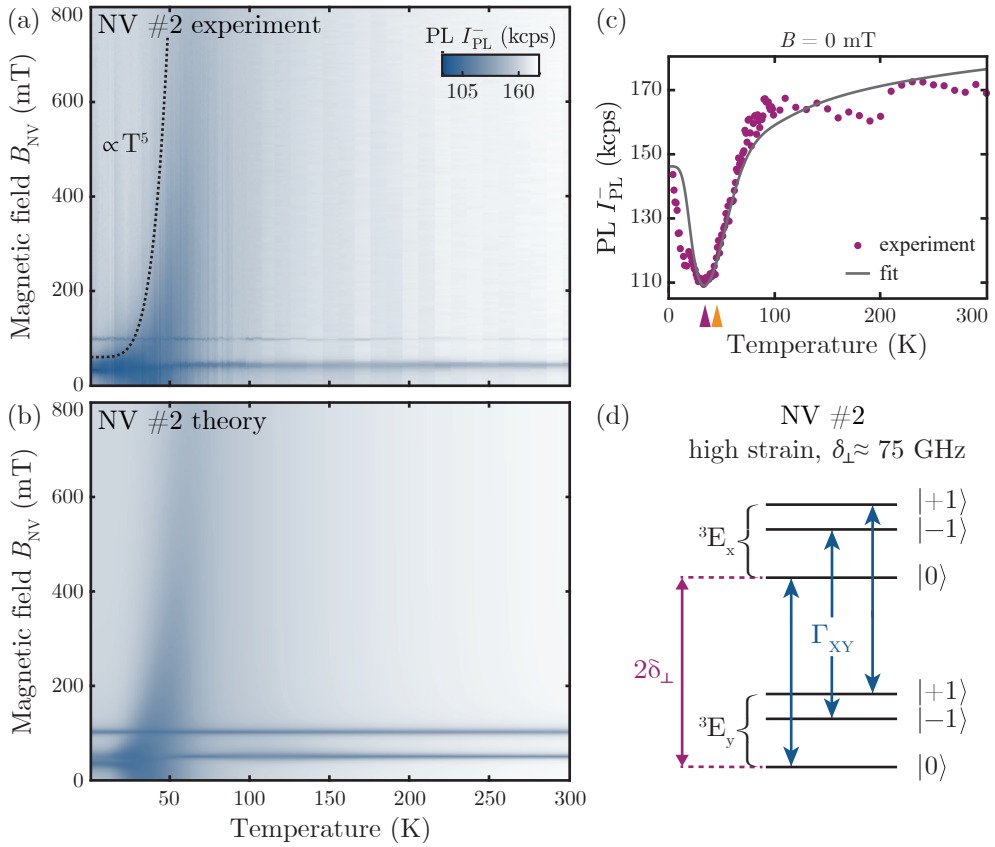

Figure 4.3.: (a) Experimental data of photoluminescence (PL) intensity I_{PL} from another single NV center (NV #2) with "high" strain ($\delta_\perp = 75 \pm 2\,\mathrm{GHz}$) as a function of temperature T and magnetic field B_{NV} applied along the NV symmetry axis same as in Figure 4.2a. (b) Model prediction as in Figure 4.2b, here for the "high" strain case. The rate Γ_{XY} is extracted from fits to data as illustrated in panel (c). All rates in the model remain identical to Figure 4.2b. (c) Raw $I_{\mathrm{PL}}(T)$ data obtained at $B_{\mathrm{NV}} = 0\,\mathrm{mT}$, together with the fit of the model to the raw data and the position of the minima in $I_{\mathrm{PL}}(T)$ for both NVs. (d) Excited state level structure for NV #2.

structure of NV #2 results in only two dips in photoluminescence, each corresponding to ESLACs occurring within one of the orbital branches as described in Chapter 3. For a high strain, splitting the ESLACs occurring between states from different orbitals are located outside our magnetic field range. These two visible ESLAC dips also show a broadening $\propto T^5$ indicated by the dotted line in Figure 4.3a, and merge into a single, broad I_{PL} dip extending over the whole accessible range in B_{NV} for $T \approx 50\,\mathrm{K}$, a slightly lower temperature than for NV #1. Upon further increasing the temperature, the strongly broadened ESLAC dips also disappear, and, starting from $T \approx 60\,\mathrm{K}$, they are replaced by the RT-ESLAC dip discussed earlier.

4.2. Lindblad master equation model

To obtain a full understanding of our data, we develop a quantitative model to describe the NV population dynamics as a function of B_{NV} and T, that explicitly takes into account the full, low-temperature ES NV level structure [10, 46] and temperature dependent, phonon-induced relaxation processes between the involved ESs. To this end, we determine the dynamics of the NV density matrix ρ through the Lindblad master equation

$$\frac{d}{dt}\rho = \frac{i}{\hbar}[\rho, H_{\mathrm{NV}}] + \sum_k L_k \rho L_k^\dagger - \frac{1}{2}\{L_k^\dagger L_k, \rho\}, \tag{4.1}$$

where H_{NV} is the full NV Hamiltonian, and L_k are the relevant collapse operators. The 10×10 density matrix ρ includes the states from the low temperature level structure depicted in Figure 4.1a, specifically the three $^3A_2$ GSs, the six ^3E ESs, and a single state representing the singlet shelving states $^1A_1$ and E_1. For H_{NV}, we employ the well-established NV Hamiltonians for the ground and excited states [10, 46] which are presented in Section 2.3. Full definitions and expressions for ρ and H_{NV}, as well as details on the formalism, are given in Appendix A.2.5

The collapse operators $L_{|i\rangle\to|j\rangle} = \sqrt{\Gamma_{ij}}\,|j\rangle\langle i|$ describe transitions from states $|i\rangle$ to $|j\rangle$ occurring at rates Γ_{ij}. In the model, we consider two different types of transitions: optical transitions as outlined in Appendix A.2.2 and orbital ones from the two-phonon processes described in Appendix A.2.4. The temperature dependence of our photoluminescence data is fully explained by considering the spin preserving, phonon-induced couplings between the orbital branches E_x and E_y [40], that are described by $L_{|X\rangle\to|Y\rangle} = \sqrt{\Gamma_{XY}(T)}\,|Y\rangle\langle X|$ and its inverse process. Here, $|X\rangle$ and $|Y\rangle$ are state vectors corresponding to the ES E_x and E_y manifolds.

In addition, we model optical excitation, spontaneous emission and intersystem crossings with collapse operators between the corresponding orbital manifolds, at rates that we obtain from the literature [36, 112] and keep constant. In the presence of a magnetic field and strain, the effective rates change with the new eigenbasis of the Hamiltonian – an effect naturally accounted for in our model through the master equation. We note that temperature dependencies have only been reported for intersystem crossing rates for $T < 20\,\mathrm{K}$ [35], and in this regime have a negligible effect on our findings as outlined in Chapter 3. In addition, the known temperature-dependent singlet lifetime [131] is phenomenologically taken into account in our model. The expressions for all collapse operators are given in Appendix A.2.5. In Appendix A.6, we also explicitly list the parameters used in the model. However, we find that our main conclusions are insensitive to the exact rates employed; i.e., we obtain largely identical results by using other values from the literature.

We model the behaviour of the photoluminescence as a function of magnetic field and temperature $I_{\mathrm{PL}}(B_{\mathrm{NV}}, T, \delta_\perp)$ by numerically solving for the steady state of the density matrix in Equation (4.1) using the effective strain value and magnetic misalignment determined at low temperature. The photoluminescence is then proportional to the total NV ES population for each value of B_{NV} and T.

4.3. Electron-phonon coupling above cryogenic temperatures

The developed model fully describes our data by taking into account phonon-induced orbital averaging [40] with symmetric rates $\Gamma_{XY} = \Gamma_{YX}$. We consider a two-phonon process from E and A_1 phonons, which couples the excited states and induces a population transfer between the orbitals. The orbital transition rates are slow at low temperatures and increase significantly with temperature. In Appendix A.2.4, we present a detailed theoretical description of the electron-phonon interaction. The quantitative nature of our model then allows us to determine the mixing rate Γ_{XY} induced by the two-phonon processes from fits to the experimental data such as the one presented in Figure 4.2c.

The resulting strain-dependent spin-conserving mixing rate between the excited state orbitals is $\Gamma_{XY} = \alpha_{\mathrm{ph}} I(\omega_{\mathrm{c}} = 60\,\mathrm{meV}, T, \delta_{\perp}) T^5$, where $\alpha_{\mathrm{ph}} = 1.4 \pm 0.2\,\mathrm{Hz/K^5}$ is the phonon-coupling strength and our actual fit parameter in the form of Equation (A.43). It combines both the coupling strength of E-symmetry phonons (η_E) and the coupling strength of A_1-symmetry phonons (η_A). I is the unitless integral over the phonon mode energies with a dependence on the cutoff frequency ω_{c}, temperature T, and non-axial strain $\delta_{\perp}$ as defined in Appendix A.2.4. In the low strain case, Γ_{XY} can also be written as $\Gamma_{XY} = (1 + \epsilon(T, \delta_{\perp})) \cdot \gamma_{\mathrm{NV}} \cdot (0.91 \pm 0.13 \cdot 10^{-6} K^{-5}) \times T^5$, where ϵ is a weakly temperature- and strain-dependent correction factor, with $\epsilon \ll 1$ for $T \approx 10 - 100\,\mathrm{K}$ and γ_{NV} is the radiative recombination rate. This equation shows clearly that at low temperatures the relaxation into the ground state γ_{NV} is the dominant rate and is illustrated in Figure A.17.

We compare our results to other literature values that consider coupling with E-symmetry phonons. Our value of $\eta_E = 150 \pm 18\,\mathrm{MHz/meV^3}$ (see Equation (A.71)) agrees well with prior results [35, 40, 78], but is here obtained in a complementary way that does not require complex, resonant laser spectroscopy. A detailed comparison of literature electron-phonon coupling strengths is given in Table A.10. The results are all in good agreement with each other and provide complementary insights into the involved mechanism.

In our model, we do not consider one-phonon processes for orbital averaging [35], since we do not recognize a significant effect of them on the temperature-dependent photodynamics of our NVs. The one-phonon processes are only dominating the two-phonon processes at low temperatures ($T < 10\,\mathrm{K}$) and only slightly bias the population towards the orbital with the lower energy in the ES [79], an effect almost indistinguishable from selective excitation by a specific laser polarization (see Chapter 3).

4.4. Temperature evolution of the NV^- photoluminescence

In Figures 4.2b and 4.3b, we present the results from the model, which show remarkable qualitative and quantitative agreement with our data, both for the high-strain and low-strain cases. The onset of the broad quenching area and the emergence of the

RT-ESLAC are quantitatively reproduced in both cases, including the marked difference in the respective onset temperatures. The simulation utilizes the magnetic field misalignment to the NV axis as measured at low temperatures, which may change slightly over the course of the experiment as the temperature increases. We attribute some differences between the model and the data to small variations in this alignment.

Our modeling results offer an intuitive way to understand our experimental findings and the evolution of the ESLAC-induced reduction in photoluminescence, I_{PL}, with temperature. At low temperatures, $T \lesssim 10\,\mathrm{K}$, the photoluminescence $I_{\mathrm{PL}}(B_{\mathrm{NV}})$ away from the ESLACs is unaffected by orbital averaging and only starts to decrease once $\Gamma_{XY} \approx \gamma_{\mathrm{NV}}$, where γ_{NV} is the NV's radiative recombination rate. With increasing temperature, the ES levels and, therefore, the ESLACs start to broaden due to orbital mixing at a rate Γ_{XY}, which is proportional to T^5. The recovery of the photoluminescence $I_{\mathrm{PL}}(B_{\mathrm{NV}})$ at $T \gtrsim 60\,\mathrm{K}$ in the high strain case, and at slightly higher temperatures in the low strain case, can then be understood as a process akin to motional narrowing in nuclear magnetic resonance [132]. Once Γ_{XY} exceeds $\lambda_{es}^{\perp}$ – the rate of spin-mixing in the NV's ES – jumps between orbital states will stop, effectively suppressing ES spin mixing processes (see Appendix A.6). Since the reduction of I_{PL} results from ESLAC-induced spin-mixing and subsequent shelving into the NV singlet states, I_{PL} will recover once $\Gamma_{XY} \gg \lambda_{es}^{\perp}$. After this point in temperature, $I_{\mathrm{PL}}(B_{\mathrm{NV}})$ is governed by the effective, RT ES level structure (Figure 4.1c) and shows the well-known RT-ESLAC. This regime is well described by our model but can alternatively also be derived by taking the partial trace of the excited state Hamiltonian $\hat{\mathcal{H}}_{es} + \hat{\mathcal{V}}_{es}$ over the orbital degrees of freedom (see Ref. [79]). For lower effective strain values, the relative energy differences play a more pronounced role, but the described mechanism remains the same. This transition is evident in the simulations displayed in Figure A.18, which shows the photoluminescence as a function of magnetic field and effective strain at selected temperatures.

Our model and data also yield the unexpected observation that the appearance of the RT-ESLAC has a strong strain dependence. The data in Figures 4.4a and b illustrate this and show how the RT-ESLAC appears much later in the magnetic field for the low-strain NV #1, compared to the high-strain NV #2. To further support this observation, we extract from our model the contribution to I_{PL} originating from the RT-ESLAC alone using a method described in Appendix A.6. We present the resulting model prediction for the relative change in $I_{\mathrm{PL}}(T, \delta_{\perp})$, evaluated at the magnetic field of the RT-ESLAC $B_{\mathrm{NV}} \approx 50.5\,\mathrm{mT}$, in Figure 4.4c. The simulations clearly demonstrate that the emergence of the RT-ESLAC depends heavily on strain, as the low-temperature energy configuration alters the effect of orbital averaging on the photoluminescence. The onset temperature of the RT-ESLAC also depends strongly on the magnetic field misalignment θ_B and shifts to lower temperatures as the magnetic field misalignment increases. Over the course of our experiment, small changes in the magnetic field alignment can occur due to the presence of minute drift and hysteresis in the magnet operation, which explains the slight discrepancy in the onset of the RT-ESLAC, especially in the low-strain case.

The excited state ODMR is closely related to the effective room-temperature level structure and the RT-ESLAC. While the temperature dependence of the ES ODMR for low-strain NVs has been assessed in a prior study [39], its quantitative understanding as presented here was missing thus far.

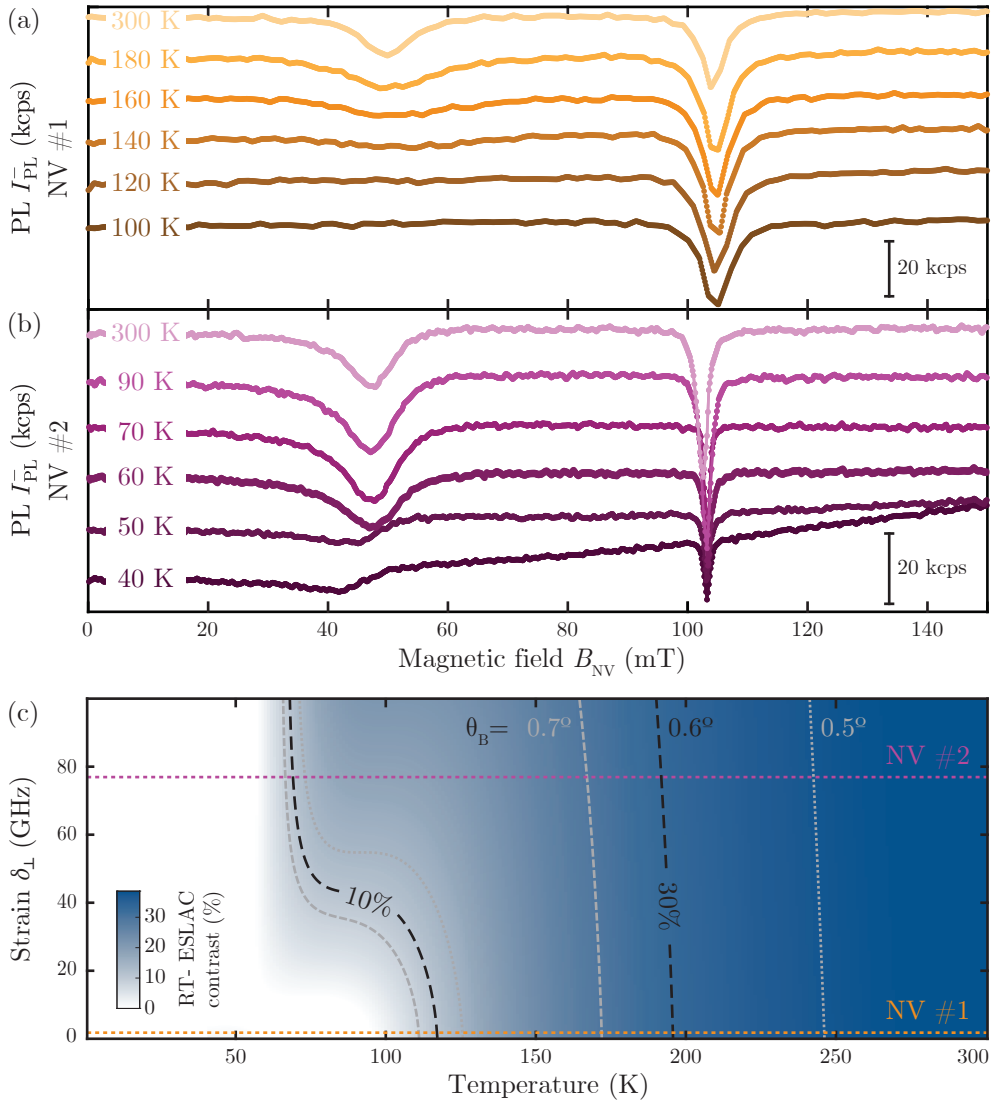

Figure 4.4.: Appearance of the room-temperature excited state level anticrossing (RT-ESLAC) for the NVs with low strain (a) and high strain (b). The data is offset for clarity. For the low-strain NV, the RT-ESLAC appears only at significantly higher temperatures compared to the high-strain NV. (c) Model prediction of the relative change in $I_{\mathrm{PL}}(T, \delta_\perp)$, evaluated at the RT-ESLAC field for a magnetic field misalignment $\theta_B = 0.6°$ (see text and Appendix A.2). Dash lines mark the position of RT-ESLAC contrast isolines for $\theta_B = 0.6°$ in black, with misalignment increments of $\pm 0.1°$ in grey.

4.5. Implications for NV-based applications

As shown in Section 3.5, a reduction in photoluminescence I_{PL} directly relates to a reduction in optical spin readout contrast $\mathcal{C}$ of the optically detected magnetic resonance [49]. Even though we did not explicitly measure this contrast during the temperature-dependent measurements, our simulations of NV #1 and NV #2 spin contrast, as seen in Figure 4.5, show the same qualitative behaviour in temperature as I_{PL}. This shows that spin initialization as well as spin readout from traditional readout techniques [69] are affected by the phonon induced spin relaxation process over a large temperature range.

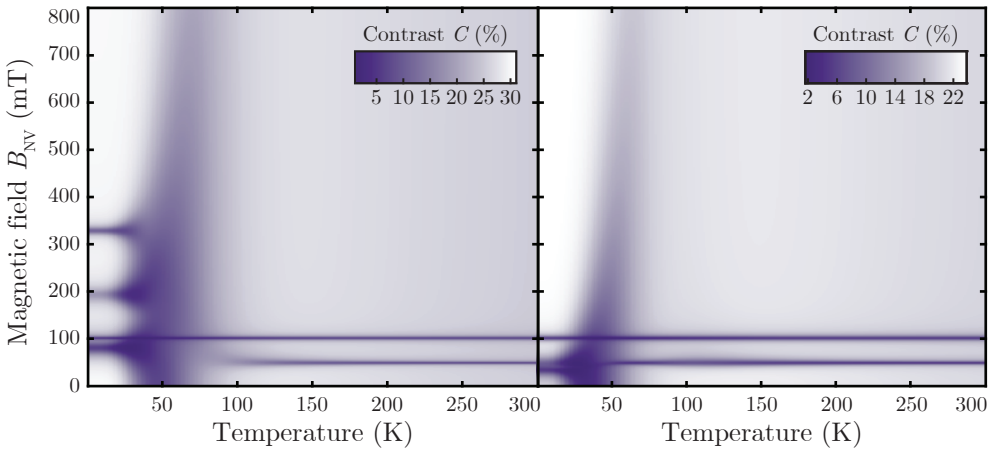

Figure 4.5.: (a) Simulated ODMR contrast $\mathcal{C}$ for NV #1 exhibiting low effective strain for microwave driving between $|2\rangle$ $({}^3A_2^0)$ and $|3\rangle$ $({}^3A_2^{-1})$ with a Rabi time of 100 ns using the parameter extracted from the fits (see Appendix A.6). (b) Same for NV #2 exhibiting elevated effective strain. The areas of reduced spin readout contrast $\mathcal{C}$ of the optically detected magnetic resonance correspond to the areas of reduced photoluminescence I_{PL}^{-}. The broad quenching effect at intermediate temperatures extends to very high magnetic fields, significantly higher than our accessible range.

This combined reduction in I_{PL} and $\mathcal{C}$ severely affects the NV's magnetic field sensitivity η as defined in Equation (3.3). Compared to typical sensitivity values at zero field at room temperature, η drops by almost an order of magnitude in areas of extended excited state mixing. Therefore, our study of the photoluminescence allows us to assess the performance of the NV^- as a sensor, highlighting the implications for measurements at intermediate temperatures.

At low temperatures, it is generally possible to avoid regions of excited state mixing by applying a bias magnetic field along the NV axis, thereby recovering PL and spin readout contrast. However, the mixing induced by phonons poses different challenges. The extended area of quenched PL for intermediate temperature ($25\,\mathrm{K} < T < 100\,\mathrm{K}$) as seen in Figure 4.5 cannot be avoided in moderate magnetic fields and severely impairs the NV sensing performance in this regime with a magnetic field sensitivity η up to more than a magnitude worse compared to its optimal value. The effect extends to very high magnetic fields, significantly higher than our accessible range,

and therefore, a bias magnetic field is not feasible for the majority of experimental setups. The effects can be slightly confined to a smaller region in temperature and magnetic field by the use of high-strain NVs, which, however, may not be practicable for certain experiments.

Generally, the reduced sensitivity of the NV needs to be considered when using the NV at intermediate temperatures, as it affects the feasibility of experiments that would otherwise be possible with NV magnetometry.

4.6. Summary and outlook

In conclusion, we have presented a comprehensive study of the magnetic field and temperature dependence of the photoluminescence emission rates of individual negatively charged Nitrogen-Vacancy centers in the limits of both low and high strain. We build on our work from Chapter 3 and bridge the gap between the already known NV center models at low- and room temperatures. Our work presents a comprehensive picture and a quantitative model of the temperature-induced orbital averaging process that was previously missing. We demonstrated that mixing in the excited state through a two-phonon process fully accounts for the previously unexplained NV PL quenching around $T \approx 50\,\mathrm{K}$ and, through a process akin to motional narrowing, also at the subsequent revival of NV PL at higher temperatures. We thereby complement past research on orbital averaging in the NV ES, allowing for deeper insight and the emergence of an effective, room-temperature ES level structure, as well as the strain dependence of the temperature onset of the room-temperature excited state anticrossing. In addition to providing fundamental insights into the photophysical properties of NV centers, our results are also relevant to applications of NV centers in quantum sensing and quantum information processing, as they predict the most sensitive regions of operation in the parameter space of magnetic field and temperature. Specifically, our experimental data and accompanying theory enable the identification of conditions away from ESLACs and broad mixing regions, where optical spin initialization and readout are most effective. This is particularly important for sensing applications that utilize NV centers operating in intermediate temperature regimes.

Our results also have implications beyond the field of NV centers in diamond. The presented methodology is applicable to other emitters and multi-level quantum systems. In particular, the approach presented here applies to any color center where LACs and spin-dependent dark states can be detected through ODMR. It offers a highly valuable tool to better understand the internal dynamics of other optical platforms and their photophysics. This includes, for example, SiV centers in SiC [133] or the charge-neutral SiV center in diamond [134], where our method is expected to shed new light on unknown ES structures, orbital averaging, or the still poorly understood temperature dependencies in SiV^0 PL [135].

5. Towards ultra-low temperature sensing with single NV centers

The Nitrogen-Vacancy center is used in various sensing applications (see Section 2.5). One of the most prominent and mature use cases is scanning NV magnetometry [18, 23, 75, 101, 136, 137] which has emerged as a robust and leading technique for the imaging of mesoscopic magnetic phenomena with high magnetic field sensitivity and nanoscale spatial resolution. NV magnetometry is based on the magnetic field dependence of the $m_s = \pm 1$ spin sublevels of the NV^-ground state, which in the presence of a magnetic field applied along the NV axis B_{NV} split due to the Zeeman effect [18]. The Zeeman splitting between those two states can be probed by ODMR using a microwave (MW) driving field from a near-field coupling device in proximity to a single NV center to manipulate its electron spin. This technique offers magnetic field sensitivities of a few $\mu T/\sqrt{Hz}$ [93] which can be improved to a few tens of $nT/\sqrt{Hz}$ [24] by coherent spin manipulation and dynamical decoupling [138].

In scanning NV magnetometry, the NV center, created by ion implantation and subsequent annealing [139, 140], is located in an all-diamond scanning probe [24, 37, 141], a few tens of nanometers from the nanopillar surface. The scanning probe itself is mounted onto a tuning fork, which is part of an atomic force microscope (AFM) [24, 141], to precisely control the tip-to-sample distance (see Appendix A.3.5). By raster-scanning the diamond probe over a sample, a nanoscale magnetic image can be recorded. The spatial resolution of this technique is predominantly determined by the NV-to-sample distance d_{NV}, with typical values of $d_{NV} \leq 80\,nm$. The proximity of the NV sensor to the sample [24] together with the photonic properties of the scanning probe, maximizes the magnetic field sensitivity [22], making scanning NV magnetometry a powerful approach for visualizing nanoscale magnetic features.

Thanks to the robustness of NV spin optical initialization and readout across a wide range of conditions, scanning NV magnetometry can be performed from room temperature down to low temperatures, within the constraints discussed in Chapters 3 and 4. While scanning NV magnetometry below 1 K has been demonstrated, performing it is not yet routinely achieved, with only one experiment reported at 350 mK [142]. Achieving such measurements is mainly limited by technical challenges, including minimizing heat load and ensuring effective thermalization, both essential for maintaining ultra-low temperatures. The charge instability of near-surface NVs further complicates operation under vacuum and cryogenic conditions.

Although all-optical magnetometry with NVs is possible [143], its implementation is highly complex and has so far been limited to proof-of-concept demonstrations. Current NV magnetometry implementations instead rely on relatively high-power microwaves for efficient spin driving, which constitute the primary source of heating in these experiments. This poses a major challenge in ultra-low-temperature systems [144], where the total cooling power is typically below 1 mW. Under such condi-

tions, achieving efficient coupling between the driving field and the NV spin requires excellent thermalization and carefully optimized, low-heat measurement techniques. Moreover, cryogenic setups are further constrained by the limited available space.

Near-surface NVs are necessary for high sensitivity, nanoscale sensing, but suffer charge instabilities [145–150]. Shallow NVs created by ion implantation, the most common method to obtain near-surface NVs, exhibit higher ionization and recombination rates compared to NVs in bulk diamond [147], and their charge stability is strongly dependent on the chemical composition of the surface [145]. Even though NV scanning magnetometry is routinely used at low temperatures [26, 29], the charge stability of near-surface NVs is further reduced in cryogenic and vacuum environments. Consequently, the measurement time available is also considerably shortened.

To investigate emerging quantum phenomena of strongly correlated electron systems at temperatures around 100 mK and below, we are implementing scanning NV magnetometry in a closed-cycle dilution refrigeration system described in Appendix A.3.1. In the following sections, we present our work addressing the challenges of implementing ultra-low-temperature scanning NV magnetometry and outline the future use of such an instrument.

In Section 5.1, we discuss the challenges of efficient microwave driving in scanning systems at low and ultra-low temperatures, constrained by limited cooling power and poor thermalization (see Appendix A.3.4). We review existing approaches to probe attachment and microwave driving in scanning NV magnetometry, highlighting their limitations for ultra-low-temperature operation.

In Section 5.2, we present a novel scanning probe device with integrated MW delivery for scanning NV magnetometry, which addresses these limitations. We demonstrate and analyze its mechanical and electrical characteristics as well as its performance for coherent spin manipulation.

In Section 5.3, we investigate how operating this integrated device affects the temperature of the NV center and the sample under cryogenic conditions, by using the temperature dependence of the NV^- photoluminescence reported in Chapter 4.

We also performed scanning NV magnetometry experiments with the integrated MW delivery device at cryogenic temperatures, which are presented in Section 5.4. We also show that this device can deliver magnetic field pulses capable of switching the magnetization of a CoFeB thin film.

Furthermore, we discuss the charge instability of near-surface NV centers in nanostructures in Section 5.5. We report on the NV^- to NV^0 charge state transition observed in our cryostat, propose a possible mechanism for the accelerated change, and test mitigation strategies relevant to low-temperature scanning NV magnetometry.

Finally, in Section 5.6, we summarize the progress toward implementing an ultra-low-temperature scanning NV magnetometer and map out the steps needed to fully realize its potential. We discuss improvements to the integrated coupling device and outline possible upgrades relevant to scanning NV magnetometry and other scanning probe techniques. In addition, we present an alternative approach to ultra-low-temperature magnetic field sensing based on the Silicon-Vacancy center, which avoids the challenges associated with the charge instability of near-surface NVs and the need for microwave driving. In addition, we highlight prospective applications in condensed matter physics, particularly for investigating material systems at around 100 mK.

The results presented here will be published in Happacher *et al.* [44].

5.1. Microwave driving in scanning NV magnetic imaging

Scanning NV magnetometry experiments require both an NV sensor with excellent spin properties and the ability to manipulate this spin effectively and reliably using MWs. In the following, we describe existing methods for attaching a diamond probe to an atomic force microscope assembly using a dedicated support structure and review state-of-the-art approaches for microwave delivery. We discuss their advantages and disadvantages, and evaluate their appropriateness for ultra-low-temperature NV scanning experiments.

The diamond probe typically consists of a tapered nanopillar on a platelet 3–30 µm in size, with the nanopillar height ranging from 2–10 µm [37, 141]. A support structure connects this diamond probe to the AFM assembly, which controls the distance between the apex of the probe and the sample during scanning. Such support structure can take different forms and be made of various materials, such as an etched silicon piece [151] or a tapered quartz rod [141, 152]. Its geometry and fixing point are designed to maintain free optical access to the nanopillar, which acts as a photonic structure. The diamond probe is typically first attached to the support structure, which is then mounted on the AFM tuning fork. This assembly process generally achieves an angular misalignment between the probe and the sample of less than two degrees. However, these support structures also present some drawbacks. The probe is fixed only on one side of the diamond platelet, creating a lever and potential breaking point. During cooldown, vibrations from phase transitions in the cryostat, such as that of nitrogen at 77 K, can also cause the probe to detach.

Efficient spin manipulation requires the MW driving field to be applied in close proximity to the NV center. Additionally, the coupling device should provide broadband transmission with minimal frequency-dependent attenuation, enabling a wide detectable magnetic field range in ODMR measurements. Various microwave delivery approaches have been developed for scanning NV magnetometry.

At room temperature, small bond-wire loops with independently adjustable positioning are commonly used to achieve stable and efficient microwave driving of the NV spin during scanning [103, 151, 152]. This approach offers the advantage of maintaining a fixed, close distance to the NV center while remaining relatively far from the sample, thereby reducing unwanted sample heating. It has, however, several disadvantages. The shape of the wire loop varies between implementations, resulting in significant differences in microwave coupling strength and the inhomogeneity of the radiated field. At high powers, thermally induced movements of the loop can lead to changes in the distance between the loop and the NV center, causing fluctuations in coupling efficiency. Positioning the antenna in situ is cumbersome because fine adjustments of the distance to the scanning probe can lead to catastrophic failures, resulting in damage or loss of the diamond scanning probe and sample.

For measurements in cryogenic environments and under applied magnetic fields, the entire setup must fit inside a small-bore superconducting magnet, requiring compact microwave delivery solutions. Bond wires, typically 30 µm in diameter and placed close to the sample [26, 153, 154], are a commonly used solution. However, they suffer from poor impedance matching and high power dissipation, leading to an uneven distribution of microwave radiation [155, 156]. Lithographically defined structures

on the sample range from planar striplines [157–159] and rings [156, 160–163] to resonators [164–171]. These structures exhibit good impedance matching and improved transmission compared to bond wires, and are also widely used for low-temperature NV magnetometry. However, omega and other resonator designs often have limited bandwidth and are therefore less suitable for scanning experiments that require operation over a wide frequency range. Another limitation of these approaches is that only areas close to the microwave line (typically within 100 µm) can be probed with high magnetic sensitivity. Additionally, variations in the distance between the wire and the NV center during scanning result in changes in the microwave intensity. These variations degrade the sensitivity of continuous-wave (CW) scanning NV magnetometry and pose practical constraints and drawbacks for pulsed sensing techniques [22, 32], and emerging quantum sensing modalities building on coherent spin manipulation [172].

An attractive alternative to the methods described above is to have the microwave delivery system fixed to the positioning stack of the scanning probe, enabling more stable and efficient coupling across the entire scanning range of the sensor. So far, efforts to integrate such near-field coupling devices on the scanning probe holder have involved bonding a wire between electrical contacts located away from the NV and manually bending it into position [152, 173]. In Figure 5.1 we show our implementation of such a device and its performance. A gold bond wire, shaped into a loop, is positioned around the diamond scanning probe in a way that ensures that the probe is the lowest point of the assembly. The close proximity of the wire to the NV center generally results in a strong coupling, with recorded π-pulse times as short as 18.5 ns. Although this implementation provides strong microwave coupling to the NV center, it suffers from complex fabrication and poor reproducibility. Manipulating the wire under an optical stereo microscope is difficult to replicate, making batch production impractical. Variations in antenna shape and distance to the NV lead to inconsistent coupling strengths. Multiple devices have shown widely differing Rabi times, with variations exceeding 100 ns at the same power. In addition, because the wire is not mechanically integrated with the support structure, thermally induced motion at high microwave powers remains problematic [152].

In summary, current microwave delivery methods for scanning NV magnetometry suffer from significant limitations that constrain both the sensitivity and versatility of the technique, particularly under low-temperature conditions. Moreover, these approaches often lack reproducibility, making it difficult to achieve consistent performance across experiments. A solution integrating the microwave delivery circuitry into the scanning probe assembly would overcome many of these limitations. This approach would provide several key advantages, including more stable microwave driving during scanning, reduced power requirements, and simplified experimental design. An example of this idea is illustrated in Ref. [173], where a planar MW loop is patterned directly on top of the diamond probe. Lithographic fabrication of microwave structures directly on the diamond scanning probe or its support is, however, extremely challenging due to the small feature sizes and the requirement for three-dimensional patterning. Another major difficulty lies in reliably establishing electrical contacts to such microscopic structures. These challenges have so far prevented the development of reproducible solutions that go beyond manually assembled bond wires [152] or side-mounted microwave lines [174].

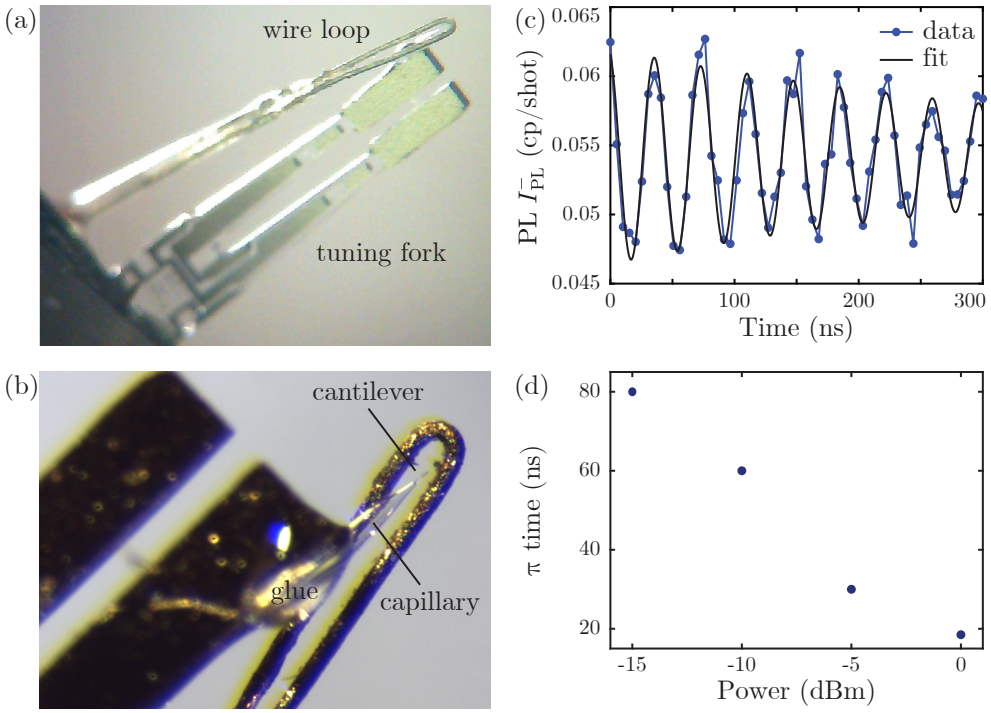

Figure 5.1.: Hand-made wire loop for efficient NV spin driving. (a) and (b) Diamond scanning probe, containing a single NV center, attached to a quartz tuning fork via a quartz capillary (see Appendix A.3.5). A thin gold wire (30 µm) is bent into a loop, and both ends are inserted into a tapered quartz theta tubing where the wires are electrically separated through the septum. The wire loop is positioned around the diamond probe under an optical microscope and held in place with glue. The wire is then carefully bent into shape with tweezers. The close proximity of the wire to the NV results in a strong MW coupling. (c) Rabi experiment with NV spin driving via the wire loop, resulting in a π-pulse of 18.5 ns for 0 dBm. An additional amplifier with a gain of 40 dB was used. (d) π-times for various MW powers for the same device.

5.2. Efficient spin manipulation with an integrated coupling device

Considering the limitations of existing methods, we propose a novel approach to an all-integrated sensor that further enhances scanning NV magnetic imaging, particularly at low temperatures. We developed a near-field microwave coupling device directly integrated into the support structure that holds the diamond probe, and which can be reproducibly fabricated in just a few steps.

Design and fabrication

The key innovation of our device is a gold microwave delivery line integrated directly onto the robust, monolithic tip-holding structure, which is mounted on the tuning fork (TF) force sensor. The rigid design and close proximity of the line to the diamond probe are intended to ensure stable and strong coupling to the NV center during scanning. The design of the probe is shown in Figure 5.2.

The fabrication of this microwave delivery and support structure involves only two steps, ensuring high reproducibility. First, the structure is manufactured using laser-enhanced etching of fused silica similar to Ref. [175]. This subtractive technique produces the required three-dimensional structure with feature dimensions ranging from millimeters to a few microns. Second, a directional metal evaporation of an Au layer (450 nm to 1.4 µm thick) on the top-surface of the structure forms the MW transmission line. The silica structure features a few µm deep groove with undercuts as seen in the cross-section of Figure 5.2b, that runs along the center of the structure and extends to a through-hole. This undercut electrically isolates both sides of the MW line, forming a coplanar MW line that extends from the TF base to the scanning tip. The groove depth determines the maximum metal layer thickness, as it prevents exposure of the sidewalls during the evaporation process. The dimensions of the electrical leads are optimized to achieve maximum impedance matching within the spatial constraints of the tuning fork. At the front, the device narrows and slopes down to form a micrometer-sized loop around a tapered 12 µm wide through-hole, as seen in Figure 5.2b. The diameter of this hole, or more precisely, the width of the slit, is about 12 µm. The thickness of the probe end is about 18 µm from the top side to the bottom side, and its width is about 60 µm. The conical inner walls of the through-hole enhance optical collection from a typical diamond pillar (NA < 0.55) [37] and bring the microwave lines closer to the NV center. The loop geometry concentrates the microwave field at its center, further increasing the driving efficiency.

In the final assembly, which is compatible with low temperatures, high magnetic fields, and vacuum environments, the device is fixed on top of the quartz tuning fork, which is soldered to a printed circuit board (PCB) as described in Appendix A.3.5. The PCB, as shown in Figure 5.2c, includes electrical connections for excitation and readout of the tuning fork, along with two mSMP microwave connectors and corresponding coplanar lines leading to the wedge-shaped termination pads of the device. The device is fixed to the front and base of the TF prong using a UV-curable adhesive. This design avoids rigid attachments in regions of high mechanical stress along the tuning fork [176], preventing degradation of its mechanical properties and preserving optimal atomic force microscopy performance.

A micro-manipulator is used to position the diamond scanning probe at the center beneath the silica loop, where it is secured with UV-curable adhesive. No change in optical count rates is observed before and after mounting, confirming that the device maintains unobstructed optical access and that the conical through-hole effectively accommodates the numerical aperture of the diamond nanopillars. Back focal plane images further confirm that the full optical field is preserved. The NV center can be easily aligned in the optical focus of the confocal microscope, thanks to the clearly visible support structure. The distance between the NV center and the microwave line is below 10 µm and is primarily determined by the dimensions of the diamond

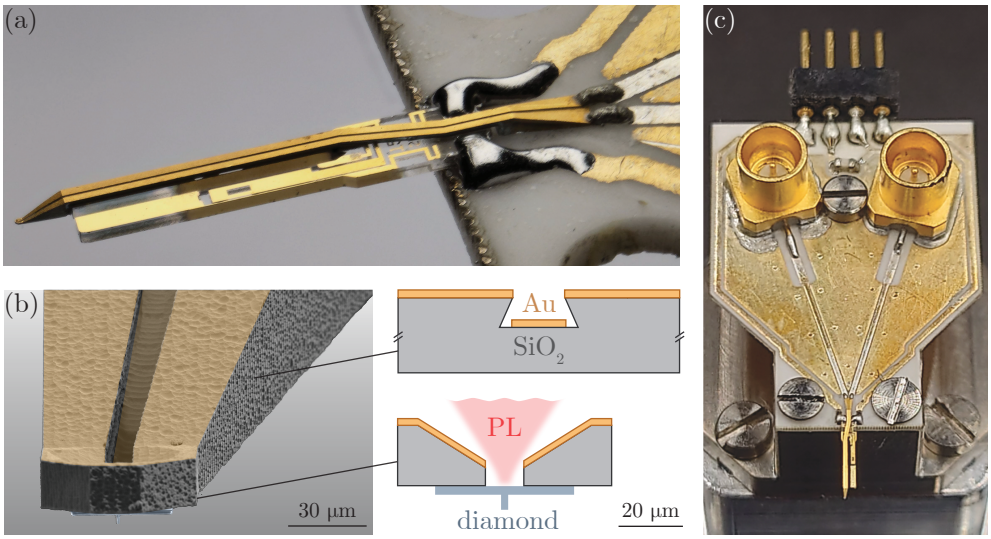

Figure 5.2.: (a) Optical image of the scanning probe assembly. The device is mounted on a tuning fork and soldered to coplanar waveguides on a ceramic PCB. (b) Scanning Electron Microscope image of a diamond scanning probe (blue) attached to the front of the device. The device consists of a SiO_2 support structure with a gold top layer. The cross-section in the upper panel shows that both sides of the transmission line are separated by a groove with undercuts. For optimal MW coupling to the diamond scanning probe, the gold transmission line creates a loop around the position of the NV center sensor. The lower panel shows that the slanted walls of the through-hole provide unrestricted optical access for the NA of our diamond photonic waveguide. (c) Optical image of the entire assembly with the tuning fork excitation and TF read-out connectors at the back of the ceramic PCB, as well as the two mSMP microwave connectors.

scanning probe. This close proximity is very difficult to achieve with any other MW delivery solutions for NV scanning experiments.

The large, symmetrical contact area between the diamond probe and the support structure enhances the mechanical robustness of the assembly, allowing it to withstand higher contact forces than previous designs [141, 151, 152]. It also minimizes the risk of probe detachment during handling, cool-down, and scanning operations. With this device, the breaking point under excessive force during AFM operation occurs at the tapered nanopillar of the probe, rather than at the attachment point to the support structure, as is the case in current implementations. The assembly constrains all degrees of freedom in positioning the diamond probe, minimizing the risk of misalignment or tilt errors. The chosen geometry ensures that the lower surface of the loop remains parallel to the sample plane once mounted. Another advantage of this design is that the device is fully reusable. The diamond probe can be detached by dissolving the adhesive in acetone and lifting it off with a micromanipulator. The device can then be cleaned with solvent and dried in a critical point dryer to remove any remaining liquid.

In summary, the integrated NV-based magnetic field sensor streamlines scanning experiments by removing the need for a separate microwave delivery system, enhancing coupling to the driving field, reducing fabrication and alignment complexity, and minimizing the risk of probe loss during handling.

Mechanical and electrical characterization

We examine the mechanical, electrical, and microwave performance of the fabricated devices. In Figure 5.3a, we show the frequency dependence of the TF mechanical amplitude, under electrical excitation before and after mounting the device. All ten tested devices have a very consistent behavior. Their mechanical quality factor is reduced by roughly a factor of five compared to the bare tuning fork in ambient conditions. Furthermore, the mass imbalance created by the device attachment produces a splitting of the tuning fork's mechanical modes. Despite a minor degradation, the mechanical properties of this assembly remain sufficient for atomic force microscopy, as demonstrated later.

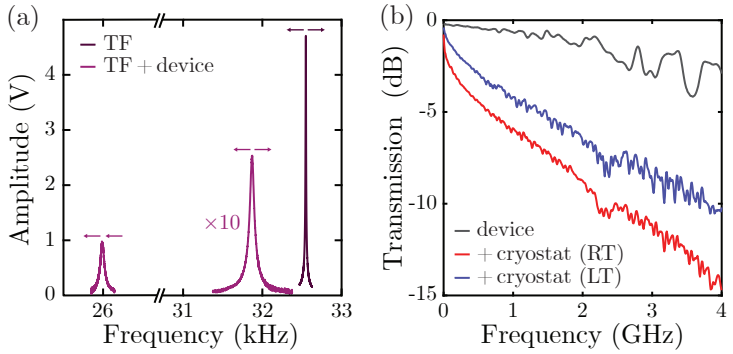

Figure 5.3.: (a) TF resonance curves in ambient conditions, before and after mounting the device. The mass imbalance reduces the Q-factor by a factor of ≈ 5 and leads to mode-splitting. As outlined in Appendix A.3.5, the TF is excited electrically with a peak voltage of 50 mV. (b) Calculated MW transmission spectrum of the device alone, as well as measured MW transmission spectra through the cryostat lines at room temperature (RT) and low temperature (LT).

We characterize the frequency response of the devices using a vector network analyzer (ZNB 4, *Rohde & Schwartz*) to measure the scattering parameter (S-parameter) in a 2-port transmission configuration. The S_{12}- and S_{21}-parameters specify the insertion loss and are therefore measures of the MW power transmitted through the device. Figure 5.3b shows the transmission characteristics of the MW delivery line for a device at room temperature and low temperatures recorded through the MW lines inside the cryostat. The transmission through the device alone is calculated by deducting the transmission of the cables up to the PCB. The device exhibits a direct current (DC) resistance slightly below 10 Ω, and its transmission decreases exponentially with increasing frequency. Based on simple geometrical considerations, the electrical DC breakdown voltage, which eventually limits the current a device

can carry, is estimated to be around 7 V in air. During our experiments, we successfully applied DC currents of up to 100 mA at 4 K without device failure, though this current level caused noticeable thermal heating. Above 2 GHz, the faster decrease in transmission and the oscillations are largely due to the thin 360 µm MW cables, solder joints, and the coplanar striplines on the ceramic PCB, rather than by intrinsic properties of the device. Across all tested devices, the transmission characteristics are nearly identical, and the small differences in magnitude above 2 GHz are attributed to variations in their electrical connections to the PCB. The consistent electromagnetic and mechanical characteristics observed across our devices are attributed to the high precision and reproducibility of the fabrication process.

Coherent NV Spin Control

To assess the practical suitability of our device for quantum sensing, we demonstrate coherent spin control of the scanning NV center at ≈ 4.2 K in a liquid helium bath cryostat. This experiment directly evaluates how efficiently the microwave signal reaches and drives the NV spin, providing a more accurate measure of coupling efficiency than the transmission curve shown in Figure 5.3b. We performed our experiments in a bias magnetic field of ≈175 mT, to optimize the NV spin readout contrast as explained in Chapter 3. All microwave power values reported refer to the power measured at the entrance of the cryostat.

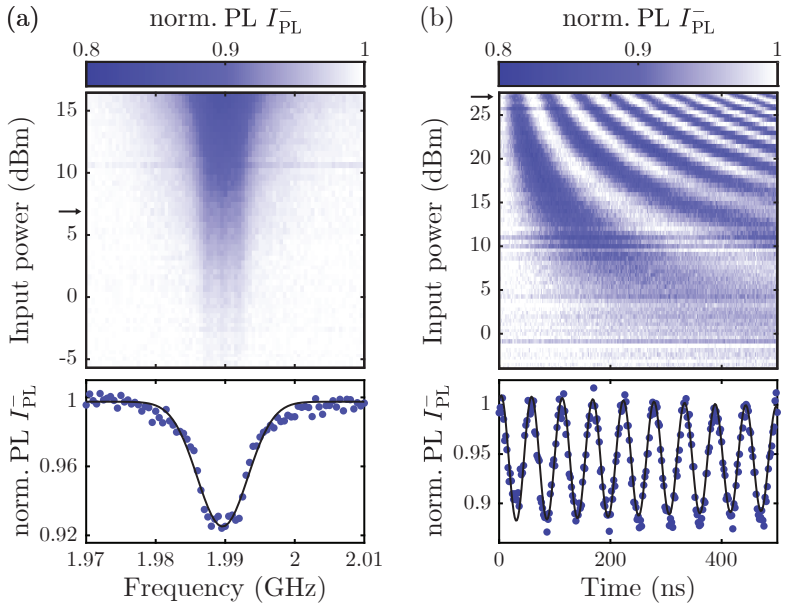

Figure 5.4.: (a) Single NV ODMR spectrum as a function of MW power P_{MW} at a magnetic field of ≈ 175 mT applied along the NV axis. At low power, the hyperfine splitting of the NV is resolved. (b) Rabi oscillations as a function of P_{MW} under resonant driving at 1.99 GHz. The line cut shows a Rabi frequency of 18.2 MHz.

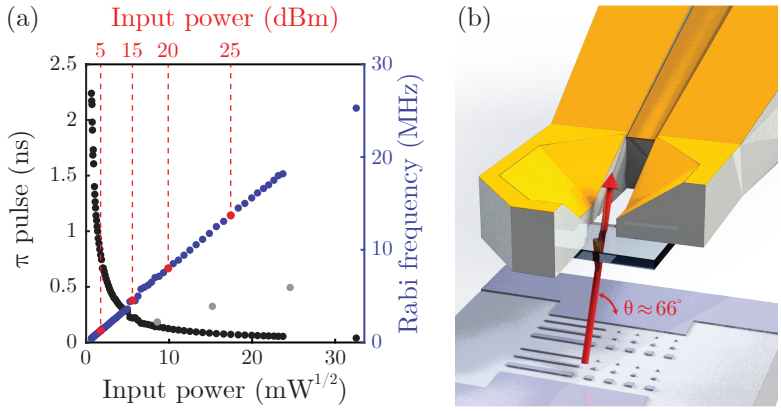

Figure 5.5.: (a) π-pulse length and Rabi frequency as a function of $\sqrt{P_{\mathrm{MW}}}$. The Rabi frequency shows a linear dependence with a slope of $0.79\,\mathrm{MHz}/\sqrt{\mathrm{mW}}$. The gray data points show a comparison with an on-chip antenna patterned directly on the sample and measured in the same experimental setup. (b) 3D rendering of the device and MW driving field vector at the position of the NV center in the scanning probe apex, derived from the coupling strengths of three differently oriented NV centers in the same diamond probe. The MW magnetic field generated by the device lies close to its symmetry plane and is tilted 66° towards its back.

First, we recorded a series of ODMR spectra for a single NV as a function of MW power P_{MW} applied to the integrated MW delivery device, as shown in Figure 5.4a. At low MW powers, where power broadening is negligible, the hyperfine structure of the NV spin resonance is clearly resolved. The single spectrum shown in the upper panel was recorded at a power of 6.8 dBm, which marks the onset of a clear power broadening [177], and where the magnetic field sensitivity is nearly optimized [32]. In this case, we calculate a DC magnetic field sensitivity of $\approx 4\,\mu\mathrm{T}/\sqrt{\mathrm{Hz}}$, which is limited by the intrinsic properties of the NV center under investigation and not the integrated device. We continue by measuring Rabi oscillations under resonant MW driving at a frequency of 1.99 GHz as a function of P_{MW} as shown in Figure 5.4b. The Rabi oscillations, with a frequency of 18.2 MHz, shown in the bottom panel of Figure 5.4b were obtained at $P_{\mathrm{MW}} \approx 27\,\mathrm{dBm}$. We compare these results with those obtained using an on-chip lithographed antenna, a commonly employed approach in scanning NV magnetometry. Applying the same MW power results in significantly lower Rabi frequencies of around 5 MHz. At the amplifier's saturation power of 30 dBm (ZHL-42W+, *Mini-Circuits*), Rabi frequencies of 25.3 MHz, corresponding to a π-pulse duration of 19.8 ns can be reached with the integrated device. These measurements are summarized in Figure 5.5a which shows the expected linear dependence of the Rabi frequency on $\sqrt{P_{\mathrm{MW}}}$ and the π-pulse duration as a function of P_{MW}.

We extended these Rabi oscillation experiments to a device with a scanning probe with three individual NV centers at the apex, each with a distinct crystallographic orientation. From the Rabi frequencies measured for each of these NV centers, and obtained under identical spin driving conditions, we were able to extract the corresponding projections of the microwave magnetic field along each NV axis. From this

information, we derived the orientation of the microwave magnetic field vector, $\mathbf{B}_{MW}$, generated by the device. The resulting vector $\mathbf{B}_{MW}$ is plotted in Figure 5.5b. It lies close to the symmetry plane of the device and is tilted $\approx 66°$ towards the back of the device. This tilt is consistent with the asymmetry of the loop, which opens at the back towards the TF. Importantly, this orientation of $\mathbf{B}_{\mathrm{MW}}$ allows efficient driving of all four NV axes in [100]-oriented diamond tips and, due to the observed field tilt, can also drive NV centers in [111]-oriented tips [120].

5.3. Sample and NV sensor temperatures

Since we aim to use our nanoscale quantum sensor in cryogenic environments, where precise control over sample temperatures is crucial, we investigate the thermal impact of our integrated MW delivery device. The transmission measurement Figure 5.6a at a frequency of around 2 GHz, shows a linear relationship between input and output power with a slope of 0.98 dB and a constant power loss of approximately 7.5 dB. This linear behavior in dB demonstrates that the device imposes a predictable and uniform resistance, which is a typical characteristic of an attenuator. Minor discontinuities in the data result from the differing sensitivity ranges of the signal analyzer used.

To quantify local heating effects, we use a thermometry method, based on the studies in Chapter 4, which showed that the photophysics of the NV center is strongly temperature-dependent due to orbital averaging effects, and results in a pronounced broad dip in NV photoluminescence intensity at a temperature of ≈ 50 K. Using our established model, we can determine the temperature experienced by the NV center, T_{NV}, under CW green illumination and as a function of P_{MW} at approximately 2 GHz. We recorded the NV^-photoluminescence, at a magnetic field of 175 mT, for varying MW powers as shown in Figure 5.6b. The constant thermal resistance established from the data in Figure 5.6a, assigns a proportionality constant between T_{NV} and MW power in mW. This allows us to fit the entire NV^-PL trace with this constant as the main fit parameter to extract T_{NV} at each value of P_{MW}.

We then plot T_{NV} as a function of the square of the Rabi frequency and fit this data with a linear dependence. The result is presented in Figure 5.6c, for both measured CW (violet) and the estimated pulsed (purple) ODMR measurements. This estimate is based on the average MW power applied in a pulsed ODMR experiment, using duty cycles that optimize sensitivity for each value of P_{MW} [32]. From the linear fit, we obtain a slope of $240\,\mathrm{mK\,MHz^{-2}}$ for CW at ≈ 2 GHz.

We find that below 7.5 dBm of applied MW power, the increase in T_{NV} remains below 1 K over the cryostat base temperature. In pulsed ODMR experiments, even with the maximum power we applied, the temperature increase is never expected to go over 500 mK. The sample temperature, measured with a Cernox 1070 sensor from *Lakeshore* mounted inside the sample holder, rose by no more than 1 K above the cryostat base temperature of 4.22 K, even at the highest applied CW microwave powers, indicating very localized heating at the tip. While the exact temperature profile between the diamond tip and the sample remains unknown, the NV temperature provides an upper bound for the local temperature T_{local} at the measurement site. The sample temperatures recorded under typical scanning NV magnetometry conditions indicate significantly lower sample heating with our device compared to

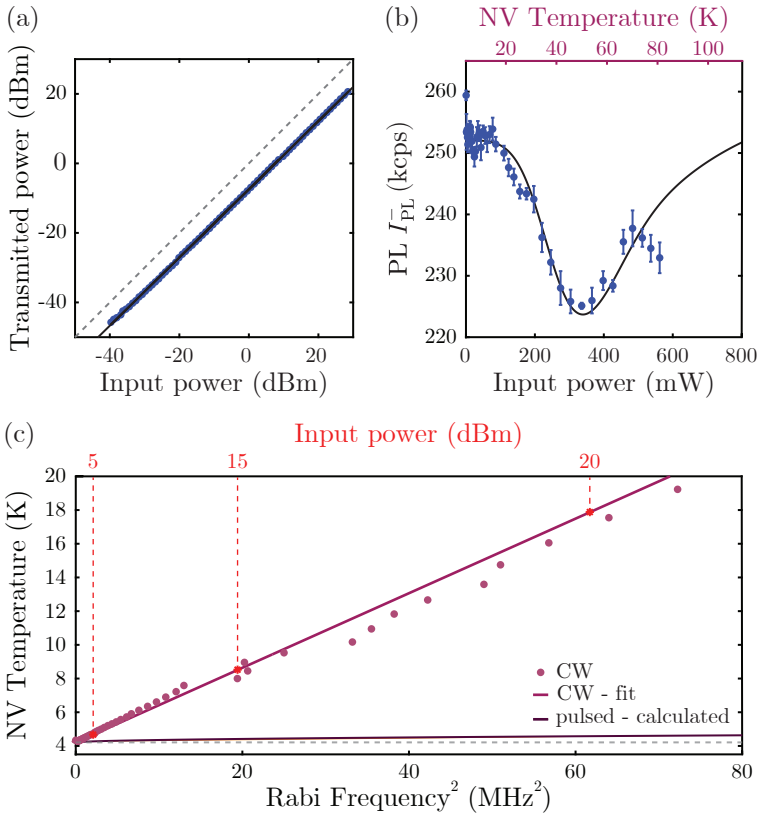

Figure 5.6.: (a) Transmission measurement at 2 GHz showing a linear relationship between MW input and output power with a near unity slope. This behavior is characteristic of a classical attenuator. (b) NV^-PL as a function of P_{MW} at ≈ 2 GHz and a magnetic field of 175 mT. The evolution of NV^-PL with MW power results from orbital averaging due to an increase in temperature. The fit (black line) obtained using the model presented in Chapter 4) gives the temperature of the NV center T_{NV}. (c) NV temperature T_{NV} as a function of the squared Rabi frequency. Violet: under continuous MW drive, as used in all experiments reported here. Purple: T_{NV} calculated from the duty cycle of the pulsed ODMR spin-control sequence. Note that in all cases, T_{NV} can be considered as an upper bound for the local temperature T_{local} at the measurement site in the vicinity of the scanning probe.

our commonly used approach [29], where in the same setup, sample temperatures of $\sim$7 K were reached using an on-chip bond antenna. This improvement is a crucial step towards ultra-low-temperature experiments on materials with low magnetic ordering temperatures.

5.4. Scanning NV magnetic imaging and local manipulation at 4 K

We demonstrate the applicability of our device for scanning NV magnetometry by imaging the stray magnetic field of a patterned Ta/CoFeB/MgO heterostructure (in short CoFeB), which is a trilayer system with a 1 nm CoFeB film in between layers of Ta and MgO. This ferromagnetic sample exhibits well-understood magnetic properties, including an out-of-plane magnetization and a moderate coercive field [102, 120, 136]. The simple geometry, consisting of micrometer-scale squares and lines with a height of 50 nm, is an ideal test structure for this purpose. An optical image of the sample is shown in Figure 5.7a.

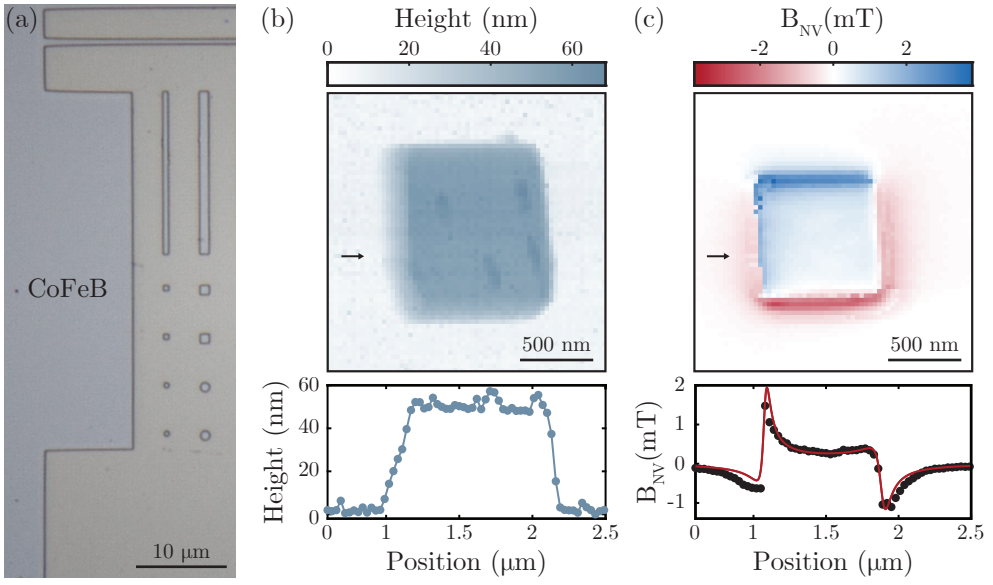

Figure 5.7.: (a) Optical image of the patterned CoFeB sample. (b) In-contact AFM image and topographic line cut across a thin-film CoFeB square. (c) Corresponding stray magnetic field map extracted from full-field CW ODMR measurements taken at each point. The stray field profile shows good agreement with the reverse-propagation protocol [178], yielding a tip-sample distance of 59.5 nm and an out-of-plane magnetization of 0.77 mA m^{-1}.

Figure 5.7b shows a typical AFM map, along with a line cut, both recorded with our device. The root mean square (RMS) roughness of the topography is 1.87 nm, which is typical for scanning NV magnetometry measurements. Past experience with scanning NV magnetometry has consistently shown detrimental cross-coupling between MW drive and AFM signals – a detrimental effect that we do not observe with our present devices, even for MW frequency sweeps spanning more than 240 MHz. In the experiment, we apply a bias magnetic field to split the two transitions of the NV ground state, and use the transition between the $|0\rangle$ and $|-1\rangle$ states for magnetometry. At each point along the line scan, we record the ODMR spectrum by

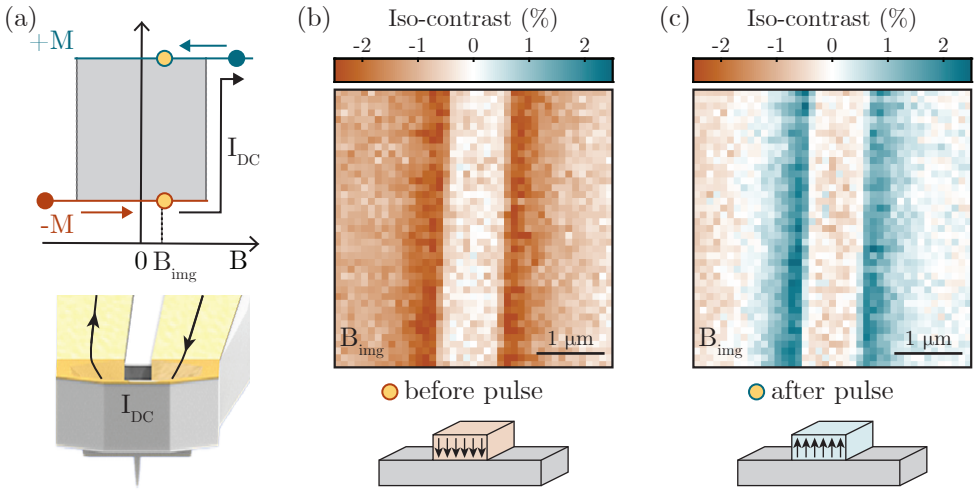

Figure 5.8.: (a) In-situ magnetic switching of CoFeB magnetization near its critical transition point induced by a DC current stimulus applied to the scanning probe MW line. Schematic sample hysteresis curve, illustrating fields for initialization (red dot), imaging (green dots), and the current-induced switching process (blue arrow). (b) and (c) Iso-B field maps obtained at $B_{\mathrm{img}} = 70\,\mathrm{mT}$ before and after applying the stimulus show the magnetization reversal.

driving the NV spin using the integrated near-field coupling device and continuously applying microwave. For each ODMR spectrum, we extract a center frequency, which is then used to calculate the magnetic field along the NV axis, B_{NV}, at the position of the NV. This corresponds to mapping the stray magnetic fields emerging from the thin magnetic CoFeB film. Figure 5.7c shows the stray magnetic field component along the NV axis, along with a line cut, that was recorded on a CoFeB square. The magnetic stray field exhibits local minima and maxima along the edges where the magnetization changes abruptly. From these data, we extract a sample magnetization of $0.77\,\mathrm{mA\,m^{-1}}$, which is fully consistent with previous reports [136], using the usual fitting approach and deconvolution of sample topography. Furthermore, the fit yields an NV-to-sample distance of 59.5 nm, which is comparable to state-of-the-art values in scanning NV magnetometry. This demonstration shows that the scanning magnetometry performance of this implementation of the manufactured integrated near-field coupling device is comparable to current MW delivery solutions.

Additionally, we show alternative ways to use the device. The proximity of the integrated MW delivery loop to the sample can be exploited to locally stimulate and switch the magnetization of the sample. Therefore, we initialized the sample in the negatively magnetized state using a large magnetic field of $-200\,\mathrm{mT}$ applied along the NV axis. We then ramped the field to just below the positive coercive threshold of $B_{\mathrm{img}} \approx 70\,\mathrm{mT}$ and acquired a reference magnetic image using iso-magnetic field imaging mode. This first image is shown in Figure 5.8b. Next, we applied a $\approx 90\,\mathrm{mA}$ current stimulus for 2 s to the MW delivery line, to locally generate a $\approx 0.9\,\mathrm{mT}$ magnetic field below the tip. Finally, we determined the resulting sample magnetization

by recording a second iso-B image at B_{img} shown in Figure 5.8c. We find that the local stimulus completely inverts the sample magnetization in the scanned area, indicating successful local switching of the sample magnetization using our device. The panel of Figure 5.8a illustrates this trajectory along the hysteresis loop. The observed magnetic transition extends across the entire imaged length of the stripe, spanning several microns, which is consistent with the size of the current loop in the device.

5.5. Low temperature charge stability of near-surface NVs

Although scanning NV magnetometry at 4 K is now routinely carried out [26], shallow NV centers experience charge instabilities [145–149], which are exacerbated at low temperatures and in vacuum environments. This is particularly true in our dilution refrigerator, originally designed for transport measurements, in which we experience an enhanced rate of charge instability.

When performing scanning NV magnetometry experiments, we are faced with a gradual transition from a predominantly NV^- to a stable NV^0 state. After conducting a range of measurements and experimenting with different mitigation strategies, we have arrived at our working hypothesis, that contaminants inside our dilution cryostat chamber accumulate on the diamond surface over time and cause band-bending, which affects the NV charge populations. The probability for the NV center to recapture an electron from the conduction band is effectively reduced and gives rise to a predominantly NV^0 population.

Our findings give a different perspective on the charge instabilities experienced by shallow NV centers, complementary to recent results for NVs in ultra-clean environments from Ref. [150]. To stabilize the shallow NVs in our scanning probes, we employ a range of mitigation strategies. Although it does not solve the problem in our system, coating the diamond surface shows particularly promising results. Metal layers are relatively successful in stabilizing the charge of the NV center, but create a strong laser-induced heating effect at the surface of the scanning probe tip. Unfortunately, this is not incompatible with low-temperature operations, because it also heats the nearby sample. Specific surface terminations have been found to stabilize near-surface NV^- [149], but control over their homogeneity is difficult to achieve. Other revival approaches, such as electron radiation, are not practical because they require the scanning probe to be taken out of the cryostat. Additional work remains necessary to stabilize the NV^- charge state and enable the full capabilities of our newly implemented scanning probe system.

Phenomenology

All the near-surface NVs in nanostructures, as used for scanning NV magnetometry [37], systematically undergo a change in their charge state from NV^- to NV^0 in our dilution refrigerator at a temperature of 4 K and below. They transition from the negative charge state (NV^-) to the neutral charge state (NV^0), which does not have the electron spin essential for quantum sensing.

We observe a consistent increase in the NV^0 portion over time. This transition has been reported by other research groups and is observed in our other refrigeration systems. However, the timescales involved are significantly different, spanning from hours to weeks. In our system, the NV changes its predominant charge state within hours during NV scanning magnetometry when the diamond probe comes into contact with a sample. Given the long time required to record scanning NV magnetometry images, up to days for a single image, we are not able to perform meaningful magnetic studies and resort to the investigation of the charge transfer and its mitigation strategies. We have also been operating a different cryogenic NV magnetometer, in which such charge transfers are almost never observed. We thus believe that the observed effects are not intrinsic to shallow NVs at low temperatures.

Interestingly, no bleaching or, more specifically, no deterioration of ODMR contrast has been observed in the absence of laser illumination within the timescale of one week. The fastest transition from NV^- to NV^0 is observed during AFM scans, where the diamond tip intermittently comes into contact with the sample, the scanning mode we ultimately want to use for magnetometry.

The introduction of Helium exchange gas (5 mbar at RT) does not influence the stability of the charge state. Once the NV center is in the NV^0 state, it stays in this state even after thermal cycling to room temperature and exposure to air at atmospheric pressure. The change appears to be permanent.

By irradiation of the diamond with a high voltage electron beam in a SEM, it is sometimes possible to change this seemingly permanent NV^0 state back to a significant fraction of NV^-. Illumination with a broadband UV lamp, centered at a wavelength of 365 nm, also significantly increases the NV^- fraction in the emission spectrum.

Based on the investigations described above, we have established the following working hypothesis: the almost irreversible change in charge state we observe is caused by contamination of the diamond surface by impurities present in the cryostat or within the probe stick. We conclude that contaminants must condensate, deposit, or be picked up onto the surface of the diamond and subsequently induce a change in the electrostatic environment which drives the change to NV^0.

Surface coating

One of the mitigation strategies we investigate is the protection of the diamond probe surface using diverse surface terminations and coatings, such as metals and oxides. We apply the metal coatings to the scanning tip and the "bottom-side" of the cantilever holding the tip. Metal coating on the NV^- scanning probes generally leads to an improvement of the stability of the NV^- charge state at the expense of a lower NV photoluminescence and reduced coherence times. Titanium layers of 1, 5 and 15 nm and a gold layer with a thickness of 1 nm were studied. We observe that, for all metal layers, the zero-field ESR line shows a strong dependence on the excitation laser power, which is attributed to local heating. A preliminary analysis reveals temperatures of up to 300 K in the vicinity of the NV when the sample space is maintained at 4 K and under high vacuum. Remarkably, for the two thinner titanium layers, the NV emission and coherence properties show slight improvements. The charge stability with a 15 nm titanium layer and, to some extent, also with a 5 nm titanium layer was better compared to an untreated scanning diamond probe; however, the very

thin titanium layer did not decrease the rate of bleaching. Likewise, a thin gold layer prevented bleaching but led to a very high background fluorescence, thereby decreasing the signal-to-noise ratio.

5.6. Summary and outlook

In this chapter, we showed our progress towards a novel implementation of a scanning NV magnetometer for operation at mK temperatures and discussed the main challenges for its experimental realization.

We presented the design and the simple, reproducible fabrication of a scanning NV magnetometry probe assembly with an integrated near-field coupling device. By integrating the microwave line directly into the support structure of the scanning probe, we achieve more efficient NV spin manipulation at lower microwave powers than existing solutions, which is crucial for operation in ultra-low-temperature systems. The next step is to perform magnetometry using pulsed-ODMR measurements, which reduces the duty cycle of the microwave [32], and should allow us to measure at temperatures around 100 mK.

In parallel, the device can be further optimized. The quality and thickness of the conductive gold layer strongly affect the transmission of the coupling leads. Improving the layer quality and increasing its thickness up to the electromagnetic field penetration depth in gold (about 1.4 µm at 3 GHz [179]) would significantly reduce attenuation. Electroplating can be used to produce thicker gold layers, improving transmission and reducing power dissipation. For low-temperature applications, superconducting materials such as niobium could further enhance performance by allowing higher currents with minimal heating. Additionally, more simulations could help optimize the geometry of the coupling structure, enhancing the effective coupling strength to the NV center and improving the homogeneity of the generated field.

Further modifications of the device could enable alternative scanning NV magnetometry modalities by adding additional electrical lines extending to the front of the device, following a design similar to that of the microwave lines. This could enable electric field tuning of the NV [34], charge-state control [54], or integrated photoelectric readout via PDMR [154]. While our platform was developed for color-center-based measurements, it can be adapted for other scanning probe techniques that require local electrical connections. These include scanning tunneling microscopy [180], scanning microwave microscopy, scanning SQUID microscopy [181], and other hybrid approaches that combine quantum sensing with conductive or RF-based measurement modes. Another promising functionality of this device is its ability to generate local magnetic fields, enabling in situ writing and manipulation of nanoscale magnetic textures, such as skyrmions and domain walls, in target samples. This concept readily extends to other forms of local stimuli, such as localized temperature gradients or electric fields. Together, these capabilities open new avenues in quantum sensing, spintronics, and hybrid quantum systems, where precise control of the magnetic environment is essential.

Additionally, we investigated the low-temperature charge stability of single near-surface NVs in our diamond scanning probes in Section 5.5. We described the phenomenology of the mechanism behind this change in charge state and attributed it,

to a large extent, to surface contaminants that induce band bending. Most mitigation strategies provide only partial improvement and do not substantially extend the available measurement time in our cryostat. Consequently, further research and technical developments are needed to enhance the charge stability of near-surface NV centers in this environment. In particular, precise control of the diamond surface chemistry appears crucial for improving the lifetime of diamond scanning probes at low temperatures.

To address NV charge stability issues, we are exploring the use of the negatively charged silicon-vacancy center (SiV^-) [182, 183], which has a lower charge transition energy and lacks a permanent electric dipole, making it less sensitive to electric noise. This approach is compatible with ultra-low-temperature operation, requiring a similar setup, with the main difference being that SiV^- magnetometry relies on all-optical resonant excitation. It requires very little power, resulting in minimal heating – an important advantage for ultra-low-temperature measurements. Operation with SiV^- is inherently best at millikelvin temperatures, where its coherence times are longest and, consequently, its magnetic sensitivity is highest [184, 185]. Another advantage of using SiV^- is its compatibility with Tesla-range magnetic fields for sensing. This is currently not achievable with NV-based magnetometers, which are limited by the high microwave frequencies required for coherent spin control at large fields. In preliminary studies, we were able to fabricate nanopillars with SiV^- which have inhomogeneously broadened linewidths within a factor of two from the lifetime limit [186].

Ultimately, our goal is to explore open questions in condensed matter physics that arise at ultra-low temperatures. The NV^- and to a similar extent the SiV^- combine high magnetic field sensitivity with nanoscale spatial resolution sufficient to probe local electron correlations and spins. At temperatures around 100 mK, reduced thermal noise enables the study of emergent quantum phases in strongly correlated materials such as unconventional superconductors, quantum Hall systems, and multiferroics.

6. Summary and outlook

6.1. Summary

In this thesis, we studied fundamental properties of single Nitrogen-Vacancy centers in diamond. We focused on the structure of the excited state and its effects on the photophysics of the NV under magnetic, electric, and strain fields at low temperatures. We investigated the charge environment of NVs under cryogenic conditions, enhancing our knowledge and understanding of the diamond material and the effects of electron charge traps. Initially, we conducted our studies only at low temperatures, but then extended them up to room temperature due to the experimental and theoretical interest in the manifestation of orbital averaging and its effect on the NV photoluminescence. We identified conditions away from excited-state level anticrossings, where optical spin initialization and readout are most effective. The detailed understanding of the defect at low temperature prompted work on the novel implementation of an ultra-low temperature NV scanning magnetometer to ultimately address questions in quantum and condensed matter physics.

After a brief introduction to the Nitrogen-Vacancy center in Chapter 2, we presented a systematic study of the electronic structure of the excited state of the negatively charged Nitrogen-Vacancy center at low temperatures in Chapter 3. We were able to directly observe the influence of electric and crystal strain fields by measurements of the magnetic field-dependent photoluminescence under non-resonant excitation. We gain additional insight into the observed behavior by employing a classical rate-equation model. This analysis provided new insights into the photophysics of the NV and its orbital structure at low temperatures, offering a new tool for its effective characterization. It enables a more comprehensive understanding of the charge state dynamics between NV^- and NV^0, as well as the impact of the excited state structure on low-temperature applications.

Using magnetic field dependent photoluminescence measurements, we investigated the photophysics of single NVs over the entire temperature range from cryogenic to room temperature in Chapter 4. The intermediate temperature range and the effect of the transition from an orbital doublet to an effective orbital singlet structure on the photoluminescence were not well understood and are of importance for variable temperature sensing applications. We found that phonon-induced orbital averaging leads to an extended region of PL quenching at temperatures around 50 K and that the overall behaviour is highly strain dependent, as particularly evident from the emergence of the RT-ESLAC at 50.5 mT. With our model based on the Lindblad master equation formalism, we showed how the structure of the ES has significant effects on the optical spin contrast. Thereby, we provided valuable knowledge on the photophysics of the NV away from the well-studied excited state configurations at low and room temperatures. The optimal use of the NV in applications at different

temperatures is achieved by avoiding regions of increased spin mixing where sensitivity to external fields is reduced.

Finally, in Chapter 5, we presented our progress and the challenges in a novel implementation of a scanning NV magnetometer at ultra-low temperatures. We primarily addressed the fundamental requirement of low heat load, which is paramount for low and ultra-low-temperature applications. We implemented highly efficient and reproducible NV driving through an integrated near-field coupling device. The microwave (MW) delivery circuit required for spin manipulation is directly integrated into the scanning probe, resulting in a very short distance between the MW coupling loop and the NV, and thus more efficient spin driving. The integrated coupling device is highly reproducible, dramatically reducing experimental complexity, minimizing applied microwave power, and eliminating intensity fluctuations due to antenna motion. We characterized the first implementation of the device and demonstrated that its optical properties and AFM performance are not only comparable to those of state-of-the-art NV scanning probe devices, but also represent an excellent alternative for scanning NV magnetometry at low temperatures. In Chapter 5, we also discussed that the charge stability of near-surface NVs in nano-pillars at low temperature was a particular challenge in our experiments. We reported on the phenomenology of the continuous change in charge state ratio in favor of NV^0 and attributed it to the formation of charge traps on the diamond surface due to deposition or pick-up of contaminants onto the diamond surface, which leads to band bending. In our particular system, we observed a significant difference in timescales of this behaviour compared to other systems. This led us to study the phenomenology and possible mitigation strategies, which yielded partial improvements in charge stability. However, more research is needed to better understand and improve the charge stability of near-surface NVs. Control over surface chemistry appears to be essential to enhance the lifetime of diamond scanning probes at low temperatures.

6.2. Outlook

In this thesis, we covered a variety of research topics centered on the Nitrogen-Vacancy center in the context of quantum applications. We studied fundamental properties of the NV and made progress in the understanding of the color center, particularly at low temperatures, while keeping metrology and sensing applications in mind.

However, some aspects of the NV physics and the diamond host material are either not yet investigated or underexplored. A better understanding would certainly benefit the development of NV applications. Attractive new potential applications of the NV center in diamond for electric and magnetic field sensing would open up investigations in condensed matter physics and novel materials. Rising interest in studying spin waves and spintronics [7] also requires more versatile and highly sensitive tools such as scanning NV magnetometry. Other promising applications of the NV electron spin and its surrounding nuclear spins lie in quantum computing and information processing, such as room temperature quantum gate operations combined with electric readout [187]. All of those future plans have to first address and overcome present technological challenges and therefore require a better understanding

of the NV physics, the diamond material, charge dynamics, diamond-metal contacts, surface effects, etc.

In the following sections, we present future research directions that either directly result from our studies or are closely related to them. First, we want to outline open fundamental research questions and then discuss current constraints and unsolved technological challenges that limit further work on the NV or its usage. Ultimately, we aim to explore the potential of our newly proposed scheme for electric field sensing based on NV excited states at low temperatures, as well as the prospects for magnetic field sensing at ultra-low temperatures. The separation into these categories is flexible, because the topics are often interconnected or overlap.

Generally, there is considerable potential in NV research and related applications, and we hope that many of the following questions will be addressed in the future, particularly those regarding surface engineering.

Fundamental research questions

The extensive research on the NV center translates well to the exploration of new color centers such as triplet centers in Silicon carbide (SiC) [188] and Boron-Vacancy centers (V_B^-) in hexagonal boron Nitride (hBN) [189]. As such, field-dependent photoluminescence measurements, as we use them throughout the thesis, are a powerful tool that can be applied to study the energy structure of any color center or photoactive defect center in solid-state materials exhibiting dark states that can be populated through magnetic field-tunable level anticrossings. This is illustrated well by a recent application of the technique in the excited state spectroscopy of V_B^- in hBN [189]. SiV centers in SiC [133] or the neutral SiV center (SiV^0) in diamond [122, 134] are also potential candidates, where this method could shed new light into unknown ES structures and orbital averaging.

In Chapter 3, we reported strong indications that the orbital g-factor of the NV is strain-dependent and would ultimately approach the classical value of $g_l = 1$ in the high strain limit. Unfortunately, we were not able to measure the actual value of g_l due to experimental constraints. So far, our extensive search for NVs in a [111]-oriented diamond with an intermediate strain level with interbranch crossings within our magnetic field range (see Appendix A.3.1) was unsuccessful. Therefore, these experiments could be performed in a cryostat with a significantly larger magnetic field range, which would allow for resolving the interbranch level anticrossings and determining a definite value for the orbital g-factor.

The intersystem crossing and the characteristics of the singlet state manifolds are the reasons for the NV's exceptional optical spin initialization and readout properties. However, various aspects need further investigation. We confirmed in Chapter 3 that the shelving state is not fully protected from ionization. This mechanism is not fully understood and could be studied in terms of spectral and power dependence to shed light on the involved processes. Furthermore, the exact location of the singlet states in energy is not fully known and could be investigated by strain engineering. Many applications, such as spin-to-charge conversion (SCC) [190] and T_1 relaxometry [191], depend on the precise knowledge of the transition rates within the NV system. Besides the charge dynamics, the transition rates to and from the singlet states, as well as their branching ratios, play an important role. Even though they have been measured

experimentally [15, 31, 112, 131], they differ significantly from NV to NV and their temperature dependence is only partially known. Due to their importance, the reasons and potential mechanisms behind this difference should be investigated further.

In Chapter 4, we found that the emergence of the room-temperature ESLAC at 50.5 mT is highly strain-dependent. For low-strain NVs, it only appears at temperatures above 100 K, whereas for high-strain NVs, it already starts to appear at around 50 K. The former is confirmed by a prior study on the ES-ODMR contrast for low-strain NVs, where they find that the contrast decreases with temperature and vanishes slightly above 100 K [39]. To further validate and strengthen our predictions, ES-ODMR could be performed with a high strain NV down to 50 K.

The interplay between the NV^-, NV^0, and the dark NV^+ charge states under various conditions is essential for the NV properties and their understanding. So far research has mostly focused on the NV^-, but significantly more understanding of the other charge states and their dynamics is needed in the context of high fidelity spin measurements, single photon generation, photostabilization [192], spin-to-charge conversion (SCC)[59, 190], PDMR mechanism [187] and quantum memory applications [60]. Also the influence of electric fields on the charge state has been investigated previously [51, 100], but a more complete understanding especially in the context of PDMR is still lacking.

The NV charge dynamics are very important for any applications of the NV and are influenced by a variety of factors such as excitation wavelength, illumination power, surface termination, doping, etc. Charge instabilities limit coherence properties and impede efficient electrical readout. The properties of the diamond material and its impurity content, as well as the surface chemistry, are getting more attention as they have a strong effect on the NV charge state. Further studies of the frequency-dependent screening effects in the diamond host material, as well as the electrical contact types and their behaviour, are very important for the implementation of applications based on the NV. The interbranch ESLAC with their high sensitivity as presented in Chapter 3 could be employed for further studies. Recent simulations on the effects of impurities and charge traps in highly N-doped diamond [193] help to understand the mechanisms at play but need to be studied further experimentally.

Further spectroscopic studies of the NV^0 charge state, particularly its response to electric fields in conjunction with the charge dynamics in the diamond, are also interesting, as this aspect has long been neglected. Recently, progress has been made in the electrical tuning of the orbital states of the NV^0 [194], which exhibits a large susceptibility to electric fields similar to that observed for the excited state of the NV^-. This could be employed to develop an NV^0 based nanoscale electric field sensor similar to the NV^-. Another particularity is a surprising change in the NV^- to NV^0 charge state ratio in a very narrow excitation band around 520 nm at low temperature [67]. This sharp feature is tentatively assigned to an electronic transition to a level located higher in energy in the conduction band of the diamond [67], but its mechanism would require more investigation.

The excitation power and wavelength have a strong effect on the local environment of the NV [34], as they can rearrange nearby charges and induce specific charge dynamics. Therefore, optical charge stabilization could be used to temporarily or permanently stabilize the NV^- charge state. In this context, blue wavelength illumination shows a lot of promise for the charge stabilization of SnV centers [195] as well

as a permanent stabilization in near-surface SiV^- [186]. The mechanisms underlying these effects remain unclear, but are likely related to charge reordering processes. The effects of this scheme should be applied to the NV and investigated further to gauge its efficiency.

Technological challenges and potentials

There are several technical areas where further research would lead to new applications and unlock new capabilities of the NV. In particular, this requires a better understanding and control of the diamond host material. Strain engineering, as well as control over specific surface terminations, would greatly improve the applicability of the NV. Two other technological advances for NV control and readout involve further improvements in MW delivery to the NV and the development of electrical contacts on a photonic structure for electric readout, as well as the implementation of additional sensing techniques.

The control of crystal strain fields would open up numerous possibilities for NV applications. Local or macroscopic strain-engineering techniques, like implantation and growth methods, need to be investigated. Advances in these areas could benefit other NV research fields, such as improved hybrid spin-nanomechanic systems [84], but pose significant technical and fundamental challenges. Also, electric field tuning could yield similar results, but investigations on diamond surface electrodes or graphitic electrode contacts directly inside the diamond [196] as well as screening effects and the influence of impurities in the diamond lattice are required.

Our findings show that in order to maintain the full sensitivity of the NV at low temperatures, an electric or magnetic field bias is required to move away from the ES level anticrossing. However, applying an external magnetic field results in a Zeeman energy. In particular, at low temperatures, the intricate interplay of often small energy scales determines the resulting electronic and magnetic phases, so that an additional magnetic field disturbs or even destroys the targeted phase being studied. Famous examples include the destruction of the superconductivity phase or its oscillatory frequencies in Josephson junctions, the Skyrmion phases, and domain wall formation and shape in magnetic systems. These types of samples need to be studied at zero external magnetic field, which does not allow for optimal NV sensitivity tuning. The full sensitivity cannot be achieved with current NVs in scanning probes, which show effective strain values higher than 20 GHz (see Chapter 3). Only NVs with close to no effective field exhibit no excited state mixing at zero magnetic field (see Figure 3.2). Therefore, reducing strain through novel or optimized fabrication methods and proper surface terminations needs to be explored to achieve low effective strain, near-surface NVs in nanostructures. This mostly technological challenge, however, has strong implications on experimental capabilities in the investigations of condensed matter physics. Additionally, this would benefit our proposed electrometry scheme, as the interbranch ESLACs of low-effective-field NVs are situated at lower magnetic field values. For near-surface NVs, the effective field mostly originates from charge traps on the surface [148] and therefore the surface termination gets special importance.

Surface states can lead to band-bending, which can severely impact the charge stability of near-surface NVs [51, 52]. This is a major challenge, particularly for low-temperature experiments, as outlined in Section 5.5, and becomes more pronounced

the closer the NV is to the surface. The NVs should be as close as possible to the diamond surface to improve signal strength and spatial resolution for sensing applications such as scanning probe magnetometry or nanoscale NMR, which is a significant challenge. The fundamental depth limit for charge stable NV^- under an ideal oxygen or fluorine termination could be as small as 0.5 nm below the surface, corresponding to the 7^{th} layer of Carbon atoms [197]. Therefore, extensive research is needed regarding surface terminations, as well as atomically thin surface layer coatings. Surface control and band-gap engineering are crucial to increase the sensitivity and stability of the NV. Various surface terminations need to be considered to establish experimental control over the homogeneity and reproducibility of the results. Homogeneous oxygen or fluorine terminations show a lot of promise on bulk diamond [149, 198] but still need to prove effective in studies on nanostructures. Additionally, atomic layers of oxides or other materials as surface coatings on top of the diamond could be considered to further stabilize and protect the NV from charge instabilities. Overcoming the limitations of surface-induced charge instabilities would be a key step forward, significantly enhancing the sensor properties of the NV, such as its coherence time.

In the context of scanning NV magnetometry, the concept of re-terminating the used scanning probe tip can be investigated and has considerable potential. During the scanning operation, NVs tend to lose contrast and charge stability over time, with different time scales at low and room temperatures. The reason is most likely the contamination of the tip surface through contact with the sample or deposition from the surrounding environment. Larger contaminants can be removed by scanning over a sharp needle; however, that gives only partial improvement if a surface change occurs. Therefore, re-terminating the surface may enable the reuse of the tip. One possible approach would be to design the entire scanning probe assembly to withstand plasma treatments, but other routes might be equally promising.

Most experiments involving Nitrogen-Vacancy centers require NVs that are charge-stable, experience low effective fields, and have narrow, lifetime-limited linewidths. These properties are mostly present in native or in-grown NVs far away from the diamond surface. This also applies to the low-strain NVs used in this thesis. The high refractive index of diamond makes the collection of photons quite difficult. However, a high photon collection is required for efficient and fast experimental schemes, resulting in the need for photonic structures [37, 129]. The deterministic placement of NVs in the photonic structure can be challenging and tedious, but a statistical approach has a lower yield. Therefore, obtaining low-effective-field NVs with high photon count rates is a challenge, limiting experimental advances. An alternative method for creating NVs in bulk diamond utilizes single high-energy femtosecond pulses to generate vacancies, followed by an annealing step [199]. These NVs have narrow lines, appear charge-stable, and seem to experience low effective fields [200]. We propose directly laser writing NVs through a prefabricated diamond solid immersion lens in the focus of the photonic structure, thereby combining high collection efficiency with a large yield of low-strain NVs.

Another technological advance in low temperature scanning magnetometry over the state-of-the-art is the all-integrated near-coupling device presented in Chapter 5. The characterization of its initial implementation demonstrates that it is suitable for NV magnetometry; therefore, we will utilize this structure in our future low- and ultra-low-temperature applications. The antenna structure can be further improved;

both the quality and thickness of the conductive layer are highly relevant for MW conductivity and can be optimized. Electromagnetic simulations can be used to further improve the geometry in terms of RF transmission and NV coupling. Another focus is optimizing the operation by a constant-amplitude driving scheme [201] to counter the frequency-dependent attenuation of the structure and to avoid any thermally driven movement of the scanning probe tip. Such a scheme would also benefit PDMR measurements [202] by simplifying MW application or even enabling specific gate structures to be simultaneously used for MW driving and DC readout.

The design of the support structure allows for easy incorporation of additional conducting lines, which can function as transmission lines or electrical leads that can be connected to the attached probe tip. This versatile extension allows to implement NV^- manipulation possibilities and multiprobe features such as NV^- optical transition tuning [34], in-situ charge tuning [48], or electric readout [202]. Also, applications such as scanning tunneling microscope (STM) [180] could be implemented alongside NV scanning. Simultaneous operation of several scanning tip-based investigation methods would enable a range of new measurements to understand condensed matter phenomena. Especially, the electric readout of the NV has great potential for a broad range of devices, such as integrating sensors or quantum gates. This requires further research on the mechanisms of photoelectric readout, NV charge state, electric contacts, and the effects of charges in the diamond. To integrate an electric readout with a scanning architecture, we propose placing electrical contacts directly on the sides of the pillar nanostructure, extending up to the apex. The short distances between the contacts, which are only a few hundred nanometers, allow the application of a large electric bias field. This could be either used for electric field biasing in electrometry applications or for photoelectric readout.

Low temperature sensing applications

The Nitrogen-Vacancy center is used in many different schemes for electric and magnetic field, crystal strain, and temperature sensing. In Chapter 5 we reported our progress on implementing an ultra-low scanning NV magnetometer which features good thermalization and an integrated low-power, highly efficient MW drive. However, the NV^- electron loss limits the measurement time in our particular system to a few hours, which is not sufficient for the nanoscale investigation of most samples. As outlined above, surface engineering or an improvement of the surface termination could solve this problem and stabilize the NV^- charge state of near-surface NVs.

Ultimately, an ultra-low-temperature NV magnetometer would be used to investigate the emergent quantum properties of strongly correlated electron systems, such as unconventional superconductors, quantum Hall systems, or multiferroics. Nanoscale imaging at temperatures around 100 mK would improve our microscopic understanding of electronic correlations occurring in this regime. Most of the experimental techniques used in current studies address the bulk properties of these materials and can not observe quantum matter at the nanoscale due to a lack of spatial resolution or sensitivity. Scanning NV magnetometry can access phase transitions with different electronic and magnetic orders, offering both high sensitivity and spatial resolution, thereby providing access to previously unexplored areas. Graphene and strontium ruthenate (Sr_2RuO_4) are particularly interesting because they exhibit a variety of

unusual electronic and transport properties due to their highly two-dimensional electronic structure [203, 204] and allow for the study of the nature of spin-ordering and the role of magnetism for superconductivity at ultra-low temperatures.

Among the various color centers, the Nitrogen-Vacancy in diamond is the most widely used for magnetometry applications. However, as we have seen in Chapter 5, NVs have significant optical coherence and charge stability issues when placed in proximity to the diamond surface, severely limiting their use under certain conditions. Another color center, the Silicon-Vacancy center in diamond, is also a suitable system for magnetic field sensing at low temperatures using its negative charge state, the SiV^- [182, 183]. In contrast to the NV^-, its electronic states have vanishing permanent electric dipole moments due to their inversion symmetry, which protects its optical properties from charge dynamics in the diamond lattice [182, 205]. Another striking difference is the location of the defects in the diamond band gap. Even in the presence of strong band banding in the vicinity of the surface, the negatively charged SiV is still electronically stable when the NV is already exclusively in its neutral charge state [57, 206]. Therefore, it is not expected to face the same problems with charge traps on the diamond surface as we experience in our system and could serve as an alternative to the NV^- for magnetic field sensing. Due to technical reasons with high-frequency MW transmission, the sensing scheme would most likely be implemented with an all-optical readout via coherent population trapping (CPT). This eliminates the need for microwaves to control the spin states, thereby significantly reducing the heat load and increasing the detectable magnetic field range. All-optical SiV^- magnetometry requires optically addressable lifetime-limited SiV^- in proximity to the diamond surface in nanostructures similar to the ones for NV centers. We were able to show this for pillar arrays [186] and are planning to produce scanning probe tips in the near future. The investigated physics with a potential SiV magnetometer at ultra-low temperatures would be similar to that for the NV, but could operate at larger magnetic fields. Generally, a scanning probe can host both a single NV and SiV center, enabling complementary measurements since the two color centers can be easily spectrally filtered, as their emission is only slightly overlapping. The challenge would be to achieve a sufficient creation yield for both species through co-implantation, thereby reaching the correct densities of one color center from each species in a pillar.

In Chapter 3, we reported on the electric field sensitivity of the excited state level anticrossings (ESLACs), which enables a microwave-free electrometry scheme building on the excited state structure of the NV. The implementation of this cryogenic electric field sensing protocol with a scanning probe would extend experimental capabilities beyond the current available methods, such as ground-state ODMR-based techniques, as it features high sensitivities paired with nanoscale resolution. It would allow us to investigate and understand the physics that govern the functioning of ferroelectric and magnetoelectric, multiferroic materials, as well as electric field-driven switching of magnetic states [207, 208]. In particular, ferroelectric thin films are important for microsensor applications, high frequency electronics, and memory applications [209] and lack diverse and precise measurement techniques. Local determination and mapping of ferroelectric properties are usually obtained via piezoresponse force microscopy, Kelvin probe force microscopy, and scanning near-field optical microscopy (SNOM) [209], which are sensitive to various surface phenomena. Our implementa-

tion of this electrometry technique complements existing methods and provides a more direct access to the electric fields from these materials. We plan to make a proof-of-concept measurement using an NV in a scanning probe configuration. For such experiments, both the interbranch and intrabranch crossings of the NV excited states can be used, where the former yield lower sensitivities but, due to their lower magnetic field positions, are accessible for high-strain NVs as typically found in scanning probes. In such an experiment, either a specific, constant electric field can be probed or the full electric field can be recorded by implementing a feedback mechanism. After careful validations of the technique and the influences of screening effects, we can apply the technique to study ferroelectric properties and investigate paraelectric-to-ferroelectric transitions [210] or ferroelectric domain configurations in thin films such as domain patterns in $PbTiO_3$ [211].

A. Appendix

A.1. Classical rate equation model for the low temperature photophysics of single NV centers

For the description of the photo-dynamics of a single NV at low temperatures, we employ a classical rate equation model for the 10-level system of the NV. Our extended version is based on previous work from Refs. [31, 76]. Using the Hamiltonians for the ground and excited states (see Chapter 2), we calculate the NV spin's photoluminescence from the steady-state populations under the influence of spin-mixing.

We also describe an extension of the model for a 12-level system to include the NV charge dynamics. For that, we incorporate the ground and excited states of the neutrally charged NV and the respective transitions into the model.

A.1.1. Definition of the states and transition rates

For the NV^- model at low temperatures, one needs to consider the interplay between the three levels in the ground state, the six levels in the two orbital branches of the excited state, and the metastable singlet [10, 46]. The singlet can be reduced to one state with rates in and out of it [36], leaving a total of ten states. We employ an extended version of a classical rate-equation model for the NV's magnetic field-dependent photophysics, similar to Refs. [31, 76].

The states for the rate equation are defined as:

Ground state:

$$\begin{aligned} |1\rangle &\equiv {}^3A_2^0 \\ |2\rangle &\equiv {}^3A_2^{-1} \\ |3\rangle &\equiv {}^3A_2^{+1} \end{aligned} \tag{A.1}$$

Excited state:

$$\begin{aligned} |4\rangle &\equiv {}^3E_y^0 & |7\rangle &\equiv {}^3E_x^0 \\ |5\rangle &\equiv {}^3E_y^{-1} & |8\rangle &\equiv {}^3E_x^{-1} \\ |6\rangle &\equiv {}^3E_y^{+1} & |9\rangle &\equiv {}^3E_x^{+1} \end{aligned}$$

Combined singlet state:

$$|10\rangle \equiv {}^1A_1/{}^1E$$

Here, the eigenstates are give in the notation of X^{m_s}, where X including the pre superscript and post subscript denote the manifold or its orbital branch, and the post subscript m_s denotes the spin level, e.g. $E_y^{-1} \equiv |E_y, -1\rangle = |\text{orbital state}, \text{spin state}\rangle$.

The NV^- can be optically excited with a green laser through a dipole-allowed transition to the excited state. The transition is spin-conserving. This excitation does have a polarization-dependence due to selection rules [10]. However, this dependence is somewhat suppressed by the non-radiative decay observed from the non-resonant optical excitation [40], leading to a small effect on the populations in the two excited state orbital-branches. Once in the excited state manifold, the NV spin can decay back to the ground state through two different decay channels: a radiative and a non-radiative decay. The radiative decay is directly from the excited state back to the ground state. The non-radiative decay path is through the intersystem crossing (ISC) to a metastable singlet state, where a difference in the rates from the $m_s = 0$ versus $m_s = \pm 1$ spin states is observed [31].

We begin with transition rates between ground- and excited-states with zero external field, where the spin quantum number is still well defined and the rates have been experimentally measured [31, 112, 131]. The basis of the transition matrix is the ten eigenvectors $\left|i^0\right\rangle$ with $i = 1, ..., 10$ labeled with subscript zero ^{0} indicating that this is the basis at zero field.

In the following, we assume that spin-conserving relaxation rates from the excited to ground states are the same for each spin state and that the non-spin-conserving transitions are zero. The non-spin-conserving transition rates have previously been shown only to be a few percent compared to the spin-conserving ones [131].

The zero-field pumping rate can be assumed to be the respective relaxation rates from the excited state to the ground state k_r (where the r stands for radiative) multiplied by a pumping parameter β which is proportional to laser power [31]. To capture the polarization dependence of the excitation, we separate this pumping parameter into one for each orbital state, β_{E_x} and β_{E_y}. The transition rates from the ground to excited states are thus defined as

$$\begin{aligned} k^0_{|1^0\rangle\to|4^0\rangle} &= \beta_{E_y}\, k_r, & k^0_{|1^0\rangle\to|7^0\rangle} &= \beta_{E_x}\, k_r, \\ k^0_{|2^0\rangle\to|5^0\rangle} &= \beta_{E_y}\, k_r, & k^0_{|2^0\rangle\to|8^0\rangle} &= \beta_{E_x}\, k_r, \\ k^0_{|3^0\rangle\to|6^0\rangle} &= \beta_{E_y}\, k_r, & k^0_{|3^0\rangle\to|9^0\rangle} &= \beta_{E_x}\, k_r, \end{aligned} \tag{A.2}$$

where the direct radiative decay transition rates from the excited to ground states are defined as

$$\begin{aligned} k^0_{|4^0\rangle\to|1^0\rangle} &= k_r, & k^0_{|7^0\rangle\to|1^0\rangle} &= k_r, \\ k^0_{|5^0\rangle\to|2^0\rangle} &= k_r, & k^0_{|8^0\rangle\to|2^0\rangle} &= k_r, \\ k^0_{|6^0\rangle\to|3^0\rangle} &= k_r, & k^0_{|9^0\rangle\to|3^0\rangle} &= k_r. \end{aligned} \tag{A.3}$$

The transition rates from the excited states to the metastable state are spin-dependent and defined as

$$\begin{aligned} k^0_{|4^0\rangle\to|10^0\rangle} &= k_{nr_0}, & k^0_{|7^0\rangle\to|10^0\rangle} &= k_{nr_0}, \\ k^0_{|5^0\rangle\to|10^0\rangle} &= k_{nr_{\pm1}}, & k^0_{|8^0\rangle\to|10^0\rangle} &= k_{nr_{\pm1}}, \\ k^0_{|6^0\rangle\to|10^0\rangle} &= k_{nr_{\pm1}}, & k^0_{|9^0\rangle\to|10^0\rangle} &= k_{nr_{\pm1}}, \end{aligned} \tag{A.4}$$

where $k_{nr_0} \ll k_{nr_{\pm1}}$ [31].

Reference	k_r	k_{nr_0}	k_{nr_1}	k_{m_0}	$k_{m_{\pm 1}}$
Robledo *et al.* [131]^{a,b}	65	11	80	3.0	2.6
Tetienne *et al.* [31]^{b}	65.9	7.9	53.3	0.98	$2 \cdot 0.73$
Gupta *et al.* [112]^{a,b}	66.8	10.5	90.7	4.8	2.2

Table A.1.: Experimentally measured transition rates at zero field. All of the rates are in MHz.

^{a} The rates assume a 5-level system, ^{b} the rates have been measured at room temperature

The rates from the metastable state to the ground states are similar for all spin states and defined as,

$$\begin{aligned} k^0_{|10^0\rangle \to |1^0\rangle} &= k_{m_0}, \\ k^0_{|10^0\rangle \to |2^0\rangle} &= k_{m_{\pm 1}}, \\ k^0_{|10^0\rangle \to |3^0\rangle} &= k_{m_{\pm 1}}, \end{aligned} \tag{A.5}$$

where $k_{m_0} \sim k_{m_{\pm 1}}$. The ratio between the rates to the $m_\mathrm{s} = 0$ and $m_\mathrm{s} = \pm 1$ states is called the branching ratio. Depending on the reference, the transition rates for $k^0_{|10^0\rangle \to |2^0\rangle}$ and $k^0_{|10^0\rangle \to |3^0\rangle}$ are specified as a sum of the two or individually (see Table A.1). In the context of our work, this difference has minimal impact on our results.

In a typical optically detected magnetic resonance (ODMR) measurement, the spin population is transferred between the spin states of the ground state via an applied microwave field. The MW transition rates are defined as

$$\begin{aligned} k^0_{|1^0\rangle \to |2\rangle^0} &= k^0_{|2^0\rangle \to |1^0\rangle} = k_{\mathrm{MW}_{-1}}, \\ k^0_{|1^0\rangle \to |3\rangle^0} &= k^0_{|3^0\rangle \to |1^0\rangle} = k_{\mathrm{MW}_1}, \end{aligned} \tag{A.6}$$

where k_{MW_x} is the driving transition rate on resonance with the transition between the $|m_s = 0\rangle = |1\rangle$ and $|m_s = x\rangle$ states. These rates are only non-zero when modeling the effect of the level anticrossings on ODMR contrast.

All these transition rates have been measured experimentally and are shown in Table A.1. There is an additional correction to the ISC rates at low temperatures, which is strain-dependent. Low-strain NVs have slightly different transition rates from the ES to the singlet manifold, which have been measured by Goldmann *et al.* [35]. This correction is omitted in this work since it has little to no effect on the overall photoluminescence. In the model, we used the parameters from Gupta *et al.* [112], which we found to yield the best agreement with our data.

A.1.2. Classical rate equation

We define the transition rate matrix at zero field in this 10-level model. The transition matrix, Q^0, gives the rates at zero electric, magnetic, and strain field and is defined

as

$$Q^0 = \begin{pmatrix} 0 & k_{\mathrm{MW}_{-1}} & k_{\mathrm{MW}_1} & \beta_{E_x}\, k_r & 0 & 0 & \beta_{E_y}\, k_r & 0 & 0 & 0 \\ k_{\mathrm{MW}_{-1}} & 0 & 0 & 0 & \beta_{E_x}\, k_r & 0 & 0 & \beta_{E_y}\, k_r & 0 & 0 \\ k_{\mathrm{MW}_1} & 0 & 0 & 0 & 0 & \beta_{E_x}\, k_r & 0 & 0 & \beta_{E_y}\, k_r & 0 \\ k_r & 0 & 0 & 0 & 0 & 0 & 0 & 0 & 0 & k_{nr_0} \\ 0 & k_r & 0 & 0 & 0 & 0 & 0 & 0 & 0 & k_{nr_{\pm 1}} \\ 0 & 0 & k_r & 0 & 0 & 0 & 0 & 0 & 0 & k_{nr_{\pm 1}} \\ k_r & 0 & 0 & 0 & 0 & 0 & 0 & 0 & 0 & k_{nr_0} \\ 0 & k_r & 0 & 0 & 0 & 0 & 0 & 0 & 0 & k_{nr_{\pm 1}} \\ 0 & 0 & k_r & 0 & 0 & 0 & 0 & 0 & 0 & k_{nr_{\pm 1}} \\ k_{m_0} & k_{m_{\pm 1}} & k_{m_{\pm 1}} & 0 & 0 & 0 & 0 & 0 & 0 & 0 \end{pmatrix}. \tag{A.7}$$

This zero-field transition matrix is extended to arbitrary fields by calculating the spin-state overlap using the Hamiltonians from Refs. [10, 46] presented in Chapter 2. Since the new eigenstates are a linear combination of the previous eigenstates, the scalar product is used to evaluate the corresponding overlap

$$|i\rangle = \sum_{j=1}^{10} \alpha_{ij} \left|j^0\right\rangle, \tag{A.8}$$

where α_{ij} is the projection of the new state $|i\rangle$ onto the zero-field basis states $|j\rangle$. The resulting transition matrix which depends on the magnetic field $\boldsymbol{B}$, the electric field $\boldsymbol{E}$ and the stress field $\boldsymbol{\delta}$ is:

$$Q(\boldsymbol{B}, \boldsymbol{E}, \boldsymbol{\delta})_{ij} = \sum_{k=1}^{10} \sum_{l=1}^{10} \alpha_{ik}^2 Q_{kl}^0 \alpha_{jl}^2. \tag{A.9}$$

Using this transition matrix for the system, we define a classical rate equation where N_i is the population in each state and $\boldsymbol{M}$ is the rate equation matrix. We assume that this is a closed-loop system, which imposes the inclusion of diagonal terms such that,

$$M_{ij} = \begin{cases} \sum_{k=1}^{10} -Q_{ik} & \text{if } i = j \\ Q_{ji} & \text{if } i \neq j. \end{cases} \tag{A.10}$$

The rate equation problem is stated in the following equation:

$$\frac{dN_i}{dt} = \boldsymbol{M} N_i, \tag{A.11}$$

where the populations in the steady state are given by the smallest eigenvalue and are normalised such that

$$\hat{N}_i = \frac{N_i}{\sum_{j=1}^{10} N_j}. \tag{A.12}$$

We calculate the photoluminescence of the negatively charged NV I_{PL}^- by summing over the relevant radiative transitions from the excited state to the ground state and populations of these states, such that

$$I_{\mathrm{PL}}^- = \sum_{i=4,5,6} \sum_{j=1}^{3} Q_{ij} \hat{N}_i + \sum_{i=7,8,9} \sum_{j=1}^{3} Q_{ij} \hat{N}_i. \tag{A.13}$$

Additional modification to the photoluminescence such as background fluorescence I_{bck} and collection efficiency $\eta_{\text{collection}}$ can also be introduced, such that

$$I^-_{\text{PL}} \equiv I^-_{\text{Total}} = \eta_{\text{collection}} I^-_{\text{PL}} + I_{\text{bck}}. \tag{A.14}$$

The ODMR contrast $\mathcal{C}$ is calculated by the photoluminescence I^-_{PL} with and without a driving field in the ground state. For example, with a microwave driving between $|1\rangle$ ($^3A_2^0$) and $|2\rangle$ ($^3A_2^{-1}$), we determine the contrast by calculating,

$$\mathcal{C} = \frac{I^-_{\text{PL}}(k_{\text{MW}_{-1}} = 0) - I^-_{\text{PL}}(k_{\text{MW}_{-1}} \neq 0)}{I^-_{\text{PL}}(k_{\text{MW}_{-1}} = 0)}. \tag{A.15}$$

A.1.3. Model extension to include the NV^0

To account for the dynamics between the two NV charge states, NV$^-$ and NV^0, we extend the model to include the energy levels of the NV^0 as well as transition rates between the two charge states. The NV^0 consists of two eigenstates, a ground state and an excited state [10]. We define them as:

$$\begin{aligned} |11\rangle &\equiv {}^2E \\ |12\rangle &\equiv {}^2A_2. \end{aligned} \tag{A.16}$$

For our model, we assume that these states are independent of magnetic, electric, or strain fields. The transition within the NV^0 charge state and between the two charge states are defined as follows:

From the excited state of the NV^0, there is a direct radiative decay down to the NV^0 ground state

$$k_{|12^0\rangle \to |11^0\rangle} = k_{r_{\text{NV}^0}}. \tag{A.17}$$

We define the transition rate from the ground state to the excited state of the NV^0 as the product of the radiative transition rate and a pumping power for the NV^0 β_{NV^0}, such that

$$k_{|11^0\rangle \to |12^0\rangle} = \beta_{\text{NV}^0}\, k_{r_{\text{NV}^0}}. \tag{A.18}$$

The recombination rate from the NV^0 excited state to the NV$^-$ ground state depends on the pumping strength and is given by

$$\begin{aligned} k_{|12^0\rangle \to |1^0\rangle} &= k_{\text{recomb}}, \\ k_{|12^0\rangle \to |2^0\rangle} &= k_{\text{recomb}}, \\ k_{|12^0\rangle \to |3^0\rangle} &= k_{\text{recomb}}. \end{aligned} \tag{A.19}$$

The ionization rate from the NV$^-$ excited state to the NV^0 ground state also depends on the pumping strength and is given by

$$\begin{aligned} k_{|4^0\rangle \to |11^0\rangle} &= k_{\text{ion}}, & k_{|7^0\rangle \to |11^0\rangle} &= k_{\text{ion}}, \\ k_{|5^0\rangle \to |11^0\rangle} &= k_{\text{ion}}, & k_{|8^0\rangle \to |11^0\rangle} &= k_{\text{ion}}, \\ k_{|6^0\rangle \to |11^0\rangle} &= k_{\text{ion}}, & k_{|9^0\rangle \to |11^0\rangle} &= k_{\text{ion}}. \end{aligned} \tag{A.20}$$

Reference	$k_{r_{\mathrm{NV}^0}}$	k_{ion}	k_{recomb}	k_{shelfion}
Craik *et al.* [65]	50	$0.037\beta_{\mathrm{NV}^0}k_r$	$0.8\beta_{\mathrm{NV}^0}k_r$	$0.36\beta_{\mathrm{NV}^0}k_r$

Table A.2.: Experimentally measured transition rates for the NV^0 and the transition rates between NV^0 and NV^-. The ionization and recombination rates in the dark are set to zero in our model because we consider continuous-wave laser excitation. All of the rates are in MHz.

The recombination rate and ionization rate in the dark between the ground state of the NV^0 and the ground state of the NV^- are given by

$$\begin{aligned} k_{|1^0\rangle\to|11^0\rangle} &= k_{\mathrm{darkion}}, & k_{|11^0\rangle\to|1^0\rangle} &= k_{\mathrm{darkrecomb}}, \\ k_{|2^0\rangle\to|11^0\rangle} &= k_{\mathrm{darkion}}, & k_{|11^0\rangle\to|2^0\rangle} &= k_{\mathrm{darkrecomb}}, \\ k_{|3^0\rangle\to|11^0\rangle} &= k_{\mathrm{darkion}}, & k_{|11^0\rangle\to|3^0\rangle} &= k_{\mathrm{darkrecomb}}, \end{aligned} \tag{A.21}$$

where, for continuous wave excitation, the dark ionization and recombination rates are effectively zero: $k_{\mathrm{darkrecomb}} = k_{\mathrm{darkion}} = 0$.

Additionally, we include a newly postulated shelf ionization transition [65] which goes from the metastable state to the NV^0 ground state and is laser driven

$$k_{|10^0\rangle\to|11^0\rangle} = k_{\mathrm{shelfion}}. \tag{A.22}$$

The rates used in our model are taken from the literature and listed in Table A.2.

We calculate the NV^0 photoluminescence, I^0_{PL}, by looking at the population and the transition rate of the radiative transition of the NV^0 which are given by the corresponding transition matrix $Q(\boldsymbol{B}, \boldsymbol{E}, \boldsymbol{\delta})_{ij}$ which is constructed similar to Equation (A.9):

$$I^0_{\mathrm{PL}} = Q_{11,\,12}\,\hat{N}_{12}. \tag{A.23}$$

Background counts and collection efficiency can be included in the same fashion as for the NV^- (see Appendix A.1.2).

A.2. Lindblad master equation model for the temperature-dependent photophysics of single NV centers

In order to model the temperature dependence of the photophysics of single NV centers, we use a Lindblad master equation to calculate the time evolution of the population in a 10-level system, similar to the model presented in Chapter 3 and Appendix A.1. This formalism allows us to take into account the temperature-dependent effects caused by electron-phonon interactions, which are ultimately responsible for the effective excited state structure at room temperature (see Section 2.4). Using only the low-temperature NV^- Hamiltonian [10, 46] from Chapter 2 in the master equation, we can calculate the NV^- photoluminescence from the resulting steady-state populations up to room temperature. Similar to Appendix A.1.3, we can extend the model to include the NV^0 to model the dynamics between the two charge states.

A.2.1. Definition of the states and combined Hamiltonian

In the simulations of the NV spin's energy levels, we use a set of eigenstates that form an eigenbasis of the combined GS and ES NV^- Hamiltonians. For simplicity, we combine the spin singlet states into a single state, resulting in 10 states: three ground states, six excited states, and one singlet state. The states are defined as:

Ground states:

$$\begin{aligned} |1\rangle &\equiv {}^3A_2^{-1} \\ |2\rangle &\equiv {}^3A_2^{0} \\ |3\rangle &\equiv {}^3A_2^{+1} \end{aligned} \tag{A.24}$$

Excited states:

$$\begin{aligned} |4\rangle &\equiv {}^3E_y^{-1} & |7\rangle &\equiv {}^3E_x^{-1} \\ |5\rangle &\equiv {}^3E_y^{0} & |8\rangle &\equiv {}^3E_x^{0} \\ |6\rangle &\equiv {}^3E_y^{+1} & |9\rangle &\equiv {}^3E_x^{+1} \end{aligned}$$

Combined singlet state:

$$|10\rangle \equiv {}^1A_1/{}^1E$$

with the notation of X^{m_s}, where the right superscript m_s indicates the spin level. For the states ${}^3E$ the right subscript indicates the orbital branch, e.g. $E_y^{-1} \equiv |E_y, -1\rangle = |\text{orbital state}, \text{spin state}\rangle$.

Following this definition, the combined Hamiltonian H_{NV} is a 10×10 matrix containing the Hamiltonians of both the ground and excited states from Refs. [10, 46] and presented in Chapter 2. It is defined as

$$H_{\mathrm{NV}} = 2\pi \begin{pmatrix} & & & 0 & \dots & 0 \\ & \hat{\mathcal{H}}_{gs} + \hat{\mathcal{V}}_{gs} & & \vdots & & \vdots \\ & & & 0 & \dots & 0 \\ 0 & \dots & 0 & & & \\ & & & & \hat{\mathcal{H}}_{es} + \hat{\mathcal{V}}_{es} & \vdots \\ \vdots & & \vdots & & & \\ 0 & \dots & 0 & \dots & & 0 \end{pmatrix}. \tag{A.25}$$

A.2.2. Optical transition rates

The NV^- spin state can be optically excited from the ground state into the excited state using green laser illumination, via a spin-conserving dipole-allowed transition. Once in the excited state manifold, the NV spin can decay back to the ground state via either a radiative decay path (k_r) or a non-radiative one (k_{nr}). The radiative decay is a direct spin-conserving decay from the excited state back to the ground state. The non-radiative decay path goes through the intersystem crossing (ISC) into a metastable singlet state, which exhibits different transition rates depending on the electron spin state, $m_s = 0$ versus $m_s = \pm 1$ spin states [31].

In the following, we assume that all spin-conserving transition rates from the excited to the ground states are independent of the electron spin state ($k_{|4,5,6\rangle\to|1,2,3\rangle} = k_r$). Furthermore, we assume that the non spin conserving transitions are zero (e.g. $k_{|6\rangle\to|1\rangle} = 0$), because they only make up be a few percent compared to the spin conserving one [131].

The transition rates from the ground to excited states and the corresponding decay transition rates from the excited to ground states are thus defined as

$$\begin{aligned} &k_{|1\rangle\to|4\rangle} = \beta_{E_y}\, k_r, \quad && k_{|1\rangle\to|7\rangle} = \beta_{E_x}\, k_r, \quad && k_{|4\rangle\to|1\rangle} = k_r, \quad && k_{|7\rangle\to|1\rangle} = k_r, \\ &k_{|2\rangle\to|5\rangle} = \beta_{E_y}\, k_r, \quad && k_{|2\rangle\to|8\rangle} = \beta_{E_x}\, k_r, \quad && k_{|5\rangle\to|2\rangle} = k_r, \quad && k_{|8\rangle\to|2\rangle} = k_r, \\ &k_{|3\rangle\to|6\rangle} = \beta_{E_y}\, k_r, \quad && k_{|3\rangle\to|9\rangle} = \beta_{E_x}\, k_r, \quad && k_{|6\rangle\to|3\rangle} = k_r, \quad && k_{|9\rangle\to|3\rangle} = k_r, \end{aligned} \tag{A.26}$$

where β_{E_x} and β_{E_y} are the pumping parameters which are proportional to laser power [31] and capture the polarization dependence of the excitation [31, 40]. The respective relaxation rates from the excited state to the ground state are defined as k_r.

The transition rates from the excited states to the metastable state are spin-dependent, whereas the rates from the metastable state to the ground states are similar for all spin states. These rates are defined as

$$\begin{aligned} &k_{|4\rangle\to|10\rangle} = k_{nr_{\pm1}}, \quad && k_{|7\rangle\to|10\rangle} = k_{nr_{\pm1}}, \quad && k_{|10\rangle\to|1\rangle} = k_{m_{-1}}, \\ &k_{|5\rangle\to|10\rangle} = k_{nr_0}, \quad && k_{|8\rangle\to|10\rangle} = k_{nr_0}, \quad && k_{|10\rangle\to|2\rangle} = k_{m_0}, \\ &k_{|6\rangle\to|10\rangle} = k_{nr_{\pm1}}, \quad && k_{|9\rangle\to|10\rangle} = k_{nr_{\pm1}}, \quad && k_{|10\rangle\to|3\rangle} = k_{m_{+1}}, \end{aligned} \tag{A.27}$$

where the optical spin contrast of the NV results from $k_{nr_0} \ll k_{nr_{\pm1}}$ [31] and the decay rates from the metastable state only have a small imbalance.

In a typical optically detected magnetic resonance (ODMR) measurement, the spin population is transferred between the spin states of the ground state via an applied

Reference	k_r	k_{nr_0}	k_{nr_1}	k_{m_0}	$k_{m_{\pm 1}}$
Robledo *et al.* [131]^{a,b}	65	11	80	3.0	2.6
Tetienne *et al.* [31]^{b}	65.9	7.9	53.3	0.98	$2 \cdot 0.73$
Gupta *et al.* [112]^{a,b}	66.8	10.5	90.7	4.8	2.2

Table A.3.: Experimentally measured transition rates at zero field. All of the rates are in MHz. Same as Table A.1

^{a} The rates assume a 5-level system, ^{b} the rates have been measured at room temperature

microwave field, and the corresponding transition rates are defined as

$$k_{|1\rangle\to|2\rangle} = k_{|2\rangle\to|1\rangle} = k_{\mathrm{MW}_{-1}}, \qquad k_{|3\rangle\to|2\rangle} = k_{|2\rangle\to|3\rangle} = k_{\mathrm{MW}_1}, \tag{A.28}$$

where k_{MW_x} is the driving transition rate on resonance with the transition between the $|m_s = 0\rangle = |2\rangle$ and $|m_s = x\rangle$ states. The transition rates $k_{|1\rangle\to|2\rangle}$ and $k_{|3\rangle\to|2\rangle}$ are in general zero in our experiments because no microwave (MW) driving field is applied. These rates are only set to non-zero when one wants to model the effect of the level anticrossings on the spin-readout contrast.

All the transition rates in Equations (A.26) and (A.27) have been measured experimentally and are shown in Table A.3. The rates from the singlet to the ground state further exhibit a temperature dependence measured in Ref. [131] which is discussed below in Appendix A.2.3.

The intersystem crossing (ISC) rates from the excited state to the singlet also exhibit a small temperature dependence below 20 K [35], which, however, has no observable effect in the context of our modeling. Therefore, we assume the rates to the ISC to be constant in our model.

A.2.3. Temperature dependence of the singlet decay rate

The lifetime of the singlet state has been experimentally measured [131] and theoretically derived [212, 213]. It exhibits a temperature dependence, with a significantly longer lifetime at low temperatures.

We use the empirical model for the lifetime τ from Robledo *et al.* [131] where they postulate the lifetime as a combination of a temperature independent decay rate $\frac{1}{\tau_0}$ and a rate coming from stimulated emission of phonons of energy ΔE with an occupation given by Bose-Einstein statistics. This yields

$$\tau(T) = \tau_0[1 - \exp\left(\frac{-\Delta E}{k_{\mathrm{B}} T}\right)] \tag{A.29}$$

with k_{B} the Boltzmann constant and T the temperature. From their data, they extract a phonon energy of $\Delta E = 16.6\,\mathrm{meV}$ and a temperature independent lifetime of $\tau_0 = 371\,\mathrm{ns}$.

The resulting rate $\frac{1}{\tau}$ for a specific temperature consists of the sum of the rates from the singlet to the $m_s = 0$, $m_{\mathrm{s}} = -1$, and $m_{\mathrm{s}} = +1$ states of the ground state

$$\frac{1}{\tau(T)} = k_{m_0} + k_{m_{\pm 1}} = k_{m_0} + k_{m_{\text{-}1}} + k_{m_{+1}}. \tag{A.30}$$

Reference	τ_0 (ns)	Branching ratio
Robledo *et al.* [131]	371	2.3 : 1 : 1
Acosta *et al.* [214][a]	462	N/A
Gupta *et al.* [112][b]	296.53	4.36 : 1 : 1

Table A.4.: Values for the temperature independent lifetime of the metastable state τ_0, which corresponds to the lifetime value at low temperatures, and the branching ratio from the metastable singlet state to the ground state spin states written in the form $k_{m_0} : k_{m_{-1}} : k_{m_{+1}}$.

[a] The value is for NV ensembles, [b] the value of τ_0 is determined from the values at room-temperature adopting the functional dependence established in Robledo *et al.* [131]

The ratio between the rates of the $m_s = 0$ and $m_s = \pm 1$ states is called the branching ratio. Table A.4 shows various rates from literature.

A.2.4. Phonon-induced transition rates between the ES orbitals

The interaction of the electron orbital in the excited state with A_1 and E symmetry phonons, up to the first order, can be written as [40, 78]

$$H_{ep} = \sum_i \hbar\lambda_i^A V^A (a_i^A + a_i^{A\dagger}) + \sum_i \hbar\lambda_i^E \left[V_x^E (a_{i,x}^E + a_{i,x}^{E\dagger}) - V_y^E (a_{i,y}^E + a_{i,y}^{E\dagger}) \right], \quad \text{(A.31)}$$

where

$$V^A = |X\rangle\langle X| + |Y\rangle\langle Y|, \quad \text{(A.32)}$$
$$V_x^E = |X\rangle\langle X| - |Y\rangle\langle Y|, \quad \text{(A.33)}$$
$$V_y^E = |X\rangle\langle Y| + |Y\rangle\langle X|, \quad \text{(A.34)}$$

are the electron orbital operators for interaction with A_1, E_x and E_y phonon modes, respectively. The orbitals are denoted X and Y with $|X\rangle = \binom{1}{0}$ and $|Y\rangle = \binom{0}{1}$, λ_i^A and λ_i^E are the electron-phonon coupling coefficients, and $a_{i,p}^M$ ($a_{i,p}^{M\dagger}$) are the annihilation (creation) operators of the i-th $M = A_1$ or $M = E$ phonon modes.

Using the Fermi golden rule, we can calculate the phonon-induced transition rates between the excited states. The transition rate between the $|i\rangle$ and $|f\rangle$ states with energies E_i and E_f, respectively, is given by

$$\Gamma_{if} = \frac{2\pi}{\hbar} \left| (H_{ep}^{(2)})_{fi} + \sum_m \frac{(H_{ep})_{fm}(H_{ep})_{mi}}{E_i - E_m} \right|^2 \delta(E_i - E_f), \quad \text{(A.35)}$$

where $H_{ep}^{(2)}$ is the second-order electron-phonon Hamiltonian, which we expect to be negligible. The summation in the second term is over all intermediate orbital states.

Only resonant phonons can drive spin transitions directly via one-phonon absorption or emission. Therefore, we expect that the dominant mechanism is a two-phonon Raman process, in the form of absorption of a phonon followed by emission of a phonon, or vice versa. Considering the initial and final phonon states $|n_k, n_l\rangle$, and

$|n_k+1, n_l-1\rangle$, respectively, the transition rate from $|X\rangle$ to $|Y\rangle$ is given by

$$\begin{aligned}\Gamma_{XY} =& 2\pi\hbar^3 \sum_{k,l} \left| \frac{\lambda_l^E(\lambda_k^A+\lambda_k^E)}{(-\hbar\omega_k)} + \frac{\lambda_k^E(\lambda_l^A+\lambda_l^E)}{\hbar\omega_l} + \frac{\lambda_k^E(\lambda_l^A-\lambda_l^E)}{E_x-E_y-\hbar\omega_k} + \frac{\lambda_l^E(\lambda_k^A-\lambda_k^E)}{E_x-E_y+\hbar\omega_l} \right|^2 \\ & \times n_l(n_k+1)\delta(E_x-E_y+\hbar\omega_l-\hbar\omega_k).\end{aligned} \tag{A.36}$$

Converting the summations to integrals and using the phonon spectral density for $M = A_1$ or $M = E$ phonon modes

$$J_M(\hbar\omega) = \sum_k (\hbar\lambda_k^M)^2 \delta(\hbar\omega - \hbar\omega_k), \tag{A.37}$$

we can then write

$$\Gamma_{XY} = \Gamma_{XY}^{EE} + \Gamma_{XY}^{AE}, \tag{A.38}$$

where

$$\begin{aligned}\Gamma_{XY}^{ME} = \frac{4\pi}{\hbar} \int & \left[\frac{J_M(\Delta_{xy}+\hbar\omega)J_E(\hbar\omega)}{(\Delta_{xy}+\hbar\omega)^2} + \frac{J_E(\Delta_{xy}+\hbar\omega)J_M(\hbar\omega)}{(\hbar\omega)^2} \right] \\ & \times n(\hbar\omega)[n(\hbar\omega+\Delta_{xy})+1]\, d(\hbar\omega).\end{aligned} \tag{A.39}$$

Here, $M = A_1, E$ are the phonon symmetries, $\Delta_{xy} = E_x - E_y = 2\delta_\perp = 2\sqrt{\delta_x^2+\delta_y^2}$ is the strain splitting, and $n(\hbar\omega) = (e^{\hbar\omega/(k_BT)}-1)^{-1}$ is the mean number of phonons at thermal equilibrium. For this calculation, we have used random phase approximation [215].

For long wavelength acoustic phonons, we have [36]

$$J_M(\hbar\omega) = \eta_M(\hbar\omega)^3, \tag{A.40}$$

where η_M is the coupling strength between the electron states and M-symmetric acoustic phonons.

We combine the above results in an analytical expression of the transition rate Γ_{XY}, which we use in the model. We get

$$\Gamma_{XY} = \frac{4\pi}{\hbar}(\eta_E^2+\eta_A\eta_E)(k_BT)^5 I(\omega_c,\delta), \tag{A.41}$$

where

$$I(\omega_c,T,\delta_\perp) = \int_0^{x_c} dx\; x(x+x_\Delta)\left[x^2+(x+x_\Delta)^2\right] \frac{1}{(e^x-1)(1-e^{-(x+x_\Delta)})}, \tag{A.42}$$

with $x_c = \hbar\omega_c/(k_BT)$ where ω_c being the cutoff frequency in the integral, $x = \hbar\omega/(k_BT)$, and $x_\Delta = \Delta_{xy}/(k_BT) = 2\sqrt{\delta_x^2+\delta_y^2}/(k_BT)$.

In contrast to other work, ω_c is not the Debye frequency. The Debye model is an oversimplification of all modes in a crystal. It considers only an acoustic type of phonons with a cutoff frequency which is obtained in such a way that the area below the density of states as a function of the mode frequency is the same as that of the real crystal. Therefore, the Debye model erases all particularities of the real modes: the positions (frequencies) at which the density of states achieves its maxima, the maximum phonon frequency, optical phonons, etc.

The optimal and simple approximation selected here includes:

- an acoustic branch with a cutoff frequency corresponding to the frequency at which the density of states (DOS) for the acoustic branch reaches a maximum (60 meV in our case); and
- an optical branch with cutoff frequencies (for optical phonons there is a low and high frequency cutoff) that matches the frequencies at which the density of states achieves its maxima which is slightly above the maximum of the acoustic branch that is mentioned before and the maximum of the optical branch (which turns to the maximum optical phonon frequency of the real crystal).

In this model, however, we consider only the acoustic part to keep the approach simple and because, as temperature rises, the acoustic phonons, ranging from low frequencies up to the frequency at which the density of states achieves its acoustic maximum at 60 meV, become more significant than the optical phonons.

In the model, we combine some parts of Equation (A.41) into an effective coupling α_{ph} and set ω_{c} to 60 meV which results in

$$\Gamma_{XY} = \alpha_{\mathrm{ph}} I(\omega_{\mathrm{c}} = 60\,\mathrm{meV}, T, \delta_{\perp}) T^5. \tag{A.43}$$

The spin-conserving transition rate from orbital X to orbital Y and vice versa is then defined as

$$k_{|Y\rangle \to |X\rangle} = k_{|X\rangle \to |Y\rangle} = \alpha_{\mathrm{ph}} I(\omega_{\mathrm{c}} = 60\,\mathrm{meV}, T, \delta_{\perp}) T^5. \tag{A.44}$$

A.2.5. Lindblad master equation

We employ the Lindblad master equation to model the time-evolution of the NV^- Hamiltonian under the influence of relaxation, laser-induced optical pumping, and phonon-induced orbital averaging. For an introduction and a derivation, we refer to Refs. [216, 217].

The Lindblad master equation is a simplified framework for describing the evolution of various open quantum systems that are weakly coupled to an environment. It tries to capture the influence of this weakly coupled environment on the system through the Lindblad operator (L). This method circumvents the need to solve the full Hamiltonian, which encompasses all quantum and semiclassical interactions between the target system and the bath to which it is coupled. Instead, it reduces this complexity to a set of effective decay rates, a common approach used to model the dephasing and relaxation of quantum states.

Under the assumptions of Markovianity and time-homogeneity, a special type of the Lindblad master equation, the Markovian master equation, describes the evolution of the density matrix (ρ) of our combined system[218]:

$$\frac{d\rho}{dt} = -\frac{i}{\hbar}[H_{\mathrm{NV}}, \rho] + \sum_l \mathcal{D}(L_l)\rho, \tag{A.45}$$

where H_{NV} the Hamiltonian of the system and

$$\mathcal{D}(L_l)\rho = L_l \rho L_l^\dagger - \frac{1}{2}\left(\rho L_l^\dagger L_l + L_l^\dagger L_l \rho\right). \tag{A.46}$$

The Lindblad operator L_l represents the l^{th} interaction with the bath.

The first term in the master equation describes the unitary evolution of the density matrix due to the Hamiltonian of the NV^- system, while the second term describes the evolution due to the interaction with the environment. The Lindblad operators L_l result in transitions between states of the system due to the interaction with the environment. Each collapse operator, $L_l = \sqrt{\Gamma_l} A_l$, describes a different aspect of the environment where Γ_l defines the strength of the interaction and can be a relaxation rate, dephasing rate, etc., and A_l describes the corresponding operator of the interaction. When all L_l are zero, the Liovillian equation of a closed quantum system is recovered.

A.2.5.1. Lindblad operators

In the next step, we define the Lindblad operators L_l, which describe the effects included in our model. First, we look at how to incorporate the relaxation and laser-induced optical pumping rates from Appendix A.2.2 and then continue to the phonon-induced transitions introduced in Appendix A.2.4.

In general the Lindblad operator representing the transition from state $|i\rangle$ to $|j\rangle$ is given by

$$L_{|i\rangle\to|j\rangle} = \sqrt{k_{|i\rangle\to|j\rangle}}\,|j\rangle\langle i|\,, \tag{A.47}$$

where $k_{|i\rangle\to|j\rangle}$ is the transition rate from state $|i\rangle$ to $|j\rangle$. The same applies to all transition rates in Appendix A.2.2.

The Lindblad operators for phonon-induced transitions between the different excited state orbitals (X and Y) are constructed slightly differently. We are concerned with transitions within the excited state manifold, such that the states in question are a subset of $|i,j\rangle = \{4\ldots9\}$ The two orbitals are defined as $|X\rangle = \left(\begin{smallmatrix}1\\0\end{smallmatrix}\right)$ and $|Y\rangle = \left(\begin{smallmatrix}0\\1\end{smallmatrix}\right)$. We define the spin-conserving transition operator from the upper orbital to the lower orbital as

$$L_\downarrow = \sqrt{k_{|Y\rangle\to|X\rangle}}\,|Y\rangle\langle X| \otimes \mathbb{1}_3, \tag{A.48}$$

where $k_{|Y\rangle\to|X\rangle}$ is the transition operator from the upper orbital Y to the lower orbital X. The operator for the spin-conserving rate from the lower to the upper orbital $L_\uparrow$ is equivalent to the flipped X and Y orbitals and indices.

A.2.5.2. Vectorization for application of Super Operators

We introduce a vectorization procedure that maps $|i\rangle\langle j| \mapsto |j\rangle \otimes |i\rangle$, such that it is possible to use the Super Operator formalism [219]. The vector form of the density matrix is obtained by stacking the columns of an $n \times n$ density matrix from left to right on top of each other to form a vector of length n^2, such that

$$\hat{\rho} = \sum_{i,j} \rho_{i,j}\,|j\rangle \otimes |i\rangle. \tag{A.49}$$

Using this vectorization, we can rewrite the Lindblad master equation from Equation (A.45) as a product between a matrix and a vector, where all the properties are

contained in the Lindbladian superoperator, given by

$$\hat{\mathcal{L}} = i(\bar{H} \otimes \mathbb{1}_{10} - \mathbb{1}_{10} \otimes H) + \sum_l \left(\bar{L}_l \otimes L_l - \frac{1}{2}\mathbb{1}_{10} \otimes L_l^\dagger L_l - \frac{1}{2}\bar{L}_k^\dagger \bar{L}_k \otimes \mathbb{1}_{10} \right), \quad \text{(A.50)}$$

where the complex conjugate is shown with an overbar (e.g. $\bar{H}$) and the adjoint with a dagger (†). l denotes all possible transitions, both optical and phonon-induced.

The time-evolution of the system in the vectorized form of the master equation [220] is given by

$$\frac{d\hat{\rho}(t)}{dt} = \hat{\mathcal{L}}\hat{\rho}(t), \quad \text{(A.51)}$$

which is computationally more efficient to calculate.

A.2.5.3. Time-dependent and steady state solution of the master equation

In the following, we will first provide a general time-dependent solution to the Lindblad master equation and then proceed to the steady state solution. The two approaches result in very similar outcomes when compared.

Time evolution of the density matrix

The time-evolved density matrix is obtained by

$$\hat{\rho}(t) = e^{\mathcal{L}t}\hat{\rho}(0) \equiv e^{\mathcal{L}t}\hat{\rho}_0, \quad \text{(A.52)}$$

where $\hat{\rho_0}$ is the vectorised initial density matrix of the system. We choose an initial population in the three states of the ground state of the NV^-:

$$\rho_0 = \frac{1}{3}|1\rangle\langle 1| + \frac{1}{3}|2\rangle\langle 2| + \frac{1}{3}|3\rangle\langle 3|, \quad \text{(A.53)}$$

which is then converted to its vectorized form $\hat{\rho}_0$ as discussed in the previous section.

We solve Equation (A.52) with a time of 3 µs, which is enough under continuous laser excitation to obtain a steady state. We get the vectorized density matrix $\hat{\rho}(t)$, which we then convert back to its matrix form. We then extract the populations of the 10 states by

$$p_i = \langle i|\rho(t)|i\rangle. \quad \text{(A.54)}$$

Steady state solution of the density matrix

In an open quantum system where the decay rates are larger than the corresponding excitation rates, there is a steady state solution for the density matrix for $t \to \infty$ [217]. In this case, the solution of the Lindblad master equation can be cast into an eigenvalue equation:

$$\hat{\mathcal{L}}\hat{\rho}_{ss} = 0\hat{\rho}_{ss}, \quad \text{(A.55)}$$

with $\hat{\rho}_{ss}$, the vectorized form of the steady state density matrix, and $\hat{\mathcal{L}}$, the Lindbladian superoperator in the given basis.

We can solve Equation (A.55) and convert the vectorized density matrix back to its matrix form. After normalization, the steady state populations of the 10 states then read

$$p_i = \frac{\langle i| \rho_{ss} |i\rangle}{\sum_{j=1}^{10} \langle j| \rho_{ss} |j\rangle}. \tag{A.56}$$

A.2.5.4. Photoluminescence

The photoluminescence of the negatively charged NV I^-_{PL} is calculated by summing over the relevant radiative transitions from the excited state to the ground state and the populations of these states, such that

$$I^-_{\mathrm{PL}} = \sum_{i=4\ldots9} k_r p_i. \tag{A.57}$$

Additional modification to the photoluminescence such as background fluorescence I_{bck}, and collection efficiency $\eta_{\mathrm{collection}}$, can also be introduced, such that

$$I^-_{\mathrm{Total}} = \eta_{\mathrm{collection}} I^-_{\mathrm{PL}} + I_{\mathrm{bck}}, \tag{A.58}$$

which for convenience is generally referred to as I^-_{PL}.

From the photoluminescence, the ODMR contrast $\mathcal{C}$ can be calculated by including non-zero microwave transition rates into the Hamiltonian, i.e., $k_{\mathrm{MW}} \neq 0$. For example, with a microwave driving between $|1\rangle$ ($^3A_2^{-1}$) and $|2\rangle$ ($^3A_2^0$), we determine the contrast by calculating

$$\mathcal{C} = \frac{I^-_{\mathrm{PL}}(k_{\mathrm{MW}_{-1}} = 0) - I^-_{\mathrm{PL}}(k_{\mathrm{MW}_{-1}} \neq 0)}{I_{\mathrm{PL}}(k_{\mathrm{MW}_{-1}} = 0)}. \tag{A.59}$$

A.3. Experimental details

In the following section, we describe the experimental setups in which we conduct the measurements, as well as a few other relevant experimental implementations. We use confocal microscopy techniques to investigate Nitrogen-Vacancy centers in diamond. Most of the experiments of Chapters 3 and 5 are performed in a closed-cycle dilution refrigerator described in Appendix A.3.1. The experiments of Chapter 4 are performed in a closed-cycle refrigerator with a variable temperature inset (VTI) described in Appendix A.3.2. For the simultaneous collection of the NV^0 and NV^- photoluminescence, we implement a dual-channel avalanche photodiode (APD) system as outlined in Appendix A.3.3. In Appendix A.3.4, we describe the construction of flexible and lightweight, thermal braids for our ultra-low temperature scanning experiments. Lastly, we present details of our tuning-fork-based AFM implementation for scanning experiments with diamond probes in Appendix A.3.5.

A.3.1. Closed-cycle dilution refrigerator setup

The closed-cycle dilution refrigerator (CF-CS81, *Leiden Cryogenics*) has a vector magnet with a maximum magnetic field of $(B_x, B_y, B_z) = (1\,\mathrm{T}, 1\,\mathrm{T}, 5\,\mathrm{T})$. The magnet allows full 1 T vectorial control; however, reaching the maximum $B_z = 5\,\mathrm{T}$ is only possible when the fields along the other axes are limited to $B_x, B_y < 0.3\,\mathrm{T}$. The cryostat can be operated either at around 4 K or with the additional dilution system at temperatures as low as 20 mK. The total cooling power at 100 mK is 1000 µW and increases with temperature. At 120 mK it is already 1400 µW. The cryostat provides free-space optical access, connecting the LT objective (inside) and a confocal microscope module (outside). The optical path also contains multiple windows with a VIS-NIR coating angled towards each other to prevent unwanted radiation from reaching the sample space.

The NV is excited with a green laser at 532 nm (Compass 315M, *Coherent*), and the excitation polarization is controlled with a liquid crystal polarization rotator (LCR-532, *Thorlabs*). The NV PL readout is performed with an avalanche photodiode (SPCM-AQRH-33, *Excelitas*) with a 650 nm long-pass filter (FELH0650, *Thorlabs*) for the NV^- and a bandpass filter (FF01-600/52-25, *Semrock*) for the NV^0. An illustration of the effects of the filters on the emission of a diamond nanopillar can be seen in Figure A.1. Nitrogen-Vacancy emission spectra are obtained with a spectrograph (HRS-500, *Princeton Instruments*) and imaged with a low-noise camera (PIXIS 100, *Princeton Instruments*).

The microwave control of the NV spin is performed using a microwave driving field from a signal generator (SG384, *Stanford Research Systems*) that is modulated via an IQ-modulator (AM0350A Quadrature Modulator, *Polyphase Microwave*) and an AWG (Spectrum generator NETBOX DN2.663-04, *Spectrum Instrumentation*). The NV photoluminescence is measured via gating the output of the APD with a TTL-router (SP995, *in-house built*), which is controlled via the AWG and whose output is measured with a data acquisition system (DAQ) from *National Instruments* (PXIE-1073, PXIe-6612, PXIe-6738 and PXI-6220).

The sample space is cooled efficiently through thermal coupling to the mixing chamber plate, which is the coldest plate in the cryostat. The sample and scanning probe holders, which are attached to the top of the positioning stacks, feature special flexible cooling braids that ensure optimal thermalization while being flexible and lightweight enough to enable smooth movement of these stacks. The fabrication of these cooling braids is outlined in Appendix A.3.4. All electrical wires are thermally anchored at each plate in the cryostat, and the MW lines contain attenuators for additional cooling. To reduce the laser power requirements for NV initialization and readout, we utilize NVs in photonic structures, specifically nanopillars, which significantly increase the collection efficiency and lower the laser power to the tens of µW range for saturation [37]. The free-space optical path inside the cryostat, which leads to the sample space at mK temperatures, is also fitted with multiple windows featuring VIS-NIR coating.

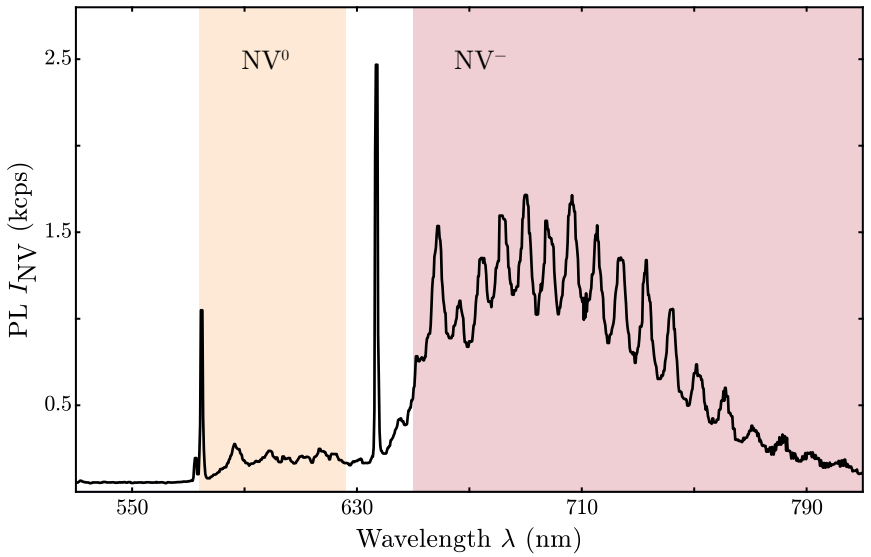

Figure A.1.: Optical emission spectrum of a single NV in a diamond nanostructure [37]. The highlighted regions indicate the regions of collected PL to separate the slightly overlapping spectra of the charge states NV^0 (orange) and NV^- (red). The modulations in the depicted spectrum arise from a cavity effect of the diamond nanostructure used to enhance NV PL collection efficiency.

A.3.2. Temperature controllable closed-cycle refrigerator setup

The closed-cycle cryostat (attoDRY2200, *attocube systems*) has a variable temperature range of $T = 2 - 300\,\mathrm{K}$. An integrated PID controller is used to stabilize the sample space temperature using two sets of heaters, one directly below the sample and another one heating the variable temperature inset (VTI). It features two different operating temperature regimes ($T \leq 15\,\mathrm{K}$ and $T > 15\,\mathrm{K}$). The temperature sensor

below the sample is a thin-film resistance temperature sensor (Cernox CX-1050-SD-HT-1z4L, *Lakeshore*).

The optical setup consists of a commercial confocal microscope (attoCFM, *attocube systems*). The NV is optically excited using a 532 nm laser (Torus, *Laser Quantum*) and a fibre-coupled AOM (Fibre-Q, *EQ Photonics*). The photoluminescence of the NV is separated using a dichoric mirror (DMLP567R, Thorlabs), filtered by a 650 nm long pass filter (FELH0650, *Thorlabs*) and recorded on an avalanche photodiode (SPCM-AQRH-33, *Excelitas*). The NV spin state is controlled via microwaves that are produced by a signal generator (SMBV100B, *Rohde & Schwartz*), controlled with an inbuilt signal generator, in-phase and quadrature (IQ) mixer, and subsequently amplified (HPA-25W-63+, *Mini Circuits*).

The cryostat has a superconducting vector magnet (1 T,1 T,1 T) with full 1 T vectorial control, operated by two magnet controllers (APS100, *attocube systems*).

A.3.3. Dual channel avalanche photo-diode setup for the NV^0 and NV^- charge states

For specific experiments, such as those in Chapter 3, we collect the photoluminescence of the two NV charge states, NV^0 and NV^-, separately and simultaneously during the measurement. Therefore, we separate the collected light by wavelength using a dichroic mirror (FF640-Di01 or FF635-Di01, *Semrock*), which is reflective for most of the light originating from the NV^0 and transmissive for the light of the NV^-. The PL from NV^- is further filtered with a 650 nm long-pass filter (FELH0650, *Thorlabs*) and the PL from NV^0 with a bandpass filter (FF01-600/52-25, *Semrock*). The NV photoluminescence for each charge state is then measured with two separate avalanche photodiodes (APDs) (SPCM-AQRH-33, *Excelitas*).

A.3.4. Construction of cooling braids

For low- and ultra-low temperature systems, the quality of thermal connections between different parts of the cryostat assembly plays a crucial role due to the limited cooling power available below 4 K. Effective cooling is typically achieved by directly clamping parts together. If no direct connection is possible, large, highly conductive parts, such as bulk pieces or braids, are used.

However, when cooling scanning systems inside the sample space of a cryostat, the task becomes more challenging, and additional difficulties arise. Due to the movements of the scanners, the connection needs to be highly flexible to avoid impeding their movement. Additionally, the components must be lightweight to avoid overloading the capacity of the piezoelectric scanners. The available sample space is also limited in volume, leaving little room for efficient clamping of the sample.

For our ultra-low-temperature scanning experiments at a base temperature of 20 mK, we developed cooling braids to connect the scanning parts of the experiment with the ultra-low-temperature part of the experiment. The cooling braids are directly connected to the sample holder on one side, and on the other, they feature a large anchor piece that can be clamped efficiently to the cooling reservoir with a large surface area. For each connection, more than one braid can be used to increase thermal conductivity while maintaining high flexibility.

The material used is oxygen-free high thermal conductivity copper (OFHC), which is widely used in cryogenics. It has an extremely high thermal and electrical conductivity due to the absence of impurities. It also features very low outgassing, which is important for cryogenic systems. We use thin, high-flexibility braids to allow for full scanner movement. They are made by *Leoni*. The specific OFHC material used for the braids is Cu-OF1 or CW007A, which has a minimum copper content of 99.95% and a maximum oxygen concentration of 0.001%. The nominal diameter of one individual braid is 1 mm and it consists of 8 strands of 64 individual wires with a diameter of 0.05 mm. The effective outer diameter is larger, approximately 1.55 mm. The braid has a weight of 10 g per meter. The copper anchoring pieces are designed and manufactured in-house. They are made of Cu-OF or CW008A material with a minimal copper content of 99.95% and a maximum oxygen concentration of 0.0005%. The material was purchased from *Bikar Metalle*.

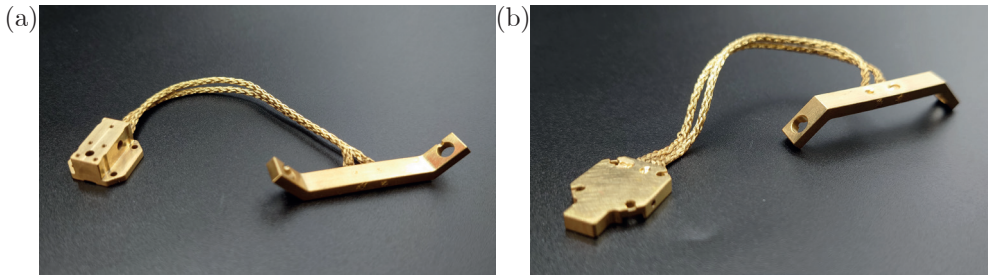

Figure A.2.: (a) Gold-plated tip holder with flexible thermal braids, which is placed on top of the nanopositioning stack. The PCB with the tuning fork holding the diamond scanning probe is glued or screwed onto it (see Appendix A.3.5). (b) Gold-plated sample holder with flexible thermal braids. A carrier PCB with the sample under investigation is placed on top of the holder, or the sample under investigation is directly attached to the holder.

The bulk copper pieces contain holes to insert the ends of the braids. The diameter of the holes for the braids from *Leoni* is 1.6 mm. The borehole has chamfered edges to prevent abrasion and scouring of the moving braids, which could result in the separation of individual copper wires, reducing overall thermal conductivity. In general, all holes are designed to feature vent holes to prevent trapped air in screw holes or through holes, which is particularly important for high-vacuum applications.

The connection between the bulk copper pieces and the braids is done using electron-beam welding by *Swissbeam*. The braids inside the holes are crimped before the weld. Multiple iterations examining grindings of the pieces yield the parameters for an optimal weld of the braid and the bulk copper pieces. The aim is to weld every single wire strand to the bulk copper pieces, which maximizes thermal conductivity.

After welding the parts together, the assemblies are electroplated with gold. This protects the surface from oxidation and ensures a good thermal contact when clamped to the cooling reservoir. In Figure A.2 we show two examples of finished assemblies.

A.3.5. Home-built tuning-fork-based AFM

We describe our home-built atomic force microscope (AFM), which we integrate with a confocal microscope (CFM) to perform scanning NV magnetometry with a single Nitrogen-Vacancy center in a diamond nanopillar [18, 23]. In contrast to optical microscopy techniques, AFM is not limited by optical diffraction and can theoretically reach atomic resolution. We fabricate diamond probes according to Refs. [37, 141] and attach them to a tuning fork (TF) fixed to a nanopositioning stack. To record nanoscale images, we use an AFM with the quartz TF as a vibrating probe in shear mode to control the distance from the sample to the NV in the diamond probe. At a constant height, we record the magnetic field-induced Zeeman splitting Δ_Z from the NV ground state by optical readout at every point on the sample. In this subsection, we motivate the choice of a tuning-fork-based AFM and describe our experimental setup, including the custom tuning fork assembly. Then, we describe the attachment of the diamond scanning probe to the tuning fork and ultimately discuss tuning fork excitation and readout, as well as the scanning probe microscopy (SPM) controller.

Tuning fork

Tuning-fork-based AFM can be operated under various environmental conditions and is ideal for our low-temperature experiments because quartz has a low thermal expansion and is insensitive to magnetic fields [221]. The tuning fork also features low dissipation. Furthermore, quartz is a piezoelectric material; therefore, the tuning fork signal can be read out electronically, simplifying the experimental requirements. The tuning fork (TF) can be driven in two ways: either mechanically, using a nearby piezo actuator, or electrically, by applying a signal to one of its electrodes [221].

Our experiment combines two titanium positioning stacks, composed of xyz-coarse positioners and xyz-piezo scanners (ANSxyz50/LT, *attocube systems*). These components are fully compatible with low-temperature and high-vacuum operation and are made from non-magnetic materials. We will refer to the positioning stack holding the sample as the "sample stack", and the one holding the tuning fork assembly as the "tip stack". The two positioning stacks are placed below a low-temperature compatible objective, allowing for confocal microscopy.

On top of the tip stack, the titanium tuning fork head is mounted (see Figure A.2 a), which holds a ceramic PCB where the tuning fork is attached. For mechanical excitation, a piezo actuator (PL022.3x, *Physik Instrumente*) is glued to the TF head with a low-temperature suitable glue (e.g., blue or green Plus Schnellfest, *UHU*). Additionally, a heater element, consisting of a 100 Ω resistor (ND3-1206EW1000GB, *ims - International Manufacturing Services*) isolated with Kapton tape, and/or a temperature sensor can be attached as well.

We solder a commercial tuning fork (mask set E158, *Micro Crystals*), with a reflow soldering process to two electrical pads on a custom PCB. The PCB is made out of ceramic and features good thermal conductivity. It also houses an additional SMD capacitor (1 pF) for stray capacitance compensation (see below) as well as four electrical contacts on a 1.27 mm raster. The first pin is for the electronic excitation of the TF, the second for the compensation of the parasitic capacitance, the third for the tuning fork readout signal, and the fourth is ground (GND), which is also connected to the titanium holder. If piezo excitation is used, the pin for the excitation signal

is grounded, and the one for the parasitic capacitance compensation is either locally floating or grounded as well. The assembly is tested by recording the amplitude and phase response of the tuning fork using a spectrum analyzer up to a frequency of 35 kHz. The shape of the resonance curve and phase response are then examined.

Scanning probes

After fabrication [37, 141], the diamond probes are still attached to the diamond frame with a small bridge. We now describe how a single diamond scanning probe is removed from the frame and attached to the TF head at the end of a tuning fork prong. We pull quartz capillaries with a pipette puller (P-2000, *Sutter Instruments*) from commercial quartz glass with an outer diameter of 1 mm (Q100-70-10, *Sutter Instruments*). We fill the tip of a capillary with UV glue (NOA81 or NOA61 from *Thorlabs*) and place it into a pipette holder assembly (HI-7, *Narishige*). Using a micro-manipulator (MPC-325 system with MPC-200 controller and two MP-225 micro-manipulators, *Sutter Instruments*) combined with an optical microscope, we place the tip of the capillary on the surface of a diamond scanning probe. This creates a UV glue droplet which is hardened with a focused UV light (M365L2 with LEDD1B, *Thorlabs*) for a few minutes. Afterwards, the bridge holding the diamond probe is broken with shear forces applied through the capillary.

The scanning probe is transferred to the end of the capillary to a second setup with an optical microscope and placed into a xyz-translation stage with a 360° turning wheel. The TF head with the tuning fork is fixed sideways in a vice on a turning wheel below the quartz capillary. We must align two angles and the final position of the probe so that the scanning probe is properly aligned with the TF head and, consequently, with the sample. We must ensure that the probe is the lowest point of the assembly, that it is within the working distance of the objective, and that the TF does not cut any light originating from the NV. First, we align the scanning probe perpendicular to the flat reference plane of the gluing setup using the first turning wheel. Second, we align the scanning probe to the bottom of the TF head using the second turning wheel. Then, we drive the scanning probe to its final position at the end of the TF prong using the xyz-translation stage. Once the pieces are aligned, we add a small drop of UV glue and glue the pieces together. Afterwards, we cut the capillary behind the glue drop towards the holder with a diamond scriber (54482, *Tedpella*), which leaves the diamond probe attached to the TF with a small piece of quartz capillary.

The attachment of a diamond probe to the antenna support structure presented in Chapter 5 differs from this procedure. In this case, the scanning probes are broken out as described above, with a quartz capillary, but from the diamond with pillars facing upwards. Then, they are turned in the micro-manipulator to align the nanopillar so that it points upwards. We place the PCB holding the TF and the antenna support structure upside down under the optical microscope of the micro-manipulator setup and drive the diamond probe in place on the tip of the support structure. We glue it on both sides of the channel with the help of a second capillary filled with UV glue using the second arm of the micro-manipulator stage. Proper alignment of the two structures is important and can be slightly adjusted by applying pressure. After hardening the UV glue, the capillary attachment point is broken with shear forces,

leaving the scanning probe attached to the antenna support structure. The two large gluing areas on both sides of the channel ensure excellent attachment and a more robust scanning probe compared to the small single attachment point of the capillary, which can be subject to bending.

AFM operation

As mentioned before, the tuning fork can be excited either mechanically with a piezo actuator or electrically by applying a voltage signal to one of the TF's electrodes, inducing a mechanical movement [222]. Both excitation methods enable AFM operation, but electrical excitation is preferred due to its direct excitation with minimal power, even though additional circuitry is required.

Mechanical excitation requires only one TF electrode for readou,t while the second one is grounded. The piezo actuator requires two independent lines for the positive and negative electrodes. The two lines do not need to be coaxial; they can also be twisted pair. An SPM controller can directly drive the piezo actuator, making the experimental setup quite simple.

Typical values for the excitation are frequencies between 25-35 kHz and voltages of 50-500 mV.

Electrical excitation, on the other hand, uses one of the electrodes for readout and the other one for the excitation. It differs from mechanical excitation as it leads to an antiresonance typically above the resonance of the TF [222] due to the stray or parasitic capacitance of the quartz material between the two electrodes. Therefore, the charges flowing over this capacitance need to be compensated in order not to distort the line shape.

In collaboration with A. Tonin from our electronic workshop, we developed an all-in-one device (SP1054, in-house built) for electrical excitation and readout of the TF, which also includes a parasitic capacitance compensation circuit (see Figure A.3). The excitation signal from the SPM controller (0-10 V) is fed into the device and attenuated. The excitation signal is delivered to the tuning fork over a coaxial cable. The device also generates an inverted excitation signal, which flows over a variable capacitor in the device and over a fixed capacitor, as close as possible to the TF, to the readout electrode of the TF. The variable capacitance can be used to adjust the total capacitance in the additional circuit to cancel out the current flowing over the parasitic capacitance of the TF, leaving only the Lorentzian-shaped resonance response [221]. Typical values for the excitation voltages at the tuning fork are in the range of 5-500 µV.

The generated charges from the TF are converted to a voltage by a low noise IV-converter with a gain of 20 V/µA. Subsequently, the signal is amplified by three-stage AC-coupled low-noise amplifiers with an adjustable gain. The resulting signal, in the range of 0 to 10 V, is fed into an SPM controller and can be used as a feedback parameter. Instead of our in-house-built readout circuit, a commercial device such as the high-frequency charge amplifier HQA-15M-10T from *FEMTO Messtechnik* can be used. The gain is 10 V/pC which is an equivalent current gain of approximately 1.6 V/µA. In our cryogenic experiments, the coaxial cables carrying the TF readout signal are several meters long, resulting in a significant cable capacitance. Therefore,

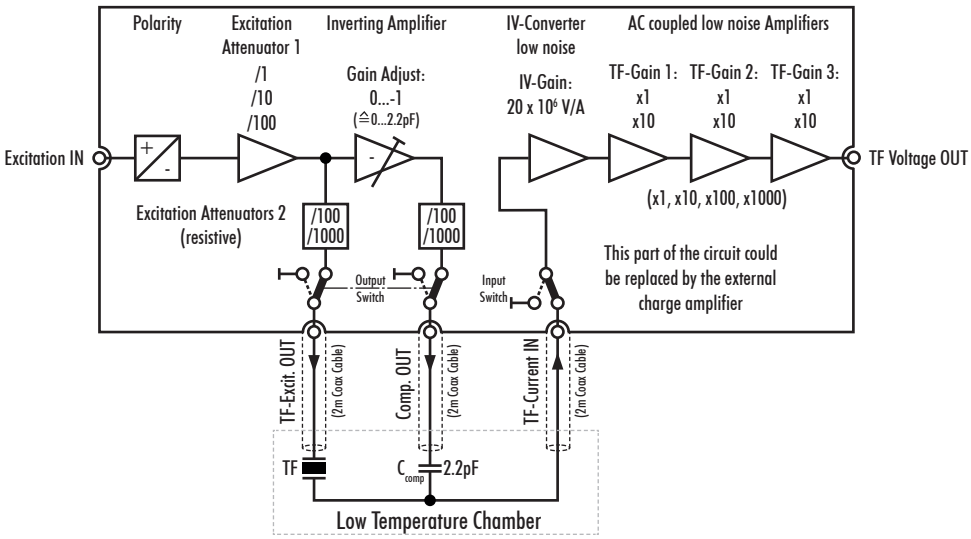

Figure A.3.: Schematics of the electrical excitation circuit and the IV-converter with subsequent amplifier. It features a polarity inverter as well as two variable attenuation stages for very low excitation amplitudes. An inverting amplifier and variable capacitor create the parasitic capacitance compensation circuit. The signal from the TF is converted to a voltage by a low-noise IV converter and subsequently amplified by three-stage, AC-coupled, low-noise amplifiers with adjustable gain.

a pre-amplifier as close as possible to the tuning fork would be ideal to improve the signal-to-noise ratio.

At low temperatures and in high vacuum, the quality factor of tuning forks increases significantly from 10^3 in air at room temperature to 10^5 in vacuum conditions [221, 222]. Additionally, the stray capacitance varies significantly between room temperature and low temperatures. Under cryogenic conditions, the antiresonance resulting from the stray capacitance between the TF electrodes during electrical excitation [222] is much further away from the actual resonance and therefore does not necessarily require a compensation circuit.

We perform amplitude-modulated (AM) AFM or frequency-modulated (FM) AFM using an SPM controller (ASC500, *attocube systems* or MFLI 500 kHz Lock-in Amplifier with MF-MD Multi-demodulator and MF-PID PID/PLL Controller, *Zurich Instruments*). The controller generates a sine wave for exciting the piezo actuator or the TF and processes the amplified response signal from the TF. A PID loop controls the distance between the sample and the scanning probe attached to the TF by adjusting the voltage of a piezo scanner. In our case, it is typically the piezo scanner of the sample stack that results in an inverted control signal.

A.4. Diamond sample fabrication and sample descriptions

In the following, we discuss the challenges associated with efficient photon collection from Nitrogen-Vacancy centers in diamond, especially in the context of low-temperature experiments. We present the photonic structures used in this work and introduce in Appendix A.4.1 our fabrication process for microscopic diamond solid immersion lenses (SILs). In Appendix A.4.2, we give a detailed description of the diamond samples used in each chapter of the thesis.

One of the fundamental problems with color centers in diamond is the poor collection of their photons [223]. Due to the high refractive index of diamond ($n = 2.42$), there is a high degree of internal reflection. Especially in cryogenic setups, the collection efficiency is further reduced due to technical reasons, such as the need for additional optical windows and the requirement for low-temperature-compatible objectives. This is one of the key challenges for experiments with diamonds and therefore a lot of research focuses around the development of efficient photon extraction using diamond structures like microscopic solid immersion lenses [109, 129, 223, 224], nanopillars [37, 141] or microcavities [225–227]. Even though their intended use cases differ, they all increase the photon collection.

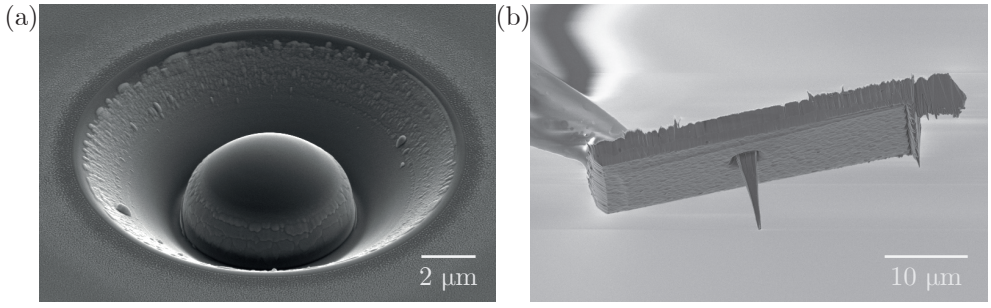

Figure A.4.: (a) Diamond solid immersion lens with a radius of 4.2 µm right after milling in the FIB. (b) Diamond scanning probe attached to a quartz capillary. The nanopillar has an apex diameter of about 300 nm.

In our work, we also use photonic structures to enhance the photoluminescence collected from the Nitrogen-Vacancy center in diamond. Our experimental setups (see Appendix A.3) feature free-space optical access to the cooled sample space, low-temperature-compatible objectives (LT-APO/VISIR, *attocube systems*), and at least one window in the optical path. The closed-cycle dilution refrigerator, which can reach a base temperature of 20 mK, features additional optical windows at various system plates, further reducing photon collection. Therefore, photonic structures are necessary for our low-temperature experiments. We use two different types of structures, microscopic diamond solid immersion lenses (SILs) and nanopillars, as shown in Figure A.4. They either contain a single NV or up to a few individual NV centers. The NVs in the SILs are generally naturally occurring or in-grown NVs, whereas the NVs in the nanopillars are typically implanted.

The SIL is a half-sphere that is milled directly in the diamond material using a focused ion beam (FIB). The NV ideally sits in the center of the lens structure, which improves the collection efficiency significantly compared to the bulk [129]. We use this structure to study native or ingrown NVs, which are micrometer deep in the diamond, far away from the surface. As a result, these NVs typically experience a low effective strain and are charge stable.

For our scanning NV magnetometry efforts, we fabricate all-diamond scanning probes with nanopillars containing single NV centers [37, 141]. The NV is located within tens of nanometers from the diamond surface. The tapered pillar acts as a waveguide to enhance the collection efficiency of photons [37]. These shallow NVs are created by ion implantation prior to fabrication and generally experience a rather high effective strain due to the vicinity of the surface (see Chapter 3).

The collection efficiency could be further improved by using an anti-reflective coating, which consists of AlO_3 or SiO_2. It decreases the optical reflection at the diamond-air interface from 17% to about 2% [228]. In our work, it is not necessary because the photonic structure alone already provides enough enhancement for our measurements.

A.4.1. Solid immersion lens fabrication

Our microscopic diamond solid immersion lenses (SILs) are fabricated in-house using focused ion beam milling, as described in Ref. [129]. In contrast to other works [109, 129], we do not fabricate the SILs around single NV centers, but simply place the SILs at arbitrary positions and post-characterize them. Therefore, the number of NVs contained inside the created SILs depends on their radius and on the native or in-grown NV concentration of the particular diamond. Our approach is significantly easier and, more importantly, much faster, but it requires NV concentrations in bulk that are higher than in typical type IIa "electronic grade" diamond. From calculations based on geometry and dimensions, the density for single NVs in SILs with a radius of 4 µm is around $0.2\,\mathrm{NV/\mu m^3}$. However, confocal microscopy characterisation of different diamond samples indicates that the actual required density might be up to an order of magnitude higher.

Using diamonds with a higher NV concentration can have detrimental effects on the NV charge stability and can lead to spectral diffusion and broadened linewidths. A large number of defects can also change the screening behaviour of the diamond and the effects of photoionization. These effects could be mitigated by limiting the NVs to a thin layer at a specific depth inside the diamond, with the optical focus of the SILs designed to fall within that layer. Such a heterostructure can be created during growth and is called a delta-doped layer. This is quite challenging to achieve with the current growth processes due to the large thickness of the overgrowth and the very low doping concentrations required.

Fabrication procedure

In the following, we outline our fabrication procedure based on Ref. [129]. The fabrication process begins with the preparation of the diamond sample for the ion milling procedure. The diamond is cleaned and fixed with crystal bond on a silicon carrier chip. It is then coated with a conductive Ti/Au layer consisting of 5 nm titanium

followed by 25 nm of gold. The metal layer is very important for the quality of the milling process as it reduces electron beam drift.

For the milling process, we use a FIB-SEM dualbeam system (Helios 400, *FEI Company*) with a gallium (Ga^+) ion beam. The sample is mounted on a standard conductive SEM holder with carbon tape, and an additional electrical connection to the diamond is made by conductive Al-tape.

Before we can mill our SIL structures, we need to determine the specific milling rate of the ion beam for diamond. Therefore, we mill a cylindrical structure in the diamond with a depth of 5 µm and a diameter of 10 µm with a beam current of 2.5 nA, a voltage of 30 kV and a magnification of 1980 (window width of 32 µm). The milling completed after 991 s and resulted in a 2.56 µm deep hole and a total milled volume of 201.1 μm^3. From the above parameters, we calculate the milling rate for diamond in our system to be about 0.812 $\frac{\mu m^3}{nA\,\mu s}$. Using these settings, we proceed to fabricate the SIL structures with precise control over their size and shape.

The FIB machine features a so-called “”stream-file input” which allows for programmatically moving the ion beam. This file format is machine-specific and contains dwell times as well as xy-coordinates for the beam as values for the 16-bit DAC of the patterning processor. The SIL structure is milled in concentric rings, as outlined in Ref. [129], with a spiral beam path to ensure a smooth surface finish. The 3D shape of the structure is created by subsequent passes, removing more material at positions with a higher total dwell time. Each pass removes less than 50 nm to achieve a good surface finish where the roughness is smaller than the optical wavelength in our experiments. We use Python scripts derived from the published code of Ref. [129] to generate the stream files for the FIB, which contain the necessary beam paths to create the SILs.

We predominantly wrote SILs with a radius of 4.2 µm, which take about 35 minutes to mill and have a very smooth surface. Most of them contain one or more NVs depending on the NV concentration of the respective diamond (see Appendix A.4.2). SILs with a radius larger than 10 µm are challenging to write because, during the prolonged milling time, beam drift occurs, jeopardizing the quality of the structure. The milling works well for [100]- and [111]-oriented diamonds.

After the milling process, we take the diamond off the silicon carrier chip and remove the conductive Ti/Au layer with an Au-etchant treatment followed by a ten-minute hydrofluoric (HF) acid bath with a concentration of 4% and a tri-acid clean.

Gallium ions from the milling process remain embedded in the diamond surface up to a depth of about 10 nm. To remove these impurities, we perform a short O_2 plasma etch. We etch the surface for 23 seconds using inductively-coupled reactive ion etching (RIE) with 60 sccm, 1.3 Pa O_2 under 700 W source and 50 W RF power. Afterwards, we clean the sample again in a tri-acid bath.

Optionally, an anti-reflective coating can be added to further enhance the collection efficiency of the sample, as described in Ref. [109].

A.4.2. Detailed sample descriptions

In the following, we provide details on the diamond samples used throughout this work. For each chapter, we provide a brief introduction and list the samples studied.

Some of them are used in several parts of the thesis and therefore appear multiple times.

Samples used in Chapter 3

In the studies in Chapter 3, we investigated single NV centers in our closed-cycle dilution refrigerator (see Appendix A.3.1) at a temperature of $T \approx 4\,\mathrm{K}$. The samples differ mainly in the type of the studied NV (native/in-grown and implanted), the single diamond crystal orientation ([100]-oriented and [111]-oriented), and the type of photonic structures (SIL and nanopillar).

Sample S1:

The sample S1 is the same sample used in Ref. [109], where extensive details on the sample and its fabrication are provided. The sample is a [100]-oriented, chemical vapor deposition (CVD) grown type IIa "electronic grade" diamond from *Element Six*. Solid immersion lenses are fabricated by focused ion beam milling around pre-localized, naturally occurring NV centers located 5-25 µm below the sample surface.

Sample S2:

This sample consists of a commercially available, [100]-oriented, CVD-grown type IIa "electronic grade" diamond from *Element Six*. NV centers are created by $^{14}N^{+}$ ion implantation at 12 keV and subsequent annealing as described in Ref. [141]. This procedure results in NV centers located ∼10 nm from the diamond surface. To increase photon collection efficiency of the NVs, cylindrical diamond nanopillars of ∼200 nm diameter are fabricated in the sample surface [141]. The sample fabrication procedure is tailored to yield an average of one NV center per diamond pillar.

Sample S3:

The sample S3 is the same sample used in Ref. [110], where extensive details on the sample and its fabrication are provided. Sample S3 was grown by CVD in the group of J. Achard and A. Tallaire with methods described in detail in Ref. [229]. NV centers are created in growth through controlled incorporation of N gas into the growth reactor and subsequent annealing. These growth conditions lead to NV centers whose quantization axis is preferentially aligned with the [111] growth direction and which typically exhibit excellent spin properties [230]. We note that the sample exhibits elevated fluorescence background levels from SiV centers, which were inadvertently created during sample growth. We investigate NVs situated in nanopillars fabricated in-house.

Prior to our experiments, samples S2 and S3 were acid cleaned using a well-established acid cleaning technique [231]. This sample cleaning method leaves the diamond surface predominantly oxygen-terminated. No acid cleaning is employed for sample S1 to preserve the pre-existing antenna and gate structures on the sample surface. Given the micron-scale depth of the NVs examined in sample S1, sample

cleaning and surface termination are of minor relevance to the behavior of the NVs studied in this sample.

Samples used in Chapter 4

In Chapter 4, we also investigate native and in-grown single Nitrogen-Vacancy centers in bulk diamond using photonic structures in our temperature controllable closed-cycle refrigerator (see Appendix A.3.2). We examine two different samples: one containing NVs with a low effective strain field and the other containing NVs with an elevated effective strain field. On both samples, we fabricate microscopic diamond solid immersion lenses (SILs) to increase photon collection efficiency. The SILs are created with focused ion beam (FIB) milling as outlined in Appendix A.4.1 according to Ref. [129] with a radius of 4.2 µm. The samples are acid cleaned using a well-established acid cleaning technique [231] which leaves the diamond surface predominantly oxygen-terminated. Afterwards, a Ti/Au antenna structure is patterned on top of the diamond next to the SILs.

Sample containing NVs with very low effective strain (Sample S4):

It is a thin [100]-oriented, chemical vapor deposition (CVD) grown type IIa "electronic grade" diamond from *Element Six* and contains a slightly larger native N concentration than usual throughout the diamond. We fabricate SILs with focused ion beam (FIB) milling as outlined in Appendix A.4.1 according to Ref. [129] with a radius of 4.2 µm and investigate naturally occurring NV centers.This sample contains NV #1.

Sample containing NVs with elevated effective strain:

The sample is sample S3 from Chapter 3 and presented in Ref. [110], where extensive details on the sample are given. N-doping was achieved during the diamond growth through controlled incorporation of N gas into the growth reactor [229]. We note that the sample exhibits elevated fluorescence background levels from SiV centers, which were inadvertently created during sample growth. We investigate NV situated in the fabricated SILs. This sample contains NV #2.

Samples used in Chapter 5

In the studies of Chapter 5, we investigate NV centers located in a parabolic diamond scanning probe a few tens of nm from the diamond surface in our closed-cycle dilution refrigerator (see Appendix A.3.1) at various temperatures between 20 mK and 4 K. The different scanning probe samples are manufactured from commercially available, [100]-oriented, CVD-grown type IIa "electronic grade" diamond from *Element Six* according to Ref. [37].

A.5. Supplementary material for Chapter 3

In the following section, we present some additional material relevant for Chapter 3. We provide details on the fitting procedures and the resulting fit parameters for the classical rate equation model from Appendix A.1 and include supplementary data and further discussions on the observation of the strain-induced enhancement of the orbital g-factor. We discuss the measurements of the NV photoluminescence dependence on laser polarization and describe experimental details on the optical detected magnetic resonance (ODMR) measurements and the calculation of the magnetic field sensitivity presented in Figure 3.6.

Fitting procedure for the magnetic field dependent photoluminescence of the NV$^-$

Using the ten-level model described in Appendix A.1, we fit the NV$^-$ photoluminescence spectra as a function of magnetic field along the NV quantization axis. The model includes all relevant levels of the NV$^-$ and the transition rates are fixed to values from Ref. [112]. The full model includes 14 parameters: three magnetic field components, three electric field components, three strain parameters (shear stress is ignored), two pumping rates, the collection efficiency, the background counts, and the effective g-factor. In general, the model is overconstrained and, as a consequence, requires some approximations to fit accurately.

We treat the combination of electric field and strain as one effective strain field, reducing the six corresponding parameters to three. Furthermore, the positions of the ESLACs in the magnetic field are independent of the z-component of the effective strain parameter, which is thus also disregarded from the fit. Therefore, we parameterize the effective strain fields in polar coordinates with $\delta_\perp = \sqrt{\delta_x^2 + \delta_y^2}$ and ϕ_δ is an angle such that $\delta_x = \delta_\perp \sin(\phi_\delta)$ and $\delta_y = \delta_\perp \cos(\phi_\delta)$. We parameterize the magnetic field in spherical coordinates, with the tilt angle of the magnetic field away from the NV quantization axis denoted as θ_B. In our experiments, the magnetic field misalignment is small with $\theta_B \sim 0$, in which case the azimuthal angle ϕ_B of the magnetic field has no significant effect on the NV excited state spectrum and can be set to $\phi_B = 0$. Finally, we define the photon collection efficiency η to be constant and identical for all NVs at $\eta = 0.005$. This leaves a fit with only 8 parameters and the NV$^-$ PL I_{PL}^- can be described as

$$I_{\mathrm{PL}}^- = f(B_{\mathrm{NV}}, \theta_B, \delta_\perp, \phi_\delta, \beta_{E_x}, \beta_{E_y}, I_{\mathrm{bck}}, g_l). \tag{A.60}$$

As discussed in Chapter 3, the effective g-factor, g_l, can only be confidently determined in the low strain regime. We thus let g_l vary as a free fit parameter for NV1-S1 only, but keep this parameter fixed for all NVs with higher strain values at $g_l = 0.14$ – the value determined for NV1-S1. As we argue in Chapter 3, g_l varies with strain, and fixing g_l for these NVs might therefore introduce certain systematic errors in our fits. However, as illustrated in Figure 3.3d (lower panel), the magnetic field values at which the $E_{x(y)}^0 \leftrightarrow E_{x(y)}^{-1}$ interbranch ESLACs occur, depend only very weakly on the value of g_l and we therefore consider these deviations to be almost negligible.

All of the fit results are summarized in Table A.5, and the fits from the NVs in Chapter 3 are shown in Figures A.5 to A.9.

NV-Sample	$\delta_\perp$ (GHz)	ϕ_δ (°)	θ_B (°)	β_{E_x}	β_{E_y}	I^-_{bck} (cps)
NV1-S1	4.444(3)	-11.6(1.3)	1.14(3)	0.0221(3)	0.0242(5)	4378(92)
NV2-S2	38.6(7)	1(59)	0.61(3)	0.085(5)	0.186(14)	70910(244)
NV3-S2	55.9(6)	-32.2(6)	0.502(10)	0.240(6)	0.64(2)	9091(231)
NV5-S2	32.0(5)	-29(3)	0.20(2)	0.43(3)	0.52(5)	83198(883)
NV4-S3	42.3(5)	-26(2)	1.06(3)	0.102(3)	0.164(7)	158011(234)

Table A.5.: Summary of the fit results of the I^-_{PL} spectra. For NV1-S1, the fit value for g_l is 0.1395(9). For all the other NVs, g_l is fixed to 0.14.

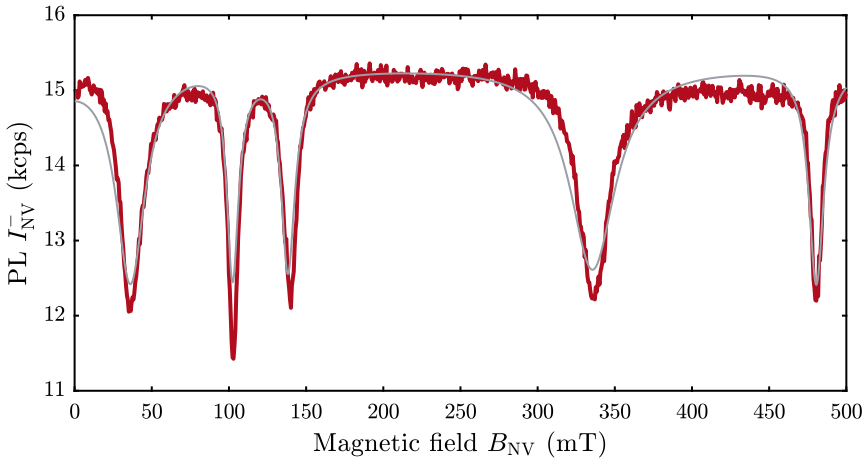

Figure A.5.: NV^- photoluminescence (PL) signal, I^-_{PL}, as a function of magnetic field, B_{NV}, for NV1-S1. The fitting values are: the strain parameters $\delta_\perp = 4.444 \pm 0.003$ GHz, $\phi_\delta = -11.6 \pm 1.3°$ and $g_l = 0.1395 \pm 0.0009$, the B-field misalignment $\theta_B = 1.14 \pm 0.03°$, the excitation and scaling parameters $\beta_{E_x} = 0.0221 \pm 0.0003$ and $\beta_{E_y} = 0.0242 \pm 0.0005$, the background fluorescence $I^-_{\mathrm{bck}} = 4378 \pm 92$ cps.

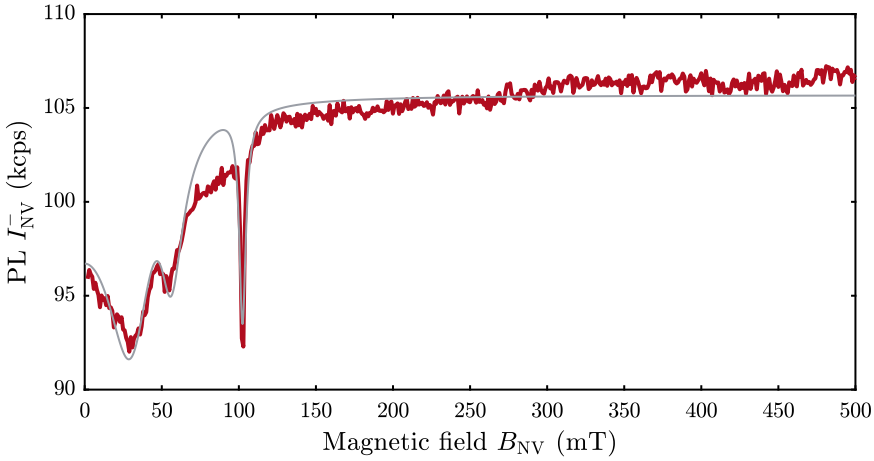

Figure A.6.: NV^- photoluminescence (PL) signal, I^-_{PL}, as a function of magnetic field, B_{NV}, for NV2-S2. The fitting parameters are $\delta_\perp = 38.6 \pm 0.7$ GHz, $\phi_\delta = 1 \pm 59°$, the B-field misalignment $\theta_B = 0.61 \pm 0.03°$, the excitation and scaling parameters $\beta_{E_x} = 0.085 \pm 0.005$ and $\beta_{E_y} = 0.186 \pm 0.014$, the background fluorescence $I^-_{bck} = 70910.429 \pm 244.9818$ cps.

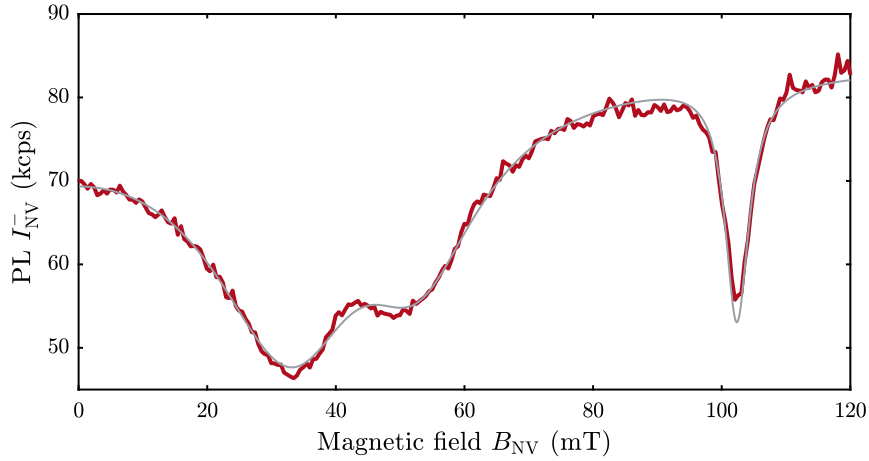

Figure A.7.: NV^- photoluminescence (PL) signal, I^-_{PL}, as a function of magnetic field, B_{NV}, for NV3-S2. The fitting parameters are: $\delta_\perp = 55.9 \pm 0.6$ GHz, $\phi_\delta = -32.2 \pm 0.6°$, the B-field misalignment $\theta_B = 0.502 \pm 0.010°$, the excitation and scaling parameters $\beta_{E_x} = 0.240 \pm 0.006$ and $\beta_{E_y} = 0.64 \pm 0.02$, the background fluorescence $I^-_{bck} = 9091 \pm 231$ cps.

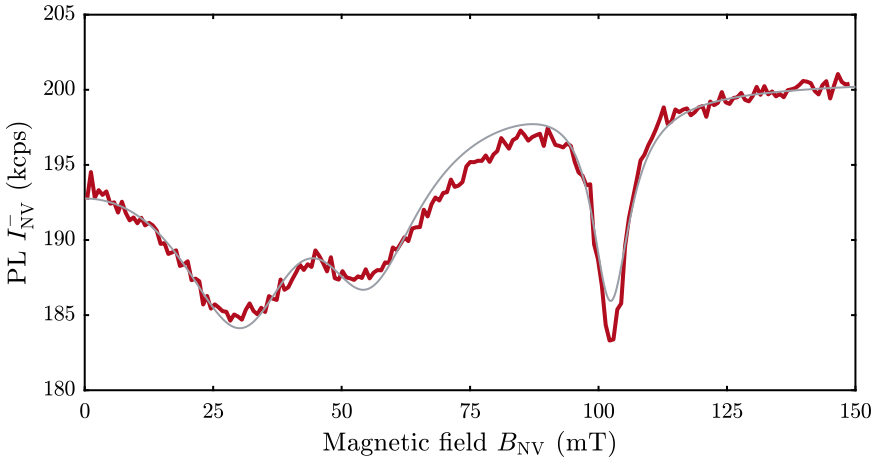

Figure A.8.: NV^- photoluminescence (PL) signal, I^-_{PL}, as a function of magnetic field, B_{NV}, for NV4-S3. The fitting parameters are: the strain parameters $\delta_\perp = 42.3 \pm 0.5$ GHz and $\phi_\delta = -26 \pm 2°$, the B-field misalignment $\theta_B = 1.06 \pm 0.03°$, the excitation and scaling parameters $\beta_{E_x} = 0.102 \pm 0.003$ and $\beta_{E_y} = 0.164 \pm 0.007$, the background fluorescence $I^-_{bck} = 158011 \pm 234$ cps.

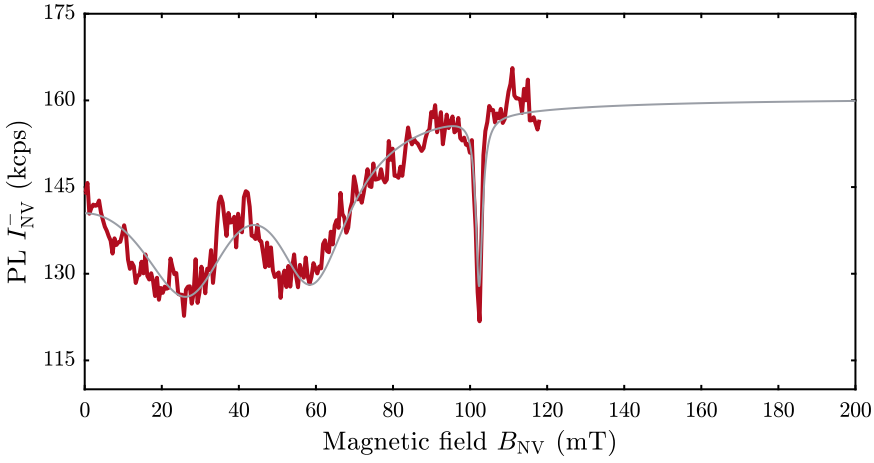

Figure A.9.: NV^- photoluminescence (PL) signal, I^-_{PL}, as a function of magnetic field, B_{NV}, for NV5-S2. The fitting parameters are: the strain parameters $\delta_\perp = 32.0 \pm 0.5$ GHz and $\phi_\delta = -29 \pm 3°$, the B-field misalignment $\theta_B = 0.20 \pm 0.02°$, the excitation and scaling parameters $\beta_{E_x} = 0.43 \pm 0.03$ and $\beta_{E_y} = 0.52 \pm 0.05$, the background fluorescence $I^-_{bck} = 83198 \pm 883$ cps. The strain values are used to calculate the ESR contrast and the sensitivity in Figure 3.6. The scaling parameters have been adapted due to the different laser power during the ESR experiment.

Fitting procedure for the magnetic field dependent photoluminescence of the two NV charge states

The NV^0 and NV^- PL can simultaneously be fitted with the 12-level model presented in Appendix A.1.3, which further includes the NV^0 ground and excited states. The transition rates for the NV^0 and its dynamics with the NV^- as well as their power dependence are all taken from the literature [65].

We first perform a fit to the corresponding NV^- photoluminescence data to extract key properties of the NV^- such as θ_B, $\delta_\perp$, ϕ_δ, β_{E_x} and β_{E_y}. In a second fit, we keep these parameters in the model constant and fit both the NV^0 and NV^- PL simultaneously. The pumping parameter for the NV^0 and the laser power-dependent shelf-ionization rate from the singlet is taken from the average between the two pumping parameters to the two NV^- ES orbitals.

Consequently, in the second fit, the only free parameters left are scaling parameters, and the NV^0 photoluminescence I^0_{PL} can be described as

$$I^0_{\mathrm{PL}} = f(\eta_{\mathrm{NV^0}}, I^0_{\mathrm{bck}}), \tag{A.61}$$

where η_{NV^0} is the collection efficiency for the NV^0 PL and I^0_{bck} are the background counts in the wavelength spectrum of the collected NV^0 PL.

Due to the new decay channels in the model, the predicted NV^- PL also needs to be rescaled when using the 12-level model. We found that merely leaving I^-_{bck} as a free parameter gives good accordance with the data. This leaves the simultaneous fit to the NV^- PL with:

$$I^-_{\mathrm{PL}} = f(I^-_{\mathrm{bck}}) \tag{A.62}$$

where I^-_{bck} is the background counts in the wavelength spectrum of the collected NV^- PL.

The NV^0 PL exactly mirrors the dips of the NV^- with peaks. This behavior cannot be explained solely by the known ionization and recombination processes between the two charge states. Only considering them would lead to the similar dips as for the NV^- PL, instead of the observed peaks. However, when introducing the recently proposed channel from the NV^- singlet to the NV^0 ground state, this behavior can be explained with our model (see Appendix A.1.3). Even when leaving more free fit parameters, without a set minimal value for the shelf-ionization rate, the behaviour of the data cannot be reproduced. The fits give a larger value of background fluorescence counts for the NV^- data. This increase could indicate some small inaccuracy with the ionization, recombination, and shelf-ionization rates and/or their dependence on laser power. The fit results are shown in Table A.6.

NV-Sample	$\eta_{\mathrm{NV^0}}$	I^0_{bck} (cps)	I^-_{bck} (cps)
NV1-S1	0.00132(3)	1258(11)	7980(8)
NV2-S2	0.001820(7)	7963(10)	79176(52)

Table A.6.: Summary of the fit results of the I^0_{PL} and I^-_{PL} spectra.

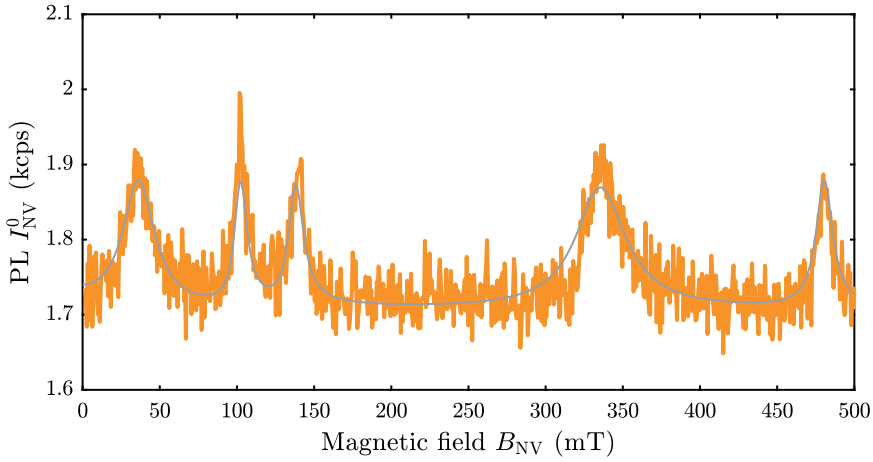

Figure A.10.: NV^0 photoluminescence (PL) signal, I^0_{PL}, as a function of magnetic field, B_{NV}, for NV1-S1. The fitting values for the NV^0 and NV^- PL are: NV^0 pumping parameter $\eta_{NV^0} = 0.00132 \pm 0.00003$, the background fluorescence for NV^0 $I^0_{bck} = 1258 \pm 11$ and the background fluorescence for NV^- $I^-_{bck} = 7980 \pm 8$.

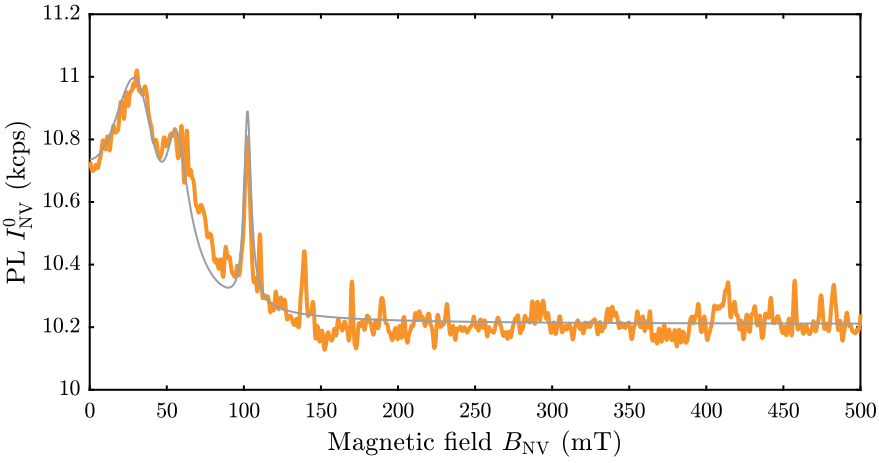

Figure A.11.: NV^0 photoluminescence (PL) signal, I^0_{PL}, as a function of magnetic field, B_{NV}, for NV2-S2. The fitting values for the NV^0 and NV^- PL are: NV^0 pumping parameter $\eta_{NV^0} = 0.001820 \pm 0.000007$, the background fluorescence for NV^0 $I^0_{bck} = 7963 \pm 10$ and the background fluorescence for NV^- $I^-_{bck} = 79176 \pm 52$.

Measurements of the orbital g_l factor

For the measurement of the interbranch level anti crossings $E_{x(y)} \leftrightarrow E_{y(x)}$ at high magnetic fields, we introduce the 111-oriented sample S3 to maximize the magnitude of B_{NV} that we can access in our experimental setup equipped with a $(B_x, B_y, B_z) = (1\,\mathrm{T}, 1\,\mathrm{T}, 5\,\mathrm{T})$ vector magnet as outlined in Appendix A.3.1.

We first characterize the strain parameter of each investigated NV with measurements of the photoluminescence as a function of magnetic field at "low" magnetic fields (see Figure 3.3a). After that we investigate $I^-_{\mathrm{PL}}(B_{\mathrm{NV}})$ for B_{NV} up to 5 T. With all NVs, we conduct the same analysis as exemplified for NV4-S3 in Chapter 3.

All NVs we investigated in S3 show $\delta_\perp$-values in the range of $30-50$ GHz. According to our model, these NVs should all exhibit their $E_{x(y)} \leftrightarrow E_{y(x)}$ interbranch ESLACs, and a corresponding reduction of I^-_{PL}, within the magnetic field sweep range shown in Figure A.12, unless g_l is significantly enhanced, as discussed in Chapter 3.

Due to slow magnetic field ramp speeds and occasional signal drifts, we mostly perform magnetic field sweeps in smaller intervals of B_{NV}, and only a few measurements cover the entire range. This data is shown in Figure A.12. Some of the data include a low-frequency envelope, which results from system drifts during the long magnetic field sweeps.

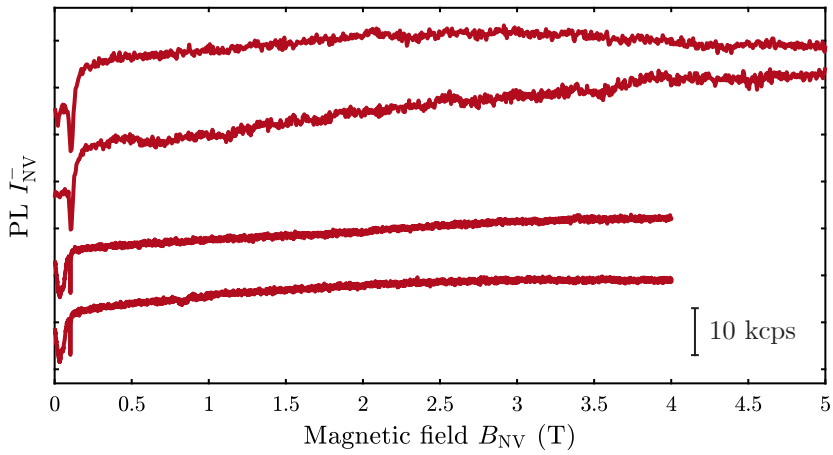

Figure A.12.: NV^- photoluminescence (PL) signal, I^-_{PL} as a function of magnetic field, B_{NV}, for multiple NVs showed with an offset. According to our model, all of the shown NV PL spectra should show PL dips in the shown magnetic field range. They are exemplary and show full field scans. Most of the performed scans were regions of magnetic field investigating of various parts of the magnetic field. To determine the strain appropriately we performed high resolution scans at low magnetic fields.

Suppression of spin-orbit mixing

The absence of high-field anticrossings could be explained by a suppression of the spin-orbit coupling for NVs with higher effective strain values. This would require a magnetic field dependence that would greatly reduce the coupling between low

and high magnetic field regimes. The excited state Hamiltonian in Equations (2.3) and (2.4) only has a non-zero mixing term for the relevant states of,

$$\lambda_{es}^{\perp}\left(\sigma_z \otimes (S_x S_z + S_z S_x) - \sigma_x \otimes (S_y S_z + S_z S_y)\right). \tag{A.63}$$

Evaluating the matrix elements between the relevant eigenstates of $E_{x(y)}^{0}$ and $E_{y(x)}^{\pm 1}$ gives

$$M_{E_x,E_y} = \frac{d_{es}^{\perp}\delta_x \lambda_{es}^{\perp}}{\sqrt{2}} \sqrt{(d_{es}^{\perp}\delta_x)^2 + (B_z g_l \mu_{\mathrm{B}})^2}, \tag{A.64}$$

where, for simplicity, we assume strain only in the x-direction. Numerically evaluating this matrix element for one of the measured NVs (NV4-S3) with $g_l = 0.1$ at $B = 0$ gives $M_{Ex,Ey} = 250\,\mathrm{MHz}$. Importantly, this term varies by less than 1% over the range of $B_{\mathrm{NV}} = 0$ to $B_{\mathrm{NV}} = 5$ T. We thus conclude that a suppression of the spin-orbit mixing does not account for the missing high-field anticrossings.

Time-dependent electric field fluctuations

Due to the high sensitivity of the excited state energies to electric fields, the missing photoluminescence dips could also be explained by electric field fluctuations, which would smear out the features in the PL. The amplitude of such fluctuations would need to be larger than 1000 V/cm and the fluctuation rate larger than 1 Hz in order to be large and rapid enough for individual features to disappear. Electric fields generated by individual trapped charges in the vicinity of NV centers in diamonds [83] can be taken as order-of-magnitude estimates for the expected electric field fluctuations. Therefore, we conclude that typical electric fields in our diamonds are orders of magnitude too small to explain the vanishing of the high-field PL dips.

The type of optical excitation (non-resonant or resonant with intermittent, green charge-repumping pulses) has an effect on the charge dynamics, primarily affecting the event frequency. Furthermore, given that the electric field amplitude quoted by Dolde *et al.* [83] is too small to induce a relevant broadening of the PL dips, the frequency at which the electric field fluctuates is of little relevance.

Green laser excitation can lead to increased electric field fluctuations compared to the case of resonant optical excitation. However, if laser broadening resulted in a direct broadening of the anticrossing features, we would not observe the reduction in PL for the interbranch ESLACs in any sample, regardless of the strain value. We observe the interbranch ESLAC dips for NV1-S1 and, in fact, for all NVs in the low-strain regime. Furthermore, the diamond samples S1 and S3, along with their NVs, are similar in nature. Therefore, we think that laser broadening can not explain the missing ESLAC dips.

Polarization dependence of the NV PL

The optical pumping to the excited state orbital doublet has a polarization dependence [40]. Therefore, it is possible to control the population of the orbitals and the resulting reduction of PL at the positions of the level anticrossings. This control is limited due to the non-radiative relaxation after pumping [40].

We control the polarization angle of the linearly polarized green laser using a liquid crystal rotator with a 1000:1 extinction ratio, placed after the dichroic mirror and before the objective.

In both high (Figure A.13) and low strain regimes (Figure A.14), we find that we can change the contrast of the PL dips. Also, the NV^0 PL shows a dependence on the laser polarization, which we show in Figure A.14 for NV1-S1.

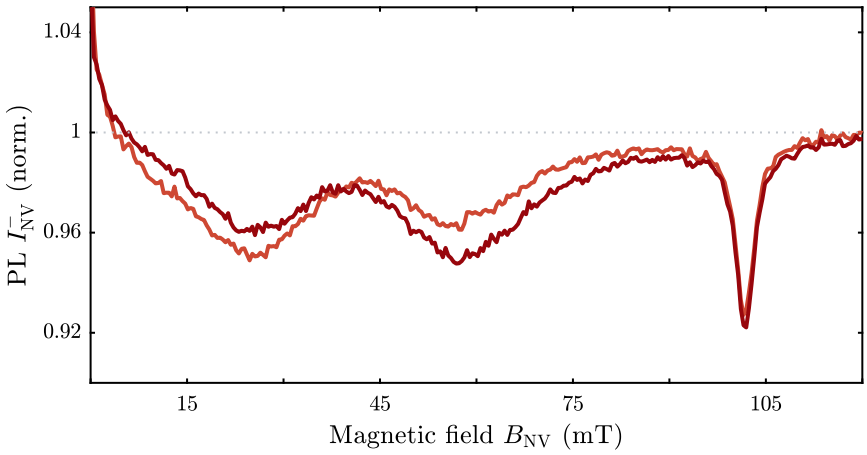

Figure A.13.: Normalized NV^- photoluminescence signal as a function of magnetic field, B_{NV}, for two orthogonal laser polarizations of an NV in S3. The two inter-branch LACs are well resolved. The initial drop in counts is attributed to a nearby NV, which is quenched with a magnetic field.

Optical detected magnetic resonance contrast and magnetic field sensitivity

In order to probe the effect of the excited state level anticrossings on the performance of magnetic field sensing, we bring single Nitrogen-Vacancy centers in nanopillars from sample S2 into close proximity (within 100 µm) of a 25 µm thick Al wire antenna. To avoid the frequency-dependent performance of the microwave circuitry at each measurement point in the magnetic field, we perform Rabi measurements to tune the microwave driving power to maintain an average π-time of 200 ns for power broadened ODMR and 1 µs for hyperfine resolved ODMR. We then performed optical detected magnetic resonance measurements with a standard pulsed ODMR technique [32] and fit the data with Lorentzian functions. The results for NV5-S2 are shown in Figure 3.6.

We are unable to detect any statistical difference in the change of sensitivity between the power-broadened and hyperfine-resolved ODMR. Additionally, we do not observe any effect on the nuclear spin polarization, which is starkly different from the room temperature excited state level anticrossing, where polarization greater than 90% has been observed [232].

To compare the experimental sensitivity and contrast with the model, we first fit the NV^- I_{PL} spectra to obtain the parameters from the model. These fit parameters

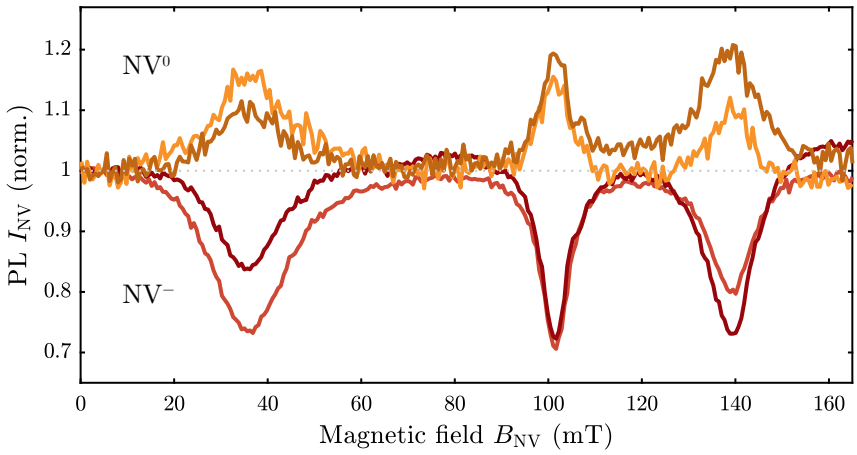

Figure A.14.: Normalized NV^- photoluminescence signal (red), and normalized NV^0 photoluminescence signal (orange), as a function of magnetic field, B_{NV}, for the low-strain NV1-S1. Two orthogonal laser polarizations have been used. The NV^0 signal shows a dependence on laser polarization at the same positions as the NV^- does. When the NV^- countrate decreases at an ESLAC, the corresponding NV^0 countrate increases and vice versa.

are then used to predict the contrast of the ODMR as a function of magnetic field, $\mathcal{C}(B)$. The combination of the fitted $I_{PL}^{-}(B)$ and the predicted $\mathcal{C}(B)$ is then used in conjunction with the average ODMR width to predict the sensitivity, $\eta(B)$. In case of NV5-S2, we show the $I_{PL}^{-}(B)$ data in Figure A.9, which is used to predict the magnetic field sensitivity.

A.6. Supplementary material for Chapter 4

In the following section, we present additional material from Chapter 4. We show the raw, unprocessed data obtained from multiple measurements of the photoluminescence as a function of magnetic field and temperature, and discuss the normalization procedure we introduce to remove slow laser fluctuations. We provide additional details on the fitting procedure using the Lindbladian master equation model described in Appendix A.2, present the resulting fits, and discuss the phonon-coupling strength. Finally, we explain the strain-dependent modeling of the photoluminescence contrast at the position of the room-temperature excited state level anticrossing, presented in Figure 4.4.

Temperature-dependent photoluminescence measurements

We measure the photoluminescence of two single NV centers in different samples, further described in Appendix A.4, as a function of magnetic field and temperature. The samples are measured in two separate experiments. First, each sample is cooled down to the base temperature of the cryostat ($\approx 2\,\mathrm{K}$). We then increase the temperature in steps to room temperature, and at each step, we record the photoluminescence during a magnetic field sweep. The results are shown in Figures A.15 and A.16.

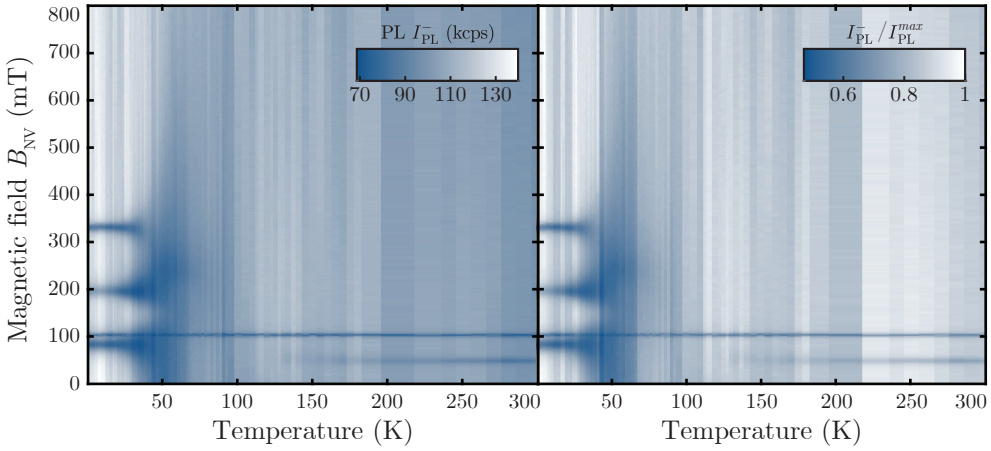

Figure A.15.: PL intensity I^{-}_{PL} as a function of B_{NV} and T for NV #1 for magnetic fields up to 800 mT. On the left, the raw data of the measurement is shown. During the measurement, the green excitation laser experienced significant drifts, leading to distortions in the recorded data. On the right, the data is corrected using the simultaneously recorded laser power.

Two additional datasets with longer integration times and a smaller magnetic field range are presented in Figures A.19 and A.20. These datasets have been acquired during the same experimental run as the other datasets corresponding to the respective NV. For each temperature, the magnetic field sweeps for the additional datasets were recorded consecutively, immediately following the measurements of the primary

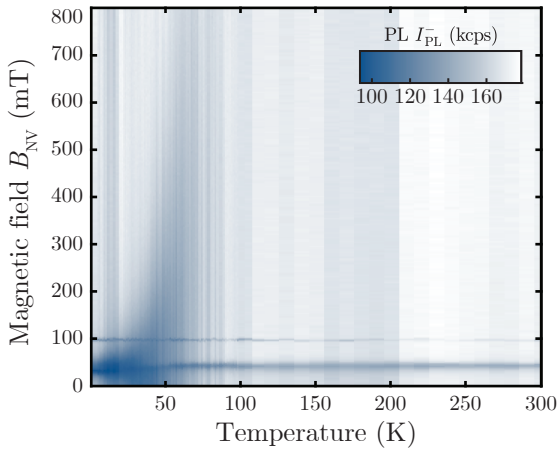

Figure A.16.: PL intensity I_{PL}^{-} as a function of B_{NV} and T for NV #2 with higher effective strain for magnetic fields up to 800 mT.

datasets. As a result, any differences in magnetic field alignment or illumination conditions between these consecutive measurements are expected to be minimal, ensuring that the datasets are directly comparable under nearly identical experimental conditions. The time each magnetic field sweep takes varies from $t = 300\,\mathrm{s}$ to $t = 800\,\mathrm{s}$ between the datasets.

Data normalisation

During the measurement series, we experienced unavoidable laser fluctuations that introduced significant noise to the PL signal. This issue was particularly prevalent for the low-strain measurement series.

For NV #1, we monitor the laser power during the measurement series and therefore we are able to remove these corresponding artefacts. We use the laser power as a normalisation factor, which is independent of changes to the NV photophysics as a function of temperature. The results of this normalisation process are shown in Figures A.15 and A.19, with the left panels showing the raw data and the right panels showing the data after being corrected for laser fluctuations. While this normalization procedure is not the one we use in Chapter 4, it clearly illustrates that the main contribution to the observed fluctuations is coming from the laser itself.

Another way to normalize the data, as used in Chapter 4, is to utilize the model itself, as outlined below. To normalize the data, we use the extracted value for the effective coupling α_{ph} (see Appendix A.6), and the NV parameters and average optical conditions in temperature of NV #1 and NV #2, to simulate the PL as a function of temperature T at $B = 800\,\mathrm{mT}$ for each of the two NVs:

$$I_{\mathrm{PL\ simulation}}^{-}(B = 800\,\mathrm{mT}, T) \tag{A.65}$$

We choose this magnetic field value because at higher magnetic field values, the PL intensity is less dependent on the NV electronic and strain properties. The normal-

ization factor for the dataset of each individual NV is

$$\nu(T) = \frac{I^-_{\text{PL simulation}}(B = 800\,\text{mT}, T)}{I^-_{\text{PL data}}(B = 800\,\text{mT}, T)}, \tag{A.66}$$

where the normalized data is

$$I_{\text{PL normalized data}}(T) = \nu(T) I_{\text{PL data}}. \tag{A.67}$$

The temperature step size, ΔT, varies throughout the experiment, with finer sampling at lower temperatures where most features occur. Specifically, data were recorded with a temperature resolution of $\Delta T = 1\,\text{K}$ for $T < 100\,\text{K}$ and $\Delta T = 5$–$10\,\text{K}$ at higher temperatures. For visualization, the pixel sizes in the figures were adjusted to reflect this varying temperature resolution.

Determining the NV parameters

To model and understand I^-_{PL} as a function of temperature and magnetic field, it is essential to precisely determine key NV parameters such as magnetic field alignment, strain, and optical pumping conditions. Using the same method detailed in Chapter 3, we fit the NV PL as a function of B, $I^-_{\text{PL}}(B)$, at the lowest obtainable temperature ($T = 2\,\text{K}$). For each NV, we extract the following parameters using the model with transition rates presented in Table A.7: the strain splitting parameter $\delta_\perp$ and ϕ_δ as well as the magnetic field misalignment θ_B, the pumping parameters β_{E_x} and β_{E_y}, and the background fluorescence I^-_{bck}. In Figures A.21 and A.23 we show the fits for both NVs, with the extracted properties summarized in Table A.8. The corresponding level diagrams for the two NVs are shown in Figures A.24 and A.22.

k_r	k_{nr_0}	k_{nr_1}	τ_0	Branching ratio
66.8	10.5	90.7	296.53	4.36:1:1

Table A.7.: The table lists the rates used in the model. All transition rates are taken from Gupta *et al.* [112], except for the singlet. The temperature dependence of the singlet decay follows the functional form of Robledo *et al.* [131] scaled to the rates of Gupta *et al.* at room temperature. All rates are expressed in MHz. We found those rates to be in the best agreement with our data, but other literature rates also give good agreement.

To account for fluctuations and changes in optical conditions over the course of the experiment, we determine an average optical pumping strength $\overline{\beta}$ and an average background $\overline{I^-_{\text{bck}}}$ over the temperature sweeps (Figures 4.2c and 4.3c in Chapter 4) for each NV. We fit our model to the $I^-_{\text{PL}}(T)$ data of NV #2 ($B = 0\,\text{mT}$) of Figure 4.3c, with the only free parameters $\overline{\beta}$, $\overline{I^-_{\text{bck}}}$ and α_{ph}. We do not observe any changes in pumping strength or background counts while sweeping over the magnetic field since these sweeps are comparatively rapid (5-15 minutes per sweep).

For NV #1, we also fit $\overline{\beta}$ and $\overline{I^-_{\text{bck}}}$ at $B = 0\,\text{mT}$ from Figure 4.2c using the extracted value for the phonon coupling strength from NV #2. However, for NV #1, we restrict the fit to the temperature range which exhibits only minor power fluctuations (i.e.

NV	$\delta_\perp$ (GHz)	ϕ_δ (°)	θ_B (°)	β_{E_x}	β_{E_y}	I^-_{bck} (kcps)
NV #1	1.685(3)	234(3)	1.05(3)	0.0634(12)	0.039(2)	18.0(7)
NV #2	75(2)	35.3(9)	1.37(3)	0.052(2)	0.089(5)	29.9(7)

Table A.8.: Summary of the fit results for the two NVs from the I^-_{PL} spectra at low temperature ($T \approx 2\,\mathrm{K}$). $\eta_{\mathrm{collection}}$ is fixed to 0.03. For details regarding the model, refer to Appendix A.2

$T < 80\,\mathrm{K}$). We fit $\overline{\beta}_{E_x}$ keeping the ratio of excitation between the branches β_{E_y}/β_{E_x} constant. The parameters we determine are shown in Table A.9.

NV	$\overline{\beta}_{E_x}$	$\overline{\beta}_{E_y}$	$\overline{I}^-_{\mathrm{bck}}$ (kcps)
NV #1	0.061(4)	$\overline{\beta}_{E_x} \cdot \beta_{E_y}/\beta_{E_x}$	19(3)
NV #2	0.0344(7)	$\overline{\beta}_{E_x} \cdot \beta_{E_y}/\beta_{E_x}$	51.5(1.3)

Table A.9.: The table shows the average optical conditions of the two NVs with temperature. The ratio between the two orbitals is kept constant at the parameters extracted from the fit at the lowest temperature.

The values extracted from the I^-_{PL} spectra of the two NVs at low temperature (Table A.8) and the values for average illumination conditions (Table A.9) are used in the Lindbladian model calculating the photoluminescence response as discussed in Appendix A.2.

Phonon-coupling parameter

Using our model, it is also possible to extract the phonon-coupling parameter and thus model the temperature dependence of the ESLAC structure. Using the determined NV parameters shown in Tables A.8 and A.9, the temperature dependence of our model is described by two parameters α_{ph}, the effective coupling incorporating the phonon coupling strength to A and E phonons and ω_{c}, the cutoff frequency in the integral in Equation (A.42). These values are required to calculate the transition frequency between the two orbitals. In our model with fix ω_{c} to 60 meV (see Appendix A.2.4), so that the phonon coupling strength α_{ph}, remains the only free parameter in the fit.

Since the data from NV #2 (higher strain) has a significantly better quality in laser stability over time, we use this dataset to extract the phonon-coupling strength $\alpha_{\mathrm{ph}} = 1.4 \pm 0.2\ \mathrm{Hz/K^5}$ for both NVs. This value is determined by fitting the NV PL as a function of temperature across a range of magnetic field values, where magnetic field values around the ESLACs and GLSAC were excluded from the fit. Additionally, our variable temperature insert has two temperature ranges ($T < 15$ K and $T > 15$ K), which results in different temperature gradients from the sample to the temperature sensor. For consistency, we exclude the temperature range $T < 15$ K from the fit.

For modeling the NV PL, we assume that the coupling strength is the same for the two NVs. Therefore, we use the determined effective coupling strength also for NV #1. Additionally, as both samples have been mounted in the same way on identical PCBs and measured in the same system (see Appendix A.3.2), we assume that the

two NVs are exposed to the same temperature at any given nominal measurement temperature. The model is then also used to normalize the fluctuation in countrate over time in the experimental data as described in Appendix A.6.

Finally, we do not include additional strain effects in our model, such as those arising from thermal expansion. Although temperature-dependent strain variations are expected, including them is unlikely to significantly improve the model, given the good agreement we observe with the experimental data.

The resulting strain-dependent spin-conserving mixing rate in the excited state orbitals is presented in Figure A.17 and shows that at low temperatures, the relaxation into the ground state k_r is the dominant rate.

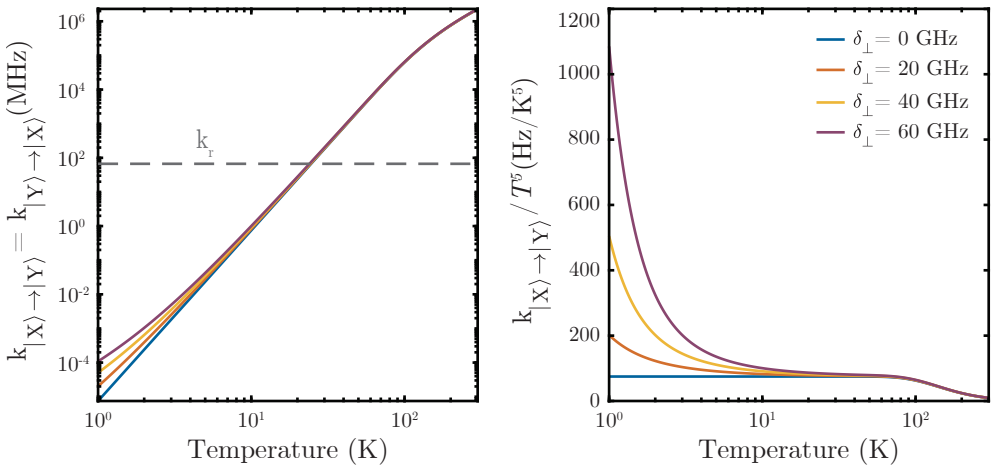

Figure A.17.: Left: Strain-dependent spin-conserving transition rates between the two orbitals as a function of temperature in MHz in a double-log plot. The dashed line indicates the radiative decay rate k_r used in the model [112]. Right: Strain-dependent transition rates divided by temperature scaling (T^5).

Comparison of the effective coupling α_{ph} to literature values

To compare the effective phonon coupling predicted in our model to the values published in the literature, we need to adopt a change in the transition rate Γ_{XY}, as we also include an additional coupling of the A_1-symmetry phonons (η_A). In previous work by Plakhotnik *et al.* [78] and as outlined in Section 2.4 the transition rate from phonon-coupling is described as

$$W = B_E T^5 I, \tag{A.68}$$

where

$$B_E = \frac{64}{\pi} \hbar \eta_E^2 k_B^5. \tag{A.69}$$

To get a comparable form, we use the defined prefactor from Equation (A.43)

$$\alpha_{\mathrm{ph}} = \frac{4\pi}{\hbar} \left(\eta_E^2 + \eta_A \eta_E\right) k_B^5. \tag{A.70}$$

where this term is a fit parameter in the model. Using the fitted value for α_{ph} and equating it to the literature value B_E, we can solve for η_E

$$\eta_E = \sqrt{\frac{\pi\alpha_{\mathrm{ph}}}{64\hbar k_B^5}}. \tag{A.71}$$

Our value of $\eta_E = 150 \pm 18$ (MHz/meV^3) extracted with this method is consistent with other measured values shown in Table A.10.

Reference	η_E (MHz/meV^3)
Our Result	150 ± 18
Plakhotnik et al. [78]	143
Goldmann et al. [35]	276 ± 15
Abtew et al. [77]	196

Table A.10.: Comparison of E-symmetry photon coupling η_E from various sources.

Emergence of the RT-ESLAC

The emergence of the room-temperature excited-state level anticrossing (RT-ESLAC) depends heavily on strain, as the specific low-temperature energy configuration alters the effect that orbital averaging has on the photoluminescence. To quantify this behavior, we calculate the PL contrast at the magnetic field value of the RT-ESLAC ($B = 50.5\,\mathrm{mT}$) as a function of temperature. To isolate the effect of the RT-ESLAC, we calculate $I^-_{\mathrm{PL}}(B,T)$ where the spin-conserving mixing rate to and from the $m_s = -1$ states in the excited state are zero ($k_{|X,-1\rangle\rightarrow|Y,-1\rangle} = 0$ and $k_{|Y,-1\rangle\rightarrow|X,-1\rangle} = 0$), which we define as $\tilde{I}^-_{\mathrm{PL}}$. All the other transition rates remain the same. This modification leaves the overall NV photophysics unchanged, except that it effectively removes the RT-ESLAC from the simulation. The resulting quantity can then be used as a normalisation reference and subtracted from all other effects in the simulation. The contrast due to the RT-ESLAC can be defined as

$$\mathcal{C}_{\text{RT-ELSAC}} = \frac{\tilde{I}^-_{\mathrm{PL}}}{\tilde{I}^{-\,max}_{\mathrm{PL}}} - \frac{I^-_{\mathrm{PL}}}{I^{-\,max}_{\mathrm{PL}}}, \tag{A.72}$$

where the superscript "max" refers to the maximum PL in that simulation. The results of this simulation are shown in Figures 4.4c of the main text. The onset temperature of the RT-ESLAC is strongly dependent on the magnetic field misalignment θ_B. In our experimental setup, small changes of the magnetic field alignment (< 1 degrees) can occur due to the presence of minute drift and hysteresis in the magnet operation, which will influence the observed onset temperature.

To further illustrate this effect, we show the evolution of the PL for different temperatures in Figure A.18.

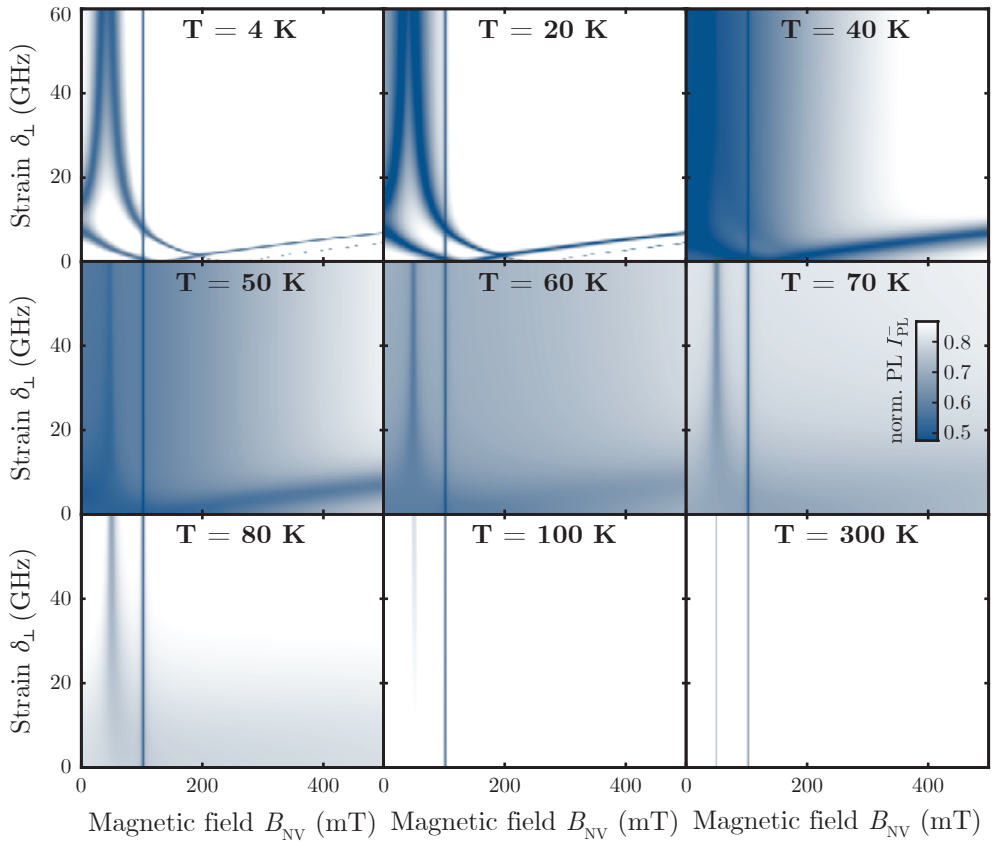

Figure A.18.: PL intensity I_{PL}^{-} as a function of B_{NV} and $\delta_\perp$, calculated with the described model for a series of temperatures, showing the transition from the low-temperature to the room-temperature excited-state structure. The colormap has been limited to fixed minimum and maximum values, rather than spanning the full range of the data, to better highlight the transition. Additionally, the $T = 300\,\mathrm{K}$ panel includes a 15% offset for clarity.

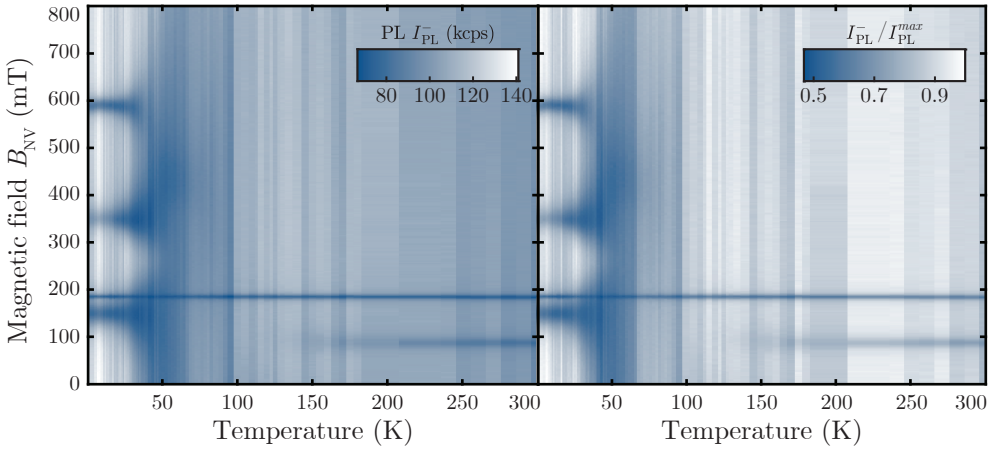

Figure A.19.: Additional PL intensity map, showing I^-_{PL} as a function of B_{NV} and T measurement of NV #1 with a smaller magnetic field range up to 450 mT and longer integration times. The raw data is shown on the left, and the data corrected for laser drifts on the right.

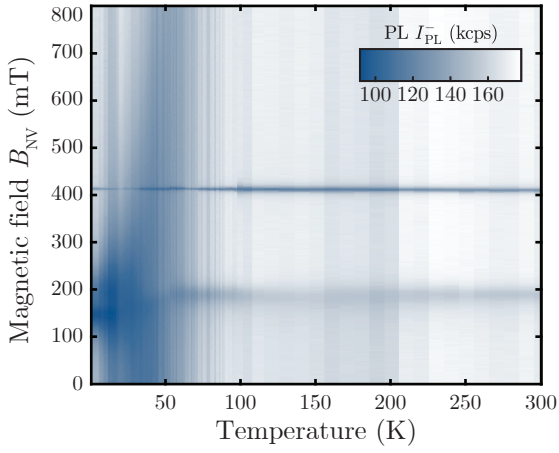

Figure A.20.: Additional PL intensity map, showing I^-_{PL} as a function of B_{NV} and T measurement of NV #2 for a smaller magnetic field range up to 200 mT and longer integration times.

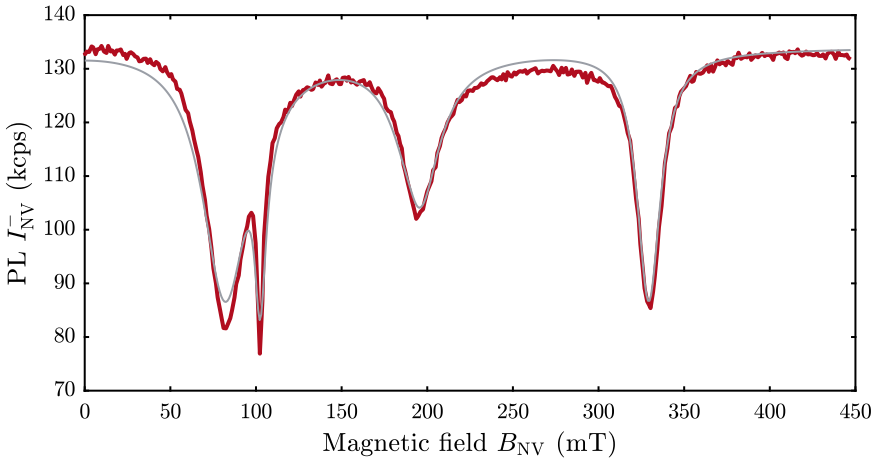

Figure A.21.: NV^- photoluminescence (PL) signal, I^-_{PL}, as a function of magnetic field, B_{NV}, for the low-strain NV (NV #1). The fitting parameters are: the strain parameters $\delta_\perp = 1.685 \pm 0.003$ GHz and $\theta_\delta = 234 \pm 2$ °, the B-field misalignment $\theta_B = 1.05 \pm 0.03°$ and $\phi_B := 0°$, the excitation and scaling parameters $\beta_{E_x} = 0.0634 \pm 0.0013$ and $\beta_{E_y} = 0.039 \pm 0.002$, the background fluorescence $I^-_{bck} = 18.0 \pm 0.7$ kcps.

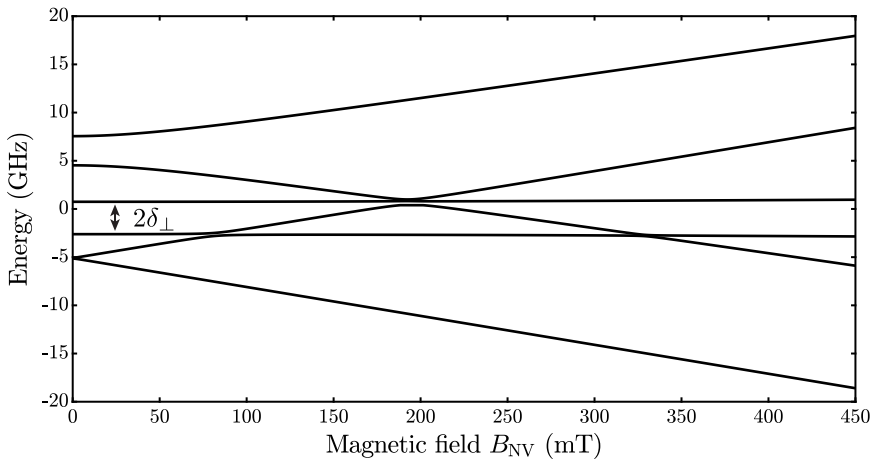

Figure A.22.: Energy level structure of the low-strain NV (NV #1). The two orbital branches are not well separated.

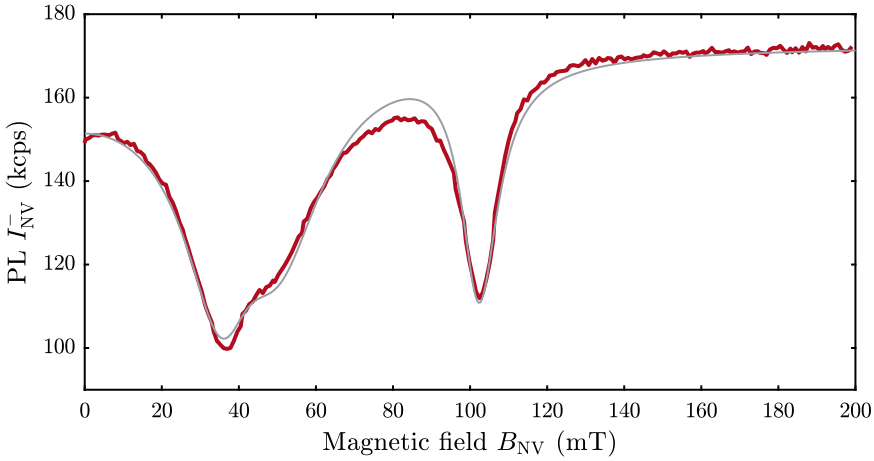

Figure A.23.: NV^- photoluminescence (PL) signal, I^-_{PL}, as a function of magnetic field, B_{NV}, for the NV with elevated strain (NV #2). The fitting parameters are: the strain parameters $\delta_\perp = 75 \pm 2$ GHz and $\theta_\delta = 35.3 \pm 0.9°$, the B-field misalignment $\theta_B = 1.37 \pm 0.03°$ and $\phi_B = 206 \pm 30°$; the excitation and scaling parameters $\beta_{E_x} = 0.052 \pm 0.002$ and $\beta_{E_y} = 0.090 \pm 0.005$, the background fluorescence $I^-_{bck} = 29.9 \pm 0.7$ kcps.

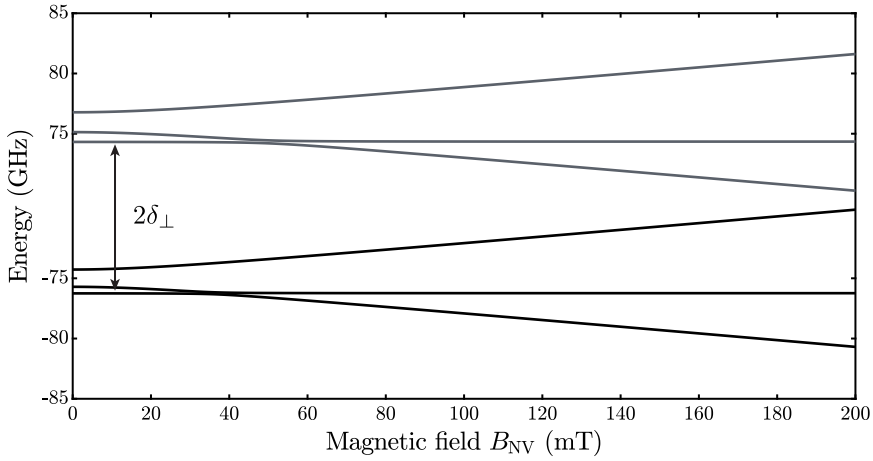

Figure A.24.: Energy level structure of the NV with elevated strain (NV #2). The orbital branches are well separated as indicated by the slightly different colors of the orbitals.

B. Bibliography

[1] K. Simonyi, *A Cultural History of Physics* CRC Press, Boca Raton, London, New York (2012).

[2] T. D. Ladd, F. Jelezko, R. Laflamme, Y. Nakamura, C. Monroe, and J. L. O'Brien, *Quantum computers*, Nature **464**, 45 (2010).

[3] M. Riedel, M. Kovacs, P. Zoller, J. Mlynek, and T. Calarco, *Europe's Quantum Flagship initiative*, Quantum Science and Technology **4**, 020501 (2019).

[4] R. W. Keyes, *Physical limits of silicon transistors and circuits*, Reports on Progress in Physics **68**, 2701 (2005).

[5] L. Johnsson and G. Netzer, *The impact of Moore's Law and loss of Dennard scaling: Are DSP SoCs an energy efficient alternative to x86 SoCs?*, Journal of Physics: Conference Series **762**, 012022 (2016).

[6] A. Hirohata, K. Yamada, Y. Nakatani, I.-L. Prejbeanu, B. Diény, P. Pirro, and B. Hillebrands, *Review on spintronics: Principles and device applications*, Journal of Magnetism and Magnetic Materials **509**, 166711 (2020).

[7] B. Dieny, I. L. Prejbeanu, K. Garello, P. Gambardella, P. Freitas, R. Lehndorff, W. Raberg, U. Ebels, S. O. Demokritov, J. Akerman, A. Deac, P. Pirro, C. Adelmann, A. Anane, A. V. Chumak, A. Hirohata, S. Mangin, S. O. Valenzuela, M. C. Onbaşlı, M. d'Aquino, G. Prenat, G. Finocchio, L. Lopez-Diaz, R. Chantrell, O. Chubykalo-Fesenko, and P. Bortolotti, *Opportunities and challenges for spintronics in the microelectronics industry*, Nature Electronics **3**, 446 (2020).

[8] D. P. DiVincenzo, *The Physical Implementation of Quantum Computation*, Fortschritte der Physik **48**, 771 (2000).

[9] G. Wolfowicz, F. J. Heremans, C. P. Anderson, S. Kanai, H. Seo, A. Gali, G. Galli, and D. D. Awschalom, *Quantum guidelines for solid-state spin defects*, Nature Reviews Materials **6**, 906 (2021).

[10] M. W. Doherty, N. B. Manson, P. Delaney, F. Jelezko, J. Wrachtrup, and L. C. L. Hollenberg, *The nitrogen-vacancy colour centre in diamond*, Physics Reports **528**, 1 (2013).

[11] D. M. Toyli, D. J. Christle, A. Alkauskas, B. B. Buckley, C. G. Van de Walle, and D. D. Awschalom, *Measurement and Control of Single Nitrogen-Vacancy Center Spins above 600 K*, Physical Review X **2**, 031001 (2012).

[12] K.-M. C. Fu, G. Z. Iwata, A. Wickenbrock, and D. Budker, *Sensitive magnetometry in challenging environments*, AVS Quantum Science **2**, 044702 (2020).

[13] M. Lesik, T. Plisson, L. Toraille, J. Renaud, F. Occelli, M. Schmidt, O. Salord, A. Delobbe, T. Debuisschert, L. Rondin, P. Loubeyre, and J.-F. Roch, *Magnetic measurements on micrometer-sized samples under high pressure using designed NV centers*, Science **366**, 1359 (2019).

[14] B. Hensen, H. Bernien, A. E. Dreau, A. Reiserer, N. Kalb, M. S. Blok, J. Ruitenberg, R. F. L. Vermeulen, R. N. Schouten, C. Abellan, W. Amaya, V. Pruneri, M. W. Mitchell, M. Markham, D. J. Twitchen, D. Elkouss, S. Wehner, T. H. Taminiau, and R. Hanson, *Loophole-free Bell inequality violation using electron spins separated by 1.3 kilometres*, Nature **526**, 682 (2015).

[15] N. Kalb, A. A. Reiserer, P. C. Humphreys, J. J. W. Bakermans, S. J. Kamerling, N. H. Nickerson, S. C. Benjamin, D. J. Twitchen, M. Markham, and R. Hanson, *Entanglement distillation between solid-state quantum network nodes*, Science **356**, 928 (2017).

[16] C. E. Bradley, J. Randall, M. H. Abobeih, R. C. Berrevoets, M. J. Degen, M. A. Bakker, M. Markham, D. J. Twitchen, and T. H. Taminiau, *A Ten-Qubit Solid-State Spin Register with Quantum Memory up to One Minute*, Physical Review X **9**, 031045 (2019).

[17] M. Pompili, S. L. N. Hermans, S. Baier, H. K. C. Beukers, P. C. Humphreys, R. N. Schouten, R. F. L. Vermeulen, M. J. Tiggelman, L. dos Santos Martins, B. Dirkse, S. Wehner, and R. Hanson, *Realization of a multinode quantum network of remote solid-state qubits*, Science **372**, 259 (2021).

[18] J. M. Taylor, P. Cappellaro, L. Childress, L. Jiang, D. Budker, P. R. Hemmer, A. Yacoby, R. Walsworth, and M. D. Lukin, *High-sensitivity diamond magnetometer with nanoscale resolution*, Nature Physics **4**, 810 (2008).

[19] F. Dolde, H. Fedder, M. W. Doherty, T. Nöbauer, F. Rempp, G. Balasubramanian, T. Wolf, F. Reinhard, L. C. L. Hollenberg, F. Jelezko, and J. Wrachtrup, *Electric-field sensing using single diamond spins*, Nature Physics **7**, 459 (2011).

[20] P. Neumann, I. Jakobi, F. Dolde, C. Burk, R. Reuter, G. Waldherr, J. Honert, T. Wolf, A. Brunner, J. H. Shim, D. Suter, H. Sumiya, J. Isoya, and J. Wrachtrup, *High-Precision Nanoscale Temperature Sensing Using Single Defects in Diamond*, Nano Letters **13**, 2738 (2013).

[21] P. Ovartchaiyapong, K. W. Lee, B. A. Myers, and A. C. B. Jayich, *Dynamic strain-mediated coupling of a single diamond spin to a mechanical resonator*, Nature Communications **5**, 4429 (2014).

[22] C. L. Degen, F. Reinhard, and P. Cappellaro, *Quantum sensing*, Reviews of Modern Physics **89**, 035002 (2017).

[23] G. Balasubramanian, I. Y. Chan, R. Kolesov, M. Al-Hmoud, J. Tisler, C. Shin, C. Kim, A. Wojcik, P. R. Hemmer, A. Krueger, T. Hanke, A. Leitenstorfer,

R. Bratschitsch, F. Jelezko, and J. Wrachtrup, *Nanoscale imaging magnetometry with diamond spins under ambient conditions*, Nature **455**, 648 (2008).

[24] P. Maletinsky, S. Hong, M. S. Grinolds, B. Hausmann, M. D. Lukin, R. L. Walsworth, M. Loncar, and A. Yacoby, *A robust scanning diamond sensor for nanoscale imaging with single nitrogen-vacancy centres*, Nature Nanotechnology **7**, 320 (2012).

[25] L. Rondin, J.-P. Tetienne, P. Spinicelli, C. Dal Savio, K. Karrai, G. Dantelle, A. Thiaville, S. Rohart, J.-F. Roch, and V. Jacques, *Nanoscale magnetic field mapping with a single spin scanning probe magnetometer*, Applied Physics Letters **100**, 153118 (2012).

[26] L. Thiel, D. Rohner, M. Ganzhorn, P. Appel, E. Neu, B. Müller, R. Kleiner, D. Koelle, and P. Maletinsky, *Quantitative nanoscale vortex imaging using a cryogenic quantum magnetometer*, Nature Nanotechnology **11**, 677 (2016).

[27] M. Pelliccione, A. Jenkins, P. Ovartchaiyapong, C. Reetz, E. Emmanouilidou, N. Ni, and A. C. Bleszynski Jayich, *Scanned probe imaging of nanoscale magnetism at cryogenic temperatures with a single-spin quantum sensor*, Nature Nanotechnology **11**, 700 (2016).

[28] F. Casola, T. van der Sar, and A. Yacoby, *Probing condensed matter physics with magnetometry based on nitrogen-vacancy centres in diamond*, Nature Reviews Materials **3**, 1 (2018).

[29] L. Thiel, Z. Wang, M. A. Tschudin, D. Rohner, I. Gutiérrez-Lezama, N. Ubrig, M. Gibertini, E. Giannini, A. F. Morpurgo, and P. Maletinsky, *Probing magnetism in 2D materials at the nanoscale with single-spin microscopy*, Science **364**, 973 (2019).

[30] J. Harrison, M. J. Sellars, and N. B. Manson, *Optical spin polarisation of the N-V centre in diamond*, Journal of Luminescence **107**, 245 (2004).

[31] J.-P. Tetienne, L. Rondin, P. Spinicelli, M. Chipaux, T. Debuisschert, J.-F. Roch, and V. Jacques, *Magnetic-field-dependent photodynamics of single NV defects in diamond: An application to qualitative all-optical magnetic imaging*, New Journal of Physics **14**, 103033 (2012).

[32] A. Dréau, M. Lesik, L. Rondin, P. Spinicelli, O. Arcizet, J. F. Roch, and V. Jacques, *Avoiding power broadening in optically detected magnetic resonance of single NV defects for enhanced dc magnetic field sensitivity*, Phys. Rev. B **84**, 1 (2011).

[33] M. Steiner, P. Neumann, J. Beck, F. Jelezko, and J. Wrachtrup, *Universal enhancement of the optical readout fidelity of single electron spins at nitrogen-vacancy centers in diamond*, Physical Review B **81**, 035205 (2010).

[34] L. C. Bassett, F. J. Heremans, C. G. Yale, B. B. Buckley, and D. D. Awschalom, *Electrical Tuning of Single Nitrogen-Vacancy Center Optical Transitions Enhanced by Photoinduced Fields*, Physical Review Letters **107**, 266403 (2011).

[35] M. L. Goldman, A. Sipahigil, M. W. Doherty, N. Y. Yao, S. D. Bennett, M. Markham, D. J. Twitchen, N. B. Manson, A. Kubanek, and M. D. Lukin, *Phonon-induced population dynamics and intersystem crossing in nitrogen-vacancy centers*, Physical Review Letters **114**, 145502 (2015).

[36] M. L. Goldman, M. W. Doherty, A. Sipahigil, N. Y. Yao, S. D. Bennett, N. B. Manson, A. Kubanek, and M. D. Lukin, *State-selective intersystem crossing in nitrogen-vacancy centers*, Physical Review B **91**, 165201 (2015).

[37] N. Hedrich, D. Rohner, M. Batzer, P. Maletinsky, and B. J. Shields, *Parabolic Diamond Scanning Probes for Single-Spin Magnetic Field Imaging*, Physical Review Applied **14**, 064007 (2020).

[38] S. A. Wolf, I. Rosenberg, R. Rapaport, and N. Bar-Gill, *Purcell-enhanced optical spin readout of nitrogen-vacancy centers in diamond*, Physical Review B **92**, 235410 (2015).

[39] A. Batalov, V. Jacques, F. Kaiser, P. Siyushev, P. Neumann, L. J. Rogers, R. L. McMurtrie, N. B. Manson, F. Jelezko, and J. Wrachtrup, *Low Temperature Studies of the Excited-State Structure of Negatively Charged Nitrogen-Vacancy Color Centers in Diamond*, Physical Review Letters **102**, 195506 (2009).

[40] K.-M. C. Fu, C. Santori, P. E. Barclay, L. J. Rogers, N. B. Manson, and R. G. Beausoleil, *Observation of the Dynamic Jahn-Teller Effect in the Excited States of Nitrogen-Vacancy Centers in Diamond*, Physical Review Letters **103**, 256404 (2009).

[41] S. E. Lillie, D. A. Broadway, N. Dontschuk, S. C. Scholten, B. C. Johnson, S. Wolf, S. Rachel, L. C. L. Hollenberg, and J.-P. Tetienne, *Laser modulation of superconductivity in a cryogenic wide-field nitrogen-vacancy microscope*, Nano Letters **20**, 1855 (2020).

[42] J. Happacher, D. A. Broadway, J. Bocquel, P. Reiser, A. Jimenéz, M. A. Tschudin, L. Thiel, D. Rohner, M. G. Puigibert, B. Shields, J. R. Maze, V. Jacques, and P. Maletinsky, *Low-temperature photophysics of single nitrogen-vacancy centers in diamond*, Physical Review Letters **128**, 177401 (2022).

[43] J. Happacher, J. Bocquel, H. T. Dinani, M. A. Tschudin, P. Reiser, D. A. Broadway, J. R. Maze, and P. Maletinsky, *Temperature-Dependent Photophysics of Single NV Centers in Diamond*, Physical Review Letters **131**, 086904 (2023).

[44] J. Happacher, J. Bocquel, P. Reiser, B. J. Shields, and P. Maletinsky, *Scanning NV magnetometer with integrated microwave spin control*, In Preparation (2023).

[45] G. Davies, M. F. Hamer, and W. C. Price, *Optical studies of the 1.945 eV vibronic band in diamond*, Proceedings of the Royal Society of London. A. Mathematical and Physical Sciences **348**, 285 (1976).

[46] J. R. Maze, A. Gali, E. Togan, Y. Chu, A. Trifonov, E. Kaxiras, and M. D. Lukin, *Properties of nitrogen-vacancy centers in diamond: The group theoretic approach*, New Journal of Physics **13**, 025025 (2011).

[47] A. T. Collins, *The Fermi level in diamond*, Journal of Physics: Condensed Matter **14**, 3743 (2002).

[48] C. Schreyvogel, V. Polyakov, R. Wunderlich, J. Meijer, and C. E. Nebel, *Active charge state control of single NV centres in diamond by in-plane Al-Schottky junctions*, Scientific Reports **5**, 12160 (2015).

[49] A. Gruber, A. Dräbenstedt, C. Tietz, L. Fleury, J. Wrachtrup, and C. von Borczyskowski, *Scanning Confocal Optical Microscopy and Magnetic Resonance on Single Defect Centers*, Science **276**, 2012 (1997).

[50] J.-P. Tetienne, N. Dontschuk, D. A. Broadway, A. Stacey, D. A. Simpson, and L. C. L. Hollenberg, *Quantum imaging of current flow in graphene*, Science Advances **3**, e1602429 (2017).

[51] B. Grotz, M. V. Hauf, M. Dankerl, B. Naydenov, S. Pezzagna, J. Meijer, F. Jelezko, J. Wrachtrup, M. Stutzmann, F. Reinhard, and J. A. Garrido, *Charge state manipulation of qubits in diamond*, Nature Communications **3**, 729 (2012).

[52] M. Kaviani, P. Deák, B. Aradi, T. Frauenheim, J.-P. Chou, and A. Gali, *Proper Surface Termination for Luminescent Near-Surface NV Centers in Diamond*, Nano Letters **14**, 4772 (2014).

[53] M. V. Hauf, B. Grotz, B. Naydenov, M. Dankerl, S. Pezzagna, J. Meijer, F. Jelezko, J. Wrachtrup, M. Stutzmann, F. Reinhard, and J. A. Garrido, *Chemical control of the charge state of nitrogen-vacancy centers in diamond*, Physical Review B **83**, 081304 (2011).

[54] Y. Doi, T. Makino, H. Kato, D. Takeuchi, M. Ogura, H. Okushi, H. Morishita, T. Tashima, S. Miwa, S. Yamasaki, P. Neumann, J. Wrachtrup, Y. Suzuki, and N. Mizuochi, *Deterministic Electrical Charge-State Initialization of Single Nitrogen-Vacancy Center in Diamond*, Physical Review X **4**, 011057 (2014).

[55] C. J. Bradley and A. P. Cracknell, *The Mathematical Theory of Symmetry in Solids: Representation Theory for Point Groups and Space Groups*, Oxford Classic Texts in the Physical Sciences Oxford University Press, Oxford, New York (2009).

[56] R. S. Mulliken, *Report on Notation for the Spectra of Polyatomic Molecules*, The Journal of Chemical Physics **23**, 1997 (1995).

[57] A. Gali and J. R. Maze, *Ab initio study of the split silicon-vacancy defect in diamond: Electronic structure and related properties*, Physical Review B **88**, 235205 (2013).

[58] M. S. J. Barson, E. Krausz, N. B. Manson, and M. W. Doherty, *The fine structure of the neutral nitrogen-vacancy center in diamond*, Nanophotonics **8**, 1985 (2019).

[59] S. Baier, C. E. Bradley, T. Middelburg, V. V. Dobrovitski, T. H. Taminiau, and R. Hanson, *Orbital and Spin Dynamics of Single Neutrally-Charged Nitrogen-Vacancy Centers in Diamond*, Physical Review Letters **125**, 193601 (2020).

[60] M. Pfender, N. Aslam, P. Simon, D. Antonov, G. Thiering, S. Burk, F. Fávaro de Oliveira, A. Denisenko, H. Fedder, J. Meijer, J. A. Garrido, A. Gali, T. Teraji, J. Isoya, M. W. Doherty, A. Alkauskas, A. Gallo, A. Grüneis, P. Neumann, and J. Wrachtrup, *Protecting a Diamond Quantum Memory by Charge State Control*, Nano Letters **17**, 5931 (2017).

[61] C. J. Meara, M. J. Rayson, P. R. Briddon, and J. P. Goss, *Density functional theory study on magnetically detecting positively charged nitrogen-vacancy center in diamond*, Physical Review B **100**, 104108 (2019).

[62] N. B. Manson and J. P. Harrison, *Photo-ionization of the nitrogen-vacancy center in diamond*, Diamond and Related Materials **14**, 1705 (2005).

[63] N. B. Manson, M. Hedges, M. S. J. Barson, R. Ahlefeldt, M. W. Doherty, H. Abe, T. Ohshima, and M. J. Sellars, *NV^-–N^+ pair centre in 1b diamond*, New Journal of Physics **20**, 113037 (2018).

[64] G. D. Fuchs, V. V. Dobrovitski, D. M. Toyli, F. J. Heremans, C. D. Weis, T. Schenkel, and D. D. Awschalom, *Excited-state spin coherence of a single nitrogen–vacancy centre in diamond*, Nature Physics **6**, 668 (2010).

[65] D. Aude Craik, P. Kehayias, A. Greenspon, X. Zhang, M. Turner, J. Schloss, E. Bauch, C. Hart, E. Hu, and R. Walsworth, *Microwave-Assisted Spectroscopy Technique for Studying Charge State in Nitrogen-Vacancy Ensembles in Diamond*, Physical Review Applied **14**, 014009 (2020).

[66] T. Gaebel, M. Domhan, C. Wittmann, I. Popa, F. Jelezko, J. Rabeau, A. Greentree, S. Prawer, E. Trajkov, P. Hemmer, and J. Wrachtrup, *Photochromism in single nitrogen-vacancy defect in diamond*, Applied Physics B **82**, 243 (2006).

[67] K. Beha, A. Batalov, N. B. Manson, R. Bratschitsch, and A. Leitenstorfer, *Optimum Photoluminescence Excitation and Recharging Cycle of Single Nitrogen-Vacancy Centers in Ultrapure Diamond*, Physical Review Letters **109**, 097404 (2012).

[68] G. Balasubramanian, P. Neumann, D. Twitchen, M. Markham, R. Kolesov, N. Mizuochi, J. Isoya, J. Achard, J. Beck, J. Tissler, V. Jacques, P. R. Hemmer, F. Jelezko, and J. Wrachtrup, *Ultralong spin coherence time in isotopically engineered diamond*, Nature Materials **8**, 383 (2009).

[69] D. A. Hopper, H. J. Shulevitz, and L. C. Bassett, *Spin Readout Techniques of the Nitrogen-Vacancy Center in Diamond*, Micromachines **9**, 437 (2018).

[70] N. Aslam, G. Waldherr, P. Neumann, F. Jelezko, and J. Wrachtrup, *Photo-induced ionization dynamics of the nitrogen vacancy defect in diamond investigated by single-shot charge state detection*, New Journal of Physics **15**, 013064 (2013).

[71] M. W. Doherty, F. Dolde, H. Fedder, F. Jelezko, J. Wrachtrup, N. B. Manson, and L. C. L. Hollenberg, *Theory of the ground-state spin of the nv$^-$ center in diamond*, Physical Review B **85**, 205203 (2012).

[72] V. M. Acosta, E. Bauch, M. P. Ledbetter, A. Waxman, L.-S. Bouchard, and D. Budker, *Temperature Dependence of the Nitrogen-Vacancy Magnetic Resonance in Diamond*, Physical Review Letters **104**, 070801 (2010).

[73] N. B. Manson, J. P. Harrison, and M. J. Sellars, *Nitrogen-vacancy center in diamond: Model of the electronic structure and associated dynamics*, Physical Review B **74**, 104303 (2006).

[74] P. Tamarat, N. B. Manson, J. P. Harrison, R. L. McMurtrie, A. Nizovtsev, C. Santori, R. G. Beausoleil, P. Neumann, T. Gaebel, F. Jelezko, P. Hemmer, and J. Wrachtrup, *Spin-flip and spin-conserving optical transitions of the nitrogen-vacancy centre in diamond*, New Journal of Physics **10**, 045004 (2008).

[75] J. R. Maze, P. L. Stanwix, J. S. Hodges, S. Hong, J. M. Taylor, P. Cappellaro, L. Jiang, M. V. G. Dutt, E. Togan, A. S. Zibrov, A. Yacoby, R. L. Walsworth, and M. D. Lukin, *Nanoscale magnetic sensing with an individual electronic spin in diamond*, Nature **455**, 644 (2008).

[76] L. J. Rogers, R. L. McMurtrie, M. J. Sellars, and N. B. Manson, *Time-averaging within the excited state of the nitrogen-vacancy centre in diamond*, New Journal of Physics **11**, 063007 (2009).

[77] T. A. Abtew, Y. Y. Sun, B.-C. Shih, P. Dev, S. B. Zhang, and P. Zhang, *Dynamic Jahn-Teller Effect in the* NV$^-$ *Center in Diamond*, Physical Review Letters **107**, 146403 (2011).

[78] T. Plakhotnik, M. W. Doherty, and N. B. Manson, *Electron-phonon processes of the nitrogen-vacancy center in diamond*, Physical Review B **92**, 081203 (2015).

[79] T. Plakhotnik, M. W. Doherty, J. H. Cole, R. Chapman, and N. B. Manson, *All-Optical Thermometry and Thermal Properties of the Optically Detected Spin Resonances of the NV– Center in Nanodiamond*, Nano Letters **14**, 4989 (2014).

[80] M. C. Cambria, G. Thiering, A. Norambuena, H. T. Dinani, A. Gardill, I. Kemeny, V. Lordi, A. Gali, J. R. Maze, and S. Kolkowitz, *A physically motivated analytical expression for the temperature dependence of the zero-field splitting of the nitrogen-vacancy center in diamond*, arXiv **2306.05318** (2023).

[81] G. D. Fuchs, V. V. Dobrovitski, R. Hanson, A. Batra, C. D. Weis, T. Schenkel, and D. D. Awschalom, *Excited-State Spectroscopy Using Single Spin Manipulation in Diamond*, Physical Review Letters **101**, 117601 (2008).

[82] P. Neumann, R. Kolesov, V. Jacques, J. Beck, J. Tisler, A. Batalov, L. Rogers, N. B. Manson, G. Balasubramanian, F. Jelezko, and J. Wrachtrup, *Excited-state spectroscopy of single NV defects in diamond using optically detected magnetic resonance*, New Journal of Physics **11**, 013017 (2009).

[83] F. Dolde, M. W. Doherty, J. Michl, I. Jakobi, B. Naydenov, S. Pezzagna, J. Meijer, P. Neumann, F. Jelezko, N. B. Manson, and J. Wrachtrup, *Nanoscale Detection of a Single Fundamental Charge in Ambient Conditions Using the* NV^- *Center in Diamond*, Physical Review Letters **112**, 097603 (2014).

[84] J. Teissier, A. Barfuss, P. Appel, E. Neu, and P. Maletinsky, *Strain Coupling of a Nitrogen-Vacancy Center Spin to a Diamond Mechanical Oscillator*, Physical Review Letters **113**, 020503 (2014).

[85] M. S. J. Barson, P. Peddibhotla, P. Ovartchaiyapong, K. Ganesan, R. L. Taylor, M. Gebert, Z. Mielens, B. Koslowski, D. A. Simpson, L. P. McGuinness, J. McCallum, S. Prawer, S. Onoda, T. Ohshima, A. C. Bleszynski Jayich, F. Jelezko, N. B. Manson, and M. W. Doherty, *Nanomechanical Sensing Using Spins in Diamond*, Nano Letters **17**, 1496 (2017).

[86] G. Kucsko, P. C. Maurer, N. Y. Yao, M. Kubo, H. J. Noh, P. K. Lo, H. Park, and M. D. Lukin, *Nanometre-scale thermometry in a living cell*, Nature **500**, 54 (2013).

[87] N. Aslam, M. Pfender, P. Neumann, R. Reuter, A. Zappe, F. Fávaro de Oliveira, A. Denisenko, H. Sumiya, S. Onoda, J. Isoya, and J. Wrachtrup, *Nanoscale nuclear magnetic resonance with chemical resolution*, Science **357**, 67 (2017).

[88] J. M. Abendroth, K. Herb, E. Janitz, T. Zhu, L. A. Völker, and C. L. Degen, *Single-Nitrogen–Vacancy NMR of Amine-Functionalized Diamond Surfaces*, Nano Letters **22**, 7294 (2022).

[89] M. P. Ledbetter, K. Jensen, R. Fischer, A. Jarmola, and D. Budker, *Gyroscopes based on nitrogen-vacancy centers in diamond*, Physical Review A **86**, 052116 (2012).

[90] A. Jarmola, S. Lourette, V. M. Acosta, A. G. Birdwell, P. Blümler, D. Budker, T. Ivanov, and V. S. Malinovsky, *Demonstration of diamond nuclear spin gyroscope*, Science Advances **7**, abl3840 (2021).

[91] K. O. Ho, K. C. Wong, M. Y. Leung, Y. Y. Pang, W. K. Leung, K. Y. Yip, W. Zhang, J. Xie, S. K. Goh, and S. Yang, *Recent developments of quantum sensing under pressurized environment using the nitrogen vacancy (NV) center in diamond*, Journal of Applied Physics **129**, 241101 (2021).

[92] A. Hilberer, L. Toraille, C. Dailledouze, M.-P. Adam, L. Hanlon, G. Weck, M. Schmidt, P. Loubeyre, and J.-F. Roch, *Enabling quantum sensing under extreme pressure: Nitrogen-vacancy magnetometry up to 130 GPa*, Physical Review B **107**, L220102 (2023).

[93] L. Rondin, J.-P. Tetienne, T. Hingant, J.-F. Roch, P. Maletinsky, and V. Jacques, *Magnetometry with nitrogen-vacancy defects in diamond*, Reports on Progress in Physics **77**, 056503 (2014).

[94] L.-S. Bouchard, V. M. Acosta, E. Bauch, and D. Budker, *Detection of the Meissner effect with a diamond magnetometer*, New Journal of Physics **13**, 025017 (2011).

[95] N. M. Nusran, K. R. Joshi, K. Cho, M. A. Tanatar, W. R. Meier, S. L. Bud'ko, P. C. Canfield, Y. Liu, T. A. Lograsso, and R. Prozorov, *Spatially-resolved study of the Meissner effect in superconductors using NV-centers-in-diamond optical magnetometry*, New Journal of Physics **20**, 043010 (2018).

[96] K. Joshi, N. Nusran, M. Tanatar, K. Cho, W. Meier, S. Bud'ko, P. Canfield, and R. Prozorov, *Measuring the Lower Critical Field of Superconductors Using Nitrogen-Vacancy Centers in Diamond Optical Magnetometry*, Physical Review Applied **11**, 014035 (2019).

[97] Y. Xu, Y. Yu, Y. Y. Hui, Y. Su, J. Cheng, H.-C. Chang, Y. Zhang, Y. R. Shen, and C. Tian, *Mapping Dynamical Magnetic Responses of Ultrathin Micron-Size Superconducting Films Using Nitrogen-Vacancy Centers in Diamond*, Nano Letters **19**, 5697 (2019).

[98] D. A. Broadway, N. Dontschuk, A. Tsai, S. E. Lillie, C. T.-K. Lew, J. C. McCallum, B. C. Johnson, M. W. Doherty, A. Stacey, L. C. L. Hollenberg, and J.-P. Tetienne, *Spatial mapping of band bending in semiconductor devices using in situ quantum sensors*, Nature Electronics **1**, 502 (2018).

[99] M. S. J. Barson, L. M. Oberg, L. P. McGuinness, A. Denisenko, N. B. Manson, J. Wrachtrup, and M. W. Doherty, *Nanoscale Vector Electric Field Imaging Using a Single Electron Spin*, Nano Letters **21**, 2962 (2021).

[100] K. Bian, W. Zheng, X. Zeng, X. Chen, R. Stöhr, A. Denisenko, S. Yang, J. Wrachtrup, and Y. Jiang, *Nanoscale electric-field imaging based on a quantum sensor and its charge-state control under ambient condition*, Nature Communications **12**, 2457 (2021).

[101] B. M. Chernobrod and G. P. Berman, *Spin microscope based on optically detected magnetic resonance*, Journal of Applied Physics **97**, 014903 (2004).

[102] J.-P. Tetienne, T. Hingant, L. Martínez, S. Rohart, A. Thiaville, L. H. Diez, K. Garcia, J.-P. Adam, J.-V. Kim, J.-F. Roch, I. Miron, G. Gaudin, L. Vila, B. Ocker, D. Ravelosona, and V. Jacques, *The nature of domain walls in ultrathin ferromagnets revealed by scanning nanomagnetometry*, Nature Communications **6**, 6733 (2015).

[103] N. Hedrich, K. Wagner, O. V. Pylypovskyi, B. J. Shields, T. Kosub, D. D. Sheka, D. Makarov, and P. Maletinsky, *Nanoscale mechanics of antiferromagnetic domain walls*, Nature Physics **17**, 574 (2021).

[104] E. Schaefer-Nolte, F. Reinhard, M. Ternes, J. Wrachtrup, and K. Kern, *A diamond-based scanning probe spin sensor operating at low temperature in ultra-high vacuum*, Review of Scientific Instruments **85**, 013701 (2014).

[105] D. A. Broadway, S. C. Scholten, C. Tan, N. Dontschuk, S. E. Lillie, B. C. Johnson, G. Zheng, Z. Wang, A. R. Oganov, S. Tian, C. Li, H. Lei, L. Wang, L. C. L. Hollenberg, and J.-P. Tetienne, *Imaging Domain Reversal in an Ultrathin Van der Waals Ferromagnet*, Advanced Materials **32**, 2003314 (2020).

[106] A. Laraoui, H. Aycock-Rizzo, Y. Gao, X. Lu, E. Riedo, and C. A. Meriles, *Imaging thermal conductivity with nanoscale resolution using a scanning spin probe*, Nature Communications **6**, 8954 (2015).

[107] Z. Qiu, A. Hamo, U. Vool, T. X. Zhou, and A. Yacoby, *Nanoscale electric field imaging with an ambient scanning quantum sensor microscope*, npj Quantum Information **8**, 1 (2022).

[108] W. S. Huxter, M. F. Sarott, M. Trassin, and C. L. Degen, *Imaging ferroelectric domains with a single-spin scanning quantum sensor*, Nature Physics **19**, 644 (2023).

[109] L. Robledo, L. Childress, H. Bernien, B. Hensen, P. F. A. Alkemade, and R. Hanson, *High-fidelity projective read-out of a solid-state spin quantum register*, Nature **477**, 574 (2011).

[110] E. Neu, P. Appel, M. Ganzhorn, J. Miguel-Sánchez, M. Lesik, V. Mille, V. Jacques, A. Tallaire, J. Achard, and P. Maletinsky, *Photonic nano-structures on (111)-oriented diamond*, Applied Physics Letters **104**, 153108 (2014).

[111] A. Wickenbrock, H. Zheng, L. Bougas, N. Leefer, S. Afach, A. Jarmola, V. M. Acosta, and D. Budker, *Microwave-free magnetometry with nitrogen-vacancy centers in diamond*, Applied Physics Letters **109**, 053505 (2016).

[112] A. Gupta, L. Hacquebard, and L. Childress, *Efficient signal processing for time-resolved fluorescence detection of nitrogen-vacancy spins in diamond*, Journal of the Optical Society of America B **33**, B28 (2016).

[113] N. R. S. Reddy, N. B. Manson, and E. R. Krausz, *Two-laser spectral hole burning in a colour centre in diamond*, Journal of Luminescence **38**, 46 (1987).

[114] D. Braukmann, E. R. Glaser, T. A. Kennedy, M. Bayer, and J. Debus, *Circularly polarized zero-phonon transitions of vacancies in diamond at high magnetic fields*, Physical Review B **97**, 195448 (2018).

[115] H. Hanzawa, H. Nishikori, Y. Nisida, S. Sato, T. Nakashima, S. Sasaki, and N. Miura, *Zeeman effect on the zero-phonon line of the NV center in synthetic diamond*, Physica B: Condensed Matter **184**, 137 (1993).

[116] D. Braukmann, *Optical Properties of Vacancies in Diamond at High Magnetic Fields*, Ph.D. thesis, TU Dortmund University, Germany (2018).

[117] J. F. Barry, J. M. Schloss, E. Bauch, M. J. Turner, C. A. Hart, L. M. Pham, and R. L. Walsworth, *Sensitivity optimization for NV-diamond magnetometry*, Reviews of Modern Physics **92**, 015004 (2020).

[118] A. Stacey, N. Dontschuk, J.-P. Chou, D. A. Broadway, A. K. Schenk, M. J. Sear, J.-P. Tetienne, A. Hoffman, S. Prawer, C. I. Pakes, A. Tadich, N. P. de Leon, A. Gali, and L. C. L. Hollenberg, *Evidence for Primal sp2 Defects at the Diamond Surface: Candidates for Electron Trapping and Noise Sources*, Advanced Materials Interfaces **6**, 1801449 (2019).

[119] D. J. McCloskey, N. Dontschuk, D. A. Broadway, A. Nadarajah, A. Stacey, J.-P. Tetienne, L. C. L. Hollenberg, S. Prawer, and D. A. Simpson, *Enhanced Widefield Quantum Sensing with Nitrogen-Vacancy Ensembles Using Diamond Nanopillar Arrays*, ACS Applied Materials & Interfaces **12**, 13421 (2020).

[120] D. Rohner, J. Happacher, P. Reiser, M. A. Tschudin, A. Tallaire, J. Achard, B. J. Shields, and P. Maletinsky, *(111)-oriented, single crystal diamond tips for nanoscale scanning probe imaging of out-of-plane magnetic fields*, Applied Physics Letters **115**, 192401 (2019).

[121] H. Zheng, Z. Sun, G. Chatzidrosos, C. Zhang, K. Nakamura, H. Sumiya, T. Ohshima, J. Isoya, J. Wrachtrup, A. Wickenbrock, and D. Budker, *Microwave-Free Vector Magnetometry with Nitrogen-Vacancy Centers along a Single Axis in Diamond*, Physical Review Applied **13**, 044023 (2020).

[122] Z.-H. Zhang, P. Stevenson, G. Thiering, B. C. Rose, D. Huang, A. M. Edmonds, M. L. Markham, S. A. Lyon, A. Gali, and N. P. de Leon, *Optically Detected Magnetic Resonance in Neutral Silicon Vacancy Centers in Diamond via Bound Exciton States*, Physical Review Letters **125**, 237402 (2020).

[123] U. Vool, A. Hamo, G. Varnavides, Y. Wang, T. X. Zhou, N. Kumar, Y. Dovzhenko, Z. Qiu, C. A. C. Garcia, A. T. Pierce, J. Gooth, P. Anikeeva, C. Felser, P. Narang, and A. Yacoby, *Imaging phonon-mediated hydrodynamic flow in WTe2*, Nature Physics **17**, 1216 (2021).

[124] A. Waxman, Y. Schlussel, D. Groswasser, V. M. Acosta, L.-S. Bouchard, D. Budker, and R. Folman, *Diamond magnetometry of superconducting thin films*, Physical Review B **89**, 054509 (2014).

[125] N. J. McLaughlin, H. Wang, M. Huang, E. Lee-Wong, L. Hu, H. Lu, G. Q. Yan, G. Gu, C. Wu, Y.-Z. You, and C. R. Du, *Strong Correlation Between Superconductivity and Ferromagnetism in an Fe-Chalcogenide Superconductor*, Nano Letters **21**, 7277 (2021).

[126] S. Ernst, P. J. Scheidegger, S. Diesch, L. Lorenzelli, and C. L. Degen, *Temperature Dependence of Photoluminescence Intensity and Spin Contrast in Nitrogen-Vacancy Centers*, Physical Review Letters **131**, 086903 (2023).

[127] S. Ernst, P. J. Scheidegger, S. Diesch, and C. L. Degen, *Modeling temperature-dependent population dynamics in the excited state of the nitrogen-vacancy center in diamond*, Physical Review B **108**, 085203 (2023).

[128] S. M. Blakley, T. T. Mai, S. J. Moxim, J. T. Ryan, A. J. Biacchi, A. R. H. Walker, and R. D. McMichael, *Spectroscopy of photoionization from the* ^1E *singlet state in nitrogen-vacancy centers in diamond*, arXiv **2301.10383** (2023).

[129] M. Jamali, I. Gerhardt, M. Rezai, K. Frenner, H. Fedder, and J. Wrachtrup, *Microscopic diamond solid-immersion-lenses fabricated around single defect centers by focused ion beam milling*, Review of Scientific Instruments **85**, 123703 (2014).

[130] D. A. Broadway, J. D. A. Wood, L. T. Hall, A. Stacey, M. Markham, D. A. Simpson, J.-P. Tetienne, and L. C. L. Hollenberg, *Anticrossing spin dynamics of diamond nitrogen-vacancy centers and all-optical low-frequency magnetometry*, Physical Review Applied **6**, 064001 (2016).

[131] L. Robledo, H. Bernien, T. van der Sar, and R. Hanson, *Spin dynamics in the optical cycle of single nitrogen-vacancy centres in diamond*, New Journal of Physics **13**, 025013 (2011).

[132] C. P. Slichter, *Principles of Magnetic Resonance*, Springer, Berlin, Heidelberg (2013).

[133] J.-F. Wang, F.-F. Yan, Q. Li, Z.-H. Liu, H. Liu, G.-P. Guo, L.-P. Guo, X. Zhou, J.-M. Cui, J. Wang, Z.-Q. Zhou, X.-Y. Xu, J.-S. Xu, C.-F. Li, and G.-C. Guo, *Coherent Control of Nitrogen-Vacancy Center Spins in Silicon Carbide at Room Temperature*, Physical Review Letters **124**, 223601 (2020).

[134] B. C. Rose, D. Huang, Z.-H. Zhang, P. Stevenson, A. M. Tyryshkin, S. Sangtawesin, S. Srinivasan, L. Loudin, M. L. Markham, A. M. Edmonds, D. J. Twitchen, S. A. Lyon, and N. P. de Leon, *Observation of an environmentally insensitive solid-state spin defect in diamond*, Science **361**, 60 (2018).

[135] U. F. S. D'Haenens-Johansson, A. M. Edmonds, B. L. Green, M. E. Newton, G. Davies, P. M. Martineau, R. U. A. Khan, and D. J. Twitchen, *Optical properties of the neutral silicon split-vacancy center in diamond*, Physical Review B **84**, 245208 (2011).

[136] J.-P. Tetienne, T. Hingant, J.-V. Kim, L. H. Diez, J.-P. Adam, K. Garcia, J.-F. Roch, S. Rohart, A. Thiaville, D. Ravelosona, and V. Jacques, *Nanoscale imaging and control of domain-wall hopping with a nitrogen-vacancy center microscope*, Science **344**, 1366 (2014).

[137] I. Gross, W. Akhtar, V. Garcia, L. J. Martínez, S. Chouaieb, K. Garcia, C. Carrétéro, A. Barthélémy, P. Appel, P. Maletinsky, J.-V. Kim, J. Y. Chauleau, N. Jaouen, M. Viret, M. Bibes, S. Fusil, and V. Jacques, *Real-space imaging of non-collinear antiferromagnetic order with a single-spin magnetometer*, Nature **549**, 252 (2017).

[138] G. de Lange, D. Ristè, V. V. Dobrovitski, and R. Hanson, *Single-Spin Magnetometry with Multipulse Sensing Sequences*, Physical Review Letters **106**, 080802 (2011).

[139] S. Pezzagna, B. Naydenov, F. Jelezko, J. Wrachtrup, and J. Meijer, *Creation efficiency of nitrogen-vacancy centres in diamond*, New Journal of Physics **12**, 065017 (2010).

[140] A. Haque and S. Sumaiya, *An Overview on the Formation and Processing of Nitrogen-Vacancy Photonic Centers in Diamond by Ion Implantation*, Journal of Manufacturing and Materials Processing **1**, 6 (2017).

[141] P. Appel, E. Neu, M. Ganzhorn, A. Barfuss, M. Batzer, M. Gratz, A. Tschöpe, and P. Maletinsky, *Fabrication of all diamond scanning probes for nanoscale magnetometry*, Review of Scientific Instruments **87**, 063703 (2016).

[142] P. J. Scheidegger, S. Diesch, M. L. Palm, and C. L. Degen, *Scanning nitrogen-vacancy magnetometry down to 350 mK*, Applied Physics Letters **120**, 224001 (2022).

[143] C. Santori, P. Tamarat, P. Neumann, J. Wrachtrup, D. Fattal, R. G. Beausoleil, J. Rabeau, P. Olivero, A. D. Greentree, S. Prawer, F. Jelezko, and P. Hemmer, *Coherent Population Trapping of Single Spins in Diamond under Optical Excitation*, Physical Review Letters **97**, 247401 (2006).

[144] G. Frossati, *Experimental techniques: Methods for cooling below 300 mK*, Journal of Low Temperature Physics **87**, 595 (1992).

[145] C. Bradac, T. Gaebel, N. Naidoo, M. J. Sellars, J. Twamley, L. J. Brown, A. S. Barnard, T. Plakhotnik, A. V. Zvyagin, and J. R. Rabeau, *Observation and control of blinking nitrogen-vacancy centres in discrete nanodiamonds*, Nature Nanotechnology **5**, 345 (2010).

[146] B. K. Ofori-Okai, S. Pezzagna, K. Chang, M. Loretz, R. Schirhagl, Y. Tao, B. A. Moores, K. Groot-Berning, J. Meijer, and C. L. Degen, *Spin properties of very shallow nitrogen vacancy defects in diamond*, Physical Review B **86**, 081406 (2012).

[147] S. Dhomkar, H. Jayakumar, P. R. Zangara, and C. A. Meriles, *Charge Dynamics in near-Surface, Variable-Density Ensembles of Nitrogen-Vacancy Centers in Diamond*, Nano Letters **18**, 4046 (2018).

[148] D. Bluvstein, Z. Zhang, and A. C. B. Jayich, *Identifying and Mitigating Charge Instabilities in Shallow Diamond Nitrogen-Vacancy Centers*, Physical Review Letters **122**, 076101 (2019).

[149] S. Sangtawesin, B. L. Dwyer, S. Srinivasan, J. J. Allred, L. V. H. Rodgers, K. De Greve, A. Stacey, N. Dontschuk, K. M. O'Donnell, D. Hu, D. A. Evans, C. Jaye, D. A. Fischer, M. L. Markham, D. J. Twitchen, H. Park, M. D. Lukin, and N. P. de Leon, *Origins of Diamond Surface Noise Probed by Correlating Single-Spin Measurements with Surface Spectroscopy*, Physical Review X **9**, 031052 (2019).

[150] J. N. Neethirajan, T. Hache, D. Paone, D. Pinto, A. Denisenko, R. Stöhr, P. Udvarhelyi, A. Pershin, A. Gali, J. Wrachtrup, K. Kern, and A. Singha, *Controlled Surface Modification to Revive Shallow NV– Centers*, Nano Letters **23**, 2563 (2023).

[151] P. Welter, J. Rhensius, A. Morales, M. S. Wörnle, C.-H. Lambert, G. Puebla-Hellmann, P. Gambardella, and C. L. Degen, *Scanning nitrogen-vacancy center magnetometry in large in-plane magnetic fields*, Applied Physics Letters **120**, 074003 (2022).

[152] T. X. Zhou, R. J. Stöhr, and A. Yacoby, *Scanning diamond NV center probes compatible with conventional AFM technology*, Applied Physics Letters **111**, 163106 (2017).

[153] R. Hanson, O. Gywat, and D. D. Awschalom, *Room-temperature manipulation and decoherence of a single spin in diamond*, Physical Review B **74**, 161203 (2006).

[154] P. Siyushev, M. Nesladek, E. Bourgeois, M. Gulka, J. Hruby, T. Yamamoto, M. Trupke, T. Teraji, J. Isoya, and F. Jelezko, *Photoelectrical imaging and coherent spin-state readout of single nitrogen-vacancy centers in diamond*, Science **363**, 728 (2019).

[155] L.-L. Yang, L. Liu, X.-Y. Pan, and D.-M. Chen, *Design and Application of a Near Field Microwave Antenna for the Spin Control of Nitrogen-Vacancy Centers*, Chinese Physics Letters **27**, 038401 (2010).

[156] L. Qin, Y. Fu, S. Zhang, J. Zhao, J. Gao, H. Yuan, Z. Ma, Y. Shi, and J. Liu, *Near-field microwave radiation function on spin assembly of nitrogen vacancy centers in diamond with copper wire and ring microstrip antennas*, Japanese Journal of Applied Physics **57**, 072201 (2018).

[157] P. Appel, M. Ganzhorn, E. Neu, and P. Maletinsky, *Nanoscale microwave imaging with a single electron spin in diamond*, New Journal of Physics **17**, 112001 (2015).

[158] M. Mrózek, J. Mlynarczyk, D. S. Rudnicki, and W. Gawlik, *Circularly polarized microwaves for magnetic resonance study in the GHz range: Application to nitrogen-vacancy in diamonds*, Applied Physics Letters **107**, 013505 (2015).

[159] D. Rudnicki, M. Mrózek, J. Młynarczyk, and W. Gawlik, *Microwave spectroscopy for diagnostics of nitrogen vacancy defects in diamond samples*, Photonics Letters of Poland **5**, 143 (2013).

[160] K. Sasaki, Y. Monnai, S. Saijo, R. Fujita, H. Watanabe, J. Ishi-Hayase, K. M. Itoh, and E. Abe, *Broadband, large-area microwave antenna for optically detected magnetic resonance of nitrogen-vacancy centers in diamond*, Review of Scientific Instruments **87**, 053904 (2016).

[161] M. Zhao, Q. Lin, L. Zhu, L. Zhao, and Z. Jiang, *Antenna for microwave manipulation of NV colour centres*, Micro & Nano Letters **15**, 793 (2020).

[162] O. R. Opaluch, N. Oshnik, R. Nelz, and E. Neu, *Optimized Planar Microwave Antenna for Nitrogen Vacancy Center Based Sensing Applications*, Nanomaterials **11**, 2108 (2021).

[163] Z. Li, Z. Li, Z. Shi, H. Zhang, Y. Liang, and J. Tang, *Design of a High-Bandwidth Uniform Radiation Antenna for Wide-Field Imaging with Ensemble NV Color Centers in Diamond*, Micromachines **13**, 1007 (2022).

[164] T. P. M. Alegre, C. Santori, G. Medeiros-Ribeiro, and R. G. Beausoleil, *Polarization-selective excitation of nitrogen vacancy centers in diamond*, Physical Review B **76**, 165205 (2007).

[165] K. Bayat, J. Choy, M. Farrokh Baroughi, S. Meesala, and M. Loncar, *Efficient, Uniform, and Large Area Microwave Magnetic Coupling to NV Centers in Diamond Using Double Split-Ring Resonators*, Nano Letters **14**, 1208 (2014).

[166] J. Herrmann, M. A. Appleton, K. Sasaki, Y. Monnai, T. Teraji, K. M. Itoh, and E. Abe, *Polarization- and frequency-tunable microwave circuit for selective excitation of nitrogen-vacancy spins in diamond*, Applied Physics Letters **109**, 183111 (2016).

[167] N. Zhang, C. Zhang, L. Xu, M. Ding, W. Quan, Z. Tang, and H. Yuan, *Microwave Magnetic Field Coupling with Nitrogen-Vacancy Center Ensembles in Diamond with High Homogeneity*, Applied Magnetic Resonance **47**, 589 (2016).

[168] Y. Masuyama, K. Mizuno, H. Ozawa, H. Ishiwata, Y. Hatano, T. Ohshima, T. Iwasaki, and M. Hatano, *Extending coherence time of macro-scale diamond magnetometer by dynamical decoupling with coplanar waveguide resonator*, Review of Scientific Instruments **89**, 125007 (2018).

[169] X. Yang, N. Zhang, H. Yuan, G. Bian, P. Fan, and M. Li, *Microstrip-line resonator with broadband, circularly polarized, uniform microwave field for nitrogen vacancy center ensembles in diamond*, AIP Advances **9**, 075213 (2019).

[170] V. Yaroshenko, V. Soshenko, V. Vorobyov, S. Bolshedvorskii, E. Nenasheva, I. Kotel'nikov, A. Akimov, and P. Kapitanova, *Circularly polarized microwave antenna for nitrogen vacancy centers in diamond*, Review of Scientific Instruments **91**, 035003 (2020).

[171] G. Mariani, S. Nomoto, S. Kashiwaya, and S. Nomura, *System for the remote control and imaging of MW fields for spin manipulation in NV centers in diamond*, Scientific Reports **10**, 4813 (2020).

[172] J. Rovny, Z. Yuan, M. Fitzpatrick, A. I. Abdalla, L. Futamura, C. Fox, M. C. Cambria, S. Kolkowitz, and N. P. de Leon, *Nanoscale covariance magnetometry with diamond quantum sensors*, Science **378**, 1301 (2022).

[173] C. Degen, J. Boss, K. Chang, and J. Rhensius, *Scanning sensor comprising a spin defect*, Patent WO 2018/167115 A1, World Intellectual Property Organization (2018).

[174] *QZabre*, https://qzabre.com/ (2023).

[175] S. Ragg, C. Decaroli, T. Lutz, and J. P. Home, *Segmented ion-trap fabrication using high precision stacked wafers*, Review of Scientific Instruments **90**, 103203 (2019).

[176] M. Spajer, B. Cavallier, S. Euphrasie, G. Matten, X. Vacheret, P. Vairac, D. Vernier, and A. Jalocha, *Thermoelastic investigation of a quartz tuning fork used in infrared spectroscopy*, Applied Physics Letters **103**, 201111 (2013).

[177] N. V. Vitanov, B. W. Shore, L. Yatsenko, K. Böhmer, T. Halfmann, T. Rickes, and K. Bergmann, *Power broadening revisited: Theory and experiment*, Optics Communications **199**, 117 (2001).

[178] P. Appel, B. J. Shields, T. Kosub, N. Hedrich, R. Hübner, J. Faßbender, D. Makarov, and P. Maletinsky, *Nanomagnetism of Magnetoelectric Granular Thin-Film Antiferromagnets*, Nano Letters **19**, 1682 (2019).

[179] E. C. Jordan and K. G. Balmain, *Electromagnetic Waves and Radiating Systems* Prentice-Hall, Englewood Cliffs, New Jersey (1968).

[180] G. Binnig and H. Rohrer, *Scanning tunneling microscopy*, Surface Science **126**, 236 (1983).

[181] A. Finkler, D. Vasyukov, Y. Segev, L. Neeman, Y. Anahory, Y. Myasoedov, M. L. Rappaport, M. E. Huber, J. Martin, A. Yacoby, and E. Zeldov, *Nano-sized SQUID-on-tip for scanning probe microscopy*, Journal of Physics: Conference Series **400**, 052004 (2012).

[182] L. J. Rogers, K. D. Jahnke, M. W. Doherty, A. Dietrich, L. P. McGuinness, C. Müller, T. Teraji, H. Sumiya, J. Isoya, N. B. Manson, and F. Jelezko, *Electronic structure of the negatively charged silicon-vacancy center in diamond*, Physical Review B **89**, 235101 (2014).

[183] L. J. Rogers, K. D. Jahnke, M. H. Metsch, A. Sipahigil, J. M. Binder, T. Teraji, H. Sumiya, J. Isoya, M. D. Lukin, P. Hemmer, and F. Jelezko, *All-Optical Initialization, Readout, and Coherent Preparation of Single Silicon-Vacancy Spins in Diamond*, Physical Review Letters **113**, 263602 (2014).

[184] J. N. Becker, B. Pingault, D. Groß, M. Gündoğan, N. Kukharchyk, M. Markham, A. Edmonds, M. Atatüre, P. Bushev, and C. Becher, *All-Optical Control of the Silicon-Vacancy Spin in Diamond at Millikelvin Temperatures*, Physical Review Letters **120**, 053603 (2018).

[185] D. D. Sukachev, A. Sipahigil, C. T. Nguyen, M. K. Bhaskar, R. E. Evans, F. Jelezko, and M. D. Lukin, *Silicon-Vacancy Spin Qubit in Diamond: A Quantum Memory Exceeding 10 ms with Single-Shot State Readout*, Physical Review Letters **119**, 223602 (2017).

[186] J. A. Zuber, M. Li, M. Grimau Puigibert, J. Happacher, P. Reiser, B. J. Shields, and P. Maletinsky, *Shallow Silicon Vacancy Centers with Lifetime-Limited Optical Linewidths in Diamond Nanostructures*, Nano Letters **23**, 10901 (2023).

[187] M. Gulka, D. Wirtitsch, V. Ivády, J. Vodnik, J. Hruby, G. Magchiels, E. Bourgeois, A. Gali, M. Trupke, and M. Nesladek, *Room-temperature control and electrical readout of individual nitrogen-vacancy nuclear spins*, Nature Communications **12**, 4421 (2021).

[188] D. J. Christle, A. L. Falk, P. Andrich, P. V. Klimov, J. U. Hassan, N. T. Son, E. Janzén, T. Ohshima, and D. D. Awschalom, *Isolated electron spins in silicon carbide with millisecond coherence times*, Nature Materials **14**, 160 (2015).

[189] N. Mathur, A. Mukherjee, X. Gao, J. Luo, B. A. McCullian, T. Li, A. N. Vamivakas, and G. D. Fuchs, *Excited-state spin-resonance spectroscopy of V_B^- defect centers in hexagonal boron nitride*, Nature Communications **13**, 3233 (2022).

[190] B. J. Shields, Q. P. Unterreithmeier, N. P. de Leon, H. Park, and M. D. Lukin, *Efficient Readout of a Single Spin State in Diamond via Spin-to-Charge Conversion*, Physical Review Letters **114**, 136402 (2015).

[191] M. Pelliccione, B. A. Myers, L. M. A. Pascal, A. Das, and A. C. Bleszynski Jayich, *Two-Dimensional Nanoscale Imaging of Gadolinium Spins via Scanning Probe Relaxometry with a Single Spin in Diamond*, Physical Review Applied **2**, 054014 (2014).

[192] I. Meirzada, Y. Hovav, S. A. Wolf, and N. Bar-Gill, *Negative charge enhancement of near-surface nitrogen vacancy centers by multicolor excitation*, Physical Review B **98**, 245411 (2018).

[193] L. Orphal-Kobin, K. Unterguggenberger, T. Pregnolato, N. Kemf, M. Matalla, R.-S. Unger, I. Ostermay, G. Pieplow, and T. Schröder, *Optically Coherent Nitrogen-Vacancy Defect Centers in Diamond Nanostructures*, Physical Review X **13**, 011042 (2023).

[194] H. Kurokawa, K. Wakamatsu, S. Nakazato, T. Makino, H. Kato, Y. Sekiguchi, and H. Kosaka, *Coherent Electric-Field Control of Orbital state in a Neutral Nitrogen-Vacancy Center*, arXiv **2307.07198** (2023).

[195] J. Görlitz, D. Herrmann, P. Fuchs, T. Iwasaki, T. Taniguchi, D. Rogalla, D. Hardeman, P.-O. Colard, M. Markham, M. Hatano, and C. Becher, *Coherence of a charge stabilised tin-vacancy spin in diamond*, npj Quantum Information **8**, 1 (2022).

[196] J. Forneris, S. Ditalia Tchernij, A. Tengattini, E. Enrico, V. Grilj, N. Skukan, G. Amato, L. Boarino, M. Jakšić, and P. Olivero, *Electrical control of deep NV centers in diamond by means of sub-superficial graphitic micro-electrodes*, Carbon **113**, 76 (2017).

[197] R. Löfgren, R. Pawar, S. Öberg, and J. A. Larsson, *The bulk conversion depth of the NV-center in diamond: Computing a charged defect in a neutral slab*, New Journal of Physics **21**, 053037 (2019).

[198] E. Janitz, K. Herb, L. A. Völker, W. S. Huxter, C. L. Degen, and J. M. Abendroth, *Diamond surface engineering for molecular sensing with nitrogen—vacancy centers*, Journal of Materials Chemistry C **10**, 13533 (2022).

[199] V. Yurgens, J. A. Zuber, S. Flågan, M. De Luca, B. J. Shields, I. Zardo, P. Maletinsky, R. J. Warburton, and T. Jakubczyk, *Low-Charge-Noise Nitrogen-Vacancy Centers in Diamond Created Using Laser Writing with a Solid-Immersion Lens*, ACS Photonics **8**, 1726 (2021).

[200] V. Yurgens, J. Happacher, J. Bocquel, Y. Fontana, T. Jakubczyk, R. J. Warburton, and P. Maletinsky, *Low strain and low charge noise in laser-written nitrogen-vacancy centers in diamond*, In Preparation (2023).

[201] W. Paul, S. Baumann, C. P. Lutz, and A. J. Heinrich, *Generation of constant-amplitude radio-frequency sweeps at a tunnel junction for spin resonance STM*, Review of Scientific Instruments **87**, 074703 (2016).

[202] E. Bourgeois, A. Jarmola, P. Siyushev, M. Gulka, J. Hruby, F. Jelezko, D. Budker, and M. Nesladek, *Photoelectric detection of electron spin resonance of nitrogen-vacancy centres in diamond*, Nature Communications **6**, 8577 (2015).

[203] A. F. Young, C. R. Dean, L. Wang, H. Ren, P. Cadden-Zimansky, K. Watanabe, T. Taniguchi, J. Hone, K. L. Shepard, and P. Kim, *Spin and valley quantum Hall ferromagnetism in graphene*, Nature Physics **8**, 550 (2012).

[204] K. D. Nelson, Z. Q. Mao, Y. Maeno, and Y. Liu, *Odd-Parity Superconductivity in Sr2RuO4*, Science **306**, 1151 (2004).

[205] A. Sipahigil, K. D. Jahnke, L. J. Rogers, T. Teraji, J. Isoya, A. S. Zibrov, F. Jelezko, and M. D. Lukin, *Indistinguishable Photons from Separated Silicon-Vacancy Centers in Diamond*, Physical Review Letters **113**, 113602 (2014).

[206] P. Deák, B. Aradi, M. Kaviani, T. Frauenheim, and A. Gali, *Formation of NV centers in diamond: A theoretical study based on calculated transitions and migration of nitrogen and vacancy related defects*, Physical Review B **89**, 075203 (2014).

[207] P.-J. Hsu, A. Kubetzka, A. Finco, N. Romming, K. von Bergmann, and R. Wiesendanger, *Electric-field-driven switching of individual magnetic skyrmions*, Nature Nanotechnology **12**, 123 (2017).

[208] S. Jiang, J. Shan, and K. F. Mak, *Electric-field switching of two-dimensional van der Waals magnets*, Nature Materials **17**, 406 (2018).

[209] N. Setter, D. Damjanovic, L. Eng, G. Fox, S. Gevorgian, S. Hong, A. Kingon, H. Kohlstedt, N. Y. Park, G. B. Stephenson, I. Stolitchnov, A. K. Taganstev, D. V. Taylor, T. Yamada, and S. Streiffer, *Ferroelectric thin films: Review of materials, properties, and applications*, Journal of Applied Physics **100**, 051606 (2006).

[210] D. G. Schlom, L.-Q. Chen, C.-B. Eom, K. M. Rabe, S. K. Streiffer, and J.-M. Triscone, *Strain Tuning of Ferroelectric Thin Films*, Annual Review of Materials Research **37**, 589 (2007).

[211] C. Lichtensteiger, M. Hadjimichael, E. Zatterin, C.-P. Su, I. Gaponenko, L. Tovaglieri, P. Paruch, A. Gloter, and J.-M. Triscone, *Mapping the complex evolution of ferroelastic/ferroelectric domain patterns in epitaxially strained PbTiO3 heterostructures*, APL Materials **11**, 061126 (2023).

[212] G. Thiering and A. Gali, *Theory of the optical spin-polarization loop of the nitrogen-vacancy center in diamond*, Physical Review B **98**, 085207 (2018).

[213] Á. Gali, *Ab initio theory of the nitrogen-vacancy center in diamond*, Nanophotonics **8**, 1907 (2019).

[214] V. M. Acosta, A. Jarmola, E. Bauch, and D. Budker, *Optical properties of the nitrogen-vacancy singlet levels in diamond*, Physical Review B **82**, 201202 (2010).

[215] M. C. Cambria, A. Norambuena, H. T. Dinani, G. Thiering, A. Gardill, I. Kemeny, Y. Li, V. Lordi, Á. Gali, J. R. Maze, and S. Kolkowitz, *Temperature-Dependent Spin-Lattice Relaxation of the Nitrogen-Vacancy Spin Triplet in Diamond*, Physical Review Letters **130**, 256903 (2023).

[216] D. Manzano, *A short introduction to the Lindblad master equation*, AIP Advances **10**, 025106 (2020).

[217] P. D. Nation, *Steady-state solution methods for open quantum optical systems*, arXiv **1504.06768** (2015).

[218] J. Preskill, *Lecture Notes for Physics 229: Quantum Information and Computation* California Institution of Technology, Pasadena (1998).

[219] S. Scopa, G. T. Landi, A. Hammoumi, and D. Karevski, *Exact solution of time-dependent Lindblad equations with closed algebras*, Physical Review A **99**, 022105 (2019).

[220] T. F. Havel, *Robust procedures for converting among Lindblad, Kraus and matrix representations of quantum dynamical semigroups*, Journal of Mathematical Physics **44**, 534 (2003).

[221] R. D. Grober, J. Acimovic, J. Schuck, D. Hessman, P. J. Kindlemann, J. Hespanha, A. S. Morse, K. Karrai, I. Tiemann, and S. Manus, *Fundamental limits to force detection using quartz tuning forks*, Review of Scientific Instruments **71**, 2776 (2000).

[222] J.-M. Friedt and É. Carry, *Introduction to the quartz tuning fork*, American Journal of Physics **75**, 415 (2007).

[223] J. P. Hadden, J. P. Harrison, A. C. Stanley-Clarke, L. Marseglia, Y.-L. D. Ho, B. R. Patton, J. L. O'Brien, and J. G. Rarity, *Strongly enhanced photon collection from diamond defect centers under microfabricated integrated solid immersion lenses*, Applied Physics Letters **97**, 241901 (2010).

[224] P. Siyushev, F. Kaiser, V. Jacques, I. Gerhardt, S. Bischof, H. Fedder, J. Dodson, M. Markham, D. Twitchen, F. Jelezko, and J. Wrachtrup, *Monolithic diamond optics for single photon detection*, Applied Physics Letters **97**, 241902 (2010).

[225] S. Johnson, P. R. Dolan, T. Grange, A. A. P. Trichet, G. Hornecker, Y. C. Chen, L. Weng, G. M. Hughes, A. A. R. Watt, A. Auffèves, and J. M. Smith, *Tunable cavity coupling of the zero phonon line of a nitrogen-vacancy defect in diamond*, New Journal of Physics **17**, 122003 (2015).

[226] D. Riedel, I. Söllner, B. J. Shields, S. Starosielec, P. Appel, E. Neu, P. Maletinsky, and R. J. Warburton, *Deterministic Enhancement of Coherent Photon Generation from a Nitrogen-Vacancy Center in Ultrapure Diamond*, Physical Review X **7**, 031040 (2017).

[227] E. Janitz, M. Ruf, M. Dimock, A. Bourassa, J. Sankey, and L. Childress, *A Fabry-Perot Microcavity for Diamond-Based Photonics*, Physical Review A **92**, 043844 (2015).

[228] T. K. Yeung, D. Le Sage, L. M. Pham, P. L. Stanwix, and R. L. Walsworth, *Anti-reflection coating for nitrogen-vacancy optical measurements in diamond*, Applied Physics Letters **100**, 251111 (2012).

[229] A. Tallaire, J. Achard, A. Boussadi, O. Brinza, A. Gicquel, I. Kupriyanov, Y. Palyanov, G. Sakr, and J. Barjon, *High quality thick CVD diamond films homoepitaxially grown on (111)-oriented substrates*, Diamond and Related Materials **41**, 34 (2014).

[230] M. Lesik, J.-P. Tetienne, A. Tallaire, J. Achard, V. Mille, A. Gicquel, J.-F. Roch, and V. Jacques, *Perfect preferential orientation of nitrogen-vacancy defects in a synthetic diamond sample*, Applied Physics Letters **104**, 113107 (2014).

[231] K. J. Brown, E. Chartier, E. M. Sweet, D. A. Hopper, and L. C. Bassett, *Cleaning diamond surfaces using boiling acid treatment in a standard laboratory chemical hood*, Journal of Chemical Health and Safety **26**, 40 (2019).

[232] V. Jacques, P. Neumann, J. Beck, M. Markham, D. Twitchen, J. Meijer, F. Kaiser, G. Balasubramanian, F. Jelezko, and J. Wrachtrup, *Dynamic polarization of single nuclear spins by optical pumping of nitrogen-vacancy color centers in diamond at room temperature*, Physical Review Letters **102**, 057403 (2009).

Acknowledgement

The last few years have been an amazing journey for me, full of ups and downs, happiness, disappointment, hard work, and ultimately also success. I learned many new skills, acquired exciting knowledge, and, probably most importantly, learned a lot about myself. I am deeply grateful for everything and would like to take this opportunity to thank everyone who has walked this amazing path with me.

First and foremost, I would like to thank Patrick for his unending support and his prudent supervision. You have been motivating and encouraging me throughout this time and have helped progress this challenging project. Through our discussions, I am able to develop new ideas and draw inspiration. You encouraged independent thinking, supported my ideas, and gave me the freedom to develop myself and pursue a variety of different projects.

Second, I would like to acknowledge my other doctoral committee members. I am very delighted to have such distinguished persons on my committee. Thanks to my second supervisor, Martino, who provided me with valuable input and ideas, as well as supported my extracurricular activities within the physics department during his time as department head. I would also like to thank my external referee, Neil. Thank you for the great discussions in Lausanne and Basel and for sharing your seemingly unending knowledge of NV physics and its history.

Over the years, several people have worked closely with me at the mK setup. However, there was also a longer time span when I was working on my own, which is when I truly came to appreciate the comfort and advantages of being part of a team. Special thanks go to Juanita. We share the same strong passion for science and an unending quest for knowledge. We have spent countless nights and days fabricating or measuring together in the lab, interpreting new data. I also enjoy our conversations about any random bit of knowledge, morals, the economy, and the scientific method. You have a down-to-earth approach, and I really enjoy working with you.

I would also like to thank two other very important people, Dominik and Marcel.li. Thank you, Dominik, for introducing the cryostat to me and the great teamwork on our quest to build a "mK NV magnetometer". I fondly remember our activities together, especially our glacier tour. Thank you also Marcel.li for all the work on the charge stability and the search for solutions and alternatives. You were a good motivator during challenging times. I enjoyed our work together and learned a lot from your extensive experience, particularly in optics. Also, our swim training during lunchtimes in the St. Jakobshallen was great.

A special thanks goes to Brendan for all the late-night discussions, collaborations, exchanges, and our friendship. I learned a lot from you, not only in physics but also in violin making.

Thank you, Mara, for the collaborations, all our discussions, the many climbing sessions, the motorcycle rides, and more.

I thank you, Natascha, for many nice conversations and our joint rooftop garden project, which was awesome.

A thanks goes to Lucas, one of the oldest members of the group, for always having a good joke and telling tales from the origins of the group. Along with this, you shared a lot of technical details with me, and we had good discussions.

I would like to thank Viktoria for our exchanges on NVs, movies, pets, and much more. I enjoyed our collaborations and the sharing of cat pictures.

Thank you, Patrick, for our engaging discussions on physics and beyond while walking around Basel. I think you will never stop trying to convince me to start underwater rugby.

A big thanks goes to the rest of my amazing office mates, Arne, James, and Kai, for creating a great atmosphere not only for work, but also for more or less recreational breaks with fail videos and political discussions. You always had good advice ready.

Thank you, Johannes, for fruitful exchanges and discussions, as well as for helping me make my first figures and sharing your best practices in figure making.

I am also thankful to the rest of the 4K team, Märta and David, for sharing their cryostat for measurements, the exchange, and collaborations.

I would also like to thank all former and present members of the Quantum Sensing Group: Mark, Daniel, Sigurd, Tomasz, Samuel, Josh, Beat, Melissa, Yannick, Lukas, Tobias, Marie, Oliver, Minghao, Silvia, Andrea, Paul, Gleb, Clément, Debarghya, Caroline, and Mykhailo. You create a welcoming environment, a fruitful atmosphere, and a good place to work and live, which I enjoyed very much over the years. I appreciated the mutual assistance and the support, as well as the large collective knowledge pool, which creates a thriving work environment. We also have fun times in and out of the office, especially the joint trip to Montpelier and our rafting trip on the Aare, which I will always remember very fondly, as well as the warm summer days when we go swimming in the Rhine with the "Wickelfisch" and the chain action around the buoys. It is awesome!

Many thanks go to our collaborators from the group of Vincent in Montpellier and Jero in Chile. We had great discussions, and you managed to give new insights and push my understanding further.

I would like to thank the technical and administrative staff at the department. They do a magnificent job of allowing us to concentrate on research. Special thanks goes to Sasha and the team at the mechanical workshop for implementing our challenging designs and giving invaluable advice, to Michael and the staff in the electronics workshop for helping on equipment design, construction, repair work and insights in electronics, to the Nano Imaging Lab, especially to Marcus, for all his help with the FIB sessions filled with good conversations, and to Laurent, Arnold, Beat, Bernd, Germaine, Jenny and Christian for everyday operations.

A big thank you also goes to many other people in the physics department who shared their experiences and knowledge with me or simply engaged in conversations on the rooftop. It is a tight community with a great collaborative spirit.

Finally, I would also like to thank everybody outside of university who accompanied me on this journey over the last few years. I had great times in and outside of Basel. This provided a good balance and stability. Special thank goes to all my friends, my family and partner for their unconditional support during this entire time.